MACROPHYSICAL PROPERTIES AND A CLIMATOLOGY OF ARCTIC COASTAL FOG IN EAST GREENLAND

GAËLLE FLORENCE GILSON
Bachelor of Science, Université catholique de Louvain, 2008
Master of Science, Université libre de Bruxelles, 2010

A Thesis Submitted to
the School of Graduate Studies of
the University of Lethbridge
in Fulfilment of the
Requirements for the Degree

DOCTOR OF PHILOSOPHY

Department of Geography
University of Lethbridge
LETHBRIDGE, ALBERTA, CANADA

MACROPHYSICAL PROPERTIES AND A CLIMATOLOGY OF ARCTIC COASTAL FOG IN EAST GREENLAND

GAËLLE FLORENCE GILSON

Date of Defence: January 26, 2018

Dr. H. Jiskoot Supervisor	Associate Professor	Ph.D.
Dr. C. Hopkinson Thesis Examination Committee Member	Professor	Ph.D.
Dr. M. Letts Thesis Examination Committee Member	Professor	Ph.D.
Dr. J. J. Cassano Thesis Examination Committee Member University of Colorado at Boulder	Associate Professor	Ph.D.
Dr. L. Flanagan Internal External Examiner Department of Biological Sciences	Professor	Ph.D.
Dr. A. Bush External Examiner University of Alberta Edmonton, Alberta	Professor	Ph.D.
Dr. S. Bubel Chair, Thesis Examination Committee	Associate Professor	Ph.D.

DEDICATION

This dissertation is dedicated to my grandparents Denise and André, age 91 and 97.

ABSTRACT

Arctic summer fog is a major transportation hazard and has implications for the cryospheric energy balance. In this thesis, the climatology and macrophysical properties of fog along the coast of East Greenland are explored, and local to mesoscale environmental conditions studied to explain regional differences. Using a combination of long-term synoptic weather observations and Integrated Global Radiosonde Archive data, novel automated methods were developed to classify liquid fog thermodynamic structure and calculate fog top elevation. Six fog types were identified; several of which could be associated with advection fog formation and dissipation processes. Temperature inversions during fog were deeper and stronger compared to non-fog conditions. At Low-Arctic locations fog was geometrically thin and occurred below the temperature inversion. Fog was thicker in the High-Arctic, often penetrating the inversion layer. The radiosonde data analysis and automated methods presented are applicable to any synoptic Arctic weather station with present weather codes.

ACKNOWLEDGEMENTS

My PhD journey was a beautiful challenge and experience that would not have been possible without the help and guidance of many individuals. This thesis is the result of support from a wonderful supervisor, encouraging committee members and colleagues, talented scientists I met at conferences, helpful and empathetic academic staff at the University of Lethbridge, and my generous and loving friends and family.

The person who undoubtedly contributed the most to my success is my dedicated PhD supervisor Dr. Hester Jiskoot. I am extremely thankful that she offered me the opportunity to conduct my PhD under her supervision and become her first PhD student in the Glaciology & Geoscience Lab. Her trust and wisdom carried me all along my PhD journey. With her scientific rigour, creativity and fairness, Hester is an inspiring model. She helped me develop as an academic thanks to her ongoing constructive feedback on all aspects of my thesis and because she offered me exceptional opportunities such as participating in prestigious graduate courses and international conferences. Under her supervision I learned to develop research ideas, write proposals and scientific manuscripts, and prepare effective presentations for conferences or teaching. Her advice went beyond my graduate programme since I also learned about research ethics and to initiate new research projects in collaboration with other scientists. Besides being a great researcher and supervisor, Hester is also a kind and generous person, who had always had a thought for me on celebration days or when I was recovering from my work-related injury. Lastly, I want to thank Hester for her availability and the considerable amount of time that she spent revising draft chapters of this thesis in great detail. I sincerely hope I will have the opportunity to keep collaborating with her beyond the scope of this thesis.

My supportive PhD supervisory committee has also played a crucial role in the accomplishment of this thesis. Drs. Matthew Letts and Chris Hopkinson are highly acknowledged for their time, ongoing encouragement, guidance and critical feedback throughout the years. Chris was very helpful with feedback on funding proposal writing, and is thanked for giving me the opportunity to teach for him, participate in field work, and learn about observation techniques in hydrology. I would like to thank Matt for giving critical feedback on part of this thesis before submission, as well as for encouraging me to seek specific expertise in Arctic boundary-layer processes. Following his suggestions and supported by Hester, I participated in the *Arctic Atmospheric Boundary Layer and Local Climate Processes* course at the University Centre in Svalbard (UNIS), which allowed me to gain the background knowledge that I was missing. During that course I had the great opportunity to meet Dr. John Cassano (CIRES), who kindly offered to become my fourth PhD committee member, and who has since provided invaluable feedback on my research. I am extremely grateful for his time, consideration and advice, and feel honoured to have him as co-author on several manuscripts. Additionally, I would like to particularly thank my two external examiners Drs. Larry Flanagan (University of Lethbridge) and Andy Bush (University of Alberta) for their valuable feedback and thorough review of my thesis.

During my participation in two international PhD courses and various conferences, I was fortunate to meet scientists from across the world whose expertise have contributed to the development of my research ideas and who helped me grow as an academic. I thank Dr. Hans Oerlemans for leading the *2014 Karthaus Summer School on Ice Sheets and Glaciers in the Climate System,* and Dr. Marius Jonassen for allowing me to live the

exceptional experience of participating in a 2016 UNIS graduate course. Fruitful discussions with Dr. Jakob Abermann (Asiaq) directed part of this work towards microwave radiometer data and opened my mind to creative research ideas. I am also grateful to have crossed paths with Dr. Robert Schemenauer (FogQuest), who is a kind and wise man and respected scientist who I was very happy to meet. Our discussions about academic career and life in general were very enlightening. I would like to especially acknowledge him for introducing me to Dr. Ismail Gultepe, one of the top fog scientists in Canada. Dr. Gultepe generously invested a week of his time to talk about fog processes and to show me his extensive suite of fog measuring instruments, which was a unique experience. In addition, he gave me the opportunity to deliver a department seminar during my visit to *Environment and Climate Change Canada*, as well as be part of his EGU-2017 session. He is further highly acknowledged for his co-authorship on the *Boundary-Layer Meteorology* manuscript.

In addition, I would like to acknowledge several scientists who I have not had a chance to meet in person, but who provided me with important information for the achievement of this thesis. I thank Dr. Timothy James for providing his time-lapse images that were an invaluable support to complement my radiosonde data analysis. Dr. Andy Rhines (University of Washington, http://www.stochtastic.com/) is acknowledged for sharing his Matlab script to extract radiosonde data. Dr. Michael Tjernström and John Cappelen provided important information regarding field data and fog measurement techniques.

During my PhD journey, I received a considerable support from colleagues and academics at the University of Lethbridge. I would like to particularly thank Drs. Phil Bonnaventure and Rob Laird who provided advice about data analysis and statistics, and

Drs. Shawn Bubel and Stefan Kienzle for contributing to my PhD comprehensive examination. Orrin Hawke, Ben Fox and Tyrell Nielsen, undergraduate students supervised by Hester, are acknowledged for their help in contributing to the development of some of the Matlab scripts for Chapter 2, researching relevant literature on fog microphysics, and retrieving CALIPSO data. The teaching seminars delivered by Dr. Doug Orr were very instructive, and helpful for developing my teaching and presentation skills. I thank Dr. Wesley Van Wychen for providing me with valuable feedback on oral presentations. All other lab mates, particularly Jade Cooley, are acknowledged for their good and productive working atmosphere. I also want to thank all graduate students I had the pleasure to meet during my stay at the University of Lethbridge, including Charmaine, Colin, Gordon, Dave, Shaghayegh, Nima, Marcus, Ashley, Linda and Thais. In addition, I would like to thank Suzanne McIntosh, Dean Rob Wood, Kathy Schrage and all medical staff for their help, support and accommodation following my work-related injury occurring in the early stages of my PhD.

I acknowledge my funding agencies for making this project possible. This PhD was supported by an NSERC Discovery Grant to Dr. Hester Jiskoot, an Alberta Innovates Technology Futures Graduate Scholarship, and various University of Lethbridge scholarships and awards. Additional funding was through a Women Scholars Award, Gem and Mineral Federation of Canada Scholarship, LPIRG, IASC-NAG and AGU student travel grants, and Karthaus and UNIS funding.

I am eternally grateful to all my former mentors who have inspired me from the beginning, and who encouraged and supported me to pursue an academic career. I sincerely hope to honour them with this thesis. I thank my former supervisors and

professors Drs. Jean-Louis Tison, Frank Pattyn and Tim Papakyriakou for their guidance and inspiration. I would like to give special consideration to Dr. Gauthier Carnat, whose passion for and commitment to Arctic sciences motivated and inspired me throughout my research. I also extend my gratitude to my exceptional former supervisors and professors Dr. Edward Keppens, Dr. Shawn Marshall and Dr. Diane Lavoie, who always believed in my potential and wrote letters of reference in support of my PhD applications. My former colleagues and friends Dr. Leanne Wake, Dr. Yue Huang and Erwan Renaudin are also highly acknowledged for their assistance with my PhD and funding applications. For this I would also like to thank Dr. Elisabeth Varennes and Nicolas Lambert, who also taught me the basics of computer programming.

Finally, this thesis would not have been possible without the help and support from my friends, family and other people who I was very fortunate to meet. I am grateful for all the friends I made in my Department, during the Karthaus summer school, UNIS course and at the various international conferences, particularly Sally, Elina, Jenny, Sharon, and Klara. I would like to thank Jody, Shirley and Hester for hosting me at their house when I encountered accommodation difficulties. I want to thank my awesome roommates and friends Kim and Maggie, and all friends who visited me in Lethbridge. I am grateful for my long-lasting friendship with Ellie, Rongxu, Stéphane and Fatiha, as well as for their emotional support. I particularly thank Rongxu for initiating me to gardening, which brought a lot of serenity into my life.

I would like to give a special thanks to Sue and Bill, my “Canadian parents”, who offered me fun, safety, and peace, and without whom my PhD journey would not have been the same. I am extremely thankful to know them and to be part of their life. I thank them a

thousand times for helping me with stress management, as well as for feeding me during the last few weeks of my thesis writing. I am also thanking all my FACES friends, particularly Megan, Dani and Maximo, for their precious emotional support during my entire PhD. I am very thankful for Joan's generosity when I needed rides to Calgary as part of my recovery.

I want to thank all my Belgian friends for their unconditional support despite the distance, especially Nathalie and James, and in addition Nicole and my godmother Brigitte for their immense emotional support throughout my degree. Claude and Maî-thé, Danielle, Laurent, Andra, Bob Le Marinel and Maribel are also acknowledged. My uncle Dr. Jean-François Van Huele is highly acknowledged for his advice and immense support. Lastly, I want to express gratitude to my mum and my grandparents, who were my best supporters and fans. My mum has been very generous and supportive throughout my PhD. I feel extremely fortunate that both my grandparents are still part of this world today and are able to witness my academic accomplishments. I hope they will be honoured and filled with pride.

TABLE OF CONTENTS

LIST OF TABLES

LIST OF FIGURES

LIST OF ABBREVIATIONS

AMAP	The Arctic Monitoring and Assessment Programme
AO	Arctic Oscillation
ASCOS	The Arctic Summer Cloud Ocean Study
BUFR	The Binary Universal Form for the Representation of meteorological data
CALIOP	Cloud-Aerosol Lidar with Orthogonal Polarization
CALIPSO	Cloud-Aerosol Lidar and Infrared Pathfinder Satellite Observation
DANM	Danmarkshavn
DDM	Dew point Depression Method
D_{Hvap}	Enthalpy of vaporisation
DMI	Danish Meteorological Institute
DMSP	Defense Meteorological Satellite Program
DOY	Day of year calendar
e	Vapour pressure
e_i	Saturation vapour pressure with respect to ice
e_w	Saturation vapour pressure with respect to liquid water
dZ	Geopotential height difference
FTE	Fog top elevation
FTP	Fog top pressure
FTT	Fog top temperature
g	Gravitational acceleration
GBI	Greenland Blocking Index
G_s	Subsurface heat flux
IGRA	Integrated Global Radiosonde Archive
ITTO	Ittoqqortoormiit
IWC	Ice water content
LHF	Latent heat flux
Lidar	Light Detection and Ranging
LLI	Low-level inversion
LWC	Liquid water content
LW_{in}	Downwelling longwave radiation
LW_{out}	Outgoing longwave radiation
METAR	Aviation Routine Weather Reports
MODIS	Moderate-Resolution Imaging Spectroradiometer
MRM	Mixing Ratio Method
MWR	Microwave radiometer
μ	Virtual potential temperature gradient
μ_s	Virtual potential temperature gradient of the surface layer
n	Number of observations
NaN	Missing observation
NAO	North Atlantic Oscillation
N_d	Cloud droplet number concentration
N_i	Ice crystal number concentration
NOAA	National Oceanic and Atmospheric Administration
N_{sat}	Number of saturated sounding levels
NSIDC	National Snow and Ice Data Center

P_0	Pressure of the ground level
PRINS	Prins Christian Sund
P_{sat}	Pressure of the uppermost saturated level
ΔP	Pressure difference
Q_M	Energy available for melt (residual)
r	Mixing ratio
R	Ideal gas constant
RH	Relative humidity
RH_i	Relative humidity with respect to ice
RH_w	Relative humidity with respect to liquid water
r_i	Saturation mixing ratio with respect to ice
r_w	Saturation mixing ratio with respect to liquid water
SBI	Surface-based inversion
SHEBA	Surface Heat Budget of the Arctic Ocean
SHF	Sensible heat flux
SIC	Sea ice concentration
SMMR	Scanning Multichannel Microwave Radiometer
SODAR	Sonic Detection and Ranging
SSM/I-SSMIS	Special Sensor Microwave Imager/Sounder
SST	Sea surface temperature
SW_{in}	Downwelling shortwave radiation
SW_{out}	Reflected shortwave radiation
SW_{bs}	Shortwave radiation absorbed by the surface
T	Dry-bulb temperature
TASI	Tasiilaq
T_d	Dew point temperature
T_{dd}	Dew point depression
T_{dds}	Surface dew point depression
ΔT	Inversion intensity
Θ_v	Virtual potential temperature
UTC	Coordinated Universal Time
vv	Horizontal visibility
w_d	Wind direction
WMO	World Meteorological Organization
w_s	Wind speed
ww	Present weather
Z	Geopotential height
Z_0	Geopotential height of the ground level
Z_{base}	Inversion base elevation
Z_{sat}	Geopotential height of the uppermost saturated level
Z_{top}	Inversion top elevation
ΔZ	Inversion depth

STATEMENT OF CO-AUTHORSHIP

The three results chapters of this thesis (Chapters 2-4) were prepared as separate manuscripts with the aim of being submitted to peer-reviewed journals. Chapter 3 has been submitted and is currently in review. Chapters 2 and 4 were prepared as paper-based thesis chapters but will be considerably shortened for future submission. I was the first author of all three chapters and was in charge of the methodological approach, data analysis, interpretation and writing. My PhD supervisor, Dr. Hester Jiskoot, provided guidance on all chapters, including on the conceptualisation, methodology and structure and writing of each chapter. Contributions from other co-authors are described below.

Chapter 2 is planned to be submitted in a reduced form to a climatology journal with three co-authors. The first co-author will be Dr. H. Jiskoot who supervised and helped in guiding this work. The other two co-authors will be Soukeyna Gueye, who did preliminary analysis on the climatology of fog in East Greenland, and Dr. J. van Boxel (University of Amsterdam) who co-supervised Gueye's work with Dr. H. Jiskoot in 2013-2014. Neither of these future co-authors had any input in the development or writing of the thesis chapter.

An earlier version of Chapter 3 was submitted to the journal Boundary-Layer Meteorology under the title "The Thermodynamic Structure of Arctic Coastal Fog Occurring during the Melt Season over East Greenland" and has four co-authors: Dr. Hester Jiskoot (PhD supervisor), Dr. John Cassano (PhD committee member), Dr. Ismail Gultepe (Environment and Climate Change Canada) and Dr. Timothy James (Swansea /

Queen's University). Dr. J. Cassano provided guidance on the methodology and interpretation of results, Dr. I. Gultepe provided guidance on process interpretation aspects, and Dr. T. James provided the time-lapse images helping in the identification and understanding of fog processes in East Greenland. All co-authors also provided general feedback on the structure and writing of the submitted manuscript.

Chapter 4 will be submitted in a reduced form to a geophysical journal with three co-authors. The first two co-authors are Dr. H. Jiskoot and Dr. J. Cassano, who both provided methodological guidance in this work. Dr. J. Cassano offered additional guidance in the results interpretation. The fourth co-author Tyrell Nielsen, undergraduate student supervised by Dr. H. Jiskoot in summer 2017, extracted CALIPSO data for the validation of the methodology presented in this chapter.

"The best prophet of the future is the past."

– Lord Byron

CHAPTER 1. INTRODUCTION

1.1 Motivation

1.1.1 Importance of fog for humans and ecosystems

Fog poses a major hazard for transportation because it reduces horizontal visibility and it is hard to forecast (Bendix, 1995). It is responsible for economic losses equivalent to those of hurricanes (Gultepe et al., 2007). In the Arctic, fog also impacts traffic safety, particularly affecting the aviation industry (Gultepe et al., 2014). Fog is associated with pollutant transportation, including sea salt and heavy metals that can be deleterious to human health, crops and ecosystems (Inoue et al 1997; Sträter et al., 2010). As a consequence, fog in urban areas is often associated with poor air quality (e.g. Meng et al., 2010). Fog over land has decreased over the past decades, possibly due to the combination of global and regional increases in temperature and an increase in air quality (Klemm and Lin, 2016). Over the oceans, fog has become more frequent because warmer and ice-free oceans evaporate more water and, as dictated by the Clausius-Clapeyron equation, warmer air can contain more moisture (Kawai et al., 2016; Vihma et al., 2016). With the reduction in summer sea ice, fog is expected to increase over the Arctic seas (Palm et al., 2010; Vavrus et al., 2011), with direct impacts for the new sea routes such as the Northwest Passage.

Despite these adverse effects, fog also has beneficial impacts on human communities and ecosystems in arid environments through its influence on the hydrological cycle. Fog has

both positive and negative influences on plant growth, especially in (semi-)arid regions including Polar regions (e.g. Gajanada et al., 2007). While photosynthesis is decreased due to lower shortwave radiation amounts, evapotranspiration is also reduced. Fog water can also be deposited on leaves and directly be absorbed by plants, providing both freshwater and essential nutrients (e.g. Lange, 2003). Fog therefore constitutes an important freshwater supply in semi-arid to arid environments, sometimes providing the majority of freshwater to flora (Desmet and Cowling, 1999; Garreaud et al., 2008; Hill et al., 2015), therefore also influencing higher trophic levels in these habitats. Additionally, some desert beetles have developed mechanisms to directly uptake fog water from the air (Guadarrama-Cetina et al., 2014). The beneficial ecological role of fog is not limited to arid regions at low latitudes. In coastal Polar regions also, fog can contribute to plant growth and metabolic activity (Billings and Peterson, 1992; Gajananda et al., 2007). The study of fog collection mechanisms in arid ecosystems has inspired humans to develop fog collectors for human use (e.g. Parker and Lawrence, 2001; Ju et al., 2013). Fog and dew are nowadays becoming important freshwater supplies for communities in semi-arid and arid regions around the world (e.g. LeBoeuf and de la Jara, 2014; Baguskas and Loik, 2015; Fessehaye et al., 2017).

1.1.2 Importance of fog for the cryosphere

The Arctic has been receiving a lot of consideration because of its vulnerability to climate change and implications for global climate (e.g. IPCC, 2013; AMAP, 2017). The enhanced warming of the Arctic, or Arctic Amplification, has resulted in recent increases in temperature at twice the rate of the global average and is driven by a variety of climatic

feedbacks (Serreze and Barry, 2011; Pithan and Mauritsen, 2014; AMAP, 2017). Although Arctic clouds are an important climate feedback, cloud-feedback does not constitute a first-order control on Arctic Amplification (e.g. Kay et al., 2016). However, fog and low clouds do play a major role in the Arctic surface energy budget, particularly on the cryospheric components, through their influence on the surface energy balance (Klein and Hartmann, 1993; Curry et al., 2000; Eastman and Warren, 2010; Cesana et al., 2012). The energy available for glacier and sea ice, firn and snow melt Q_M (in W m^{-2}) is calculated with the surface energy balance equation:

$$Q_M = SW_{in} + SW_{out} + LW_{in} + LW_{out} + SHF + LHF + G_s, \qquad \text{(Equation 1-1)}$$

where SW_{in} is the incoming shortwave radiation, SW_{out} the reflected shortwave radiation, LW_{in} the incoming longwave radiation, LW_{out} the outgoing longwave radiation, SHF the sensible heat flux, LHF the latent heat flux and G_s the subsurface heat flux (usually negligible on glaciers: Hock, 2005). For glaciological applications, fluxes are positive when directed towards the glacier surface, while for meteorological applications the convention is reversed. If Q_M is negative, there is a net loss (gain) of energy from the surface (atmosphere), whereas if Q_M is positive and ice, firn, or snow temperature has been raised to the melting point, glacier melt can occur and there is a net loss of energy from the atmosphere.

Fog is often associated with temperature inversions (i.e. increase of temperature with elevation: Oke, 1987). Fog and temperature inversions affect glacier, sea ice and snow melt rates through their direct or indirect influence on several components of the surface energy balance equation (Equation 1-1 and Figure 1-1). Direct influences include the

cloud albedo effect, reducing SW_{in}, and the cloud longwave radiation forcing, trapping the longwave radiation emitted by the Earth's surface (LW_{out}) and backscattering it to the surface (LW_{in}). Fog and temperature inversions both have an indirect effect on LW_{in} and *SHF* by influencing the air temperature. Fog can also affect *LHF* through its influence on the vapour gradient. If very dense fog is present, the air can become supersaturated and condensation can occur. The energy released in the surrounding environment by this process raises the ice temperature and can contribute to glacier melt (e.g. Hock and Holmgren, 1996). Temperature inversions and fog also influence each other, but the exact influence remains an open question (Mernild et al., 2008; Hulth et al., 2010). During the Arctic melt season, the advection of cold oceanic air over coastal areas both creates temperature inversions, because the cold and dense air settles below the warmer air of the land (Busch et al., 1982), and brings fog inland (Alt, 1979). The vertical structure of the boundary layer and the presence of temperature inversions also determines the vertical extent of fog.

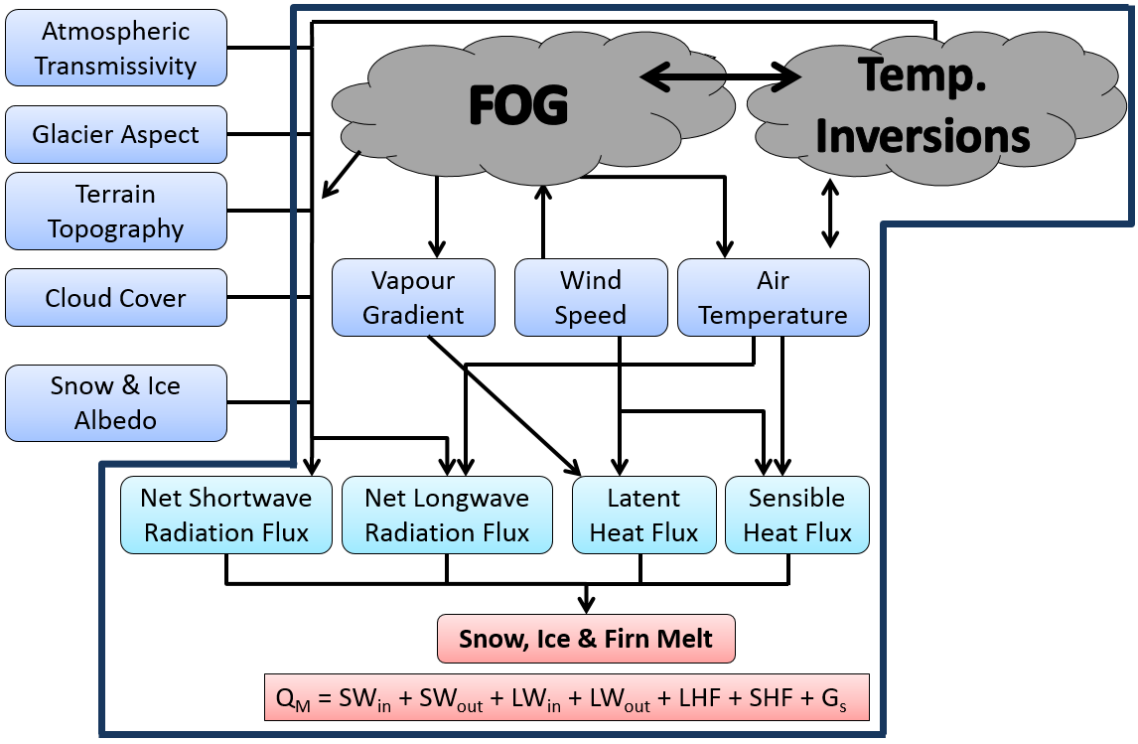

Figure 1-1. Schematic of the effect of fog and temperature inversions on glacier surface energy balance. Variables outside the thick line box are factors other than fog and temperature inversions influencing the glacier surface energy balance. Double arrows indicate two-way relationships, and single arrows unidirectional influences. Each variable influences one or more components of the glacier surface energy balance equation (see also Equation 1-1). Q_M is the energy available for melt in W m^{-2}.

Several studies have highlighted reduced glacier melt due to the presence of sea fog and temperature inversions (Alt, 1979, Braun et al., 2004; Koerner, 2005; Mernild et al., 2008; Hulth et al., 2010; Mernild and Liston, 2010). However, temperature inversions and fog are sometimes associated with increased melt over sea ice surfaces (Chutko and Lamoureux, 2009; Tjernström et al., 2015).

Because many glaciers are located, or terminate, in coastal Arctic regions, and glacier melt occurs in summer when solar radiation and ocean and atmospheric temperatures are at their maximum (Nilsson and Bigg, 1996), and glacier albedo at the minimum, sea fog

can potentially significantly influence the ablation over those glaciers (Jiskoot et al., 2012). Although the effects of clouds have recently been incorporated into current glacier and ice sheet surface energy balance models (e.g. Jiskoot and Mueller, 2012; Conway and Cullen, 2016; Van Tricht et al., 2016), neither fog radiative effects nor temperature inversions are accounted for, and the traditionally assumed linear lapse rate may not accurately predict glacier melt rate (Hulth et al., 2010). It is therefore important to improve the understanding of Arctic fog and related temperature inversions in order to refine glacier melt calculations (Mernild and Liston, 2010). Also, a better understanding of fog processes in the Arctic is necessary to improve fog forecasting and nowcasting, hence transportation safety, in those remote regions.

1.2 Background

1.2.1 The definition, characteristics and classifications of fog

1.2.1.1 Definition

Fog is a low-level hydrometeor with the base at or very near the Earth's surface. It is composed of suspended liquid or supercooled water droplets or ice crystals that lead to a reduction of horizontal visibility below 1000 m (NOAA, 1995; WMO, 1995). Although fog is often classified as a low-level stratiform cloud, fog and clouds are strictly speaking different types of hydrometeor (WMO, 2017). Based on visibility ranges, fog can be classified in up to four categories: light fog (> 1000 m, or > 5/8 mile = mist), moderate fog (500 - 1000 m, or 5/16-5/8 mile), thick fog (320-500 m, or 1/5-5/16 mile), and dense/heavy fog (< 320 m, or < 1/5 mile) (Baliles, 1959). The visibility threshold between

fog and mist is somewhat arbitrary, and in practice both can have a visibility range of 1-5 km (Baliles, 1959; NOAA, 1995). For traffic safety applications, dense fog is usually defined as causing a visibility lower than 400 m (e.g. Friedlein, 2004; LaDochy, 2005; Hautiére et al., 2006). Following Baliles (1959), fog is defined as having horizontal visibility < 1000 m and dense fog is classified as visibility < 500 m.

1.2.1.2 Microphysical properties

The formation of liquid fog requires condensation of liquid water onto condensation nuclei, and thus requires both saturation of the air and the presence of aerosol particles near the Earth's surface.

Saturation with respect to liquid water refers to the state of equilibrium between the water vapour and a liquid water surface. It is expressed by the mixing ratio r (g kg^{-1}):

$$r = 0.622 \frac{e}{P-e}, \qquad \text{(Equation 1-2)}$$

where e is the vapour pressure (mb) and P is the atmospheric pressure (mb). P-e represents the dry air pressure.

Saturation is reached when the mixing ratio r becomes equal to the saturation mixing ratio with respect to liquid water r_w (g kg^{-1}), which is a function of both T and P:

$$r = r_w(T, P) = 0.622 \frac{e_w}{P-e_w}, \qquad \text{(Equation 1-3)}$$

where T is the dry-bulb air temperature (K) and e_w the saturation vapour pressure with respect to liquid water (mb).

The saturation vapour pressure e_w is a function of T, which is expressed in the well-known Clausius-Clapeyron relation:

$$ln\left(\frac{e_{w_1}}{e_{w_2}}\right) = \frac{D_{Hvap}}{R}\left(\frac{1}{T_2} - \frac{1}{T_1}\right), \qquad \text{(Equation 1-4)}$$

where D_{Hvap} is the enthalpy of vapourisation, R is the ideal gas constant (8.3145 J mol^{-1} K^{-1}), and e_{w1} and e_{w2} are saturation vapour pressures corresponding to temperatures T_1 and T_2, respectively. T_1 and T_2 are different temperatures at local or regional spatial scales.

The state of saturation in the air is expressed in terms of relative humidity with respect to liquid water RH_w:

$$RH_w = 100\ \frac{e}{e_w} \qquad \text{(Equation 1-5)}$$

RH_w during fog is generally near 100 % over mid-latitudes. In the Arctic, where subzero temperatures are common, RH_w can be lower than 100 % while the air is saturated with respect to ice ($RH_i \geq 100$ %) (Hardy, 1998). The air can become saturated with respect to ice without being saturated with respect to liquid water because the saturation mixing ratio with respect to ice r_i (g kg^{-1}) is smaller than r_w for a given T (Triplet and Roche, 1986). In this particular case, Equation 1-3 becomes:

$$r = r_i(T, P) = 0.622\frac{e_i}{P - e_i}\ , \qquad \text{(Equation 1-6)}$$

where e_i is the saturation vapour pressure with respect to ice (mb).

In this case, Equation 1-5 becomes:

$$RH_i = 100\ \frac{e}{e_i} \qquad \text{(Equation 1-7)}$$

From the above relationships it can be derived that three mechanisms can lead to saturation and subsequent condensation: (1) the addition of water vapour to the air, (2) cooling of the air to its dew point temperature, or (3) mixing of two air parcels close to saturation.

Low visibility is an important parameter related to fog because it is responsible for important economic losses due to traffic disruptions and accidents (e.g. Gultepe et al., 2007). The reduction of visibility due to the suspension of water droplets (or ice crystals) in the air has been measured in the field and parameterised as a function of both the liquid (or ice) water content and the water (or ice) droplet number concentration (Gultepe et al., 2006; Gultepe et al., 2014; Gultepe et al., 2015). Visibility for liquid fog is parameterised as follows:

$$vv = \frac{1.002}{(LWC \times N_d)^{0.6473}}, \qquad \text{(Equation 1-8)}$$

where *vv* is the horizontal visibility (km), *LWC* is the liquid water content (g m^{-3}) and N_d the cloud droplet number concentration (cm^{-3}) (Gultepe et al., 2006).

Under very cold conditions (T < -30°C: ice fog), only ice crystals are present so that the moisture content is described in terms of ice water content. Visibility in ice fog can then be parameterised with the following equation for ice crystals between 10-200 µm in size:

$$vv = \frac{1.19}{(IWC \times N_i)^{0.5066}}, \qquad \text{(Equation 1-9)}$$

where *IWC* is the ice water content (g m^{-3}) and N_i the ice crystal number concentration (cm^{-3}) (Gultepe et al., 2014: Eq. 1).

For particles smaller than 50 μm another parameterisation of *vv* in ice fog is given (Gultepe et al., 2015: Eq. 6):

$$vv = \frac{0.24}{(IWC \times N_i)^{0.5147}} \qquad \text{(Equation 1-10)}$$

Fog microphysical properties depend on the conditions in which fog forms, hence they are significantly different over land and over sea (Gultepe et al., 2009). For example, N_d is highly variable in marine fog (Lewis, 2004). The droplet radius size depends on the amount of water and the number of condensation nuclei available. Marine fog forms on marine aerosols, such as sea salt and sulfuric acid, and is composed of fewer condensation nuclei, therefore forming bigger water droplets than in the case of land fog. As a result, sea fog is generally denser and leads to a lower visibility compared to land fog. Since fog formation requires condensation, RH_w of the air is generally at 100 %. However, RH_w can be lower than 100 % in marine fog because water droplets condense on soluble aerosols. Droplet effective size for mid-latitude marine fog is below 30 μm in 90 % of the time (Gultepe et al., 2006; Gultepe et al., 2009). A few measurements made at McMurdo Station, Antarctica, during the austral summer, revealed a range in droplet size of 2.5-3.8 μm, which is less than approximately half the size of droplets measured by Gultepe et al.

(2009) in marine fog off the coast of Nova Scotia, Canada. Several studies have been conducted on the droplet size of summer Arctic coastal fog in Alaska and Greenland. Over Barrow, Alaska, Kumai (1973) found fog to have a wide range of droplet sizes between 3.3-65 μm, a maximum N_d of 24 droplets cm^{-3} and *LWC* values up to 0.15 g m^{-3}. Over Greenland, measured ranges of droplet effective size, N_d and *LWC* were 1-33 μm, 3-18 droplets cm^{-3} and 0.02-0.17 g m^{-3}, respectively (Reiquam and Diamond, 1959; Kumai and Francis, 1962). Values of *LWC* in Arctic marine fog are typically lower than in mid-latitude marine fog because of the lower specific humidity of the air at lower temperatures (e.g. Kawai et al., 2016). N_d is also typically lower over Polar regions, where the aerosol loading can even be a limiting factor for condensation and fog formation (Mauritsen et al., 2011).

1.2.1.3 Classifications of fog

Fog can be classified based on its temperature (T) as warm fog (T > -10°C) or cold fog (T < -10°C) (Petterssen, 1956). Warm fog consists of liquid water droplets (liquid fog: T > 0°C) or supercooled water droplets (freezing fog: T < 0°C). Cold fog includes mixed-phase fog (T > -30°C) and ice fog (T < -30°C). Mixed-phase fog is composed of supercooled water droplets and ice crystals, whereas ice fog is formed from the deposition of water vapour onto ice nuclei. Ice fog is mainly observed in the Arctic winter under clear-sky and calm conditions. Liquid fog has a significantly larger radiative effect on the Arctic surface energy budget than ice fog has due to the higher emissivity of liquid water (Cesana et al., 2012). Chapter 2 of this thesis will present summer fog types in coastal East Greenland, based on statistics of fog temperature.

Fog can also be classified based on the processes leading to its formation, with the most common types being radiation, advection, and steam or evaporation fog (Gultepe et al., 2007; WMO, 2017). *Radiation fog* forms overnight, by radiative cooling of the Earth surface to dew point temperature, and under conditions of subsidence and light wind to calm conditions. In the morning, the solar elevation angle is low and sun rays are reflected at the fog top thus keeping the atmosphere inside the fog layer cool. During the day, the sun warms the fog which raises the saturation vapour pressure and evaporates droplets, eventually penetrating the fog and leading to its dissipation. This dissipation mechanism occurs in all fog types. *Advection fog*, also called *sea fog* or *marine fog*, is a type of fog which forms when a warm moist marine air mass travels over a cold surface, which can be a cooler water mass, sea ice, or land surface. The dry-bulb temperature of the air mass decreases as mixing occurs in contact with the cold surface. Saturation is reached and fog can form once the dry-bulb temperature decreases to the dew point temperature value of the air mass. *Steam* or *evaporation fog* originates from the presence of cold air with low water vapour pressure over warmer water. As a result of the difference in water vapour pressure, evaporation occurs and mixing allows the cold air to become supersaturated and form fog by condensation (Saunders, 1964; Gultepe et al., 2007). Over marine waters steam fog is also coined *sea smoke*. Other fog types include valley, upslope, hill and frontal fog (WMO, 2017). *Valley fog* occurs in valley bottoms or topographic depressions due to differential cooling, but usually dissipates in late morning hours (e.g. Dorninger et al., 2011). *Upslope fog* forms as moist air masses are forced to ascend and cool adiabatically until saturation is reached. *Hill fog* is when a cloud base is lower than the tops of hills or mountains (e.g. Camanchacas in Chile: Garreaud et al.,

2008); this fog may be viewed from below as a stratus cloud deck (WMO, 2017). *Frontal fog* or *precipitation fog* is formed when warm rain falls in colder air, such as under warm frontal inversions (Toth et al., 2010). Saturation occurs through evaporation of warm droplets that add water vapour and saturate the cold surrounding air. Chapter 3 of this thesis will analyse fog types and processes occurring in coastal East Greenland during the Arctic melt season from upper-air data analysis.

1.2.1.4 Macrophysical properties

Fog can be a very local phenomenon as well as cover an entire country. In the Arctic, our understanding of the spatial extent of fog is limited because most measurements are made at specific locations or over small areas (Przybylak, 2016). Satellite imagery provides an opportunity to quantify fog spatial extent, although it is difficult to distinguish from low stratus clouds (Bendix, 1995; Gultepe et al., 2007). Determination of fog spatial extent has been done over mid-latitude regions using Moderate-Resolution Imaging Spectroradiometer (MODIS) (Bendix et al., 2005) and the Cloud-Aerosol Lidar and Infrared Pathfinder Satellite Observation (CALIPSO) (Kawai et al., 2015; Cermak, 2016). Lazzara (2008) developed a fog detection method from MODIS over Antarctica using principal component analysis, but did not quantify fog coverage over large areas. Jiskoot et al. (2015) modified the MODIS fog detection algorithm developed by Bendix et al. (2005) and applied it to East Greenland. Results from case studies showed that advection fog can penetrate up to 90 km inland and a fog event can cover up to 5000 km^2 of glacierized terrain (Jiskoot et al., 2015).

Radiation fog, formed by radiative cooling of the ground, can be as shallow as 1 m thick or can reach thicknesses over 150 m (Bendix et al., 2005). Advection fog is generally the most vertically extensive fog type. Over both mid-latitude and Polar regions, advection fog can reach elevations of 200-700 m a.s.l., thus fog thickness up to several hundreds of metres (e.g. Gajananda et al., 2007; Gao et al., 2007; Huang et al., 2015; Tjernström et al., 2015; Sotiropoulou et al., 2016).

Apart from steam fog, which occurs in a convective boundary-layer (Pilié et al., 1979), fog often displays a sharp top level because it occurs under stable boundary-layer conditions (Koračin, 2017). Fog therefore frequently occurs concurrently with low-level tropospheric temperature inversions (i.e. increase of temperature with elevation: Oke, 1987). The most common process leading to the establishment of temperature inversions is radiative cooling over land which occurs frequently at night or in winter. In summer, or during the day, common mechanisms of temperature inversions involve subsidence or advection processes (Busch et al., 1982). Temperature inversions are characterised by their base height, top height and intensity. The inversion base height gives useful indication of the geostrophic drag coefficient (Overland, 1985), which has important consequences for boundary-layer dynamics (Oke, 1987). Knowledge of the inversion top height is useful for aerosols and pollution tracking (Oke, 1987; Shaw, 1995), tropospheric ozone destruction monitoring (Tarasick and Bottenheim, 2002) as well as surface energy balance considerations (Mernild and Liston, 2010, O'Neill et al., 2015; Smith and Bonnaventure, 2017). The inversion intensity, the temperature difference between the top and the bottom of the inversion, influences turbulent heat and moisture fluxes between the low atmosphere and the surface (Oke, 1987; Zhang et al 2011; Pithan et al., 2014).

1.2.2 Geography of fog

Observations of fog are commonly done with the use of WMO present weather codes from synoptic weather stations worldwide, which include ship measurements (Dorman et al., 2017), and Aviation Routine Weather Reports (METAR) (e.g. Pagowski et al., 2004). Details of the identification of fog from WMO present weather codes are given in Chapter 2. Global distributions of land and marine fog from a combination of these sources are summarised in Figures 1-2 and 1-3, respectively. Note that observations of fog over land include coastal regions, which are influenced by the advection of fog of oceanic origin (e.g. Cappelen et al., 2001). The general global pattern of fog frequency can be summarised as follows. As a note of caution, land fog seems to be overrepresented in densely populated areas due to a bias in the density of weather observations. In addition, urban areas have higher pollution levels and thus more condensation nuclei (e.g. Klemm and Lin, 2016). In winter, radiation fog, including valley fog, is common in central Europe. Fog is also frequent in coastal areas where moderate topography (1000-2000 m a.s.l.) allows ascending air to condensate (upslope fog). Typical examples include Germany, Poland, Taiwan, Korea, California and Oregon. Additionally, fog is occasionally observed in winter over less populated regions, such as the Arctic and Antarctica. During the summer months, the majority of fog occurs along coasts or in areas of moderate topography, and advection fog and upslope fog are frequent in coastal mountain ranges bordering cold oceanic upwelling zones. This is the case for the Chilean and Namibian coasts, where fog water is also an important freshwater resource (see Sect. 1.1.1).

Summer coastal fog frequently occurs across the Arctic (Figure 1-2b) and along the Antarctic Peninsula (Figure 1-2a) due to the presence of cold polar oceanic currents and broken sea ice (Dorman et al., 2017). The highest marine fog frequencies are encountered in summer under stable boundary-layer conditions overlying cold oceanic currents (Dorman et al., 2017). In the northern hemisphere, these conditions occur in the following regions: on the western side of the North Atlantic (Grand Banks and Labrador Current) and in the North Pacific oceans (Sea of Okhotsk and Kuril Islands, northeast of Japan) (Fig. 1-3b).

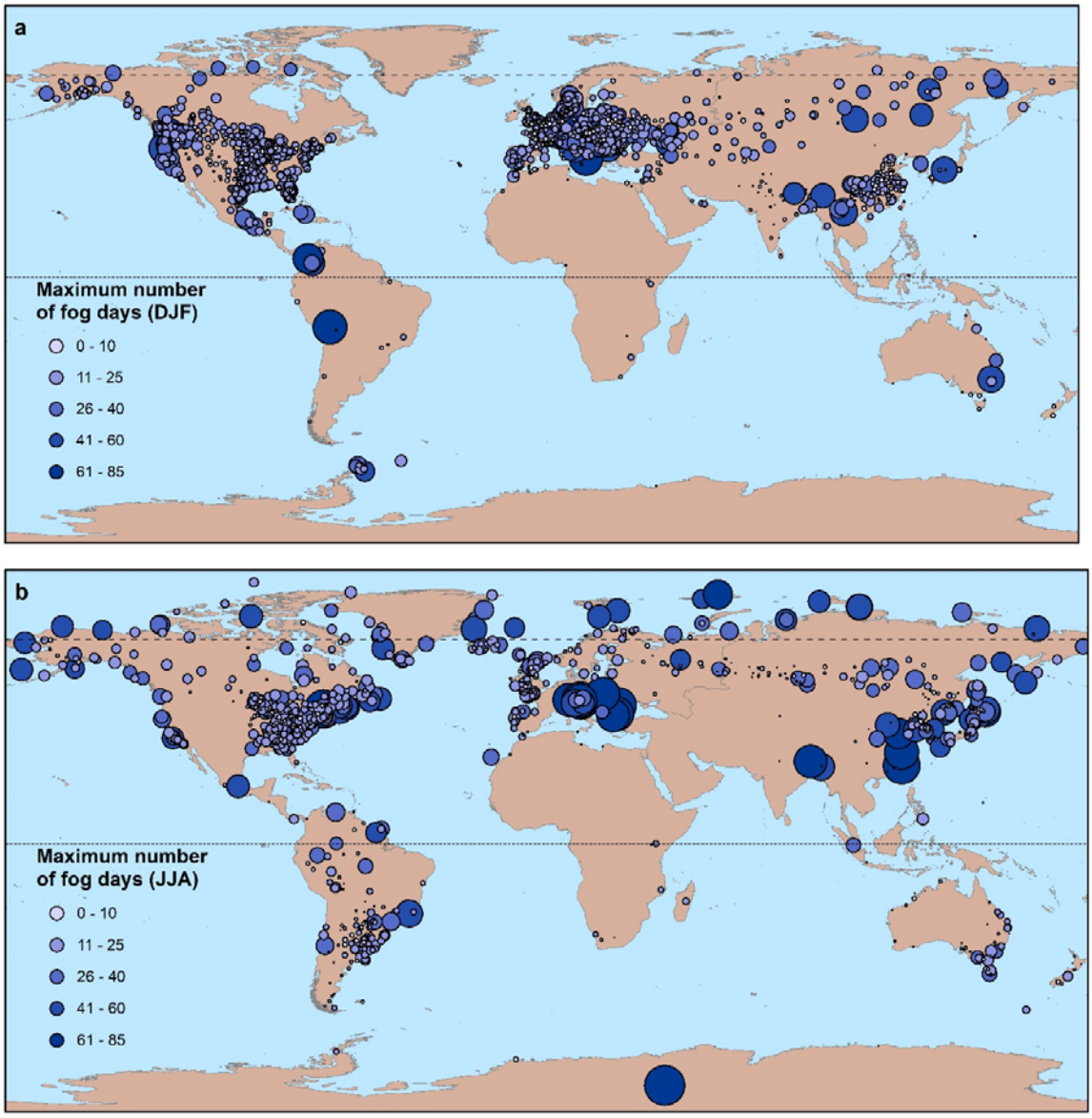

Figure 1-2. Maximum number of fog days observed on land during (a) December, January, February (DJF), and (b) June, July, August (JJA) between 1991 and 2010 (adapted from Sobik and Błaś, 2016). The dotted line is the Equator and the dashed line is the Arctic Circle (66°33' N).

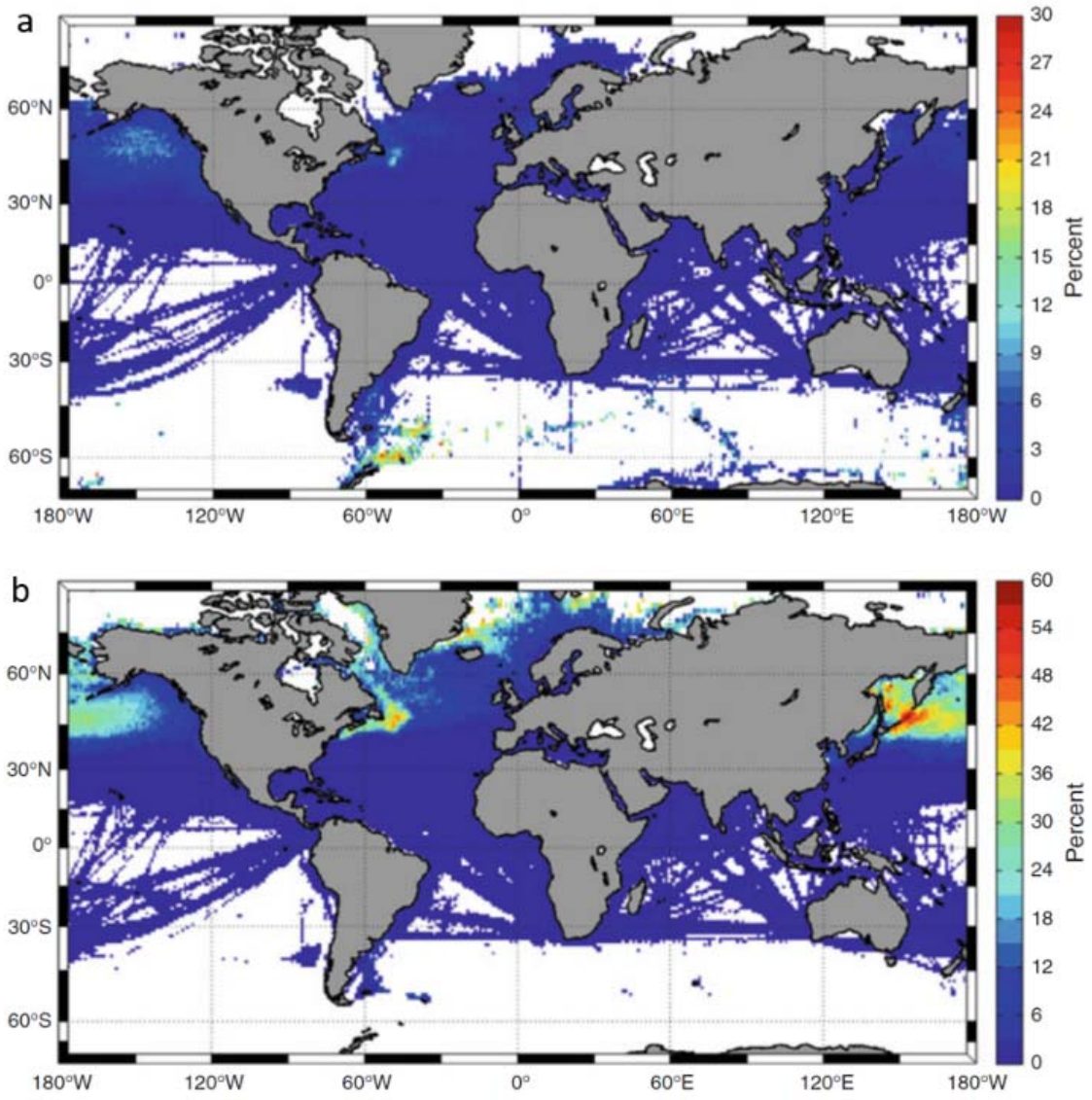

Figure 1-3. Percentage of marine fog occurrence per 1° grid point during (a) December, January, February, and (b) June, July, August between 1950 and 2007 (from: Dorman et al., 2017).

1.2.3 Fog in the Polar regions

The Polar regions include the Arctic and Antarctic. The Arctic is the region of the Earth situated north of the Arctic Circle (66°33'N – see dashed line on Figure 1-2). However, alternative but more commonly used definitions of the Arctic exist, depending on the subject of study or application (e.g. climatology, ecology). The Arctic Monitoring and Assessment Programme (AMAP) defines the Arctic as the area located north of the Arctic Circle, supplemented by all marine and terrestrial areas north of 60°N in north America and north of 62°N in Asia. In addition, it is extended to the Hudson Bay, the Labrador Sea and the Aleutian Islands (AMAP, 2017). The Antarctic defines the region of the Earth located south of the Antarctic Circle (66°33'S). A broader definition of the Antarctic describes the region south of the Antarctic Convergence, which is approximately 60°S (Hanessian, 1960).

Fog is ubiquitous in summer in the Polar marine regions, particularly along the marginal sea ice zone (Figure 1-4a). The Greenland Sea and Denmark Strait area between Iceland and Greenland has one of the highest fog occurrences in the Polar regions during summer (Figure 1-4a). Even though observation density is low in the Southern Ocean, a region of high fog occurrence is visible around and north of the Antarctic Peninsula (Figure 1-4b). More information on marine fog occurrence can be found in Dorman et al. (2017).

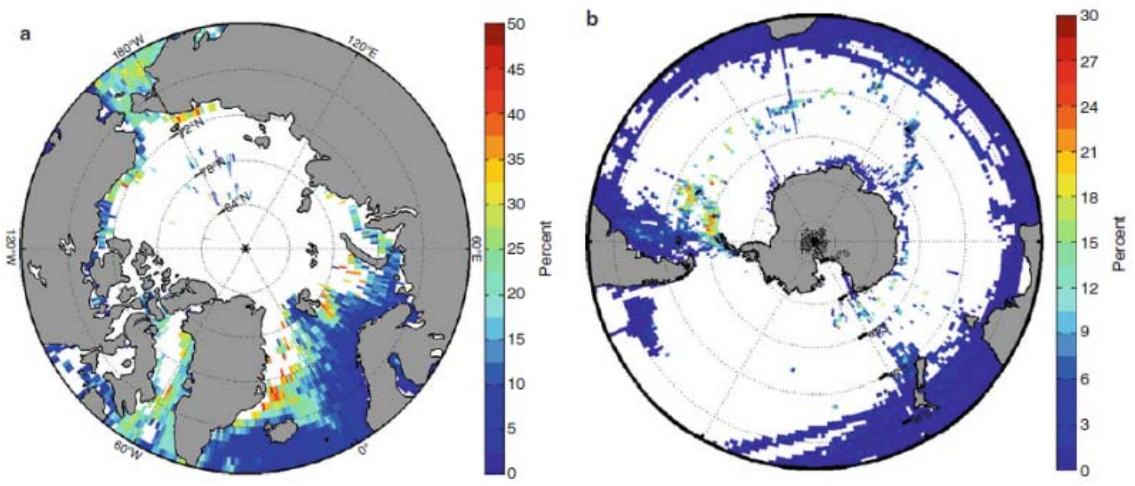

Figure 1-4. Percentage of marine fog occurrence per 1° grid point during the warm season for (a) the Arctic (JJA) and (b) the Antarctic (DJF) between 1950 and 2007 (from: Dorman et al., 2017).

Several general climatologies of Arctic and Antarctic fog occurrence exist (Prik, 1960; Ukhanova, 1971; Hanesiak and Wang, 2005; Lazzara, 2008; Khalilian, 2016). Marine fog is more frequent in the Arctic than over mid-latitudes during summer and fall (June-November). In the Arctic, typical marine fog occurrences are 15-25 %, whereas in the Antarctic region fog occurs 2-15 % of the time (Dorman et al., 2017). During the warm season, fog in the Polar regions is predominantly in the liquid or supercooled phase (> -10°C: Petterssen, 1986). Fog in that season mainly originates from the advection of warm oceanic air over cold surfaces (sea ice, ice shelves, cold land masses, or cold oceanic currents) and is therefore of the advective type (Nillson and Bigg, 1996; Svendsen et al., 2002, Hanesiak and Wang, 2005; Gajanada et al., 2007; Lazzarra, 2008). Note that radiation fog can still occur at night during the warm season and it is frequent over the Greenland Ice Sheet (Miller et al., 2013). In the cold season, ice fog and steam fog are the predominant fog types in the Polar regions. Ice fog occurs through intense radiative

cooling of the surface under strong anticyclonic conditions, although it can also be related to locally increased anthropogenic emissions (Gotaas and Benson, 1965; Bowling et al., 1968; Lazzara, 2008; Gultepe et al., 2014). Steam fog or "Arctic sea smoke" usually occurs during cold air outbreaks over relatively warm water or over areas with high sensible heat fluxes, such as polynyas or open leads within the pack ice.

1.2.4 Integrated Global Radiosonde Archive balloon soundings

Balloon soundings with radiosonde instruments provide vertical profiles of temperature, humidity and wind conditions in the troposphere and lower stratosphere, and are therefore excellent vehicles to measure fog macrophysical properties. Long-term worldwide records of standardised low-resolution radiosonde observations are available since the 1940s through the Integrated Global Radiosonde Archive (IGRA: Durre et al., 2006) for about 2700 locations (https://www.ncdc.noaa.gov/data-access/weather-balloon/integrated-global-radiosonde-archive, accessed December 2017). Figure 1-5 shows the current network of IGRA radiosondes as of 2017. In addition, higher-resolution radiosonde observations are available from select field campaigns over land or sea, which provide detailed vertical structure of the boundary layer over short temporal windows (e.g. the Arctic expeditions *Surface Heat Budget of the Arctic Ocean* (SHEBA): Uttal et al., 2002; and the *Arctic Summer Cloud Ocean Study* (ASCOS): Tjernström et al., 2014). In this thesis, data from low-resolution profiles taken at three IGRA stations in East Greenland and the high-resolution profiles during fog from the ASCOS expedition will be used.

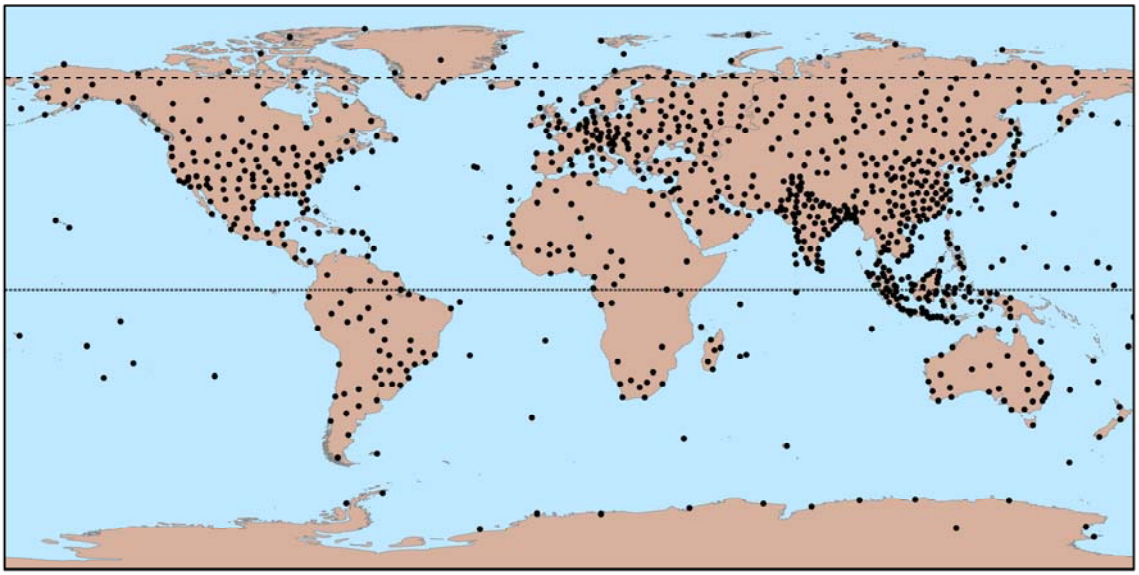

Figure 1-5. Locations of Integrated Global Radiosonde Archive stations in 2017 (black dots). The dotted line is the Equator and the dashed line is the Arctic Circle (66°33' N). IGRA data from: https://www.ncdc.noaa.gov/data-access/weather-balloon/integrated-global-radiosonde-archive.

1.3 Thesis aims, objectives and structure

1.3.1 Rationale

Both fog and temperature inversions have implications for climate studies and more specifically for calculation of the earth surface energy balance. However, our understanding of the exact association between fog and temperature inversions remains limited, which complicates our ability to quantify their influence on the surface energy balance, which is particularly important for glacier and sea ice studies (Norris, 1998; Mernild et al., 2008; Hulth et al., 2010). The analysis of inversion characteristics and fog vertical extent is therefore one of the aims of this thesis (Chapters 3 and 4). Additionally, while fog and temperature inversions in Arctic coastal areas have been associated with a decrease in glacier melt at lower elevations (Alt, 1979; Braun, et al. 2004; Koerner, 2005; Mernild et al., 2008; Mernild and Liston, 2010), their influence on each component of the

surface energy balance remains to be quantified (e.g. Tjernström et al., 2015). This requires measurements of fog microphysical properties such as droplet effective size, droplet size distribution, droplet number concentration and liquid water content (e.g. Gultepe et al., 2006). In the absence of such field measurements in large parts of the Arctic, fog macrophysical properties such as visibility, fog top elevation and fog development processes derived from archived weather and radiosonde data can be used as proxies for fog microphysical properties, and eventually of their radiative effect on surface energy balance. Furthermore, compared to winter season and ice fog (e.g. Gultepe et al., 2014), summer Arctic fog has not been extensively studied (e.g. Prik, 1960; Kumai, 1973; Gathman and Larson, 1974; Alt, 1979; Nilsson and Bigg, 1996; Hanesiak and Wang, 2005; Heintzenberg et al., 2006). It is therefore crucial to establish a climatology of Arctic fog during the melt season to move toward better understanding of the influence of liquid fog on the radiative and turbulent flux components of the surface energy balance. Establishing such melt season fog climatologies in combination with an increase in knowledge of fog formation and dissipation processes is crucial both for glacier surface energy balance studies and for fog forecasting in Polar regions (Gultepe et al., 2006; Hulth et al., 2010). Establishing a summer fog climatology for East Greenland is therefore a second main aim of this thesis (Chapter 2).

1.3.2 Aims

This thesis will present a climatology of fog and its macrophysical properties over coastal East Greenland, one of the Arctic regions with the highest summer fog occurrence. The dissertation aims to answer the following research questions:

1. What is the annual and seasonal frequency of occurrence of fog in East Greenland over the past 20 to 60 years?
2. What are the annual and daily timing patterns of fog, and how do these relate to wind and sea ice conditions?
3. Which types of fog occur in East Greenland and what are their temperature, humidity and visibility characteristics?
4. Can we classify fog according to their thermodynamic profiles from radiosondes and can we infer fog processes from specific profiles?
5. Can we optimise fog top elevation retrievals from IGRA radiosonde profiles so that they can be applied to all thermodynamic profiles?
6. How thick is fog in East Greenland and how does this compare to fog in other Polar regions?
7. How often do temperature inversions occur in East Greenland, what are their characteristics and how do these compare with temperature inversions in other Polar regions?
8. How do fog and temperature inversion properties relate to each other?
9. What are the regional differences in all the above characteristics of fog and temperature inversions along the East Greenland latitudinal transect?

10. How much glacier surface area in East Greenland can potentially be affected by overlying fog and temperature inversions?

1.3.3 Objectives and structure

To answer these ten research questions three main research objectives were formulated and each of these objectives will be dealt with in a separate chapter.

Objective 1 (Chapter 2) is to establish a climatology of Arctic fog in coastal East Greenland based on present weather and visibility data between 1958-2016. It will address the first two research questions and, in part, questions 3 and 9. For this analysis, present weather codes corresponding to fog at the station with a visibility below 1000 m are considered to be representative of true fog conditions.

Objective 2 (Chapter 3) is to extract thermodynamic profiles from radiosonde data to characterise and understand fog macrophysical properties and processes. It will address research question 4, and in part, 3 and 9, and is composed of four sub-objectives (2a-d):

- Objective 2a is to extract IGRA soundings corresponding to fog occurring in surface present weather and visibility observations at three East Greenland coastal locations. For soundings launched between two synoptic fog observations, it is assumed that fog is present at the time of the launch. For all soundings, the surface level is analysed and the dew point depression at that level is considered to be representative of saturation and thus fog conditions;

- Objective 2b compares fog thermodynamic profiles from low-resolution IGRA radiosondes over coastal East Greenland with high-resolution profiles from a field campaign over the Arctic pack ice (ASCOS). To validate whether IGRA is suitable for thermodynamic profile identification, it is hypothesised that coastal East Greenland is influenced by similar environmental conditions as the central Arctic Ocean (i.e. oceanic influence);
- Objective 2c is the development of a novel automated classification method of fog thermodynamic profiles into distinct classes from archived radiosonde profiles;
- Objective 2d is to infer fog processes for some or all of the fog thermodynamic classes generated under Obj. 2c by i) applying process-understanding from fog literature to characteristic thermodynamic profiles; ii) by directly comparing the thermodynamic profiles at one station to a series of nearby time-lapse images of fog, and iii) by analysing air mass back-trajectories corresponding to select fog thermodynamic profiles.

Objective 3 (Chapter 4) is to understand the relationship between fog and temperature inversions over East Greenland. It will attempt to answer research questions 5-10 and includes four sub-objectives (3a-d):

- Objective 3a is to extract melt-season temperature inversion characteristics from archived radiosonde profiles;
- Objective 3b is to develop an automated method to calculate fog top height from archived radiosonde profiles, under the assumption that temperature and humidity gradients vary linearly between sounding levels, and that fog top elevation

corresponds to the elevation at which the atmosphere becomes subsaturated above a continuous saturated fog layer;

- Objective 3c, the main part of this chapter, is to understand and quantify the relationship between fog and temperature inversion characteristics;
- Objective 3d relates fog occurrence and inversion characteristics to land-terminating glacier hypsometry in East Greenland. This comparison assumes that average fog and temperature inversion conditions retrieved from radiosonde profiles are representative of average fog and temperature inversion conditions above coastal glaciers in the area. It is assumed that fog top elevation and inversion characteristics are uniform in space over a region within 400 km of the weather station, although both are usually affected by topography (e.g. Gultepe, 2015). A linear extrapolation of radiosonde profiles constitutes a very simplistic approach for a first assessment of the potential impact of fog and inversions on coastal glaciers, which is nonetheless useful for future applications in glacier surface energy-balance models.

Chapter 5 is the final chapter in this thesis and provides an overall summary, general conclusions, and perspectives for further work on Arctic fog and temperature inversions using synoptic weather observations and archived radiosonde records.

Because each of the results chapters is constructed as a stand-alone manuscript there is some overlap between the introduction, background, and data source sections, as well as between these and the introductory material presented in Chapter 1.

CHAPTER 2. A CLIMATOLOGY OF ARCTIC FOG IN EAST GREENLAND

2.1 Introduction

This chapter provides an exploratory analysis of Arctic fog climatology at four meteorological stations along the coast of East Greenland since 1958. It is meant to serve as a background for Chapters 3 and 4, which focus on fog macrophysical properties retrieved from upper-air observations at three of the four stations. General climatological analysis of all Greenland meteorological stations can be found in various reports from the Danish Meteorological Institute (e.g. Cappelen et al., 2001; Cappelen, 2015). Over the period 1961-1990, fog mostly occurred from May to September and peaked in July over all Greenland locations. Ittoqqortoormiit, central East Greenland, had the highest frequency of fog occurrence, with on average 21 fog days and 20 % of fog observations in July (Cappelen et al., 2001). Further preliminary research on fog climatology in East Greenland was done by Gueye (2014) in an MSc thesis under the supervision of Dr H. Jiskoot, using synoptic-time (3-hourly) observations between 1958 and 2005. The work by Gueye (2014) included analysis of fog frequency of occurrence, fog timing and duration, air temperature, relative humidity, sea ice break-up and climate indices. This study showed that most summer fog occurred at temperatures around 0°C and with relative humidity above 90 %. Fog occurrence and duration were higher at northernmost latitudes, where temperatures were lower, sea ice more extensive and summer daylight duration longer. Gueye (2014) found some marginally significant increase fog frequency in Southeast Greenland and decrease in fog frequency and duration in Northeast Greenland. In this chapter, we expand upon the work by Gueye (2014) by: i) including

the weather observations between 2005 and 2016; ii) exploring additional conditions during fog, including analyses of vertical and horizontal visibility and wind speed and direction during fog, and the relationship between fog and sea ice concentration; and iii) optimising data presentation and providing statistical analysis of differences among locations and fog types. Both a switch from manned to automated observations and a switch from synoptic to hourly observations took place at the start of the 2005-2016 period (Bødtker, 2003). In addition, this most recent decade was warmer than normal in Southeast Greenland (Cappelen, 2015; Abermann et al., 2017) and increased surface mass loss from the Greenland Ice Sheet was observed (van den Broeke et al., 2016; AMAP, 2017).

The fog climatology details provided by this thesis research will lead to a better understanding of environmental conditions during fog occurrence at high-latitude locations during the melt season. Results from this chapter will be used throughout this thesis to better understand regional differences in fog formation and dissipation mechanisms (Chapter 3), as well as fog macrophysical properties (Chapter 4). More generally, an established climatology can be used to better predict fog occurrence at high latitudes and improve fog forecasting and nowcasting, both of which are crucial for aviation and marine activities in these remote locations where observational data are scarce (Gultepe et al., 2006). This knowledge is also important for an accurate representation of fog and low clouds in global and regional climate models (Kattsov et al., 2005; Flato et al., 2013), and for glacier and ice sheet energy balance and mass balance models (Braithwaite et al., 2006; Hulth et al., 2010).

2.2 Background

Fog is a suspension of water droplets or ice crystals near the Earth surface that leads to a reduction of horizontal visibility to below 1000 m (WMO, 1995). It constitutes a major hazard for aviation, maritime and land transportation, including in the Arctic where new sea routes are opening (Smith et al., 2013; Gultepe et al., 2014). Fog has been frequently reported in summer over the Arctic Ocean (Nilsson and Bigg, 1996; Tjernström et al., 2012; Przybylak, 2016) and in coastal regions of Greenland (Cappelen et al., 2001), Svalbard (Svendsen et al., 2002), Jan Mayen (Hulth et al., 2010), the Canadian Arctic (Hanesiak and Wang, 2005; Khalilian, 2016), the Eurasian Arctic (Przybylak, 2016), and even Antarctica (Lazzara, 2008). Fog is more frequent in the Arctic summer compared to the Antarctic summer (15-25 % vs. 2-15 %), and both are more frequent than summer fog at mid-latitudes (Dorman et al., 2017). Highest fog occurrences are along the marginal sea ice zone and where strong ocean temperature gradients exist. One region with frequent fog occurrence is along the East Greenland coast, in part because of the persistent summer sea ice (Cappelen, 2015; Dorman et al., 2017).

Summer fog in the Polar regions originates from the advection of warm moist oceanic air over cold sea water, sea ice or ice shelves that provide a cooling surface on which the air mass can condensate. As such, it can be classified as “sea fog”, “marine fog” or “advection fog”. Another type of sea fog can occur, when a cold and dry air mass advects over open water. This is referred to as “steam fog” or “Arctic sea smoke” (Przybylak, 2016), but is usually restricted to the cold season (Saunders, 1964; Cappelen et al., 2001). Over the land, fog formed by radiative cooling of the ground is the dominant type and

mainly occurs in winter, when it is composed of ice crystals at temperatures below -30°C (Glickman, 2000). As opposed to winter fog, summer high-latitude fog is primarily composed of liquid droplets (e.g. Kumai, 1973; Lazzara, 2008). The terms "sea fog" and "summer fog" used in this chapter refer to Arctic summer sea fog.

The onset of summer fog in the Polar regions has been linked to the timing of sea ice break-up (Brooks, 1979). Over the Arctic Ocean, Prik (1960) observed a correlation between the number of fog days in July and August and sea ice concentration, with an average maximum of 9 fog days per 10-day period for sea ice concentrations from 70 to 90 %. In Antarctica, Lazzara (2008) found an increase in fog occurrence at McMurdo Station after 2001, during which time two icebergs detached from the Ross Ice Shelf, creating favourable conditions for local landfast sea ice expansion. However, only a limited correlation was found between fog occurrence and local sea ice concentration, suggesting remote moisture sources for fog formation.

Sea ice and low clouds exert a strong influence on each other as well as on the Arctic surface energy budget. While sea ice break-up provides moisture and aerosols for condensation, longwave radiation emission from low clouds causes sea ice to melt (Shupe and Intrieri, 2004; Eastman and Warren, 2010; Tjernström et al., 2015). The decreasing trend in Arctic sea ice cover contributes to the enhanced warming of the Arctic, known as the "Arctic Amplification" (Serreze and Barry, 2011). Arctic low clouds and fog usually exert a net warming effect on sea ice surfaces, except over low albedo areas and with high solar elevation angles during the middle of the melt season (Curry et al., 1988; Shupe and Intrieri, 2004). Fog and low clouds are also important for the surface energy and mass

balance of Arctic glaciers because they can reduce or suppress melt at lower elevations (Alt, 1979; Braun et al., 2004; Koerner, 2005; Mernild et al., 2008; Hulth et al., 2010). Low clouds enhance mass loss from the Greenland Ice Sheet (Bennartz et al., 2013; Van Tricht et al., 2016), except over low albedo areas of the ablation zone (Wang et al., 2016; Hofer et al., 2017). Arctic glaciers and the Greenland Ice Sheet are important freshwater reservoirs, representing 0.27 m and 7.36 m of sea-level equivalent, respectively (Vaughan et al., 2013). It is of crucial importance to accurately model glacier and ice sheet surface energy and mass balance and their response to fog and low clouds, in order to better constrain the timing and magnitude of global sea-level rise, which is a concern for coastal infrastructures and populations worldwide.

Fog and low cloud occurrence can change due to changes in the amount of water in and the temperature of the atmosphere. These factors both affect relative humidity and potential saturation. In addition, atmospheric aerosol concentration also influences fog occurrence. Over the mid-latitudes, summer sea fog has increased over the past decades (Kawai et al., 2016), while (mostly radiation) fog in populated and urban areas has generally decreased due to a combination of warming and a reduction in air pollution (Klemm and Lin, 2016). In the Polar regions, trends in fog occurrence vary regionally. Summer fog at McMurdo Station, Antarctica, has significantly decreased since the 1970s (Lazzara, 2008). Hanesiak and Wang (2005) found a decrease in fog in the eastern Canadian Arctic between 1950 and 2004, but an increase in the southwest Canadian Arctic over the same period. In the western Canadian Arctic Archipelago, Khalilian (2016) found a decrease in the proportion of fog occurrence relative to all low visibility events between 1980 and 2015. Along the East Greenland coast, Gueye (2014) found a

slight though significant increase in fog occurrence in the southeast and a decrease in the northeast for the period 1958-2005. Over the Arctic Ocean, cloud cover and fog frequencies are expected to increase significantly with climate change, as sea ice is decreasing (Palm et al., 2010) and the subsequent open-ocean evaporation and temperature are increasing (Vavrus et al., 2011), although current and future regional changes are uncertain (Eastman and Warren, 2010). There is, therefore, a need to establish a precise fog climatology in the Arctic and further examine environmental conditions in which fog forms.

2.3 Study Site

Four World Meteorological Organization (WMO) synoptic weather stations, operated by the Danish Meteorological Institute (DMI), with archived present weather and visibility observations along the coast of East Greenland were selected. These are, from north to south: Danmarkshavn (WMO number 4320), Ittoqqortoormiit (WMO number 4339, formerly Scoresbysund), Tasiilaq (WMO number 4360, formerly Ammassalik/ Angmagssalik) and Prins Christian Sund (WMO number 4390, presently also named Ikerasassuaq) (Table 2-1; Figure 2-1). These stations represent a latitudinal gradient in temperature, sea ice and daylight conditions (e.g. Abermann et al., 2017). Climate ranges from Low Arctic in Southeast Greenland, with seasonal sea ice, to High Arctic in central east and Northeast Greenland (CAVM, 2003), where sea ice concentration is over 80% most of the year and 24-hour daylight is characteristic of the summer months (Cappelen, 2015).

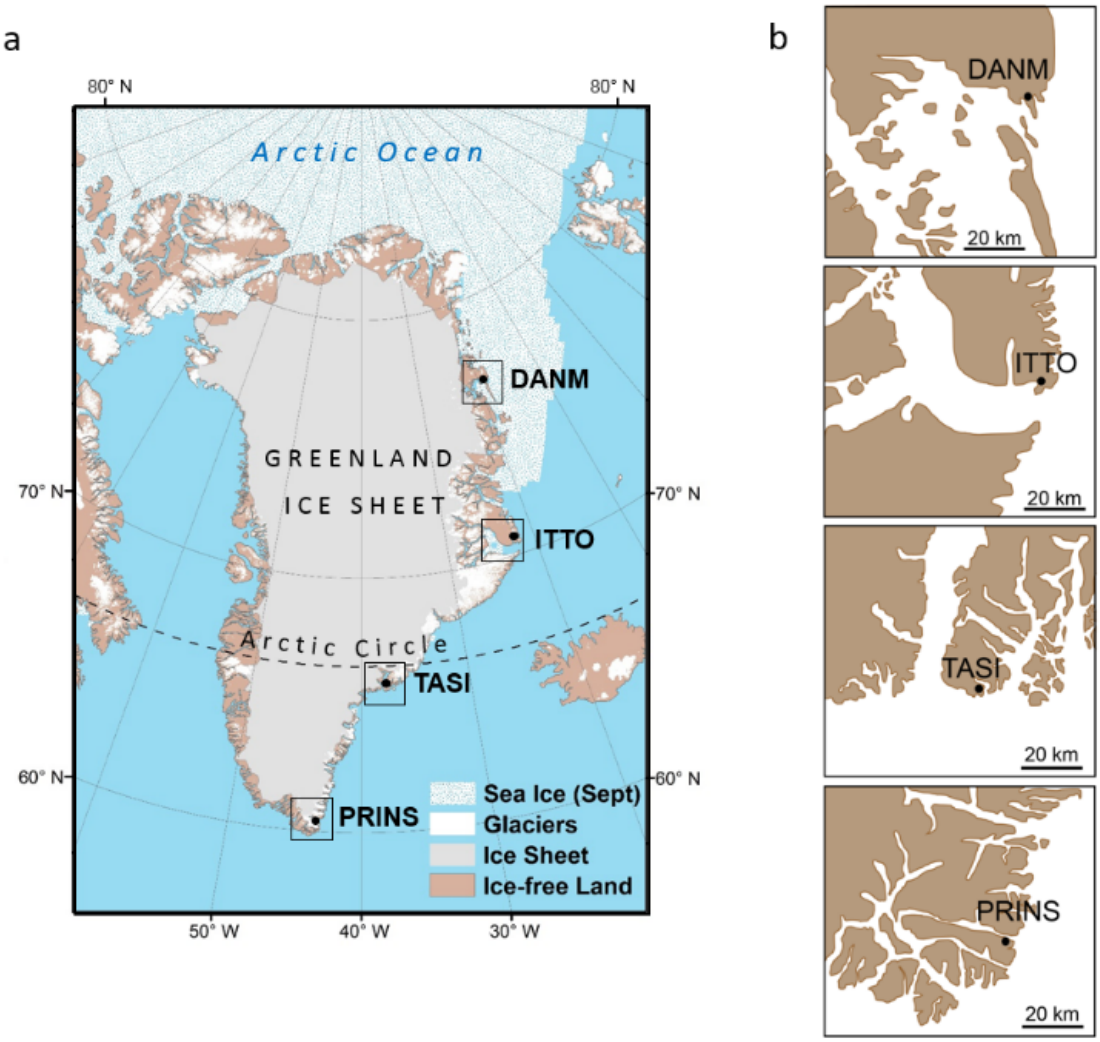

Figure 2-1. (a) Location of the four WMO synoptic weather stations operated by DMI along the coast of East Greenland: Danmarkshavn (DANM), Ittoqqortoormiit (ITTO), Tasiilaq (TASI) and Prins Christian Sund (PRINS). The sea ice limit represents the average minimum September extent (shapefile from the National Snow and Ice Data Center: https://nsidc.org, NSIDC-0051). The Greenland Ice Sheet was reconstructed from hydrologic outlets (NSIDC-0372, Lewis and Smith, 2009) and surrounding glaciers from the Randolph Glacier Inventory (http://www.glims.org/RGI/, Pfeffer et al., 2014). (b) Schematic maps representing the distribution of land (brown) and water (white) around each station.

Wind circulation in Greenland is strongly influenced by the presence of the Greenland Ice Sheet, which acts as a topographic barrier so that winds generally blow along the coasts (Cappelen et al., 2001). The thermal gradient between sea ice in the Arctic Basin and the open ocean further south establishes a predominately northerly wind direction in the Fram Strait region (van Angelen et al., 2011). This northerly wind in turn affects the export of sea ice from the Arctic Ocean, hence sea ice distribution in East Greenland through the cold and low-salinity East Greenland Current (Vinje, 2001). In addition to these large-scale circulation patterns, smaller scale thermal wind regimes influence the weather in Greenland. The strong thermal gradient between the ice sheet and the ocean triggers katabatic winds that flow from the centre of the ice sheet towards its margins (Steffen and Box, 2001). On average, a permanent snow cover is present for much of the year in coastal East Greenland except in July and August in Danmarkshavn, and between June and September for the three southern stations (Cappelen et al., 2001). When land is snow free, strong local sea breezes are established by the thermal gradient between the sun-heated land and the cold and frequently ice-covered offshore waters.

Moisture and heat transport in the Arctic occurs through low-level (970-990 hPa) poleward advection from lower latitudes (Jacobson and Vihma, 2010). The advection of heat and moisture to the Arctic is mainly dependent on large-scale circulation, and hence on the location of the high and low pressure systems. Three major centres of action determine large-scale atmospheric circulation in the Arctic: the Siberian High, the Aleutian Low and the Icelandic Low (Serreze and Barry 2005). In addition, a high pressure system is frequently observed above the Greenland Ice Sheet (Hanna et al., 2013). Because of the general position and relative strengths of these high and low

pressure areas, one of the major transport routes is through the North Atlantic cyclone track (Serreze and Barry, 2005). Greenland climate variability is influenced by internal oscillation patterns in atmospheric circulation. The strength of the poleward advection of moisture is strongly correlated with the Arctic Oscillation (AO) index, which describes the major mode of variability in the Arctic (Serreze and Barry 2005). The AO is an indicator of the strength of the polar vortex, a stratospheric low-pressure area which acts to keep the cold Arctic air near the geographic North Pole (Thompson and Wallace, 1998).When the AO is in a positive phase, the polar vortex is intensified, restricting the cold arctic air to northernmost latitudes and causing horizontal advection of moisture towards the pole, resulting in enhanced precipitation rates (Rogers et al., 2001; Grove and Francis, 2002). During a negative phase of the AO, meridional transport is reduced and local processes such as evaporation have a larger contribution to the atmospheric moisture content of the Arctic (Zhong et al., 2018). Another mode of variability closely related to the AO is the North Atlantic Oscillation (NAO) (Ambaum et al., 2001). NAO describes the gradient of sea level pressure between the Icelandic Low and the Azores High, the two centres driving the atmospheric circulation in the North Atlantic (Serreze and Barry, 2005). During the positive phase of the NAO, these two centres of action are strengthened and a poleward shift in cyclone activity occurs in the North Atlantic (Serreze and Barry, 2005), together with reduced precipitation in southeast Greenland (Box, 2006). During the negative phase, the Icelandic Low shifts to the southwest, favouring the advection of warm air in southern Greenland (Serreze and Barry, 2005; Hanna et al., 2013). Finally, air temperature in Greenland is particularly sensitive to the Greenland Blocking Index (GBI), which describes the obstruction of regional air circulation due to the presence of an impermanent, but frequent, high pressure system centred over the Greenland Ice Sheet. A

strong GBI corresponds to a blocked meridional circulation and high summer temperatures in Greenland (Hanna et al., 2013).

The North Atlantic region is Greenland's main heat and moisture source, which is driven by low-level easterly winds from the Nordic Seas to eastern Greenland, although evapotranspirative processes in Arctic Canada and Eurasia provide some additional moisture in spring and summer (Koenig et al., 2014). Therefore, changes in sea ice extent in the North Atlantic directly affect temperature, precipitation, and fog in Greenland, which in turn affects climate in other parts of the Arctic (Koenig et al., 2014). Climate in southeast Greenland is strongly influenced by the proximity of the semi-permanent Icelandic Low, the warm Irminger Current and the passage of lows, whereas local environmental conditions such as the presence of sea ice have a stronger impact on climate in northeast Greenland (Grove and Francis, 2002; Hanna and Cappelen, 2003; Cappelen, 2015). In addition, each of the four East Greenland stations is under the influence of distinct local climatic conditions that are determined by distance from the coast (Table 2-1) and to the Greenland Ice Sheet, as well as local topography and fjord configuration.

Table 2-1. Geographic coordinates and distance to open water of WMO synoptic weather stations in East Greenland.

	WMO ID	Latitude[a] (°N)	Longitude[a] (°W)	Elevation[a] (m a.s.l.)	Distance from shore (km)	Distance from ocean (km)
Danmarkshavn	4320	76.7694	18.6681	11	0.12	6.47
Ittoqqortoormiit	4339	70.4844	21.9511	70	0.17	12.60
Tasiilaq	4360	65.6111	37.6367	53	0.25	2.24
Prins CS	4390	60.0500	43.1667	88	0.80	2.21

[a] From Cappelen (2015)

2.4 Data Sources and Methods

2.4.1 Data and observations

Fog was identified from the combination of present weather (*ww*) and horizontal visibility (*vv*) data (WMO, 1995) available at the four WMO synoptic coastal weather stations in East Greenland. Data were acquired by H. Jiskoot from DMI for the period 1958-2016, but were quality-controlled by DMI for the period 1958-2012 only. Observations started in 1958 at three of the stations (Figure 2-2) but synoptic observations started in 1981 at Ittoqqortoormiit, after this station replaced nearby station 34339 (Cappelen et al., 2001).

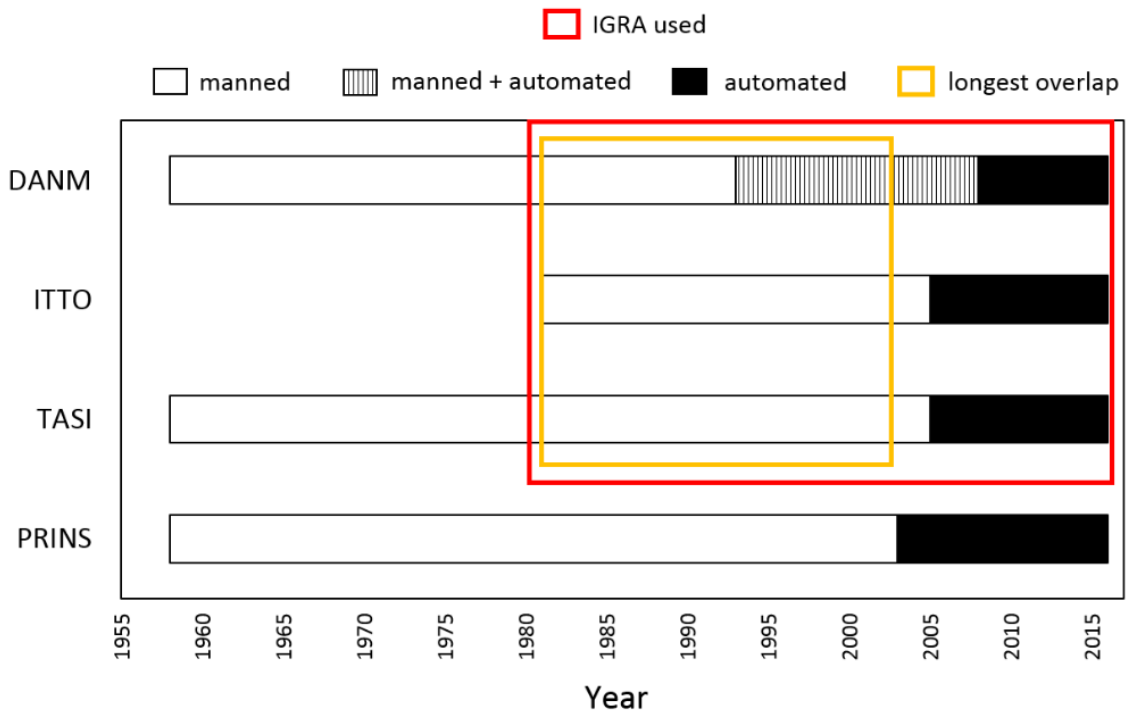

Figure 2-2. Time period of available DMI manned and automated present weather and visibility observations at Danmarkshavn (DANM), Ittoqqortoormiit (ITTO), Tasiilaq (TASI) and Prins CS (PRINS). The yellow box is the longest overlap period for predominantly manned observations for the three stations Danmarkshavn, Ittoqqortoormiit and Tasiilaq. The red box is the time period for which upper-air observations from the Integrated Global Radiosonde Archive (IGRA) were extracted at these three stations.

Present weather (*ww*) is the weather that is experienced at the time of observation, and includes various types of fog. Horizontal visibility (*vv*) is reported as the prevailing visibility, defined as the maximum visibility over at least one-half of the horizon circle (table 4377: WMO, 1995). Two types of observations and formats of *ww* and *vv* were used in this chapter. Between 1958 and the early 2000s, *ww* and *vv* were reported by human observers at synoptic times (3-hourly sampling resolution) and are hereafter referred to as "manned observations" (Figure 2-2). Automation of East Greenland weather stations started in the early 2000s (Bødtker, 2003), when *ww* and *vv* became reported hourly through the Vaisala FD12P present weather sensor with an accuracy of ± 10 % of Meteorological Optical Range (Claus Nehring, pers. comm, May 2016). These

data are hereafter referred to as "automated observations" (Figure 2-2). Manned observations of fog were reported as *ww* codes 11, 12, 28 and 40-49 (table 4677 from WMO, 1995; Table 2-2). Automated observations of fog between the start of the automation and 2012 were reported as *ww* codes 20 and 30-35 (table 4680 from WMO, 1995; Table 2-2), and from 2013 onwards as BUFR codes (these raw data have not gone through DMI quality assurance). For this research BUFR *ww* codes 130-135 corresponding to fog (table 0 20 003 from WMO, 1995) were converted to the standard automated *ww* codes 30-35. In all cases *vv* is reported in 100-m increments (table 4377 from WMO, 1995).

Table 2-2. Present weather (*ww*) codes corresponding to fog observations at a manned and automated weather station. After WMO (1995: tables 4677, 4680 and 0 20 003).

	ww (manned observations)		*ww* (automated observations)
	Sky visible	*Sky invisible*	
Shallow fog, in patches[1]	11		-
Shallow fog, continuous	12		-
Fog in the past hour[2]	28		20
Fog, unspecified	**-**		**30**
Fog at a distance[3]	**40**		**-**
Fog in patches	41		31
Fog, thinning[4]	**42**	**43**	**32**
Fog, unchanging[5]	**44**	**45**	**33**
Fog, thickening[6]	**46**	**47**	**34**
Fog depositing rime	**48**	**49**	**35**

[1]Shallow fog or ice fog not deeper than 2 m. [2]Fog or ice fog during the preceding hour but not at the time of observation. [3]Fog or ice fog at a distance at the time of observation, but not at the station during the preceding hour, or fog or ice fog extending to a level above the observer. [4]Fog which visibility increased during the past hour. [5]Fog which visibility did not change during the past hour. [6]Fog which visibility decreased during the past hour. Real fog codes are indicated in bold font. "-" indicates no code available (WMO, 1995).

Fog is further classified in separate codes based on whether it "has become thinner or thicker during the preceding hour", hereafter referred to as "thinning" and "thickening" fog, or as "no appreciable change during the preceding hour", hereafter referred to as "unchanging fog" (Table 2-2). In addition, manned *ww* observations distinguish fog based on sky visibility, which is an approximation of fog opacity or vertical visibility in METAR aviation weather reports. All these fog codes represent fog conditions observed at the weather station, with a horizontal visibility < 1000 m, and will be hereafter referred to as "real fog" cases. Present weather codes to describe shallow fog thinner than 2 m above ground level, fog at a distance and fog in patches also exist. These fog codes, together with "fog in the past hour" (Table 2-2) are either not observed directly at the weather station or horizontal visibility is only < 1000 m within fog banks (WMO, 1995). These will hereafter be referred to as "marginal fog" cases. Together, real fog and marginal fog will be referred to as "all fog" cases.

Although fog depositing rime has a distinct *ww* code, there is no distinction among liquid fog, freezing fog and ice fog in the codes. Therefore, weather data for the same four synoptic weather stations were also acquired from DMI (free of charge from http://research.dmi.dk/data/). In this thesis, dry-bulb air temperature (T) and relative humidity with respect to liquid water (RH_w) simultaneous with the fog observation were used, as well as mean wind speed (w_s) and direction (w_d) over the 10-minute period preceding the observation (Cappelen, 2015). Accuracies of the T/RH_w sensors HMP45D and HMP155 that are currently in use vary between 0.4°C at -20°C and 0.2°C at 20°C, and the RH_w accuracy is ± 3 % for a RH_w = 90-100 % (Vaisala, 2006).

In addition to surface meteorological observations, two data sources were used to investigate upper-air and sea ice conditions. Wind speed and direction were extracted at the 850 hPa pressure level from the Integrated Global Radiosonde Archive (IGRA) radiosonde database for Danmarkshavn, Ittoqqortoormiit and Tasiilaq only, as Prins CS does not operate a radiosonde (Durre et al., 2006; see also Chapters 3 and 4). This upper-air analysis was performed to understand air mass origin and dynamics during fog. In order to investigate the relationship between sea ice and fog frequency of occurrence and fog geometrical thickness at coastal locations, sea ice concentration (*SIC*) was extracted from the daily 25-km resolution passive microwave sea ice concentration product from the National Snow and Ice Data Center (NSIDC-0051, Cavalieri et al., 1996) based on outputs from the Nimbus-7 Scanning Multichannel Microwave Radiometer (SMMR) and the Special Sensor Microwave Imager/Sounder (SSM/I-SSMIS) onboard the Defense Meteorological Satellite Program (DMSP) satellites. The accuracy of this sea ice product is generally ± 5 % in winter and ± 15 % in summer, and it is higher for high *SIC* and/or highly reflective or thick sea ice (Cavalieri et al., 1992).

All data in this chapter are presented in Coordinated Universal Time (UTC). In summer, the local solar time in Danmarkshavn and Ittoqqortoormiit is 1.5 hours after UTC, and in Tasiilaq and Prins CS it is 2.5 hours after UTC. In winter, the local solar time in Danmarkshavn is 1.5 hours after UTC, in Ittoqqortoormiit it is 2.5 hours after UTC, and in Tasiilaq and Princ CS it is 3.5 hours after UTC.

2.4.2 Methodology

2.4.2.1 Missing data

Prior to analysing fog climatology in coastal East Greenland, monthly sums of missing present weather (*ww*) and visibility (*vv*) observations ("NaN" counts) at synoptic times or intermediate synoptic hours (i.e. every 3 hours starting from 0000 UTC, hereafter referred to as "synoptic times") were calculated for the entire period of record (Figure 2-2). These missing data are reported in checkerboard plots for all four stations to highlight months and years of missing observations. NaN counts for *ww* and *vv* observations were analysed every three hours only to allow for a continuity between manned (three-hourly) and automated (hourly) observations. If the monthly sum of NaNs was higher than zero in both *ww* and *vv*, this month was reported as having missing observations. For months with synoptic observations where *ww* was missing but *vv* was available, the proportion of $vv < 1000$ m was calculated in order to quantify the maximum proportion of missing fog observations. This comparison between monthly sums of NaN in *ww* and *vv* allowed us to highlight real gaps in the data as well as to calculate the maximum potential proportion of missing fog data, and therefore assess the effect of missing data on the presented climatology.

2.4.2.2 Frequency of occurrence

Fog was identified from present weather codes *ww* corresponding to fog (see Table 2-2) with a visibility $vv < 1000$ m. Shallow fog, fog at a distance and fog in patches represent

fog types with *vv* generally > 1000 m or only partially obscuring the field of view and were therefore deemed to not represent "real" and continuous fog conditions. In addition, fog seen over the ocean might not reach coastal areas, and "fog at a distance" is sometimes used to indicate low stratus cloud above the observer instead of fog. These "marginal" fog types were therefore not included in the presented coastal fog climatology to avoid overestimating fog frequency. However, an analysis of macrophysical properties including these marginal fog types is presented in Chapter 4 to investigate the differences in inversion characteristics among these fog codes and those representing proper and continuous "real" fog cases.

For the analysis of fog frequency, a time series of yearly sum of fog observations reported at synoptic times were first used to identify possible discontinuities in the data due to change in recording or measurement practices. Fog frequency was then analysed through monthly sums of fog observations at synoptic times ("synoptic fog observations"), and monthly sums of days with one or more synoptic fog observations ("fog days"). Both analyses were performed over the entire study period (Figure 2-2) and, thus, only include fog observations at synoptic times. These frequencies were reported in checkerboard plots for each of the four stations to highlight months and years of high fog frequency. For this purpose, the monthly number of synoptic fog observations was calculated relative to the total number of fog observations over the entire period to quantify the monthly distribution of synoptic fog observations over the year. The average monthly number of real fog days and all fog days (marginal plus real) were plotted for all four stations to investigate regional differences in the timing of fog onset. Subsequent analyses were focused on the summer months (May-August) only because fog peaks in the melt season

and has its main influence on the Arctic surface energy budget during this time. In order to determine the relative fog frequency among stations chi-square tests (χ^2) at the 95 % confidence level were performed on summer synoptic fog observations and fog days at Danmarkshavn, Ittoqqortoormiit and Tasiilaq with data between 1981 and 2003, the longest period of overlap of predominantly manned observations (see Figure 2-2). Note that, as none of the distributions presented in this chapter were normally or lognormally distributed, all statistical tests used are nonparametric.

2.4.2.3 Timing and duration

The seasonal and daily timing of fog events can provide an indication of environmental conditions promoting fog formation and dissipation mechanisms (e.g. Gultepe et al., 2009). To explore regional differences in the timing of fog occurrence, monthly sums of hourly fog observations were calculated for the 2006-2016 automated observation period and reported in checkerboard plots. The proportion of morning fog was used to investigate the diurnal variation of fog occurrence. It was calculated as the ratio between the sum of hourly fog observations between 0000 UTC and 1100 UTC and the total daily sum of hourly fog observations. Chi-square statistical tests (χ^2) were performed at the 95 % confidence level to determine whether the relative proportion of morning fog differed among stations for the entire melt season (May – August). Additionally, binomial tests were performed at the 95 % confidence level for each station, to investigate a possible difference in morning fog proportion between the early (May – June) and late melt seasons (July – August) linked to environmental conditions. The same analysis was

performed on local time instead of UTC time to account for meridional variations in solar noon.

As an estimation of fog duration, the frequency distribution of sequential hourly, automated, fog observations was calculated for the 2006-2016 time period, as well as the frequency distribution of sequential three-hourly manned fog observations for the two longest periods of overlap among stations (1958-1977 and 1993-2003, Figure 2-2). Average fog durations were compared among stations for significance through Kruskal-Wallis tests at the 95 % confidence level for each period of overlap.

2.4.2.4 Air temperature

Air temperature is an important variable to analyse because it gives an indication about the fog phase and, therefore, its microphysical and radiative properties (Petterssen, 1956; Gultepe et al., 2007). The frequency distribution of dry-bulb air temperature during fog, rounded to the nearest integer, was retrieved at each DMI station for the summer months (May – August). Median dry-bulb air temperature values during fog were then calculated for each station and relative proportion of summer fog occurring at temperatures above -10°C, between -30°C and -10°C and below -30°C was used to estimate the proportion of liquid or supercooled, mixed-phase and ice fog, respectively (c.f. Petterssen, 1956).

2.4.2.5 Relative humidity

Relative humidity indicates the level of saturation of the air and is important for fog formation (see Chapter 1). Statistics of RH_w during fog were represented as box and whisker plots at each station for the summer months (May – August) to investigate possible regional differences in saturation. In addition, time series of the yearly range of RH_w were plotted to examine possible biases in RH_w measurements.

2.4.2.6 Visibility

Visibility during fog is dependent on fog microphysical properties, such as the liquid water content, fog droplet size and droplet number concentration (See Chapter 1). In addition to its proxy for these properties, it is an important variable to analyse because the reduction of horizontal visibility linked to fog occurrence is a major hazard for transportation. The analysis of visibility was divided into three parts.

A) The frequency distribution of visibility for each manned fog code was calculated at all stations (1958-2004). Manual observations have the advantage of distinguishing fog types based on vertical visibility (sky visible or invisible). Vertical visibility measurements made with Vaisala CT25K ceilometer exist over East Greenland coastal sites during sky-obscuring conditions after 2004 (automated observations) but were not included in this analysis. This frequency analysis allows investigation of possible correlations between horizontal and vertical visibility. For this purpose, statistics (mean and standard deviation) were calculated for the three main fog types (thinning fog *ww* = 42, 43; unchanging fog *ww* = 44, 45; or thickening fog *ww* = 46, 47: see Table 2-2)

under each sky regime (visible vs. invisible), as well as for all three fog types combined under each sky regime. Wilcoxon Rank-Sum tests were performed at the 95 % confidence level on each fog type between sky regimes to investigate whether sky-obscuring fog was associated with lower *vv*. In addition, the sum of very dense fog events ($vv \leq 100$ m) with an invisible sky was calculated for all manned fog observations and for all stations.

B) Three fog types from automated present weather codes, i.e. *ww* = 32 (thinning fog), *ww* = 33 (unchanging fog), *ww* = 34 (thickening fog), were analysed for differences in visibility. The purpose of this analysis is twofold. First, its comparison with the frequency distribution of visibility reported from manned codes facilitated identification of possible biases in either dataset. Second, it allowed investigation of possible correlations among distinct fog stages and horizontal visibility ranges. For this purpose, Kruskal-Wallis tests were performed at the 95 % confidence level on visibility data from 2006-2016 (automated observations) during the three fog type present weather codes for each station, and on each of the fog present weather codes (*ww* = 32, *ww* = 33, *ww* = 34) among the four stations to highlight possible regional differences in visibility for each fog stage.

C) All manned and automated fog weather codes for the period 1958-2012 were used in combination, to investigate visibility. Statistical results were presented as box and whisker plots, and Kruskal-Wallis tests at the 95 % confidence level were used to test whether horizontal visibility during all combined fog stages significantly differed among stations. The same analysis was used for the automated observations from the 2006-2012 time period only, and results compared to those from the combined manned and automated fog codes.

2.4.2.7 Wind

To investigate the origin and dynamics of fog over East Greenland coastal locations, summer wind roses were created for wind at the surface (DMI) and at the 850 hPa pressure level (IGRA) for each station during both foggy conditions and all weather conditions (including fog). Surface observations only included manned *ww* codes, spanning the period 1958 to approximately 2003, and fog codes used were *ww* = 42-49 (Table 2-2). Upper-air observations were extracted from IGRA from 1980 to 2012 when fog was reported at the synoptic weather station from *ww* observations (Table 2-2) or when fog was reported both immediately before and immediately after a balloon launch (see Chapter 3). The time period selected for IGRA data starts in 1980 to avoid inhomogeneities due to sonde changes (see Chapter 4). The wind roses obtained were used to identify the origin of surface and upper winds during fog and compare it to the general climatology for each site. However, wind roses did not include calm wind conditions (w_s = 0 m s^{-1}), which frequency of occurrence was calculated for each station from surface wind observations. Mean and standard deviation of w_s were calculated both including and excluding calm conditions. Kruskal-Wallis tests were performed at the 95 % confidence level to determine which station had the lowest or highest w_s during both foggy and all-weather (including foggy) situations in summer.

Because fog in coastal East Greenland is often associated with local sea breeze (Cappelen, 2015), it is of interest to examine whether there is a latitudinal variation in sea breeze occurrence and how this relates to varying environmental conditions. Sea breezes

are typically more frequent in the afternoon because the thermal gradient between the heated land and the cold ocean is greater at that time of the day. To explore this, separate summer wind roses excluding calm wind conditions were constructed for the morning (defined as 0000 – 1100 UTC) and the afternoon (1200 - 2300 UTC), under both foggy and all weather (including foggy) conditions. Predominant directions of sea breezes were visually determined as the main onshore afternoon wind direction during fog using the coastal geography (e.g. Figure 2-1b), using wind roses with 16 cardinal points (see Appendix 1). In this way, sea breeze directions were delimited as sectors 80-190° for Danmarkshavn, 170-280° for Ittoqqortoormiit, 100-190° for Tasiilaq and 55-100° for Prins CS. The frequency of sea breeze occurrence was then calculated as the proportion of w_d corresponding to those sectors. Binomial tests at the 95 % confidence level were used to analyse if significant differences exist in the frequency of occurrence of morning and afternoon sea breezes at each station during both all-weather and fog conditions. In order to establish which station had the most frequent sea breeze during either fog or all-weather conditions, chi-square statistical tests (χ^2) were performed on the frequency of occurrence of morning and afternoon sea breeze at all four stations. The proportion of morning and afternoon sea breezes were further tested for significance at each station through binomial tests in order to determine which station had the strongest diurnal variation in sea breeze during either fog or all-weather situations. Finally, the last observation of each long-duration fog event was compared to its subsequent non-fog *ww* observation, and both these "last fog observations" and "post-fog observations" were plotted on wind roses. Binomial tests were used at each station on these two categories to investigate whether winds after the end of fog events switched from onshore to offshore or other.

2.4.2.8 Sea ice

Since the peak frequency in summer fog in coastal East Greenland varies among locations (See Table 2-3 and Figure 2-9), and because it is known that Arctic sea fog occurrence is related to sea ice break-up (Brooks, 1979), the possible link between sea ice and fog was investigated. The daily average sea ice concentration (*SIC*) was obtained for the nearest offshore pixel at each location from the 25 by 25-km NSIDC-0051 grid. For this purpose the nearest pixel to the east of each station was selected (Figure 2-3). Only *SIC* data after 1988 were selected in order to avoid data gaps in the sea ice product (Cavalieri et al., 1996).

SIC was first averaged over the melt seasons of 1988-2012, and its mean and standard deviations plotted as time series between the onset (1 May: DOY 121) and end (31 Aug: DOY 243) of the melt season, in conjunction with the time series of average cumulative fog day occurrence over the same period. The purpose of these overlapped time series is to highlight a possible relationship between fog onset (or significant increases in fog occurrence) and sea ice break-up. Additionally, average cumulative fog day frequency was plotted as a function of offshore *SIC* during the melt season (1988-2012), to examine whether there was a direct or lagged correlation between rapid changes in either variable. Finally, examples of time series of daily offshore *SIC* and individual hourly fog events for the melt season of 1998 were presented for Danmarkshavn and Tasiilaq. The purpose of analysing time series over a specific season is to gain insight into the timing of fog occurrence relative to sea ice break-up, and to determine if increased occurrence of fog occurs before sea ice breaks up (*SIC* close to 100 %).

In Chapter 4 of this thesis a novel method developed to retrieve fog top elevation (*FTE*) from radiosonde data (IGRA) is presented. We, therefore, used retrieved *FTE* in this chapter to investigate possible correlations between fog macrophysical properties and sea ice. After verifying that *SIC* and w_s were not statistically correlated, the relationship between *SIC* and *FTE* was investigated. A linear correlation analysis was performed over the 1988-2016 time period only to avoid data gaps in the sea ice product. In addition, two other conditions were applied: $SIC \geq 20$ % because of a ± 15 % data accuracy in summer (Cavalieri et al., 1992; Cavalieri et al., 1996), and $FTE < 800$ m, as higher values tend to be outliers (from Chapter 4). Correlations between *FTE* and offshore *SIC* were performed for each summer month at Danmarkshavn, Ittoqqortoormiit and Tasiilaq. The nonparametric Spearman's rank correlation coefficient at the 95 % confidence level was used because none of the distributions were normally or log-normally distributed.

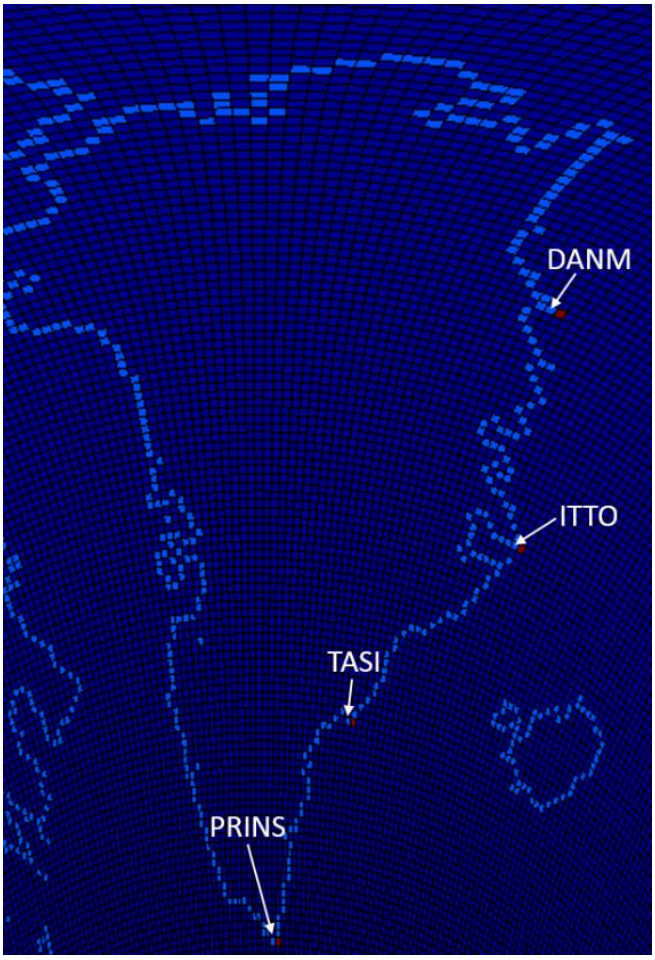

Figure 2-3. NSIDC sea ice product 25 by 25-km pixel grid (https://nsidc.org, NSIDC-0051). Red pixels represent the nearest offshore sea ice pixel east of Danmarkshavn (DANM), Ittoqqortoormiit (ITTO), Tasiilaq (TASI), and Prins CS (PRINS).

2.5 Results

2.5.1 Frequency of fog occurrence

2.5.1.1 Data coverage and missing synoptic observations

The total number of observations of "real" fog (see Sect 2.4.2.2) available in the period 1958-2016 at the four East Greenland synoptic stations are: 4564 for Danmarkshavn, 1994 for Ittoqqortoormiit, 3613 for Tasiilaq and 1965 for Prins CS. A considerable number of *ww* observations are missing at each station, particularly after the switch to automated observations in about 2004 (Figure 2-4). This corresponds to 4-10 % of *ww* data over the entire study period. However, fewer *vv* data than *ww* data are missing over the same time period (Figure 2-5). This can be explained by a large number of missing *ww* being coincident with visibilities > 30 km. Only 6-9 % of missing *ww* data correspond to *vv* < 1000 m, in which case it is not clear whether this low visibility is due to fog, snow, rain or other low-visibility weather conditions. Over the period 1958-2016, these low-visibility occurrences represent a maximum of 2 % of missing *ww* observations.

From the combination of missing observations in both *vv* and *ww* data, it appears that the only real data gaps (when both *vv* and *ww* are missing) occur in January 2011 at Danmarkshavn, from August 2007 to January 2009 at Ittoqoortoormiit and Tasiilaq, and from 1981 to 1992 at Prins CS. These time periods will therefore be excluded from the subsequent analysis in this chapter.

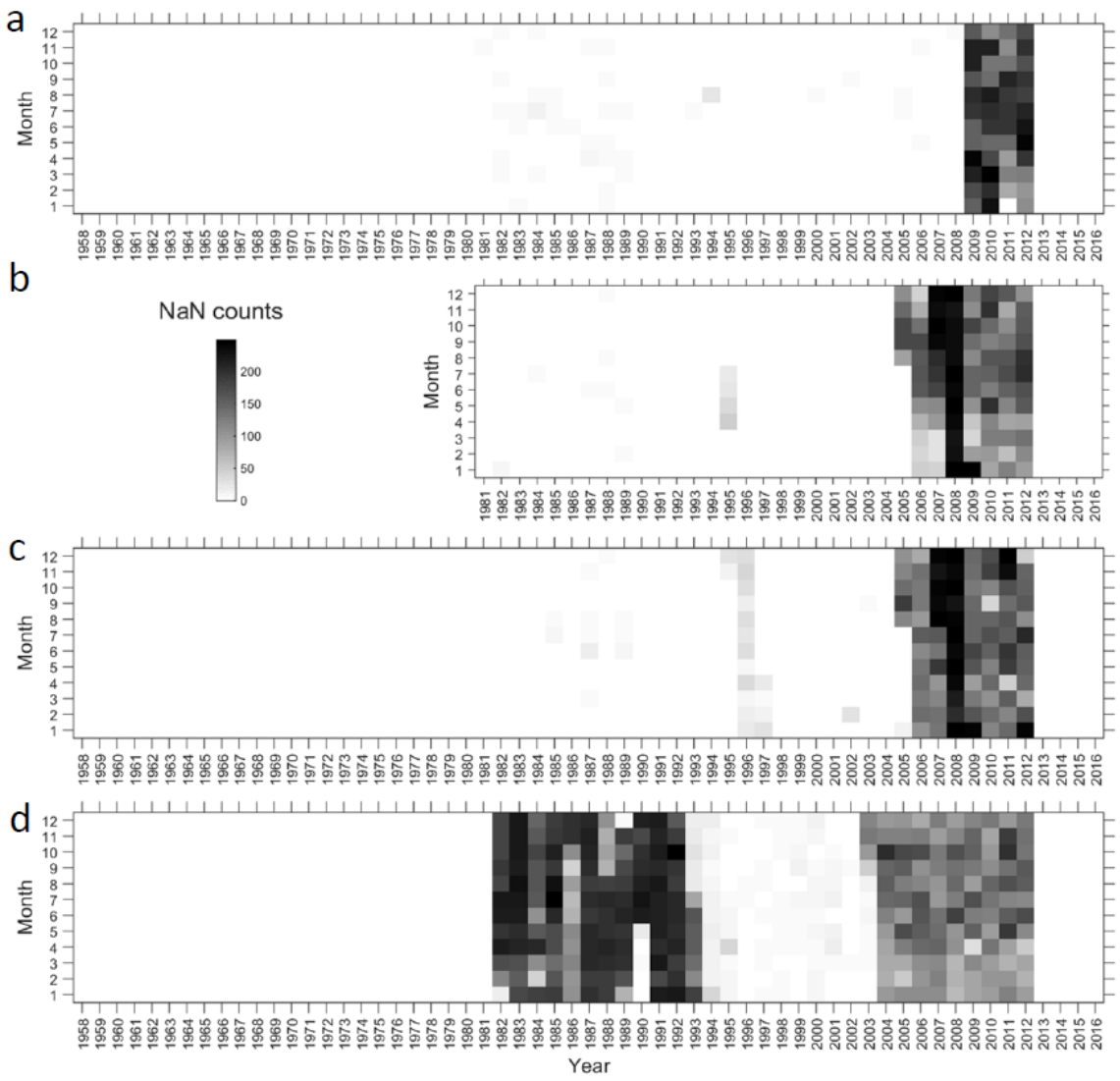

Figure 2-4. Monthly sum of missing synoptic present weather codes (NaN counts) at (a) Danmarkshavn 1958-2016, (b) Ittoqqortoormiit 1981-2016, (c) Tasiilaq 1958-2016, and (d) Prins CS 1958-2016.

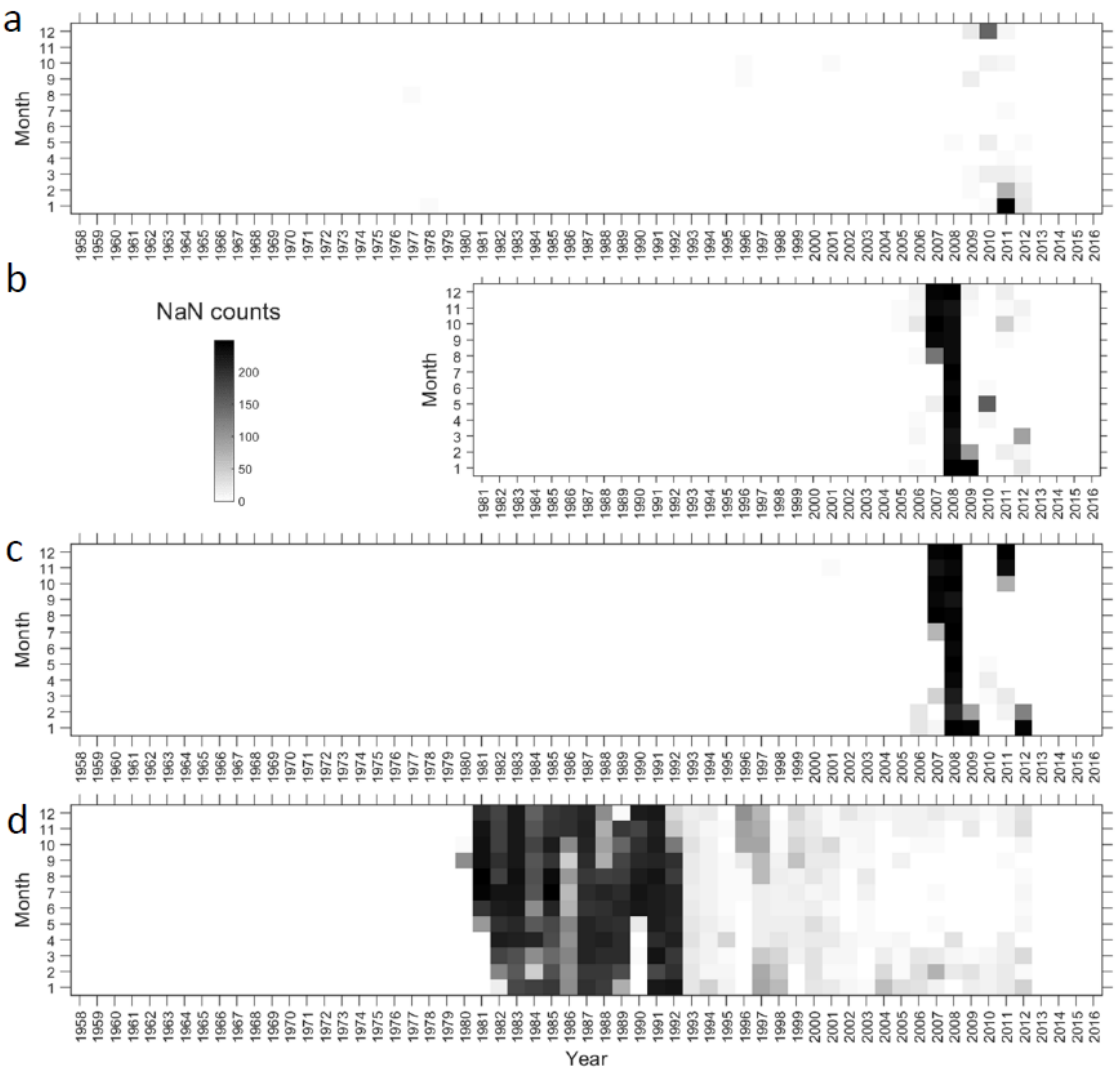

Figure 2-5. Monthly sum of missing synoptic visibility observations (NaN counts) at (a) Danmarkshavn 1958-2016, (b) Ittoqqortoormiit 1981-2016, (c) Tasiilaq 1958-2016, and (d) Prins CS 1958-2016.

2.5.1.2 Frequency of synoptic fog observations

Figure 2-6 displays the time series of the yearly sum of synoptic fog observations at Tasiilaq, and is given as an example to highlight observation-frequency inhomogeneities in the data. There are two discontinuities (vertical red dashed lines): one that corresponds to the automation of weather stations in the early 2000s, and one that corresponds to the year 2013, after which data were not verified by DMI. The same pattern is observed for

all four stations. Trend analysis without adjustment for inhomogeneities on these data can therefore only be performed on the time period corresponding to manned observations, 1958-2004. This was done by Gueye (2014) and will not be repeated in this thesis.

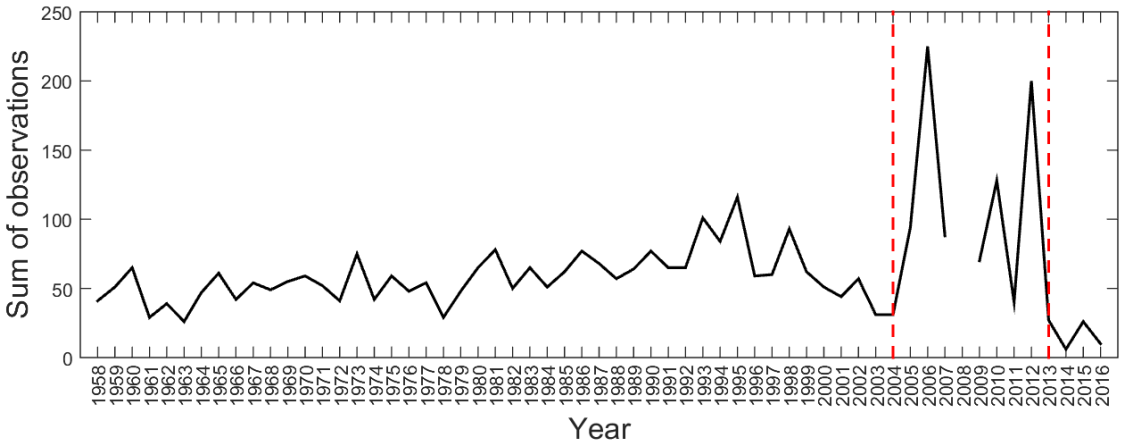

Figure 2-6. Yearly sum of synoptic fog observations at Tasiilaq. Vertical red lines indicate the switch from manned to automated observations (left line) and the switch to the 2013-2016 unchecked present weather dataset.

In total, only 1-2 % of present weather observations at each of the four stations represent real fog conditions. Analysis of monthly sum of fog observations reveals that fog in East Greenland mainly occurs in the summer months between May and August/September (Figure 2-7). The highest fog counts occur after 2001 for Danmarkshavn, and after 2005 for the other three stations, which coincides with the switch from manned to automated observations. This reflects a data inhomogeneity, but, since this chapter is not focused on trend analysis, no adjustment was made for this.

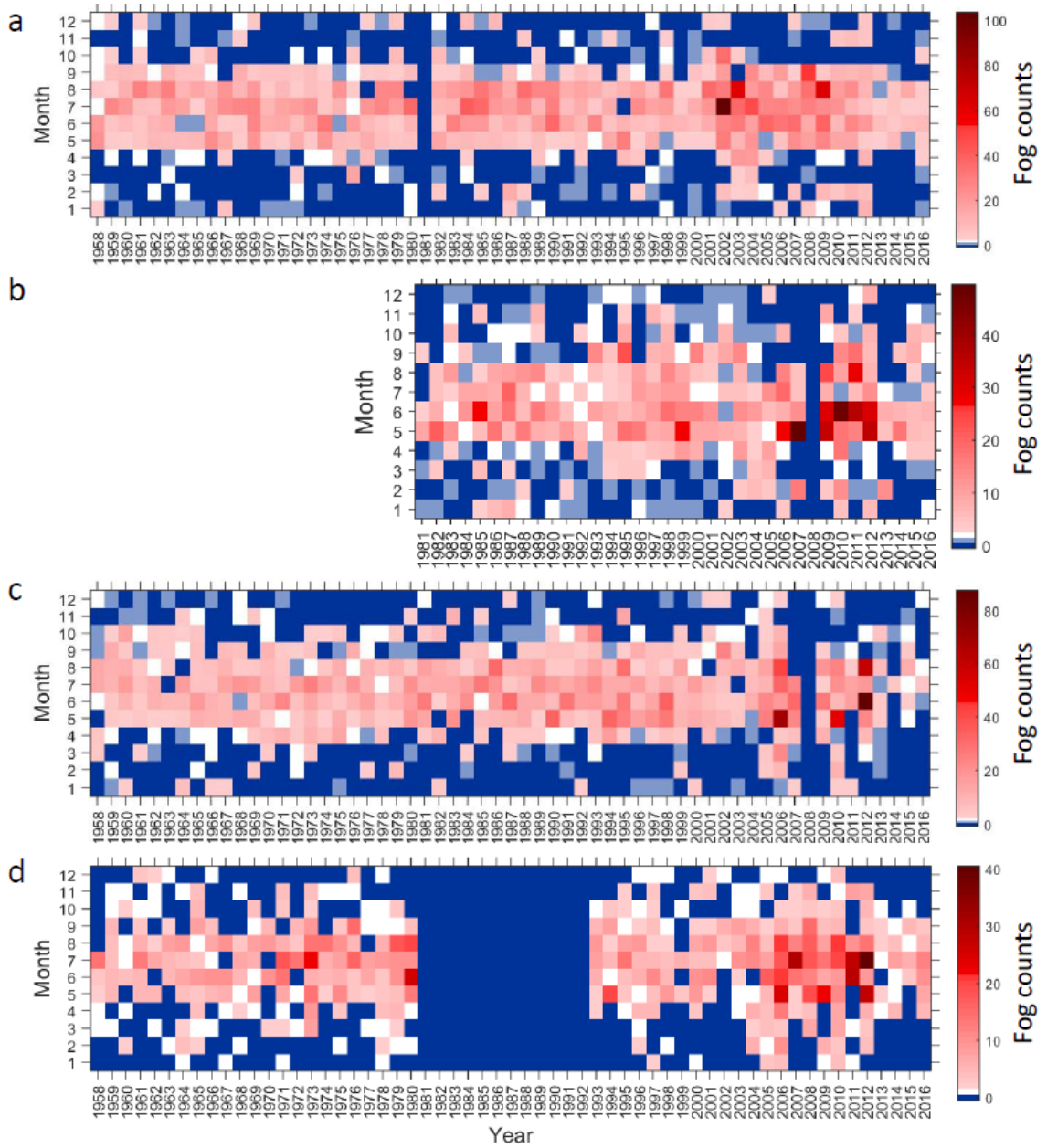

Figure 2-7. Monthly sum of synoptic fog observations for (a) Danmarkshavn, (b) Ittoqqortoormiit, (c) Tasiilaq, and (d) Prins CS. White is the median fog count value, blue is frequencies below the median, and red is frequencies above the median. Note the different colour bar ranges for each panel.

Between two thirds and three quarters of fog observations in coastal East Greenland occur between May and August (Table 2-3). The month with highest fog frequency (based on the sum of synoptic observations) is July for Prins CS and Danmarkshavn, May for Ittoqqortoormiit, and June for Tasiilaq. In Table 2-4, synoptic fog count frequencies are

compared among Danmarkshavn, Ittoqqortoormiit and Tasiilaq for the longest overlap period available with a minimum of missing data (1981-2003). Prins CS was excluded from this analysis because of its high number of missing observations during this period. Based on synoptic observation counts, fog at the station (real fog) occurs only 2-6 % of the time during summer. Tasiilaq has highest real fog frequency of occurrence in all months (4.1-6.1 %). In May, however, fog frequency of occurrence at Tasiilaq is not statistically different from Ittoqqortoormiit and in August, Tasiilaq and Danmarkshavn have similar fog frequencies. In the early melt season (May-June), Danmarkshavn is the station with the lowest fog occurrence (2.1-3.4 %), while in the late melt season (July-August), the lowest fog frequencies are encountered at Ittoqqortoormiit (2.9 %). When considering all fog codes (marginal and real fog), Ittoqqortoormiit is the station with the highest fog occurrence (on average 29 % of summer synoptic observations and 15 % of annual observations). Frequencies of summer and annual all fog observations are 11 % and 5 % at Danmarkshavn and 13 % and 6 % at Tasiilaq.

Table 2-3. Monthly sums of synoptic fog observations and relative annual frequency in percentages (brackets) at Danmarkshavn (DANM), Ittoqqortoormiit (ITTO), Tasiilaq (TASI) and Prins CS (PRINS) for the period 1958-2016. Statistics for summer are the sum of the months of May, June, July and August. Numbers in bold are the months of highest fog occurrence. Total numbers are not comparable among stations due to missing years of observations.

	DANM sum (%)	ITTO sum (%)	TASI sum (%)	PRINS sum (%)
Jan	53 (1)	51 (3)	43 (1)	20 (1)
Feb	107 (2)	77 (4)	52 (1)	48 (2)
Mar	46 (1)	52 (3)	69 (2)	52 (3)
Apr	139 (3)	124 (6)	209 (6)	103 (5)
May	593 (13)	**456 (23)**	647 (18)	281 (14)
Jun	875 (19)	446 (22)	**793 (22)**	342 (17)
Jul	**1119 (25)**	217 (11)	728 (20)	**466 (24)**
Aug	1030 (23)	237 (12)	580 (16)	351 (18)
Sep	373 (8)	172 (9)	240 (7)	161 (8)
Oct	110 (2)	83 (4)	157 (4)	55 (3)
Nov	47 (1)	52 (3)	58 (2)	61 (3)
Dec	72 (2)	27 (1)	37 (1)	25 (1)
Summer	3617 (79)	1356* (68)	2748 (76)	1440** (73)

* Fog data only reported from 1981 to 2016.
** Missing fog data between 1981 and 1992.

Table 2-4. Monthly frequency of synoptic fog observations relative to all present weather observations (%) at Danmarkshavn (DANM), Ittoqqortoormiit (ITTO), and Tasiilaq (TASI) for 1981-2003. Sign. diff indicates stations with significantly lower (-) or higher (+) relative fog frequencies compared to other stations ($p < 0.05$). Stations with blanks are not statistically different from each other for a specific month.

	DANM	Sign. diff	ITTO	Sign. diff	TASI	Sign. diff
	%		%		%	
May	2.1	-	4.8		5.0	
Jun	3.4	-	5.0		6.1	+
Jul	4.4		2.9	-	5.3	+
Aug	4.5		2.9	-	4.1	

2.5.1.3 Fog days

Maximum cumulative sums of real fog days per month are 18 at Danmarkshavn (July 2002), 14 at Ittoqqortoormiit (June 1985), 17 at Tasiilaq (June 2012), and 13 at Prins CS (July 1973) (Figure 2-8). Figure 2-9a shows the average sum of real fog days per month (expressed as count and percentage) at each station for the period 1958-2016, and includes temporal data gaps. The range in percentages of fog days occurring in summer is 8-22 % (Table 2-5). Real fog is most frequent over Danmarkshavn, occurring up to 20 % of the time or 7 days a month in July and August. Danmarkshavn is also the only location that has a significantly higher number of real fog days in August. This late melt season peak in fog days contrasts with an earlier melt season peak in fog days at the more southern stations Ittoqqortoormiit (May-June) and Tasiilaq (June-July). A similar seasonal north-south pattern was found when only the longest period of overlap among stations (1981-2003) was considered (results not shown). However, when considering all fog codes (real and marginal), the average monthly number of fog days, peak in fog occurrence and station with the highest fog frequency differ. In this case, Ittoqqortoormiit has the highest fog occurrence (up to 15 all fog days instead of 6 real fog days, see Figure 2-9). This all fog frequency peaks in June at Ittoqqortoormiit, though at Tasiilaq and Danmarkshavn it peaks in July with 8 to 12 average monthly number of fog days, respectively.

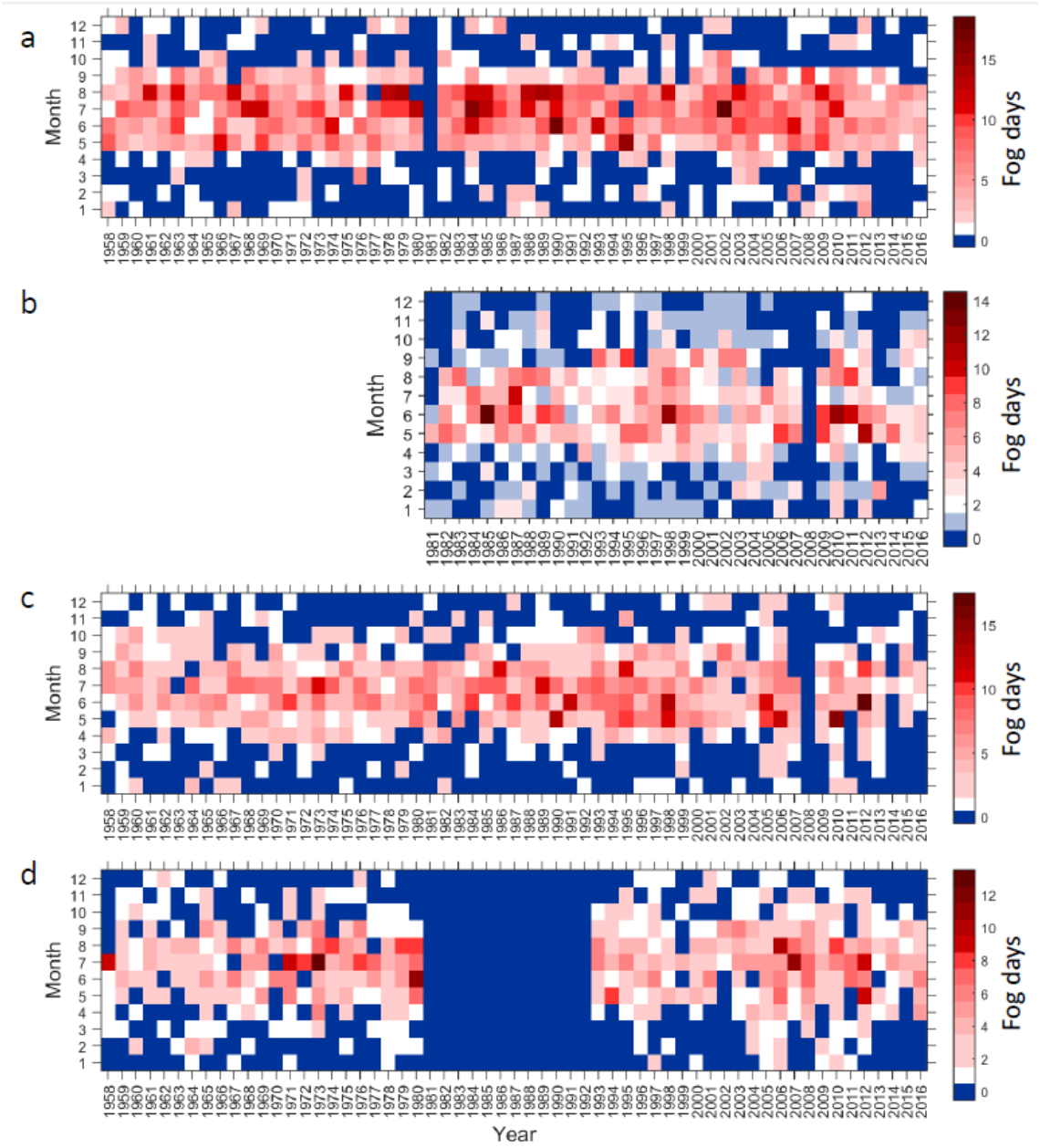

Figure 2-8. Monthly sum of real fog days for (a) Danmarkshavn, (b) Ittoqqortoormiit, (c) Tasiilaq, and (d) Prins CS. White is the median fog day value, blue is frequencies below the median, and red is frequencies above the median. Note the different colour bar ranges for each panel.

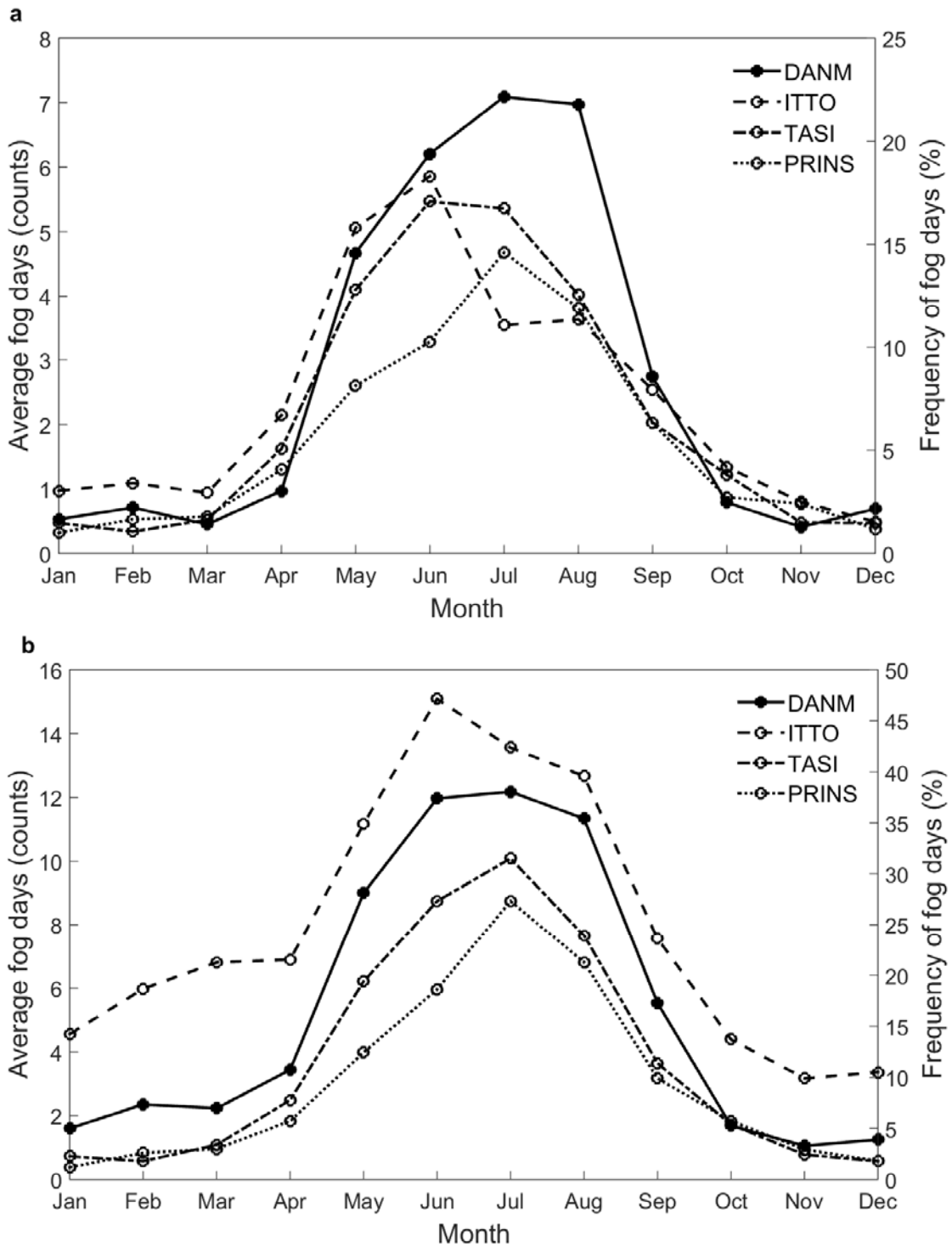

Figure 2-9. Monthly average number of days with fog (left y-axis) and monthly average percentage of days with fog (right y-axis) at Danmarkshavn (DANM), Ittoqqortoormiit (ITTO), Tasiilaq (TASI) and Prins CS (PRINS) for (a) fog at the station (real fog) and (b) fog at the station and marginal fog (all fog). See Table 2-2 for WMO fog codes used.

Table 2-5. Average monthly frequency of fog days at Danmarkshavn (DANM), Ittoqqortoormiit (ITTO), and Tasiilaq (TASI) for 1981-2003. "-" and "+" denote the station with significantly lowest and highest fog days, respectively, in comparison with other stations. Stations with blanks have no significant difference with each other for a specific month.

	DANM days		ITTO days		TASI days
May	4.1		4.9		5.2
Jun	7.0		5.8		6.1
Jul	7.7		4.0	-	6.1
Aug	8.0	+	4.0		4.4

2.5.2 Time and duration of fog occurrence

At each station, fog displays a diurnal cycle, with a daily maximum in the late morning, before solar noon, and a daily minimum in the late afternoon (Figure 2-10). At Tasiilaq, fog has the highest diurnal variation, with 90 % of summer fog occurring between 0000 and 1100 UTC (Table 2-6). However, this only significantly differs from Danmarkshavn, where 35 % of fog observations occur between 1200 and 2300 UTC ($\chi^2 = 18$, df = 1, $p < 0.001$). During the early melt season (May-June) at Ittoqqortoormiit, fog displays a similar daily timing distribution as Danmarkshavn, with 29 % of fog occurring after 1200 UTC. This is significantly different from the late melt season (July-Aug) daily timing distribution at Ittoqqortoormiit, where only 15 % of fog occurs in the afternoon ($\chi^2 = 86$, df = 1, $p < 0.001$). Additionally, there is a non-significant tendency for fog at the other three stations to be less restricted to morning hours in the early melt season compared to the late melt season (χ^2 range = 0.3-2.8, df = 1, p range = 0.09-0.60) and a non-significant tendency for fog at Prins CS to be less restricted to morning hours compared to fog at Tasiilaq ($\chi^2 = 0.8$, df = 1, $p = 0.38$). Fog timing conclusions from tests performed on local time instead of UTC time remain the same (not shown).

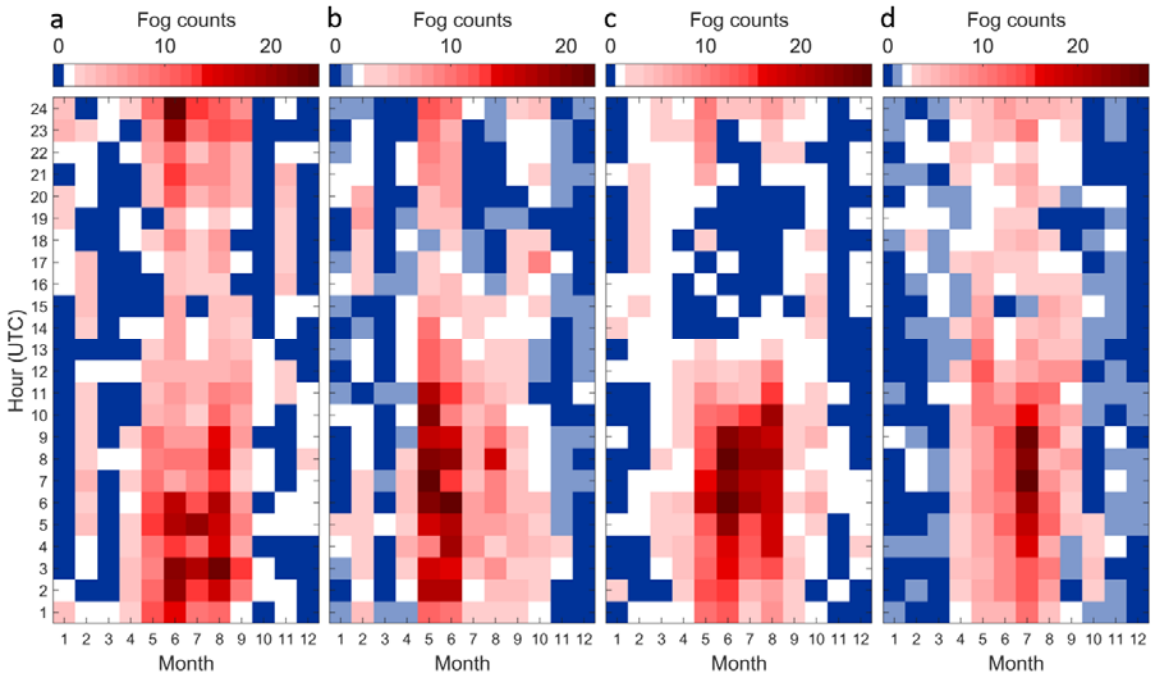

Figure 2-10. Time of fog occurrence with the count of hourly observations in the period 2006-2016 at (a) Danmarkshavn, (b) Ittoqqortoormiit, (c) Tasiilaq, and (d) Prins CS. White is the median fog count value, blue is frequencies below the median, and red is frequencies above the median. Note the different colour bar ranges for each panel.

Table 2-6. Total number of fog observations (n) in early summer (May-June), late summer (July-Aug), and all summer (May-Aug); frequency of morning fog occurring between 0000 and 1100 UTC (% in brackets). Percentages in bold are significantly different ($p < 0.01$) between early and late melt season ("May-June" vs. "July-Aug") or among stations ("Tot summer").

	DANM n (morning fog %)	ITTO n (morning fog %)	TASI n (morning fog %)	PRINS n (morning fog %)
May-June	482 (60)	520 (**71**)	400 (88)	312 (71)
July-Aug	625 (68)	179 (**85**)	386 (92)	434 (76)
Tot summer	1107 (**65**)	699 (74)	786 (90)	746 (74)

The results discussed above suggest a longer fog duration at Danmarkshavn compared to Tasiilaq, because Danmarkshavn has less of a diurnal variation in fog occurrence and may therefore occur throughout the day. Using hourly observations in the automated observation period average fog duration was calculated as ~ 1.5 hours. Tasiilaq has the longest average fog duration (1.6 ± 1.7 h, Figure 2-11c), although this is not significantly

different from the other stations. Conclusions obtained from three-hourly observations (not shown) are comparable to those obtained from hourly observations. We, therefore, conclude that, even though fog at Danmarkshavn is not as restricted to the morning as fog at Tasiilaq, it is not more continuous and the average fog duration is the same at all sites.

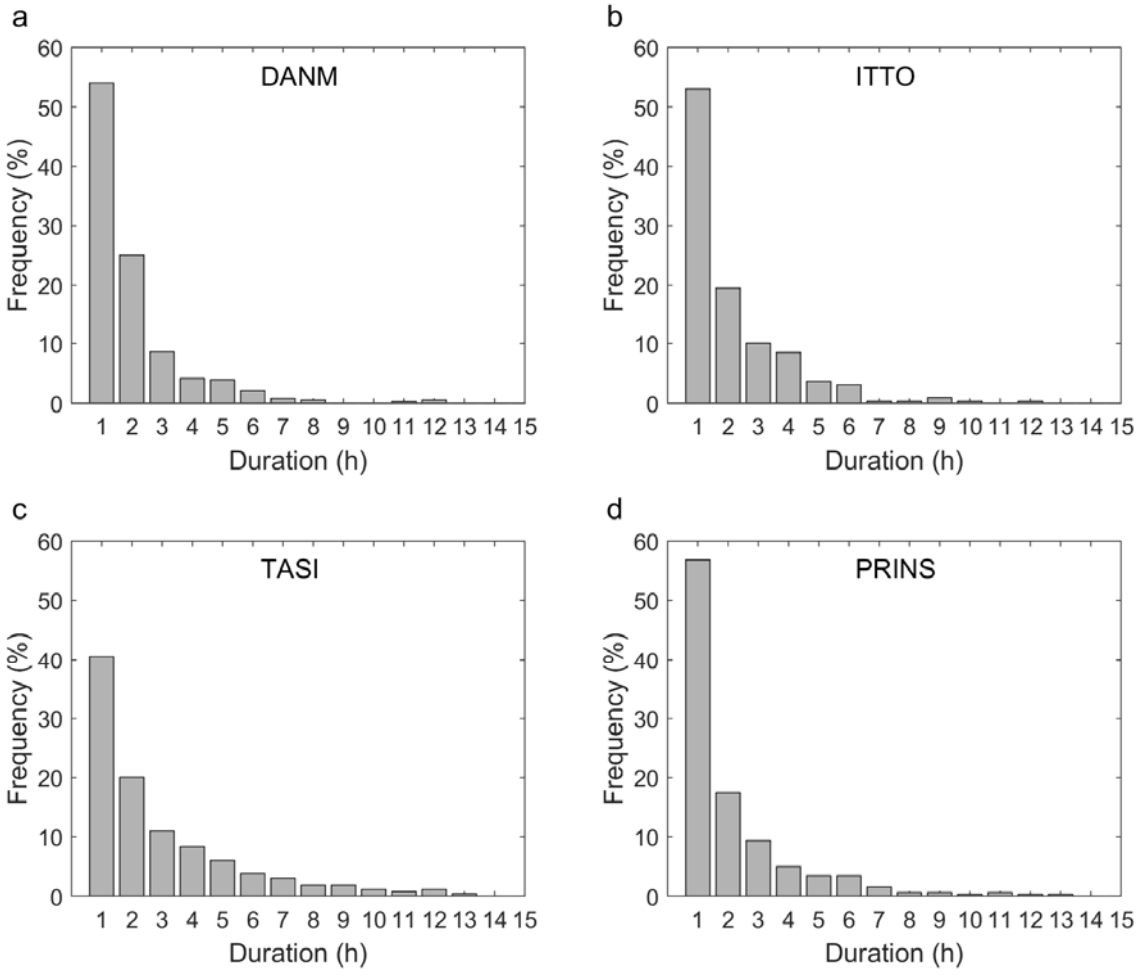

Figure 2-11. Fog duration determined from the sum of subsequent hourly automated fog observations (summers of 2006-2016) at (a) Danmarkshavn (DANM), (b) Ittoqqortoormiit (ITTO), (c) Tasiilaq (TASI), and (d) Prins CS (PRINS).

Since the majority of synoptic fog observations and fog days occur between May and August, the remainder of the climatological analysis in this chapter will be restricted to these melt season months, which will be referred to as "summer". Additionally, unless stated otherwise, the analysis will be performed using synoptic observations up to 2012 only, because data from 2013 onwards were not quality-checked by DMI.

2.5.3 Temperature during summer fog

Temperature during fog is reported in Figure 2-12 for all four stations. Fog usually occurs around 0°C for all stations (median values are -0.6°C, -0.8°C, 0.5°C for Danmarkshavn, Ittoqqortoormiit and Tasiilaq, respectively), except the southernmost (Prins CS, median = 3°C). All fog temperature distributions are negatively skewed. The long tails in the negative values for Danmarkshavn and Ittoqqortoormiit signify that even in summer very low temperatures can occur during fog at higher latitudes. Table 2-7 summarises frequencies of synoptic fog observations with temperatures above -10°C (supercooled or liquid fog), between -30°C and -10°C (mixed-phase fog), and below -30°C (ice fog) (Petterssen, 1956). According to these temperature thresholds, summer fog is predominantly liquid or supercooled (> 95 %), with mixed-phase fog only occurring sporadically in early summer months at the two northernmost stations while ice fog does not occur.

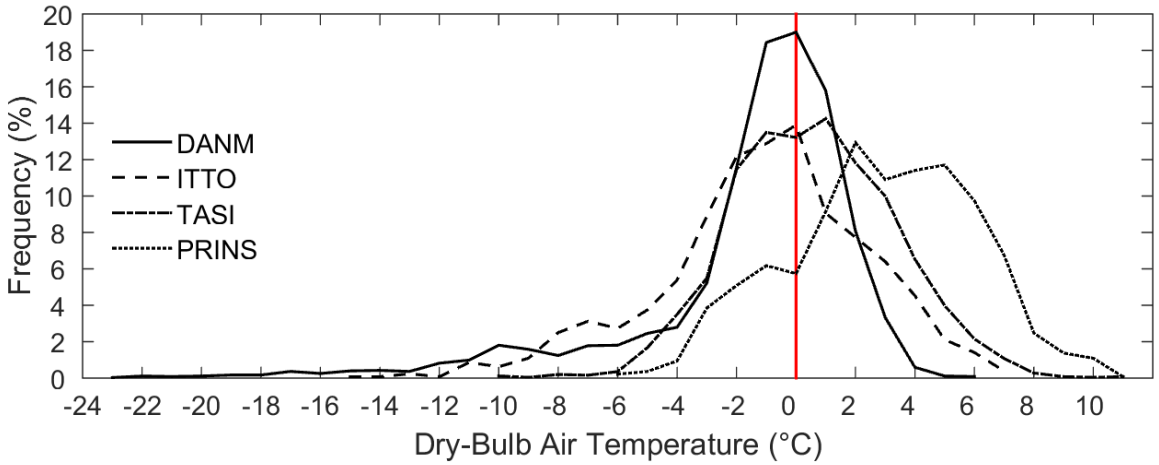

Figure 2-12. Frequency distribution of dry-bulb air temperature during summer fog at Danmarkshavn (DANM), Ittoqqortoormiit (ITTO), Tasiilaq (TASI), and Prins CS (PRINS). The red vertical line is 0°C.

Table 2-7. Frequencies in percentages of supercooled/liquid (T > -10°C), mixed-phase (-10°C ≥ T > -30°C) and ice fog (T ≤ -30°C) during summer at Danmarkshavn (DANM), Ittoqqortoormiit (ITTO), Tasiilaq (TASI), and Prins CS (PRINS). After Petterssen, 1956.

	DANM %	ITTO %	TASI %	PRINS %
T > -10°C	96	99	100	100
-10°C ≥ T > -30°C	4	1	0	0
T ≤ -30°C	0	0	0	0

2.5.4 Relative humidity during summer fog

Most summer fog in East Greenland occurs with high relative humidity with respect to liquid water (RH_w > 93 %: Figure 2-13), which corresponds to a dew point depression threshold T_{dd} < 1°C (Hardy, 1998). This will become of importance in Chapters 3 and 4, where a method will be developed to detect fog from saturation in radiosonde data. The two Low-Arctic stations display median RH_w values close to or equal to 100 % suggesting fog is in the liquid or supercooled phase (Table 2-7). The relatively lower RH_w values at Prins CS compared to Tasiilaq are due to problems with RH_w sensors at that location, as

emphasized in Figure 2-14. Most of these issues correspond to the use of the hygroscopic hair (Ulrik, pers comm, 1 March 2016). RH_w at High-Arctic locations can be as low as 85 %, which is directly related to lower temperatures at these stations (Figure 2-12).

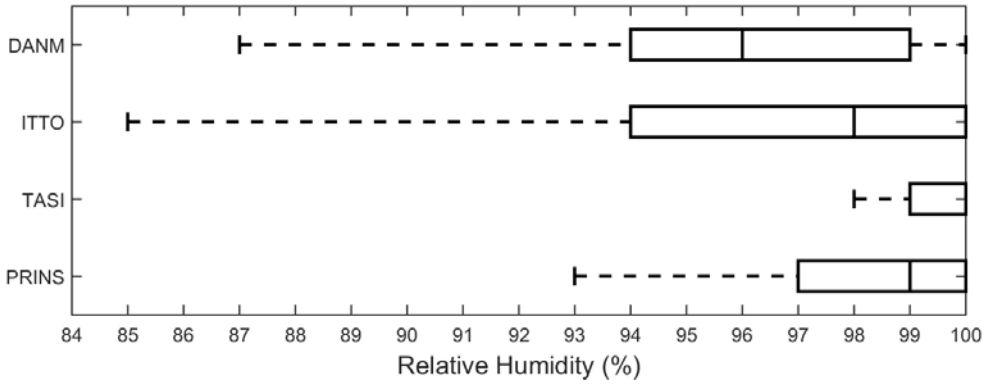

Figure 2-13. Frequency distribution of relative humidity with respect to liquid water during summer fog at Danmarkshavn (DANM), Ittorqoortoormiit (ITTO), Tasiilaq (TASI), and Prins CS (PRINS). Box and whisker plots show the median (horizontal line), lower and upper quartiles (bottom and top of box), and 5th and 95th percentiles (range).

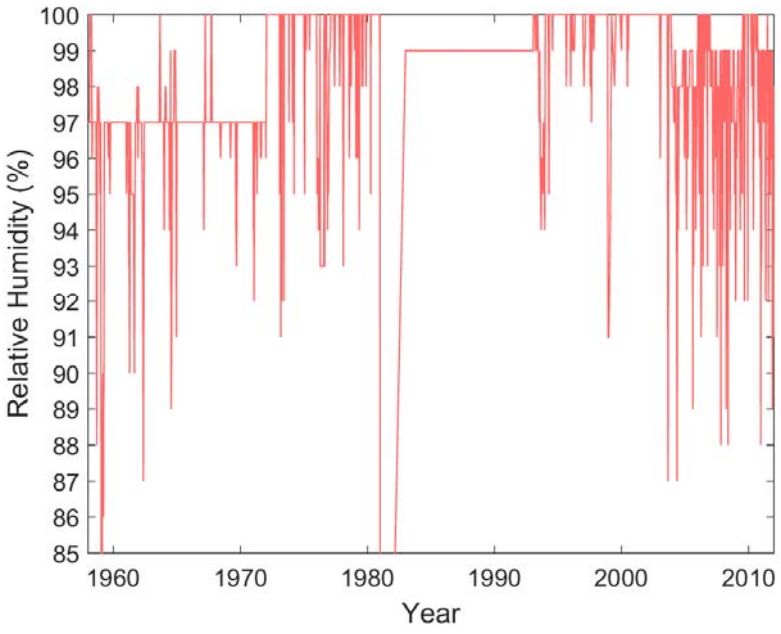

Figure 2-14. Time series of the yearly range of relative humidity with respect to liquid water during summer fog at Prins CS.

2.5.5 Visibility

Figure 2-15 shows the distribution of horizontal visibilities for each manned present weather observation code representing fog. The peak at 500-m visibility is not seen in the automated fog present weather code distributions (Figure 2-16) and may point to a human observer bias in the measurements. The analysis of visibility distributions reveals that unchanging and thickening fog display similar positively skewed distribution frequencies, in contrast to the normal to negatively skewed pattern observed for thinning fog. This is seen under both the visible (*ww* = 44, 46 vs. 42) and invisible sky regimes (*ww* = 45, 47 vs. 43), which suggests that fog microphysics differ among fog stages. When the sky is invisible, horizontal visibility is significantly lower (by 150-180 m on average), except for thinning fog at Danmarkshavn and Ittoqqortoormiit (Table 2-8). This suggests that vertical and horizontal visibilities are related to each other. Under very dense fog (*vv* ≤ 100 m), fog events with sky invisible indeed occurred 5 to 13 times more frequently than fog events with sky visible (Table 2-9). This confirms that very dense fog is usually also sky-obscuring.

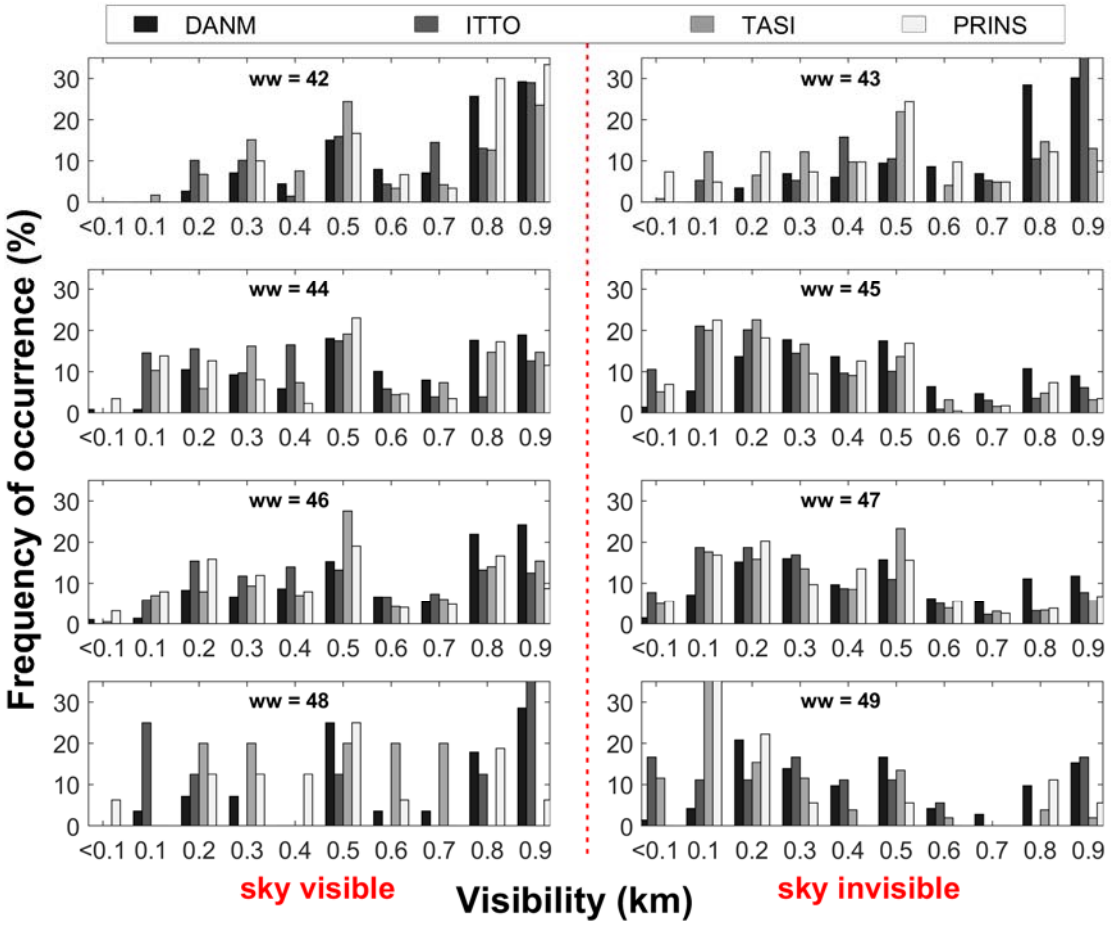

Figure 2-15. Horizontal visibility (km) for each fog code (*ww*, see Table 2-2) in summer from the manned weather stations between approximately 1958 and 2003 at Danmarkshavn (DANM), Ittoqqortoormiit (ITTO), Tasiilaq (TASI), and Prins CS (PRINS). Paired panels from top to bottom: fog thinning; unchanging; thickening; and depositing rime.

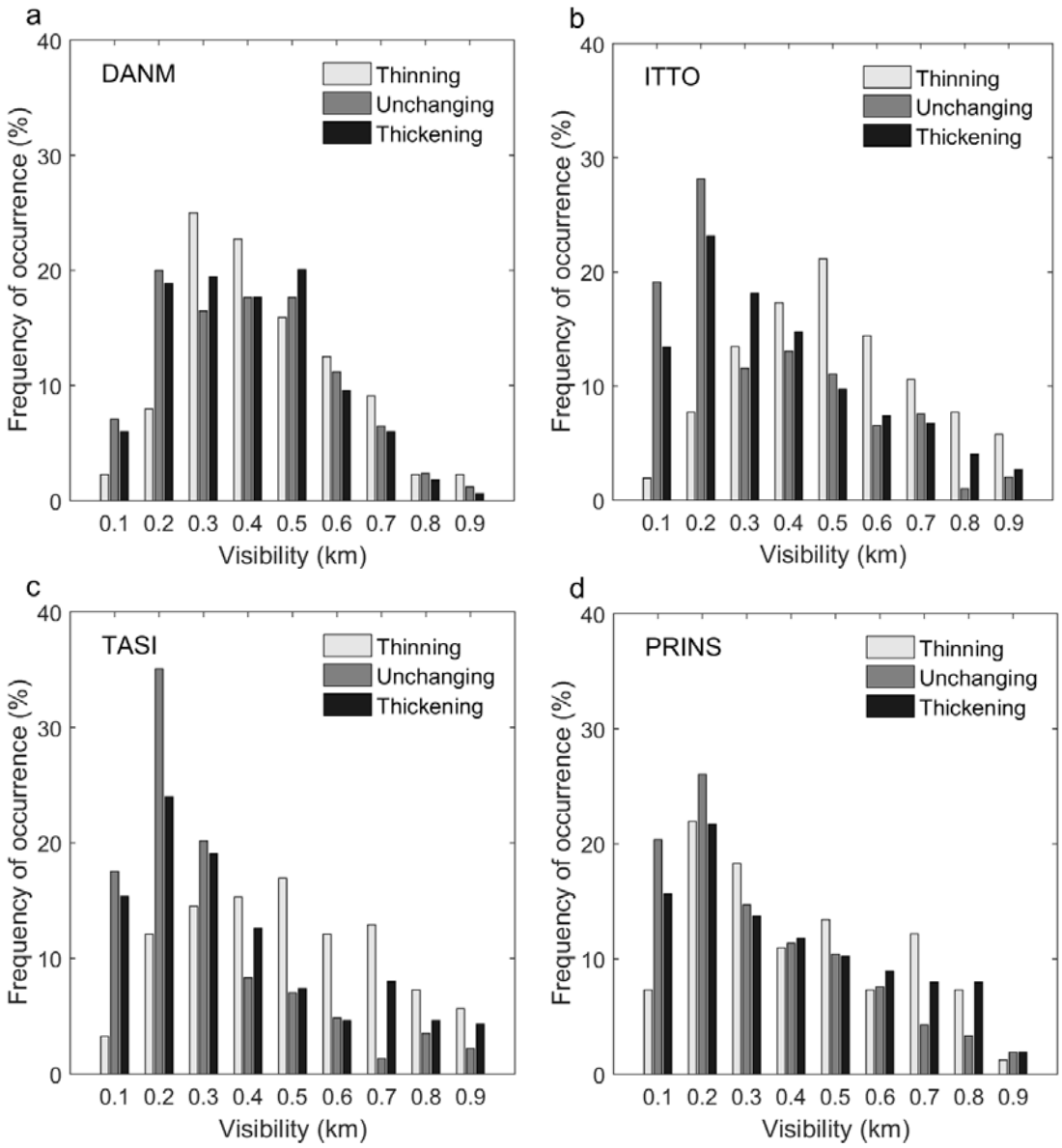

Figure 2-16. Horizontal visibility (km) for each automated fog code in summer at (a) Danmarkshavn, (b) Ittoqqortoormiit, (c) Tasiilaq, and (d) Prins CS. "Thinning" is *ww* 32, "unchanging" is *ww* 33, and "thickening" is *ww* 34 (See Table 2-2).

Table 2-8. Horizontal visibility number of observations (n), and mean and standard deviation (km) during summer fog when the sky is visible and invisible from manned observations and for all fog stages (*ww* = 42, 44, 46 vs. 43, 45, 47), thinning fog (*ww* = 42 vs. 43), unchanging fog (*ww* = 44 vs. 45), and thickening fog (*ww* = 46 vs. 47) at Danmarkshavn (DANM), Ittoqqortoormiit (ITTO), Tasiilaq (TASI), and Prins CS (PRINS). Means in bold significantly differ under the visible and invisible sky regimes ($p < 0.01$).

	Horizontal Visibility							
	DANM		ITTO		TASI		PRINS	
	n	km	n	km	n	km	n	km
All fog stages								
Sky visible	766	**0.63** ± 0.24	470	**0.51** ± 0.26	557	**0.55** ± 0.25	319	**0.52** ± 0.28
Sky invisible	2205	**0.48** ± 0.25	641	**0.34** ± 0.26	1871	**0.37** ± 0.24	673	**0.35** ± 0.25
Thinning fog								
Sky visible	125	0.70 ± 0.21	91	0.63 ± 0.25	161	**0.58** ± 0.26	43	**0.72** ± 0.20
Sky invisible	132	0.70 ± 0.22	29	0.63 ± 0.26	152	**0.52** ± 0.26	55	**0.50** ± 0.26
Unchanging fog								
Sky visible	274	**0.60** ± 0.24	159	**0.46** ± 0.26	114	**0.53** ± 0.26	114	**0.47** ± 0.28
Sky invisible	1197	**0.47** ± 0.24	303	**0.31** ± 0.25	771	**0.33** ± 0.22	298	**0.32** ± 0.25
Thickening fog								
Sky visible	367	**0.63** ± 0.25	220	**0.51** ± 0.26	282	**0.54** ± 0.25	162	**0.49** ± 0.27
Sky invisible	876	**0.47** ± 0.26	309	**0.35** ± 0.25	948	**0.38** ± 0.24	320	**0.36** ± 0.25

Table 2-9. Number of observations of very dense summer fog events ($vv \leq 100$ m) with invisible ("inv") and visible ("vis") sky, and the ratio between very dense fog with invisible and visible sky at Danmarkshavn (DANM), Ittoqqortoormiit (ITTO), Tasiilaq (TASI), and Prins CS (PRINS).

	DANM	ITTO	TASI	PRINS
n_{inv}	142	401	150	143
n_{vis}	31	30	29	13

The analysis of combined manual and automated station visibility observations (Figure 2-17) reveals that fog over coastal East Greenland occurs with the majority of observations below 500 m, which is classified as dense to very dense fog (see Chapter 1). However, fog at Danmarkshavn, the northermost station, is significantly less dense than fog at the other three stations (Figure 2-17: significant at $p < 0.001$). This is also clear from the stronger negative skew of Danmarkshavn's horizontal visibility distribution frequencies in the manned observations (Figure 2-15) and the absence of positive skew in the automated observations at Danmarkshavn (Figure 2-16). Even though the shapes of

distributions differ between automated and manned observations, the general conclusion of higher visibility at Danmarkshavn remains the same when performing the statistical analysis on automated observations only (not shown). Higher visibility conditions at that site could possibly be caused by either a higher proportion of thinning fog (Table 2-8) or different environmental conditions, such as the presence of sea ice during most of the summer. Table 2-10 further explores the tendency for fog at Danmarkshavn to have higher visibility values compared to the other three stations, and reveals that this is significant for unchanging and thickening fog only. Additionally, thinning fog has significantly higher visibilities than the other two types of fog at all sites except Prins CS, where visibility does not differ among fog types. However, Danmarkshavn had one of the lowest proportion of thinning fog (high visibility values) and the highest proportion of thickening fog (low visibility values), suggesting that, if visibility only depended on the relative frequency of fog type, Danmarkshavn should have the lowest average visibility.

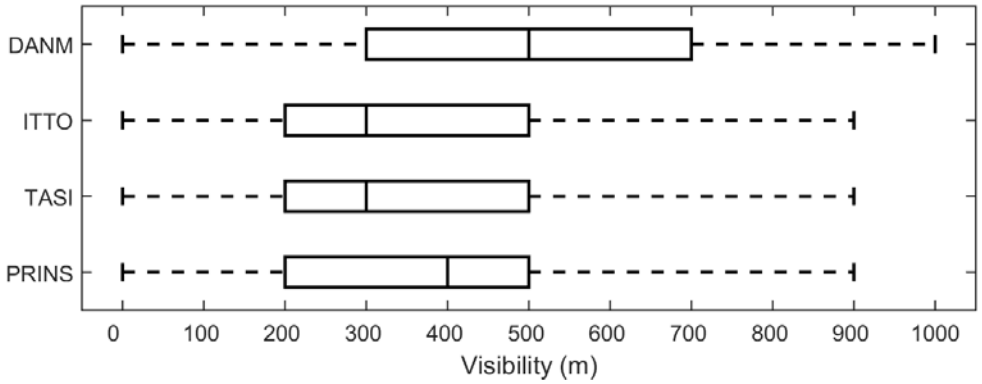

Figure 2-17. Horizontal visibility during summer fog from 1958-2012 at Danmarkshavn (DANM), Ittoqqortoormiit (ITTO), Tasiilaq (TASI), and Prins CS (PRINS).

Table 2-10. Horizontal visibility mean and standard deviation (km) during summer fog from automated observations (2006-2016) and for thinning fog (*ww* = 32), unchanging fog (*ww* = 33), and thickening fog (*ww* = 34) at Danmarkshavn (DANM), Ittoqqortoormiit (ITTO), Tasiilaq (TASI), and Prins CS (PRINS). Means in bold significantly differ among stations (black) or among fog stages (italics red) ($p < 0.01$).

	Horizontal Visibility							
	DANM		ITTO		TASI		PRINS	
ww	n (%)	km	n (%)	km	n (%)	km	n (%)	km
32	75 (15)	***0.47*** ± 0.18	101 (20)	***0.47*** ± 0.21	116 (19)	***0.47*** ± 2.18	70 (14)	**0.38** ± 0.21
33	143 (28)	**0.39** ± 0.18	180 (35)	0.31 ± 0.20	210 (35)	0.30 ± 1.94	190 (38)	0.33 ± 0.21
34	297 (58)	**0.39** ± 0.19	235 (46)	0.35 ± 0.21	273 (46)	0.37 ± 2.40	245 (49)	0.38 ± 0.23

2.5.6 Wind

A large proportion of fog events occur under calm conditions (w_s = 0 m s^{-1}): 42 % at Danmarkshavn, 58 % at Ittoqqortoormiit, 72 % at Tasiilaq and 49 % at Prins CS. The vast majority of fog events not taking place under calm conditions occur with surface wind speeds between 1-4 m s^{-1} and wind directions predominately from the nearest open water source (Figure 2-18). At Danmarkshavn (average w_s = 2.5 ± 1.4 m s^{-1}), fog comes from an easterly-southerly direction which corresponds to the open ocean (Figure 2-18). At Tasiilaq (w_s = 2.1 ± 1.2 m s^{-1}), the predominantly southerly wind direction during fog also denotes an oceanic origin; the secondary peak in northerly directions may represent

fog originating from Sermilik or Ammassalik fjords, or fog retreating from these fjords towards the ocean. Surface wind directions are similar under foggy and all-weather conditions at Tasiilaq. When considering the frequency of fog occurring under calm conditions (not included in Figure 2-18), the calmest conditions for all fog events occur at Tasiilaq (w_s = 0.58 ± 1.14 m s^{-1}, $p < 0.001$). This site is also the calmest under all weather conditions, with an average summer wind of 1.4 m s^{-1} (Cappelen et al., 2001). Fog at Prins CS (w_s = 2.7 ± 2.0 m s^{-1}) has a predominant easterly wind direction, which can be explained by the channeling of fog formed over the ocean into the E-W oriented Prins CS fjord. This contrasts with the predominant northerly wind direction and high wind speeds occurring at that location during all weather conditions. Fog occurs at the lowest wind speeds at Ittoqqortoormiit (w_s = 1.8 ± 1.5 m s^{-1}: significantly different than the other locations at $p < 0.001$), where it originates from the large Scoresby Sund fjord and not from the open ocean. Fog at Danmarkshavn and Prins CS have the highest wind speeds ($p < 0.001$). These are also the windiest places under all weather conditions, especially at Prins CS where average wind speed is 5 m s^{-1} in summer (Cappelen et al., 2001).

The comparison between surface and higher-level winds during fog reveals a 90° rotation clockwise from the surface up over Danmarkshavn and Tasiilaq. These predominantly veering winds suggest the prevalence of warm air advection processes during fog (Croft et al. 1997). Upper-level winds during fog at these locations contrast with their upper-level winds during all weather conditions: southerly (ocean) vs. northwesterly (ice sheet) over Danmarkshavn and westerly (ice sheet) vs. easterly (ocean) directions over Tasiilaq. Upper winds typically originate from the north over Ittoqqortoormiit during both fog and all-weather conditions.

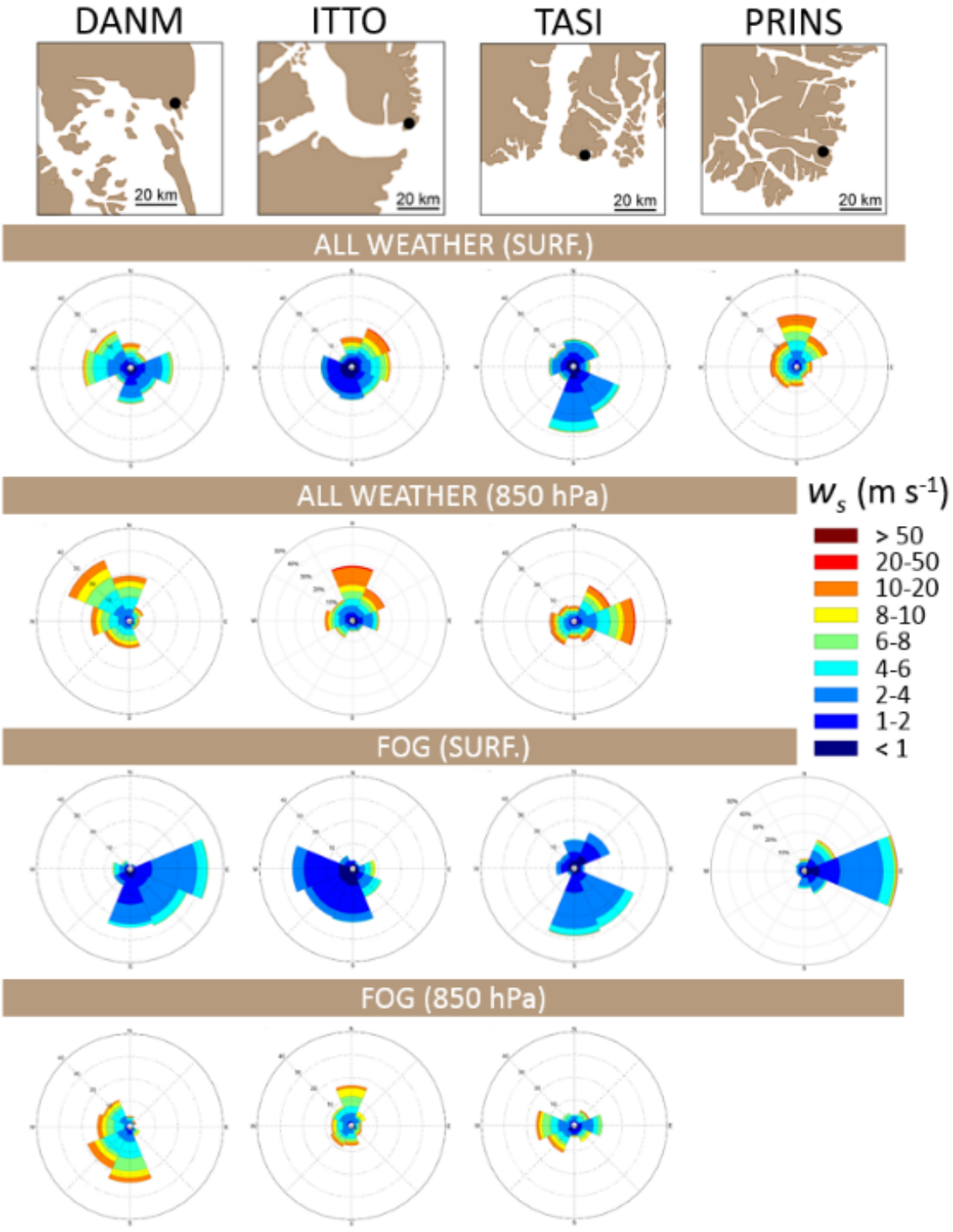

Figure 2-18. Wind speed and direction for all summer weather (ALL WEATHER) and summer fog observations (FOG) at the surface (surf. from DMI) and aloft (850 hPa level from IGRA) over Danmarkshavn (DANM), Ittoqqortoormiit (ITTO), Tasiilaq (TASI), and Prins CS (PRINS). Top panels show schematic maps representing the distribution of land (brown) and water (white) around each station. Surface winds are from 1958 to the end of manned observations (appr. 2003) and upper winds are from 1980 to 2012. Note that the scale is different for Prins CS, with the outermost circle representing 50 % frequency instead of 40 % for the other stations.

Sea breezes are significantly more frequent during fog than under all weather conditions, at all sites, both in the morning and afternoon (Figure 2-19). Sea breezes are more frequent in the afternoon compared to the morning, under both foggy and all weather conditions, and for all sites. Under all weather conditions, Tasiilaq has the highest frequency of sea breezes, followed by Danmarkshavn, Ittoqqortoormiit and Prins CS (morning and afternoon). The diurnal variation in sea breeze occurrence is also strongest with decreasing latitude. When fog is present, Danmarkshavn has the highest frequency of sea breezes, with 75 % of occurrence in the morning and 86 % in the afternoon. Nevertheless, Tasiilaq has the highest diurnal variation in sea breeze frequency during fog, with an increase of 52 % of sea breeze occurrence in the afternoon compared to the morning. In contrast, Danmarkshavn only has a 15 % increase in sea breeze occurrence in the afternoon. There is a tendency for sea breeze frequency during fog to decrease with decreasing latitude, although this is not statistically significant. In the morning, sea breezes are dominant during fog at Danmarkshavn only, whereas in the afternoon, they are dominant over all locations. There was no significant difference in sea breeze frequency between foggy conditions and immediately after the end of fog, though winds were slightly stronger after fog and there was a higher proportion of offshore winds at Ittoqqortoormiit and Prins CS (see Appendix 2).

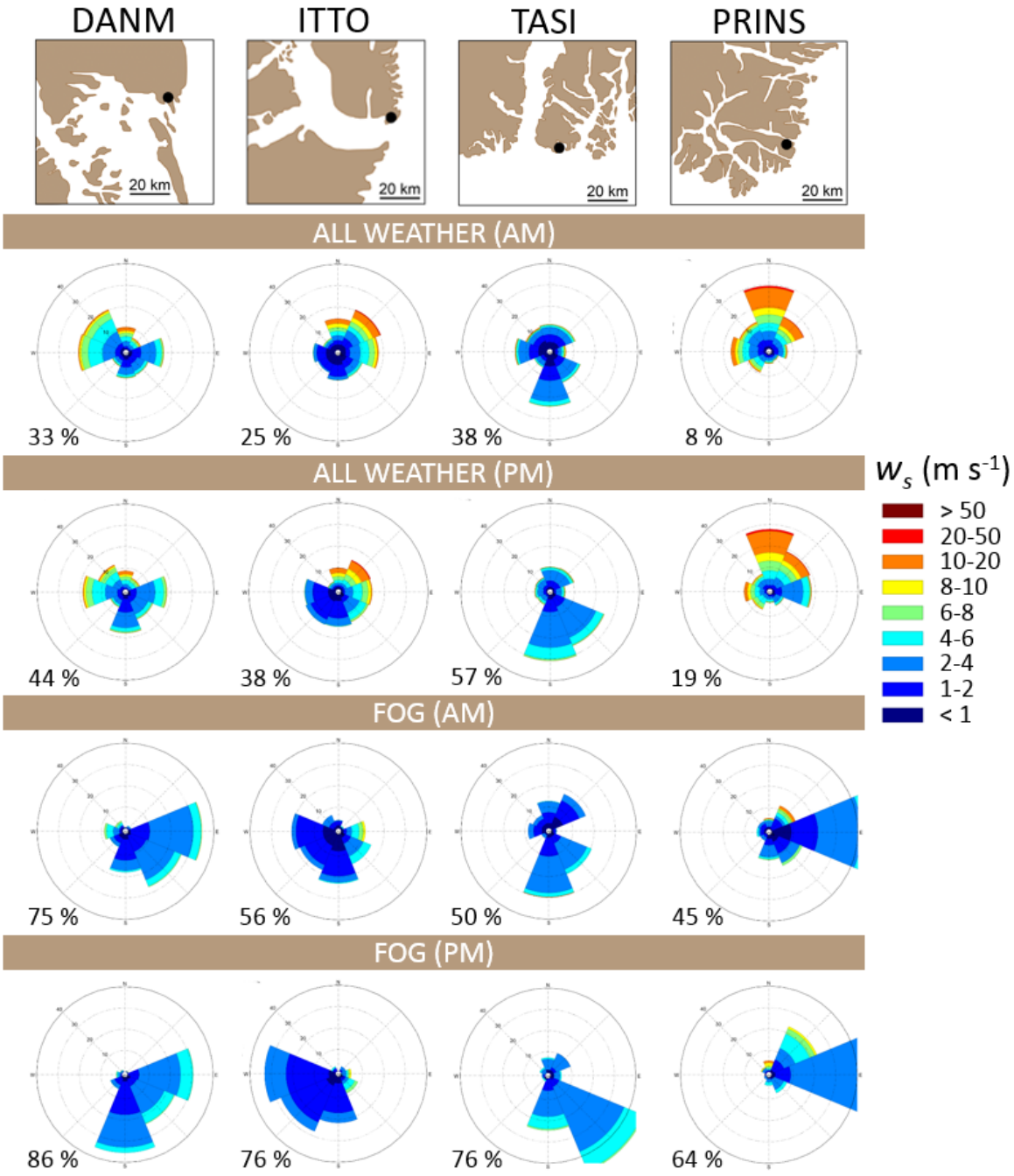

Figure 2-19. Wind roses with surface wind speed and direction for all summer weather (ALL WEATHER) and summer fog (FOG) observations in the morning (AM: 0000-1100 UTC) and afternoon (PM: 1200-2300 UTC) from 1958 to the end of manned observations (appr. 2003) over Danmarkshavn (DANM), Ittoqqortoormiit (ITTO), Tasiilaq (TASI), and Prins CS (PRINS). The outermost circle represents 40 % frequency of occurrence. The percentages displayed next to each wind rose correspond to the frequency of sea breeze. Top panels show schematic maps representing the distribution of land (brown) and water (white) around each station.

2.5.7 Sea ice concentration

The timing of sea ice break-up is highly variable from year to year (Figure 2-20, grey shading) and depends on atmospheric and oceanic heat fluxes, oceanic currents, pressure and winds (Marshall, 2012). On average, sea ice starts to break up in June around Tasiilaq, while it starts to break up later in the melt season at Danmarkshavn (Figure 2-20, black lines). This is related to the colder climate and a sustained flux of sea ice from the Arctic Ocean through the Fram Strait in northeast Greenland. At Danmarkshavn, there is generally offshore sea ice remaining throughout the melt season. Further south, at Tasiilaq, sea ice is usually absent by August, although this station exhibits a very high interannual variability. Ittoqqortoormiit has an average maximum concentration of 75 % early in the melt season. This lower *SIC* denotes the presence of the year-round Scoresby Sund Polynya (Sandel and Sandel, 1991). Sea ice starts to break up even more by the end of May and is mostly gone by August. Even though Prins CS is located at the southern tip of Greenland, it is influenced by the presence of seasonal sea ice (Cappelen, 2015), reaching a maximum average of 25 % in the early melt season. The sea is usually completely ice-free in August at that location.

The red line in Figure 2-20 confirms that the vast majority of fog days take place during the melt season (see also Table 2-3 and Figure 2-9). The month of sea ice break-up coincides with the month of highest fog occurrence at Danmarkshavn, Ittoqqortoormiit and Tasiilaq. From Figure 2-20, fog onset graphically corresponds to the onset of sea ice break-up at these locations. On average, 50 % of cumulative yearly fog day occurrence is reached by DOY 198 (17 July) at Danmarkshavn, by DOY 174 (23 June) at Tasiilaq, and

DOY 163 (12 June) at Ittoqqortoormiit. These approximately correspond to a *SIC* of 50 %. At Prins CS, 50 % of cumulative yearly fog day occurrence is reached by DOY 188 (7 July) when *SIC* is generally no more than 10 % (Figure 2-20d).

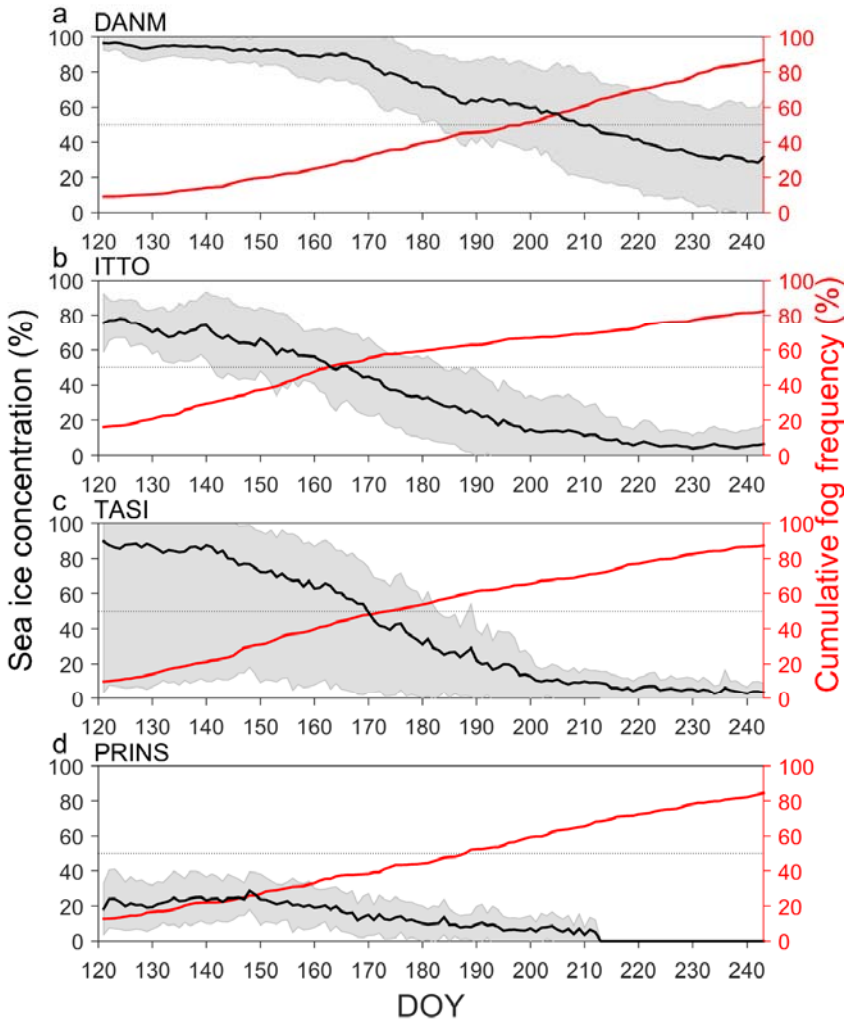

Figure 2-20. Average (black curve) and standard deviation (grey shading) of daily sea ice concentration, and average cumulative frequency of fog days (red curve) between 1 May (DOY 121) and 31 August (DOY 243) in 1988-2012 in a pixel offshore of (a) Danmarkshavn (DANM), (b) Ittoqqortoormiit (ITTO), (c) Tasiilaq (TASI), and (d) Prins CS (PRINS). The horizontal dotted line is 50 % frequency in both sea ice concentration and average cumulative fog day occurrence. Gridded sea ice concentration data from NSIDC (https://nsidc.org, NSIDC-0051).

Figure 2-21 shows that most fog days at Danmarkshavn, Ittoqqortoormiit and Tasiilaq occur at the time of initial sea ice break-up, when leads start to form. Even though most fog at Prins CS occurs during the melt season, sea ice break-up is not as strongly related to fog onset as at the other stations. The initial inflection points in Figure 2-21 (e.g. for Danmarkshavn at cumulative fog day frequency of 30 %) also denote a rapid increase in fog occurrence before the rapid sea ice break-up starts. This might suggest a common atmospheric control on the onset of both parameters.

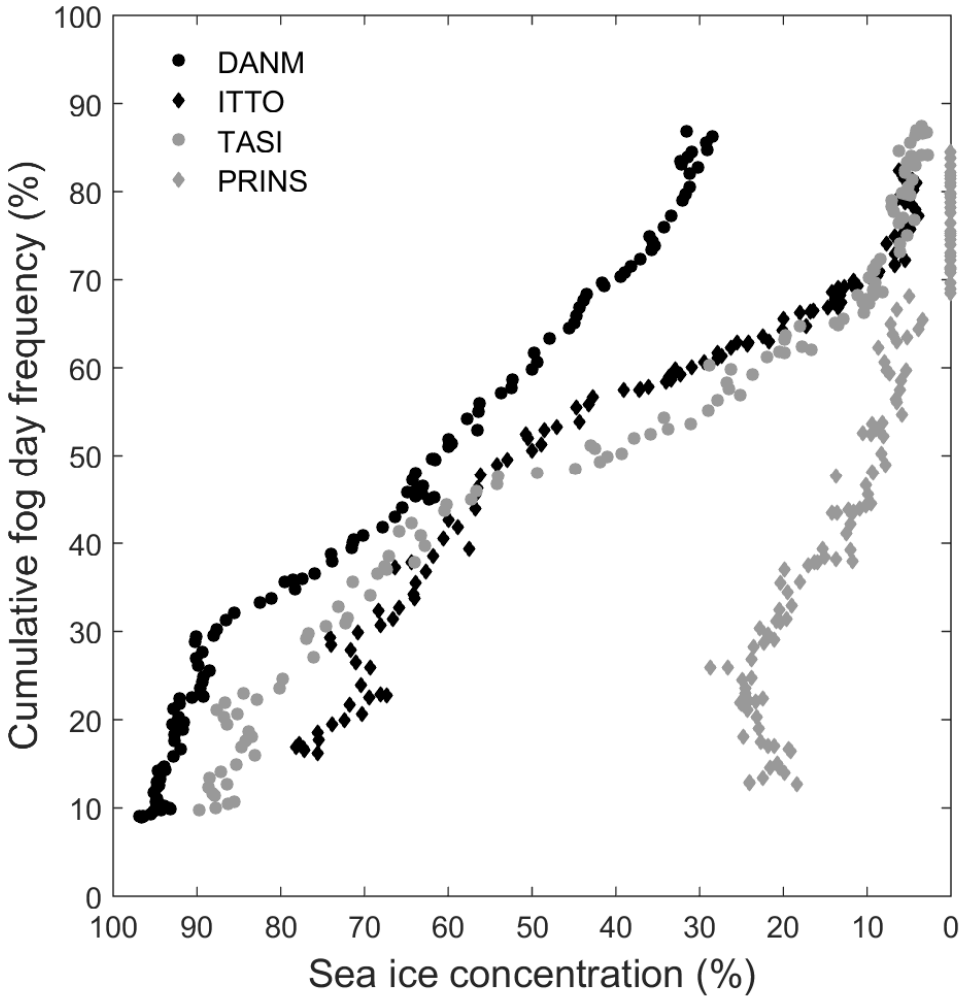

Figure 2-21. Average cumulative fog day frequency (in percentage) as a function of offshore sea ice concentration averaged over the melt seasons of 1988-2012 at Danmarkshavn (DANM), Ittoqqortoormiit (ITTO), Tasiilaq (TASI), and Prins CS (PRINS). Gridded sea ice concentration data from the offshore pixel is from NSIDC (https://nsidc.org, NSIDC-0051)

Figure 2-22 shows the time series of individual fog observations in relation to offshore *SIC* at Danmarkshavn and Tasiilaq for the melt season of 1998. Even though the vast majority of fog events occur after sea ice starts to break up (yellow arrow), fog onset at Danmarkshavn starts before break-up.

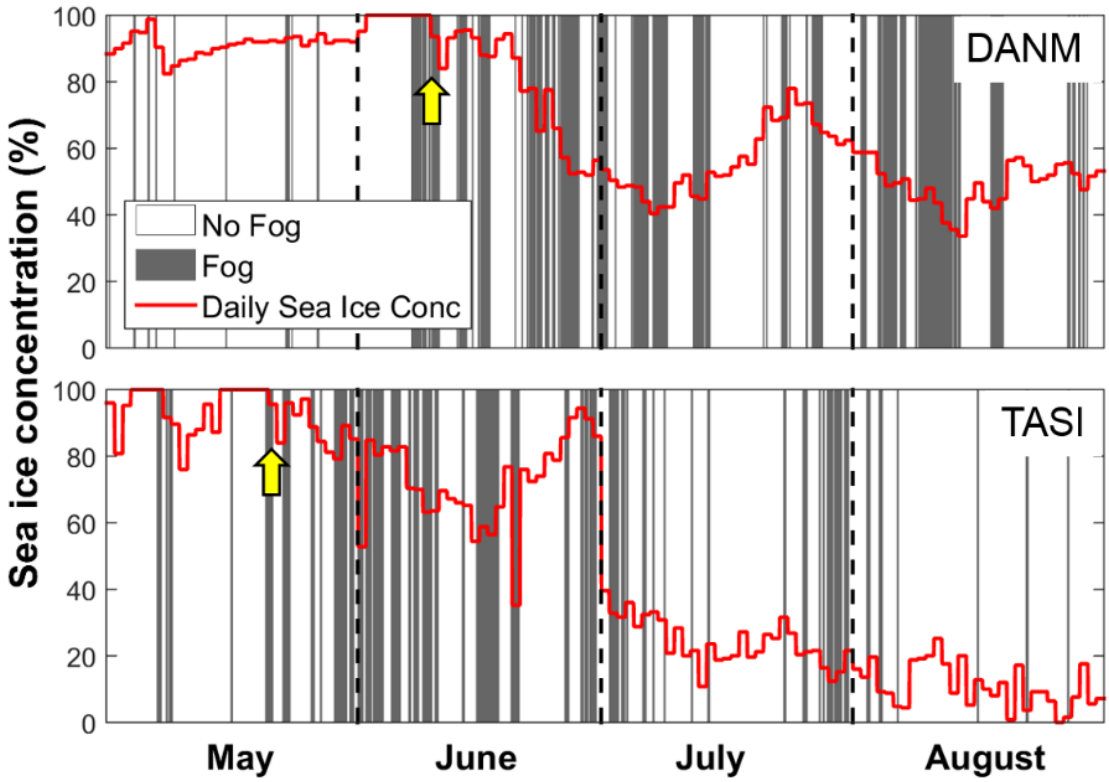

Figure 2-22. Time series of fog events (grey bars) and daily offshore sea ice concentration (red curve) at Danmarkshavn (DANM) and Tasiilaq (TASI) for the summer of 1998. Gridded sea ice concentration data is from NSIDC (https://nsidc.org, NSIDC-0051). The yellow arrow represents the start of sea ice break-up for each location. Vertical dotted lines separate months.

At Danmarkshavn, *FTE* is significantly negatively correlated with *SIC* during the month of sea ice break-up (July, Figure 2-23). Although the data are scattered, the regression slope suggests that *FTE* increases by ~ 60 m for every 10 % decrease in *SIC*. Note that the very thin fog in this graph (~ 20 m) is likely only from one sounding level (Chapter 4)

and may therefore not be accurate. Removing these would not change the overall inferences made from this graph.

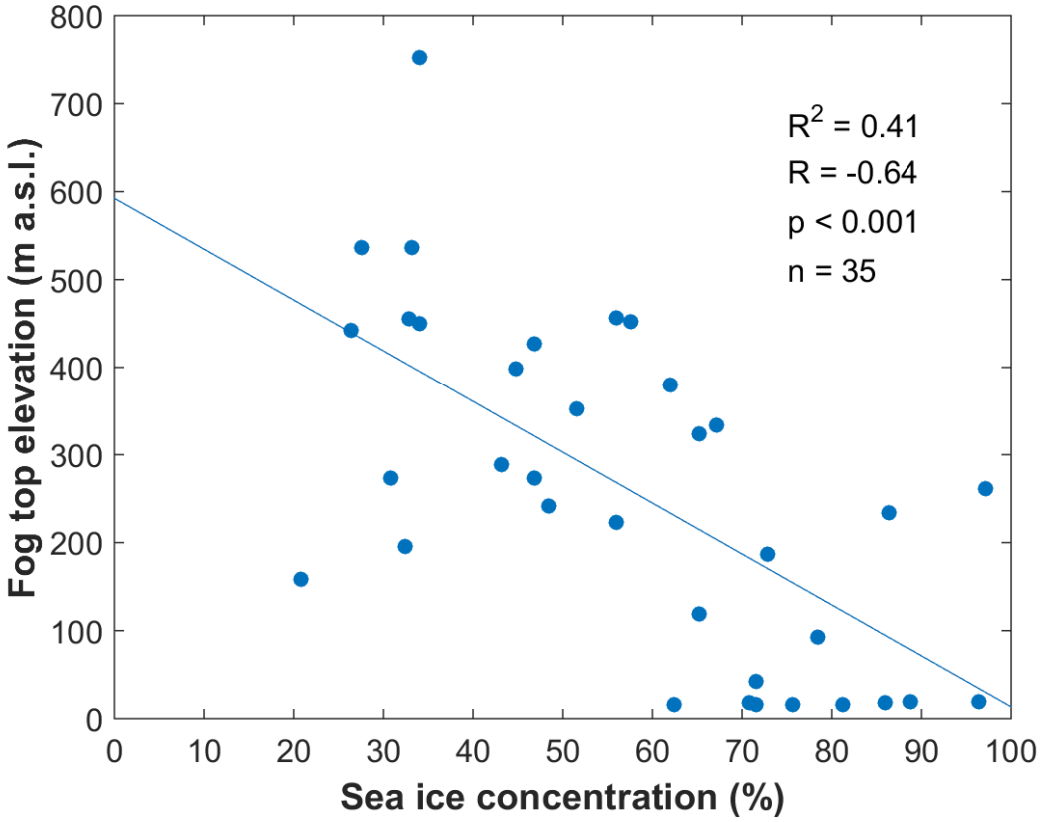

Figure 2-23. Relationship between IGRA-derived fog top elevation (see Chapter 4) and offshore sea ice concentration during the month of sea ice break-up (July) at Danmarkshavn. Gridded sea ice concentration data is from NSIDC (https://nsidc.org, NSIDC-0051). The blue line is the least-square regression line and R is the Pearson product-moment correlation coefficient.

2.6 Discussion

Fog occurring along the coast of East Greenland is mainly a summer phenomenon, as for other high-latitude coastal regions (Lazzara, 2008; Khalilian, 2016; Dorman et al., 2017). The highest frequencies of fog at the station are observed in the early melt season at Ittoqqortoormiit and Tasiilaq, and in the late melt season at Danmarkshavn, which is the same as what Gueye (2014) reported using the same dataset as used in this chapter, but only up to 2005. The average fog day frequencies are up to 7 fog days per month during the late melt season, which is similar to values reported by Ukhanova (1971) over coastal East Greenland. However, these statistics are lower than the 21 average monthly fog days published by Cappelen et al. (2001), who in addition suggest that Ittoqqortoormiit has the highest number of fog days, and not Danmarkshavn as presented here. They also report that fog usually peaks in July. Differences between their study and the one presented in this chapter may in part be explained by the fact that the former includes fog at a distance, fog in patches, shallow fog and fog in the past hour (J. Cappelen, pers. comm. Nov. 2017). This is less restrictive than our identification of "real fog", which was restricted to fog occurring at the stations only for the purpose of the concurrent analysis of upper-air conditions presented in Chapters 3 and 4. In order to facilitate the comparison of fog frequencies between and among studies in different regions, where it is common practice to include all fog-related weather codes to establish annual and seasonal fog climatologies (Dorman et al., 2017), we also established the average monthly number of fog days over the period 1958-2016 for all fog-related weather codes in our study region. Results obtained from this analysis are similar to Cappelen et al. (2001) for East Greenland: fog peaks in July at most locations and is most frequent at Ittoqqortoormiit, although the

average fog frequency does not exceed 15 monthly fog days. The average number of days with fog per month over coastal East Greenland is similar to values found for other coastal areas across the Arctic, yet higher than fog days at inland or lower-latitude locations (Cappelen, 2015; Dorman et al., 2017) and lower than over the Arctic Ocean, and the Greenland Sea and Eurasian seas. In these Arctic marine locations fog occurs on average 20 days or more in July (Ukhanova, 1971).

The occurrence of Arctic summer fog along the East Greenland coast is strongly related to sea ice break-up, which is in accordance with previous studies at other Arctic locations (Prik, 1960; Brooks, 1979). The majority of fog starts to occur once sea ice breaks up because more moisture (e.g. Eastman and Warren, 2010; Palm et al., 2010), sea salt (Struthers et al., 2010; Hudson et al., 2011) and biogenic cloud condensation nuclei (Leck and Bigg, 1999; Orellana et al., 2011) become available, while a cooling surface (sea ice and cold water) remains in the local environment to cool the air mass down to its dew point temperature. The differential timing of fog onset along the East Greenland coast corresponds to the onset of sea ice break-up at each site. A late season peak in fog occurrence at Danmarkshavn is associated with a later onset of sea ice break-up at that high-latitude location, which is characterised by sea ice concentrations above 80 % for most of the year (Cappelen, 2015). The early fog onset at Ittoqqortoormiit may be related to the occurrence of year-round open waters of the Scoresby Sund Polynya at the mouth of Scoresby Sund (Sandel and Sandel, 1991). Early in the melt season, the fjord surface waters are usually cold due to glacier melt and icebergs from the numerous tidewater glaciers draining into Scoresby Sund (e.g. Dowdeswell et al., 1992; Murray et al., 2010). This provides the cold surface needed for advection fog to form. Fog can sometimes

occur before sea ice break-up because melt ponds and leads start to form a few days before the actual break-up (Petrich and Eicken, 2010). Also, the fog moisture source may be located further away than the nearest offshore 25 x 25 km sea ice grid cell. For example, at Tasiilaq, the moisture source could be located further offshore, beyond the "sea ice corridor" separating the coast from the open ocean. Even though Danmarkshavn has pack ice reaching further offshore compared to Tasiilaq, the presence of the nearby North East Water Polynya (Schneider and Budéus, 1994) can provide moisture to that area. In a future study, sea ice concentration could be averaged over these regions of year-round open water and, in combination with back-trajectory analysis, investigated in relation to fog occurrence to determine whether these regions are moisture sources for fog.

The analysis of surface and upper wind directions, together with the analysis of sea ice concentration, strongly suggests that fog in coastal East Greenland is mostly of the advective type and that local sea breeze brings fog inland. Surface winds during fog are usually < 4 m s^{-1}, which are typical of advection fog in both mid-latitude and polar regions (Lazzara, 2008; Kim and Yum, 2017), and originate from the ocean at all locations except at Ittoqqortoormiit where they come from the 29-km wide and 300-km long Scoresby Sund fjord at low wind speeds (typically < 2 m s^{-1}). Tasiilaq generally has the calmest conditions, and Danmarkshavn and Prins CS the windiest conditions, which concurs with Cappelen et al. (2001). Sea breezes during fog are stronger at Danmarkshavn and are sustained during the day, which can be explained by a strong thermal gradient between the cold ice-covered ocean, and the snow-free and sun-heated land. However, the highest diurnal variations in sea breeze occurs at the two southern

sites, which is likely related to the diurnal solar cycle in combination with local katabatic wind influence.

Fog occurrence displays a diurnal cycle at all locations, which is a characteristic similar to that of mid-latitude marine fog (e.g. Hansen et al., 2007). This is related to daily variations in shortwave heating that lead to fog dissipation in late morning and prevent fog from forming before the night (Gultepe et al., 2009). North of the Arctic Circle, fog still displays a diurnal cycle although it is less restricted to morning hours and can take place throughout the day (Gueye, 2014; Khalilian, 2016). Fog is 2 to 9 times as frequent in the morning compared to the afternoon, which is higher than the 50 % increase in fog frequency in the morning reported for Antarctic fog at 78°S (Lazzara, 2008). This higher morning fog frequency over East Greenland compared to Antarctica for corresponding austral latitudes is difficult to explain with the influence of the diurnal solar cycle only. Mesoscale systems, horizontal advection and local topography all influence the sensitivity of fog to the solar diurnal cycle (e.g. Eastman and Warren, 2014). In East Greenland, the lower sensitivity of fog to the solar diurnal cycle at Danmarkshavn and Ittoqqortoormiit can be due to a combination of factors. Firstly, diurnal variations of temperature (related to the solar diurnal cycle) are smaller with increasing latitude during the melt season. A comparison of surface air temperature among stations during June 2013 reveals a temperature amplitude of ~ 6°C at Tasiilaq, ~ 4-5°C at Ittoqqortoormiit and ~ 2°C at Danmarkshavn. An amplitude of 2°C, even though it is not negligible, has a weaker impact on fog dissipation than a 6°C amplitude. Secondly, the concentration of sea ice, which is higher at Danmarkshavn and in the early melt season at Ittoqqortoormiit, promotes fog formation. The presence of sea ice also increases thermal gradients between

the ocean and the snow-free land in the late melt season (Cappelen et al., 2001), leading to a stronger sea breeze. Sustained sea breeze throughout the day could maintain or enhance fog occurrence during afternoon hours. The influence of sea ice and cold waters in promoting fog formation throughout the day has previously been discussed by Gueye (2014) and Khalilian (2016). From the combined results on diurnal fog patterns it can be hypothesised that the combination of high latitude and a strong across-shore thermal gradient makes afternoon fog less likely to dissipate at High-Arctic locations during the melt season.

Despite the fact that fog is less restricted to morning hours at high latitudes, fog duration does not differ among stations, as opposed to results obtained by Gueye (2014) for the period 1958-2005. This can be explained by the difference in calculating fog duration between that study and the present study. Gueye (2014) analysed "non-continuous" fog duration, whereas we restricted our analysis to sequential fog observations only. On average, fog lasts 1.5 hour but long-duration fog events can last up to 13 hours, even though several days to weeks of fog can occur sequentially (e.g. Figure 2-22). The average fog duration is similar to statistics reported for Antarctic fog (Lazzara, 2008), although extreme fog events were reported to last up to 30 hours at McMurdo Station. This difference can either reflect shorter long-duration fog in East Greenland or differences in fog identification methods. Lazzara (2008) used only manned fog observations at synoptic times and included fog at a distance, fog in patches, shallow fog, and fog in the last hour, which can possibly result in more extensive long-duration fog events. No firm conclusion can be drawn with respect to long-duration fog events because

either different fog codes were included or different methodologies were used. Nevertheless, the average fog duration compares well between both regions.

On average, summer fog in East Greenland occurs at air temperatures around the freezing point, which corresponds to findings from Gueye (2014). To our knowledge, a climatology of air temperatures during summer fog over other Arctic locations does not exist. Nonetheless, fog in East Greenland takes place at higher temperatures compared to Antarctic summer fog, which occurs at average air temperatures around -6°C over a permanently snow-covered ground (Lazzara, 2008). The lowest summer temperatures during fog in East Greenland are recorded at Danmarkshavn and the highest temperatures at Prins CS, which is directly related to latitude. This impacts statistics of relative humidity with respect to liquid water (RH_w) because saturation with respect to ice can be reached at RH_w below 100 % at subzero temperatures (Hardy, 1998). Although RH_w below 100 % are typically encountered at the two High-Arctic locations, summer fog in East Greenland is predominantly liquid or in the supercooled phase (> -10°C). This is consistent with direct observations of liquid fog made at other Polar locations (Kumai, 1973; Lazzara, 2008), and has important climatic implications because liquid-bearing clouds, due to their high emissivity, exert a strong influence on the Arctic surface energy budget and particularly the cryosphere (Shupe and Intrieri, 2004; Bennartz et al., 2013).

Fog is generally dense over coastal East Greenland, with visibility typically below 500 m. These are similar to values reported during coastal summer fog in the western Canadian Arctic (Khalilian, 2016). Dense fog conditions are characteristic of marine fog because of the dominance of sea salt condensation nuclei on which large droplets form (Gultepe et

al., 2009; Liu et al., 2016). Even though detailed fog microphysics are not available from standard WMO synoptic weather stations, the analysis of visibility in relation to different fog codes in this chapter revealed possible indications for microphysical differences in fog stages: i) vertical visibility is related to horizontal visibility: the sky is usually invisible during dense fog, ii) thinning fog has significantly higher visibility than unchanging or thickening fog, iii) there is a tendency for unchanging fog to have lower visibility than other types although results were not significant, iv) visibility is higher at Danmarkshavn than at other stations, and v) horizontal visibility does not differ among fog codes at Prins CS. These results suggest that fog microphysics differs under thinning fog and unchanging or thickening fog. With its highest horizontal visibility, thinning fog could represent fog dissipation stage but also spatial variability in fog density, unchanging fog mature fog stage (lowest *vv*), and thickening fog developing fog stage (intermediate *vv*). Further analysis on this process interpretation is done in Chapter 3: even though this analysis did not include a systematic comparison of vertical profiles with fog codes, manual checking of multiple profiles did not reveal a direct correlation between fog codes and fog onset or dissipation. Fog geometrical thickness, which is inversely related to vertical visibility, is higher at Danmarkshavn (see Chapter 4), although visibility during fog is still higher at that location. This suggests that fog microphysical properties are distinct at Danmarkshavn compared to the other locations, which can be due to different environmental conditions such as lower temperatures, longer distance moisture transportation, and the presence of sea ice throughout the summer. Cold air has a lower specific humidity compared to warm air, leading to a lower *LWC* (e.g. Kawai et al., 2016) and, hence, a higher visibility (Chapter 1). Additionally, cloud condensation nuclei are less dense over the Arctic pack ice, compared to the open

ocean (Heintzenberg et al., 2006; Mauritsen et al., 2011). With perennial sea ice cover near Danmarkshavn, it is possible that the boundary layer has a lower aerosol load, which could lead to a higher visibility at that location (Chapter 1). However, detailed and comprehensive field measurements of fog microphysics would be needed to confirm this.

The analysis presented in this chapter further revealed that there are several data gaps and inhomogeneities in present weather and visibility observations at the WMO standard synoptic weather stations operated by DMI in East Greenland. We recommend that homogenisation methods such as those described in Zhang and Seidel (2011) or Hanesiak and Wang (2005) be applied to this dataset before long-term analysis of fog frequency is attempted. It is of particular importance to include data from the 2000s onwards because of the warmer than normal conditions observed in Southeast Greenland during this period (Hanna et al., 2013; Abermann et al., 2017), which are consistent with future climate projections (IPCC, 2013). This time period also corresponds to the transition from manned to automated observations and from three-hourly to hourly sampling resolution. Adjustment for data inhomogeneities resulting from the transition from visual to automated parameters is necessary in order to understand long-term trends and variability in fog frequency and to establish an accurate fog climatology. It is, however, more difficult to adjust for possible manual visibility biases (e.g. 500 m peak, see Figure 2-15).

2.7 Summary and conclusions

In this chapter, the climatology of Arctic coastal fog was investigated from archived synoptic present weather and visibility data available at four WMO weather stations along the East Greenland coast between 1958-2016. Fog predominantly occurs in the melt season, when it is mostly in the liquid or supercooled phase and hence can have important implications for the Arctic surface energy budget (Shupe and Intrieri, 2004; Bennartz et al., 2013). Fog is generally dense (visibility < 500 m) and is associated with local sea breezes and advection of oceanic air over sea ice and cold waters. Sea ice break-up and fog onset are near-coincident in timing along the East Greenland coast, except at the southernmost station. Further analysis is necessary to establish this more firmly, and should include a more thorough regional analysis of sea ice cover (i.e. more pixels around each station) and a simultaneous analysis of air temperature, sea surface temperature, back trajectories and terrestrial snow melt patterns (e.g. Pedersen et al., 2016).

Danmarkshavn, the northernmost station, is characterised by lower temperatures and relative humidity with respect to liquid water during fog, as well as higher sea ice concentrations and stronger sea breeze than at the other stations. Together with a lower diurnal thermal amplitude, this may result in a reduction of fog dissipation processes in the afternoon. In addition, visibility during fog is higher at Danmarkshavn, which suggests fog at this location has different microphysical properties such as aerosol properties and/or liquid water content, which in part may be related to the lower air temperature and more northern latitude.

The fog observation and visibility data used in this chapter are plagued by inhomogeneities resulting from changes in instrumentation, reporting practices, and relocation of stations. Data homogenisation techniques must be applied to these datasets, especially if including data after 2000. Nonetheless, these data represent a unique opportunity to access decades of fog observations in remote Arctic locations. In future studies, extensive field campaigns would be useful to investigate fog microphysics over different Arctic sites to understand spatial differences in aerosol sizes and composition, and their impact on fog and low-cloud formation (e.g. Gultepe et al., 2004). In-depth studies of Arctic coastal fog would offer an opportunity to better understand micro- and macrophysical properties of fog throughout the Arctic. Because of its oceanic origin, Arctic coastal fog can give a glimpse of Arctic sea fog properties over the ocean, which is only sparsely sampled due to logistic constraints (Ukhanova, 1971; Dorman, 2017). However, fog is ubiquitous over Arctic seas in the melt season and exerts a strong influence on sea ice energy budget (Tjernström et al., 2015). It is important to establish a comprehensive climatology of fog throughout the Arctic, including regional trends in fog occurrence, to assess how Arctic fogginess will change as a result of decreasing sea ice, warming air and water temperature, and increased poleward advection of heat, moisture and aerosols (e.g. Eastman and Warren, 2010; Vavrus et al., 2011; AMAP, 2017), as well as how Arctic fogginess will impact the Arctic surface energy budget during the melt season.

CHAPTER 3. ARCTIC FOG TYPES AND PROCESSES FROM RADIOSONDE DATA OVER EAST GREENLAND

3.1 Introduction

Climate models highlight the Arctic as a region of crucial importance and vulnerability to global climate change because it responds to anthropogenic radiative forcing at a much higher rate than do lower latitudes. This "Arctic Amplification" is driven by positive climatic feedback (Serreze and Barry, 2011; Pithan and Mauritsen, 2014). Although the main contributor to Arctic Amplification in summer is the ice-albedo feedback (Serreze and Francis, 2006; Taylor et al., 2013), clouds also play an important role as they affect the surface energy budget through competing mechanisms. Clouds cool the surface by reducing the amount of incoming shortwave radiation (shortwave cloud forcing), while the associated increase in downward longwave energy flux warms the surface (longwave cloud forcing) (e.g. Nardino and Georgiadis, 2003; Shupe and Intrieri, 2004). Because low-level clouds are ubiquitous during the Arctic melt season (e.g. Curry et al., 1996) when solar radiation is at its highest level, they exert a strong influence on the Arctic surface energy budget. The net result is usually a warming effect at the surface (Zhang et al., 1996; Nardino and Georgiadis, 2003; Serreze and Barry, 2011; Bennartz et al., 2013), except for a few weeks in mid-summer when surface albedo is low and solar elevation angle high (Curry et al., 1988; Shupe and Intrieri, 2004). Despite the recent extensive research on Arctic clouds (e.g. Curry et al., 1996; Eastman and Warren, 2010; Vavrus et al., 2011; Tjernström et al., 2012; Van Tricht et al., 2016), fog and boundary-layer clouds are still considered difficult to predict and remain one of the largest uncertainties in climate modelling (IPCC, 2013). Fog and low-level cloud cover and frequency over the

oceans are expected to increase via more moisture becoming available from declining seasonal sea ice, though regional changes are uncertain (Eastman and Warren, 2010; Palm et al., 2010; Vavrus et al., 2011; Liu et al., 2012). It is therefore necessary to establish the thermodynamic structure and a precise climatology of Arctic fog to better understand processes leading to its formation and dissipation, and to assess how future changes in sea ice conditions and poleward advection of moisture and heat will affect its occurrence.

Fog is a cloud at the Earth's surface which reduces horizontal visibility below 1 km (NOAA, 1995). It can be a major transportation hazard and is responsible for important economic losses, especially in the Arctic (Gultepe et al., 2007). Formation and dissipation of fog can be very important for prediction applications. Fog is frequent in the Arctic summer, with sea fog being the most common fog type (e.g. Rae, 1951; Alt, 1979; Nilsson and Bigg, 1996; Cappelen et al., 2001; Svendsen et al., 2002; Hanesiak and Wang, 2005; Tjernström et al., 2012). Summer sea fog can originate from two processes: the advection of a warm and moist air mass over a cold surface (sea ice, cold waters, or cold land surface) or by the downward migration of a low cloud base (Cotton and Anthes, 1989; Koračin et al., 2001). Arctic sea fog peaks when sea ice starts breaking up because this condition provides both moisture and heat fluxes to the boundary layer while the remaining ice offers a cooling surface. A cold sea breeze created by the gradient of temperature between the heated land and the cold ocean advects fog up to a few tens of kilometers inland before it dissipates due to increased thermal turbulence (Alt, 1979; Cappelen, 2015). Overnight and early morning infrared cooling favours fog development and growth. During daytime, shortwave heating counteracts infrared cooling and the mixing of warm dry air from aloft into the fog layer by eddies evaporates fog droplets.

This mixing can eventually penetrate the entire fog layer and lead to its dissipation (e.g. Gultepe et al., 2016). Dissipation can also occur through fog transferring to a low stratus cloud due to increased mechanical (wind speed and shear) or thermal (heating) turbulence (Cotton and Anthes, 1989; Koračin et al., 2001). Topography is an additional factor for fog formation and dissipation, through its influence on wind circulation and differential cooling processes (Gultepe et al., 2016). In addition, subsidence can favour fog formation through the establishment of a strong inversion from adiabatic warming of the subsiding air (Telford and Chai, 1984) and moisture fluxes into the boundary layer due to the presence of a humidity inversion (Curry et al., 1988). Synoptic-scale high pressure systems act to enhance fog formation through lowering of an entire cold stratus deck (Koračin et al. 2001). However, a large subsidence rate can accelerate fog dissipation because the dry and warm subsiding air causes fog droplets to evaporate (e.g. Roach et al. 1982).

Fog is generally associated with temperature inversions (an increase of temperature with elevation: Oke, 1987), which occur in over 80 % of Arctic summer soundings (Kahl, 1990; Gardner and Sharp, 2007; Deser et al., 2010; Devasthale et al., 2010). Although thermal inversions are not a prerequisite for fog formation (Telford and Chai, 1984), fog development and maintenance are promoted by the presence of a temperature inversion (Cotton and Anthes, 1989; Croft et al., 1997). Advection fog often displays a thermodynamic structure with a surface-based inversion because it forms over a cold surface (Pilié et al., 1979; Leipper, 1994; Huang et al., 2015). Cold sea breeze may then transport sea fog over land where it penetrates into the low layer of the warm continental air, which also establishes a temperature inversion (Alt, 1979; Lewis et al., 2003;

Cappelen, 2015). Fog grows vertically when radiative cooling results in an increase in liquid water content at the fog top. This radiative cooling also generates instability and turbulence in the fog layer (Cotton and Anthes, 1989), which can lead to a transition from a surface-based inversion to an inversion with an elevated base (Sotiropoulou et al., 2014; Kim and Yum, 2017). In the case of stratus-base lowering, fog forms in the mixed-layer below the inversion base as cloud-top radiative cooling generates instability and mixing of cool air below the cloud layer, which results in an increase of relative humidity (Pilié et al., 1979; Leipper, 1994). Mature fog, conversely, can occur in the presence of elevated temperature inversions (Leipper, 1994; Zhang et al., 2009; Huang et al., 2015).

Since most fog occurs in the Arctic melt season, it can have important implications for the cryosphere. Warm advection fog has been correlated with episodes of intense sea ice melt (Tjernström et al., 2015), while fog advected over coastal areas, in combination with temperature inversions, has been found to significantly decrease glacier ablation at lower elevations (Alt ,1979; Braun et al., 2004; Koerner, 2005; Mernild et al., 2008; Hulth et al., 2010; Mernild and Liston, 2010). However, temperature inversions influence the Arctic surface energy budget in a complex way, depending on their structure (surface-based vs. elevated) and concurrent cloud cover. In the Canadian Arctic, temperature inversions were found to be correlated with enhanced episodes of melt of sea ice and glaciers, potentially due to a more frequent poleward advection of heat associated with a weaker polar vortex (Gardner and Sharp, 2007; Chutko and Lamoureux, 2009).

Despite its hazard for transportation and interactions with the cryosphere, few studies have focused on Arctic fog (e.g. Prik, 1960; Kumai, 1973; Gathman and Larson, 1974;

Alt, 1979; Nilsson and Bigg, 1996; Hanesiak and Wang, 2005; Heintzenberg et al., 2006; Gultepe et al., 2014). Due in part to a lack of detailed understanding of its physical processes, fog, and in particular Arctic fog, remains difficult to predict (Bendix, 1995). Although fog and low-level stratiform clouds are usually associated with stable boundary-layer conditions and frequently occur in the presence of temperature inversions, few studies have investigated the exact relationship between them. Most of these studies have focused on the common Arctic stratocumulus summer clouds, though some have included fog in their analysis. Sedlar and Tjernström (2009) suggested a classification of Arctic stratocumulus clouds with respect to inversion base height, and they identified two cloud regimes with distinct microphysical and radiative properties over the Arctic pack ice: optically thick, liquid-bearing clouds capped by the inversion base, and the more frequently observed mixed-phased clouds penetrating into deep and strong inversions, characterised by a smaller optical thickness and a longer lifetime. These distinct thermodynamic structures were also observed for Arctic fog, where fog top extended above the inversion base over melting sea ice (Sotiropoulou et al., 2016). Sedlar et al. (2012) hypothesised that warm and moist horizontal advection was responsible for the penetration and persistence of clouds inside the inversion base. Despite the identification of distinct cloud thermodynamic profiles, transition processes between such regimes have as of yet not been investigated.

The aim of this chapter is to develop a novel classification of the thermodynamic structure of melt season Arctic fog types in relation to thermal inversions and air parcel stability, to aid in our understanding of fog macrophysical properties and development processes. For this purpose, an automated classification method for fog thermodynamic

structure was developed based on a combination of surface weather observations and radiosonde profiles. We first applied this classification to high-resolution radiosonde data from the Arctic Summer Cloud Ocean Study (ASCOS) over the Arctic Ocean (Tjernström et al., 2014), and subsequently to lower resolution radiosonde profiles from the Integrated Global Radiosonde Archive (IGRA) measured at three East Greenland coastal locations in the melt seasons of 1980-2012. Supported by the analysis of time-lapse images and back trajectories, we argue that the presented classification has the potential to improve our understanding of the formation, development, and dissipation of predominantly liquid-phase Arctic coastal fog. This knowledge will improve fog physical parameterisation in forecast models in these remote regions.

3.2 Study site and observations

3.2.1 Study area

One region with particularly high fog frequencies is coastal East Greenland, where fog is present on average 20 % of the time in July (Cappelen, 2015). Along the East Greenland coast, three World Meteorological Organization (WMO) synoptic weather stations with concurrent radiosonde data were selected to cover a latitudinal range from low Arctic to high Arctic environments (CAVM, 2003). From north to south, these stations are Danmarkshavn (WMO ID 4320, 11 m a.s.l., 76.77°N, 18.67°W), Ittoqqortoormiit formerly Scoresbysund (WMO ID 4339, 70 m a.s.l., 70.48°N, 21.95°W) and Tasiilaq (WMO ID 4360, 54 m a.s.l., 65.61°N, 37.64°W) (Fig. 3-1). Danmarkshavn and Ittoqqortoormiit are characterised by a 24-hour daylight period and sea ice concentrations over 80% due to the East Greenland Current transporting sea ice south through the Fram

Strait (Vinje, 2001). Tasiilaq, where the climate is strongly influenced by the proximity of the Icelandic Low and the warm Irminger Current (Hanna and Cappelen, 2003; Cappelen, 2015), has a seasonal sea ice cycle as well as a stronger diurnal solar cycle. Southeast Greenland is also more affected by katabatic winds, especially when the Icelandic Low is located between the East Greenland coast and Iceland (Klein and Heinemann, 2002). In addition to weather and radiosonde data, time-lapse images near Tasiilaq, and ASCOS data (Tjernström et al., 2014) from the *Oden* research icebreaker were used (Fig. 3-1). In summer, the local solar time in Danmarkshavn and Ittoqqortoormiit is 1.5 hours, and in Tasiilaq 2.5 hours, after UTC. All time indications used in this chapter are given in UTC time.

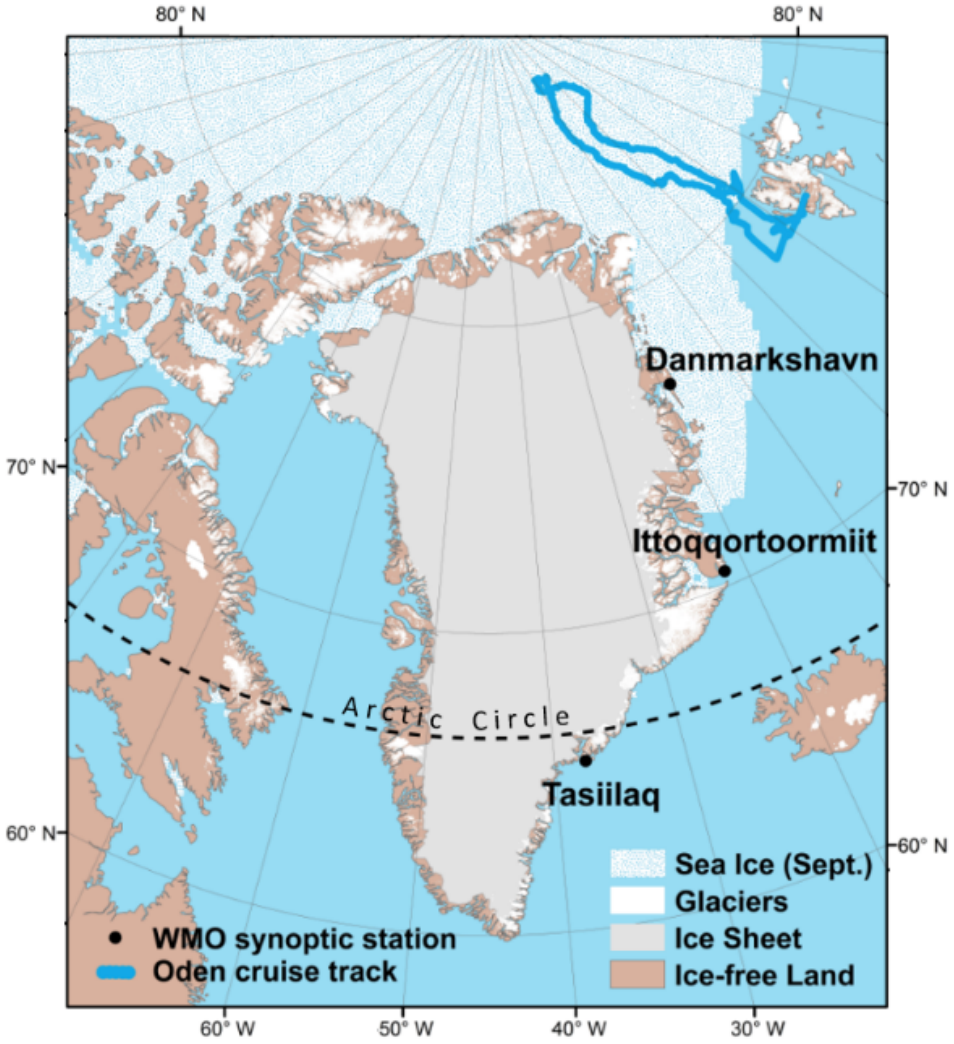

Figure 3-1. Locations of WMO coastal synoptic weather stations with radiosonde observations along the East Greenland coastline (DMI, 1980-2012) and of the *Oden* cruise track in the central Arctic Ocean during ASCOS (Aug-Sept 2008, Tjernström et al., 2014). The sea ice limit represents the average minimum September extent (shapefile from the National Snow and Ice Data Center: https://nsidc.org, NSIDC-0051). The Greenland Ice Sheet was reconstructed from hydrologic outlets (NSIDC-0372, Lewis and Smith, 2009) and surrounding glaciers from the Randolph Glacier Inventory (http://www.glims.org/RGI/, Pfeffer et al., 2014). The time-lapse camera was located 15 km to the northwest of Tasiilaq; with a southwest-oriented viewshed across Sermilik Fjord.

3.2.2 Data observations and instruments

This study uses a combination of ground and radiosonde data collected at three synoptic weather sites in East Greenland from 1980 through 2012. These datasets are complemented by a month of time-lapse images near Tasiilaq to identify major fog physical processes, and observations from radiosondes with higher sampling rates collected in the central Arctic Ocean during an Arctic ship campaign (Fig. 3-1). The purpose of using this second dataset is to test the developed algorithm on high-resolution radiosonde profiles before applying it to the more widely available lower-resolution radiosonde dataset. In addition, 500-hPa geopotential level weather charts (http://www1.wetter3.de/Archiv/) and 120-h air mass back trajectories from NOAA's HYSPLIT model (Stein et al., 2015) were analysed to understand mesoscale and synoptic conditions during fog and evaluate air mass origin, in order to describe large-scale dynamical effects on Arctic sea fog formation.

3.2.2.1 Surface weather observations

Fog conditions were extracted from a combination of archived present weather and horizontal visibility observations provided by the Danish Meteorological Institute (DMI). Observations were made every three hours, starting at 0000 UTC. In the early 2000s, the sampling resolution switched to hourly observations, coincident with a change from manned to automated observations as reported in METAR (aviation) and DMI files (Bødtker, 2003). Present weather "*ww*" and horizontal visibility "*vv*" are reported as codes (WMO 1995: tables 4677, 4680 and 4377). Current automated synoptic weather stations use the forward-scatter FD12P Vaisala Present Weather Sensor (Claus Nehring,

pers. comm, May 2016), which has an accuracy of ± 10% for Meteorological Optical Range measurements (Vaisala, 2002).

The majority of fog observations in East Greenland occur between May and August (66-82 %: Cappelen at al., 2001; Gueye, 2014; see also Chapter 2), which coincides with the Arctic melt season (Serreze et al., 2007a). Our analysis is therefore restricted to warm fog, defined as liquid or supercooled fog with a temperature above -10°C (Petterssen, 1956). Fog at a distance or in patches were excluded, as these might be missed by the radiosonde.

One month of 30-min interval time-lapse images from Sermilik Fjord, 15 km northwest of Tasiilaq were used to complement weather and upper-air observations from Tasiilaq station. A Canon EOS 50D 28 mm SLR camera (1800 x 1200 pixels) was set up between 5 July and 5 August 2011 to overlook the 9 km-wide fjord mouth in a southwestward direction. The 1452 time-lapse images were visually analysed to understand fog processes at the mouth of Sermilik Fjord. Fog frequency was compared between the camera and the weather station at hourly intervals, when *ww* was available at Tasiilaq. Additionally, when fog was observed at the camera at the time of balloon launches (see Sect. 3.2.2.2), upper-air thermodynamic profiles from Tasiilaq were retrieved and analysed (see Sect. 3.3).

3.2.2.2 Upper-air observations

Historic radiosonde data for the three East Greenland synoptic WMO sites were acquired through the quality-controlled Integrated Global Radiosonde Archive (IGRA portal: https://www.ncdc.noaa.gov/data-access/weather-balloon/integrated-global-radiosonde-archive, Durre et al., 2006; Durre and Yin, 2008). IGRA measurements used in this study include pressure, geopotential height, dry-bulb temperature, dew point depression, virtual potential temperature (gradient), and zonal and meridional wind components. Radiosonde balloons were launched twice daily, usually at about 1100 and 2300 UTC. IGRA profiles were reported at mandatory pressure levels (1000, 925, 850, 700, 500 hPa, etc.) as well as significant thermodynamic levels, in order to account for slope discontinuities in temperature and humidity profiles between mandatory levels (Durre et al., 2006). All downloaded raw IGRA soundings have gone through user-input pre-processing in which some of the lower level sonde measurements may have been adjusted using surface station data. In addition, although IGRA reports observations at a "surface level", these are not always measured by the radiosonde and can come from a nearby weather station (Durre et al., 2006). All stations changed from radiosonde model RS18/21 to RS80 in the early 1980s (Gaffen, 1993), with an increase in sonde accuracy (e.g. Antikainen et al., 2002). For this reason and to minimise data and location inhomogeneities, our analysis was restricted to data from 1980 onwards. After this main sonde switch, there has been an alternate use of Vaisala sonde types RS80, RS90 and RS92, which have an accuracy of 1 hPa, 0.5 K, 5 % (relative humidity) and 25 m (derived resolution for geopotential height). In order to account for data inaccuracies introduced by the pre-processing of the radiosonde data, the potential use of weather station data for the surface level, and

instrument switches, a thorough sensitivity analysis of the dew point depression threshold was conducted (see Sect. 3.5.3) to verify the robustness of the thermodynamic profile classification.

In addition to Greenland radiosondes, two upper-air datasets from the Arctic Summer Cloud Ocean Study (ASCOS: www.ascos.se, Tjernström et al., 2014) aboard the Swedish icebreaker *Oden* in the northern Greenland Sea and Arctic Ocean pack ice from Aug-Sept 2008, were used in this analysis (Fig. 3-1). The 6-hourly 5 m reported vertical resolution Vaisala RS92 radiosondes were analysed in combination with 5-minute 7 m vertical resolution (near the surface; the vertical resolution decreases with height) temperature profiles obtained from a 60 GHz scanning radiometer. Temperature retrievals from that microwave radiometer were found to be sufficiently accurate to be used in combination with radiosonde profiles (Sotiropoulou et al., 2014). The purpose of this analysis was to validate the interpretation of fog thermodynamic profiles from IGRA and understand short-term evolution of the boundary layer.

3.3 Methods

Each radiosonde profile that was simultaneous with a fog event reported in the present weather data (*ww*) of the DMI synoptic station was extracted. Additionally, radiosonde launches occurring two hours after and one hour before two consecutive fog present weather observations were analysed as it was assumed that fog persisted over this entire 3-hour time interval. Hereafter, these long-duration fog events will be referred to as "non-simultaneous" sounding observations. Total numbers of melt season (May-August) fog

soundings, simultaneous and non-simultaneous with surface weather observations, are reported in Table 3-1. Non-simultaneous soundings represent the majority of extracted radiosonde profiles over Ittoqqortoormiit and Tasiilaq, occurring at 68 %, and 75 % of the time, respectively. After the year 2000, more soundings coincided with the timing of synoptic fog observations because of the increased sampling rate in ground observations. Only radiosondes with a minimum of five levels between the surface and the 700 hPa pressure level in both the dry-bulb temperature and dew point depression profiles were included in this analysis (Table 3-1, numbers in brackets). Fewer levels could either result in a correct but smooth profile or in an unreliable sounding. Since Kahl et al. (1992) determined five levels to be a minimum to study low-level inversion properties, it was decided to use this strict threshold, with the risk of excluding some reliable smooth soundings.

Table 3-1. Total number of soundings and fog soundings in the melt seasons (May-August) of 1980-2012. "Simultaneous" refers to soundings occurring at the same time as surface weather observations, and "non-simultaneous" to those in between two consecutive surface weather observations. Numbers in brackets exclude soundings with fewer than 5 levels below the 700 hPa pressure level in either the dry-bulb temperature or the dew point depression profiles (after Kahl et al., 1992). "Fog frequency" is the percentage of all melt season soundings retained for fog analysis.

	Danmarkshavn		**Ittoqqortoormiit**		**Tasiilaq**	
	All	≥ 5 levels	All	≥ 5 levels	All	≥ 5 levels
All melt season soundings	6745		6556		7013	
Total fog	236	[187]	152	[121]	149	[114]
Simultaneous	103	[99]	41	[39]	35	[28]
Non-simultaneous	133	[88]	111	[82]	114	[86]
Fog frequency (%)		[3.5]		[2.3]		[2.1]

Each radiosonde profile was analysed for saturation gradient, temperature inversion type, stability, and approximation of fog top height with respect to inversion base. The radiosonde data were used to obtain the following parameters:

- Dew point depression ($T_{dd} = T\text{-}T_d$, with T the dry-bulb air temperature and T_d the dew point temperature) was used to calculate the saturation, where the lowest tropospheric level had to be saturated for fog to be detected in the radiosonde profile, and the geopotential height of the uppermost saturated level determined the fog top height (see Chapter 4). Using the 166 soundings coinciding with fog observations (Table 3-1), it was determined that the 1°C value of surface dew point depression (T_{dds}) threshold (e.g. Meyer and Rao, 1999; Kim and Yum, 2010; Koračin et al., 2014) captured almost 100 % of fog observations at Danmarkshavn and Tasiilaq, and about 75 % at Ittoqqortoormiit (Fig. 3-2). Despite having to exclude about a quarter of potential fog soundings at Ittoqqortoormiit, a fixed T_{dd} threshold equal to T_{dds} was used for all stations. The 1°C used for T_{dd} threshold corresponds to relative humidity with respect to liquid water $RH_w > 93$ % (Hardy, 1998).
- Dry-bulb temperature (T) was used to classify fog based on the inversion type, whereby surface-based inversions (SBI, negative temperature lapse rate from the ground surface up) were separated from low-level inversions (LLI, elevated inversion base below the 700 hPa pressure level, as suggested by Kahl et al. (1992). By extension, the term "low-level" will be used in this paper to refer to air parcels above the surface but below 700 hPa). Geopotential height provided the height of the inversion base above the ground surface.
- The virtual potential temperature (Θ_v) gradient ($\mu = d\Theta_v/dz$) was analysed to determine air parcel stability. The saturated air parcel at the surface was statically stable (unstable) if μ was positive (negative), or neutral if it was zero. In addition, an air parcel was classified as unstable if it was above a superadiabatic air parcel

and its lapse rate was zero (Stull, 1988). For this analysis, neutral lapse rates were regarded as unstable lapse rates. The stability of the surface layer, μ_s, was defined as the stability of the air parcel delimited by the surface level and the next level aloft. By extension, the term "surface layer" will be used in this paper to refer to the air parcel delimited by the first two sounding levels. Even though other studies have used the equivalent potential temperature to study the stability of the boundary layer (e.g. Sedlar et al., 2012; Shupe et al., 2013; Sotiropoulou et al., 2014), choosing Θ_v was motivated here by its availability in IGRA files, therefore reducing the potential for introducing calculation errors, as well as to remain consistent with boundary layer theory (Stull 1988) and previous studies on sea fog turbulence (Telford and Chai, 1984; Nilsson, 1996; Nakanishi and Niino, 2006).

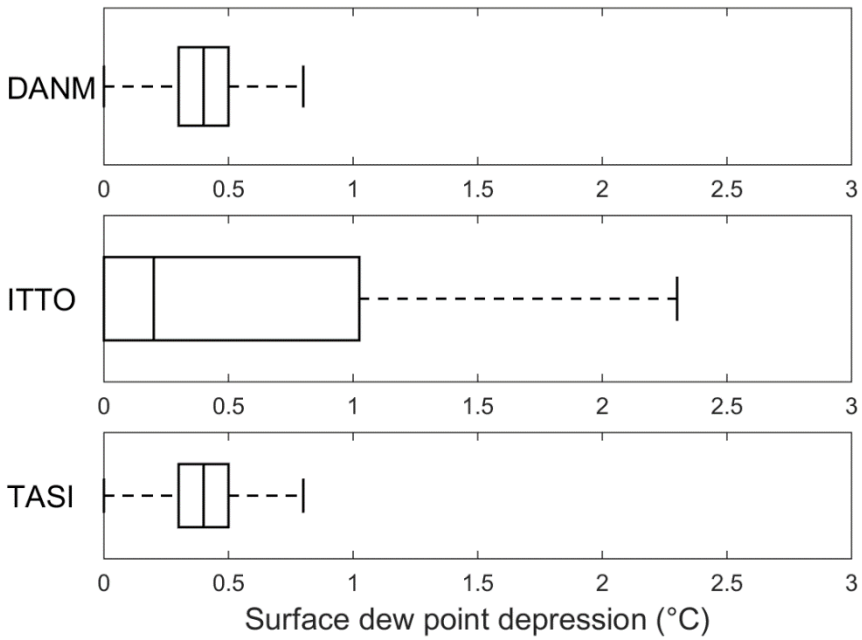

Figure 3-2. Dew point depression statistics during fog from surface level of soundings simultaneous with fog observations at the nearby weather station (1980-2012). Box and whisker plots show the median (horizontal line), lower and upper quartiles (bottom and top of box), and 5th and 95th percentiles (range).

For each of the fog events captured by radiosonde (Table 3-1) a standardised combined graph of surface observations and upper-air profiles, including a Skew-*T* Log-*P* diagram, was generated (see Appendices 3 and 4), in order to facilitate the initial identification of distinct thermodynamic profiles. Ultimately, all thermodynamic profiles were automatically classified into one of six distinctive fog sounding types, through a script developed for this purpose (Appendix 5). This classification was based on their thermodynamic vertical profile differences in saturation gradient, temperature inversion type, stability, and approximation of fog top height with respect to inversion base, as explained above. This automated thermodynamic characterisation was inspired by the classification of stratiform clouds capped by a LLI or residing inside a LLI by Sedlar and Tjernström (2009), who discriminated these two distinct types of clouds based on their physical, optical, and temporal properties. Comparison of thermodynamic profile classes among stations were tested through chi-square statistical tests (χ^2), while statistics for each single station were tested through binomial tests at the 95 % confidence interval.

The fog sounding type classification was first performed on the 46 high-resolution radiosonde profiles with identified fog events from ASCOS, in an attempt to validate the classification applied to IGRA data. The identification of fog events during ASCOS was derived from a subjective probability product (Tjernström et al., 2012), in which only observations with horizontal visibilities < 5 km and ceilings < 100 m a.g.l., or horizontal visibilities < 1 km, or horizontal visibilities < 2 km and ceilings < 80 m a.g.l., and no concurrent precipitation with either one, were retained for the classification of fog. To determine saturation and classify the identified fog events, it was decided to apply two different T_{dd} thresholds: at 1°C and at 0.5°C. The second T_{dd} threshold was chosen

because the radiosonde model Vaisala RS92 used during ASCOS (Tjernström et al., 2014) provides more accurate humidity measurements than the older models used at WMO synoptic stations (Antikainen et al., 2002; Steinbrecht et al., 2008; Vaisala, 2017).

3.4 Results

3.4.1 Fog thermodynamic profiles

Using an automated characterisation of each sounding, thermodynamic profiles from both ASCOS (Section 3.4.2) and IGRA (Section 3.4.3) radiosondes could be classified into six major fog classes as described in Fig. 3-3. Class 1 are excluded events because the dew point depression threshold suggests there is no saturation in the radiosonde profile; Class 2 is fog with a SBI; Class 3 has a fog top below the LLI base; Class 4 has a fog top capped by the LLI base; Class 5 has a fog top above the LLI base; and Class 6 has fog with an overlying saturated (stratus) layer within the LLI. Class 2 exhibits some variability in humidity profiles (not shown), but the differences were small and had too few cases, preventing further subdivision of Class 2. In addition, fog occasionally occurs without any inversion (stable layer with isothermal or positive temperature lapse rate profile), but these arose in < 1 % of IGRA observations and were not considered further in this analysis. Examples for each class are presented in Appendix 3.

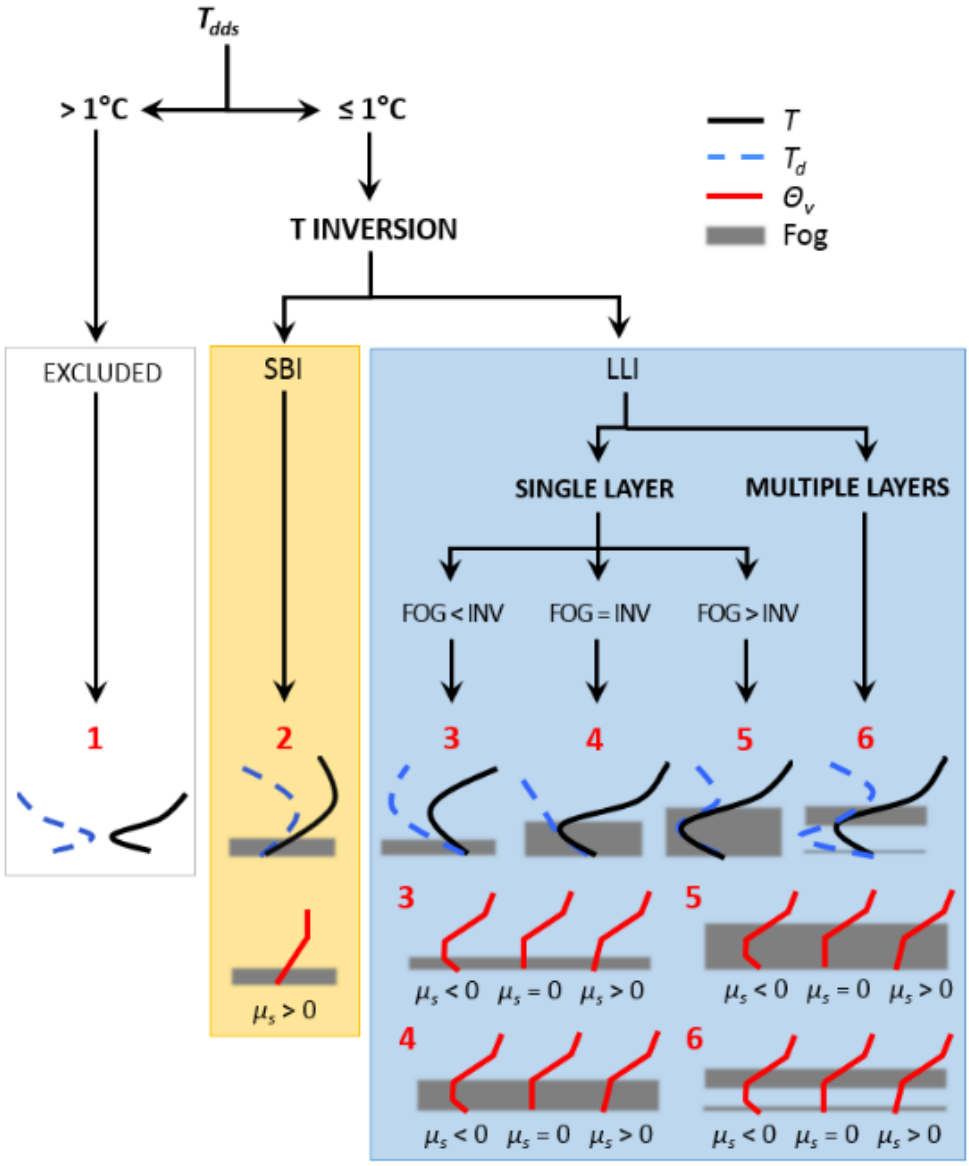

Figure 3-3. Six fog classes (red numbers) based on surface dew point depression value (T_{dds}), lower tropospheric inversion type, and fog top height relative to the inversion base. White box: fog events not captured by radiosonde (T_{dds} > 1°C). Yellow box: fog with SBI. Blue box: fog with LLI, described for fog top below (<), coinciding with (=) or above (>) the inversion base (INV). Classes 2-5 have no significant low-level cloud layer above the fog, thus are classified as "single layer" cases. Class 6 corresponds to a thin fog layer overlain by a low stratus in a LLI ("multiple layers"). Stability profiles for each class are in red: Θ_v is the virtual potential temperature and μ_s the virtual potential temperature gradient at the surface (μ_s < 0: unstable, μ_s = 0: neutrally stratified, μ_s > 0: stably stratified).

3.4.2 Thermodynamic profiles during ASCOS

The proposed thermodynamic classification was first applied to a month of high-resolution radiosonde data from ASCOS, of which 46 fog soundings were identified. The relative frequencies of each fog class using the two T_{dd} thresholds are presented in Fig. 3-4, and typical profiles in Fig. 3-5. The vast majority of fog occurs with a LLI, of which Class 5 is observed most frequently and is the most vertically extensive fog type. Transitions between Classes 5 (fog) and 1 (stratus) are common. Class 6 occurs in > 75 % of the time, at the onsets of fog lifting or stratus-base lowering (Fig. 3-5a). Class 4 predominantly occurs in the dissipating stages of fog events (Fig. 3-5e), as does Class 3. Changing the T_{dd} threshold does not change the number of fog cases, but the T_{dd} = 0.5°C threshold results in more fog classified as Class 1 and 6, and less Class 5. Multiple low-level cloud layers are frequently observed based on ASCOS soundings (e.g. Fig. 3-5 e-f).

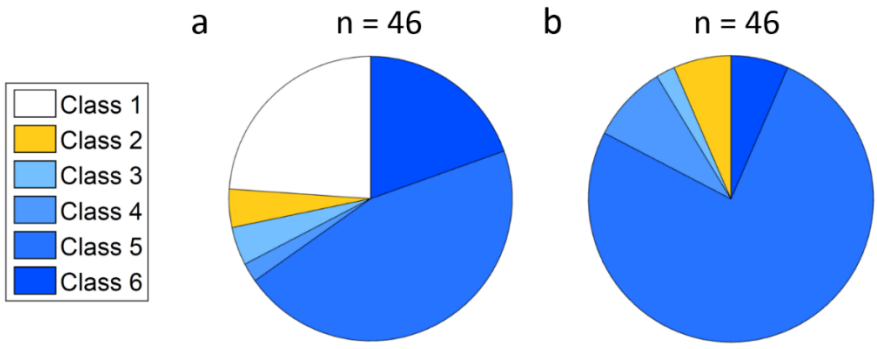

Figure 3-4. Fog class frequency during ASCOS, for a dew point depression threshold of (a) 0.5°C and (b) 1°C.

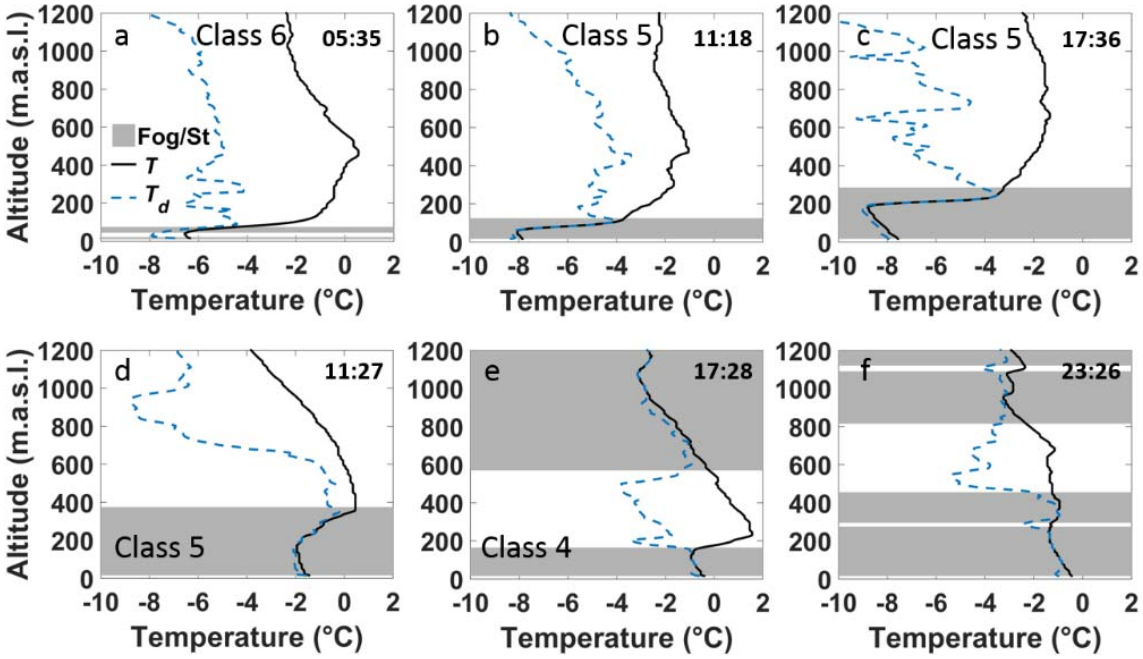

Figure 3-5. Examples of ASCOS radiosonde profiles during (a-c) fog formation (Classes 6 and 5; 22 Aug 2008), and (d-f) fog dissipation processes (Classes 5 and 4; 23 Aug 2008). Note that (f) is the transition of Class 5 to the inversion being eroded. The solid black line is the dry-bulb temperature T, the dashed blue line is the dew point temperature T_d, and grey shadings represent fog and/or low stratus layers determined with $T_{dd} \leq 1$°C. Time (upper right corner) is given in UTC.

Visual analysis of temperature profiles retrieved from the ASCOS microwave radiometer between the 6-hour interval ASCOS radiosonde launches provided us with information on the short-term (1-min interval) evolution of the boundary layer during fog or when fog was forming or dissipating. The following key observations on the relationship between Arctic fog and temperature inversions were made from the combination of these ASCOS radiosonde and microwave radiometer profiles:

- Fog usually requires a low temperature inversion to form (LLI or SBI) as opposed to what was stated by Telford and Chai (1984);
- Erosion of the inversion (profile becoming isothermal, e.g. Fig. 3-5f) often occurs during the dissipating stages of fog;
- Transitions between SBI and LLI are observed during fog.

3.4.3 Thermodynamic profiles from IGRA

A total of 422 IGRA soundings corresponding to fog conditions were analysed. Occurrence statistics are reported in Fig. 3-6 and Table 3-2, and class frequencies displayed in Table 3-3. The same six fog classes were observed during both the ASCOS campaign and IGRA profiles over East Greenland. As with ASCOS profiles (Sect. 3.4.2), most fog in East Greenland occurs with a LLI (Classes 3-6: 66-79 %, $p < 0.001$). Fog with a SBI (Class 2) represents only 12-14 % of soundings and does not differ significantly among stations. Excluded soundings (Class 1) are most common at Ittoqqortoormiit (21 % of soundings, $\chi^2 = 4.98$, $p = 0.015$, $df = 2$), which is related to the 1°C T_{dd} threshold (see Fig. 3-2). Deep fog layers penetrating the inversion base (Class 5) are dominant ($p < 0.001$) over Danmarkshavn, where they reach 28 % of occurrence, and this was also the dominant class over the Arctic Ocean. There is a nearly-significant ($p = 0.054$) tendency towards a higher occurrence of this class over Danmarkshavn compared to the other stations. For all three stations combined, Class 5 was the most dominant class (23 %, $p = 0.002$). Shallow fog layer occurrence below an inversion base (Class 3) significantly increases with decreasing latitude (χ^2 range = 6.52-9.85, $p < 0.001$, $df = 2$, see Table 3-3), where it is also the dominant class (33 %, $p < 0.001$). This class was more frequent in East Greenland than in the High-Arctic pack ice during ASCOS. Class 6 was the least frequent class reported for all stations combined (10 %, $p < 0.001$). While all fog with a SBI (Class 2) was characterised by stably stratified conditions ($\mu > 0$), fog with a LLI (Classes 3-6) could occur under either stable ($\mu > 0$) or neutral/unstable conditions ($\mu \leq 0$) (Table 3-2). There is a tendency towards more unstable surface conditions for classes with a LLI (Classes 3-6); however, this was only significant for Class 6 (p range = <

0.001-0.021). Even though there is a tendency for fog at Ittoqqortoormiit to occur most often under unstable conditions, this was not statistically significant and it is concluded that all sites present similar characteristics in terms of stability occurrence for each specific class.

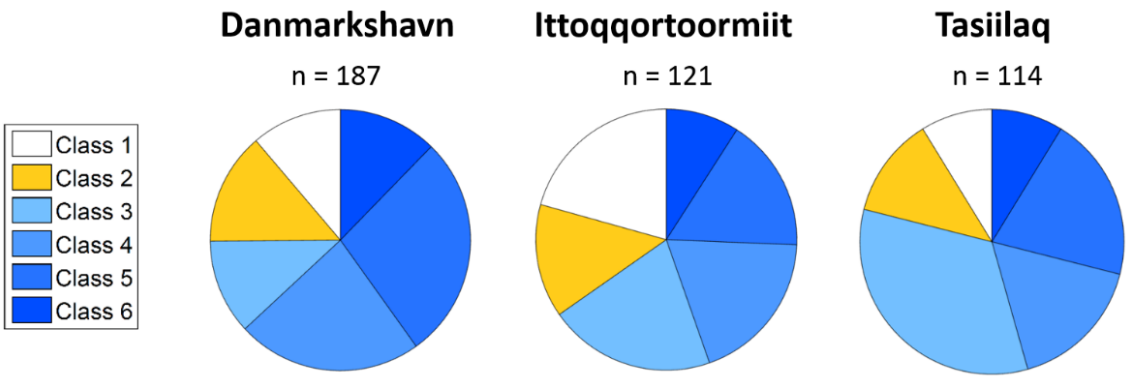

Figure 3-6. Fog class frequency at the three study sites. See Table 3-2 for the exact percentages in each class.

Table 3-2. Statistics of fog classes for Danmarkshavn, Ittoqqortoormiit and Tasiilaq. Classes 3-6 can have neutral/unstable ($\mu_s \leq 0$) or stable ($\mu_s > 0$) surface layers. Class 2 always has stable surface layers ($\mu_s > 0$). *n* is the number of observations, *f* is the frequency of occurrence of a subclass ($\mu_s \leq 0$ or $\mu_s > 0$) with respect to the total number of observations for a station's class, and *F* is the frequency of occurrence of a class with respect to the total number of observations for that station.

	Danmarkshavn			**Ittoqqortoormiit**			**Tasiilaq**		
	n	***f* (%)**	***F* (%)**	***n***	***f* (%)**	***F* (%)**	***n***	***f* (%)**	***F* (%)**
Class 1	21		11	25		21	10		9
Class 2	26		14	17		14	14		12
Class 3	22		12	25		21	38		33
$\mu_s \leq 0$	15	68		17	68		24	63	
$\mu_s > 0$	7	32		8	32		14	37	
Class 4	43		23	23		19	19		17
$\mu_s \leq 0$	26	60		17	74		13	68	
$\mu_s > 0$	17	40		6	26		6	32	
Class 5	52		28	20		17	23		20
$\mu_s \leq 0$	25	48		14	70		14	61	
$\mu_s > 0$	27	52		6	30		9	39	
Class 6	23		12	11		9	10		9
$\mu_s \leq 0$	22	96		11	100		9	90	
$\mu_s > 0$	1	4		0	0		1	10	
TOTAL	**187**		**100**	**121**		**100**	**114**		**100**

Table 3-3. Observed number of occurrence, expected values (italics) and chi-square values (χ^2, in brackets) of fog thermodynamic classes over Danmarkshavn, Ittoqqortoormiit and Tasiilaq. Significant χ^2 values at the 95 % confidence level are in bold. The overall χ^2 and p-value of the contingent table are 31.043 and 0.0006, respectively.

	Danmarkshavn	**Ittoqqortoormiit**	**Tasiilaq**
Class 1	21 *24.82* (0.59)	25 *16.06* **(4.98)**	10 *15.13* (1.74)
Class 2	26 *25.26* (0.02)	17 *16.34* (0.03)	14 *15.40* (0.13)
Class 3	22 *37.67* **(6.52)**	25 *24.37* (0.02)	38 *22.96* **(9.85)**
Class 4	43 *37.67* (0.76)	23 *24.37* (0.08)	19 *22.96* (0.68)
Class 5	52 *42.10* (2.33)	20 *27.24* (1.92)	23 *25.66* (0.28)
Class 6	23 *19.50* (0.63)	11 *12.62* (0.21)	10 *11.89* (0.30)

Figure 3-7 panels a and b display 120-h (5-day) air mass back trajectories for the years 2000 to 2012 for Classes 3 and 5 at Tasiilaq and Danmarkshavn, respectively. These two classes represent the highest fog type occurrences (Table 3-2). Figure 3-7c and d display the 850 hPa level wind direction frequencies from radiosonde data for the entire study period (1980-2012) for these classes at the respective stations. All distributions were tested for their significance using binomial statistical tests at the 95 % confidence level. This analysis of back trajectories and frequency distributions of upper air wind directions suggests that certain fog classes coincide with distinct air mass origins. Class 5 at Danmarkshavn is mostly of oceanic origin (18 out of 27 back trajectories). The majority of these air masses originated from lower latitudes, but some were from the Arctic Ocean.

Figure 3-7c indicates that 58 % of Class 5 soundings were related to winds from the ice sheet (western to northern wind directions between 225° and 360°). In contrast, over 80 % of air masses originated from the ice sheet ($p = 0.028$), for all other fog classes except for Class 6 (61 %). Classes 5 and 6 are in fact the only classes for which upper winds have a predominantly southerly direction (56 % frequency with $p = 0.001$, and 52 % frequency with $p = 0.011$, respectively), although there is a large variability of air-mass origin as demonstrated by the back trajectories in Figure 3-7a. These observations suggest that Classes 5 and 6 are mostly associated with oceanic air masses.

For Class 3 over Tasiilaq, 11 out of 15 back trajectories originated from the ice sheet and were associated with anticyclonic conditions over Greenland (Fig. 3-7b). Compared to other classes at Tasiilaq, Class 3 has the highest frequency of wind originating from the ice sheet (65 %; $p = 0.002$). This is in contrast with Danmarkshavn, where Class 2 is almost always associated with air masses originating over the ice sheet (92 % frequency of upper winds, $p < 0.001$, not shown). When Class 2 was observed, surface winds were predominantly calm, with backing or neutral vertical wind profiles, and clear anticyclonic conditions occurring over Greenland according to the back trajectories and weather charts. Based on these three conditions and the thermodynamic profiles of Class 2, we infer that some Class 2 fog cases may be radiation fog (e.g. Roach et al., 1976; Croft et al., 1997).

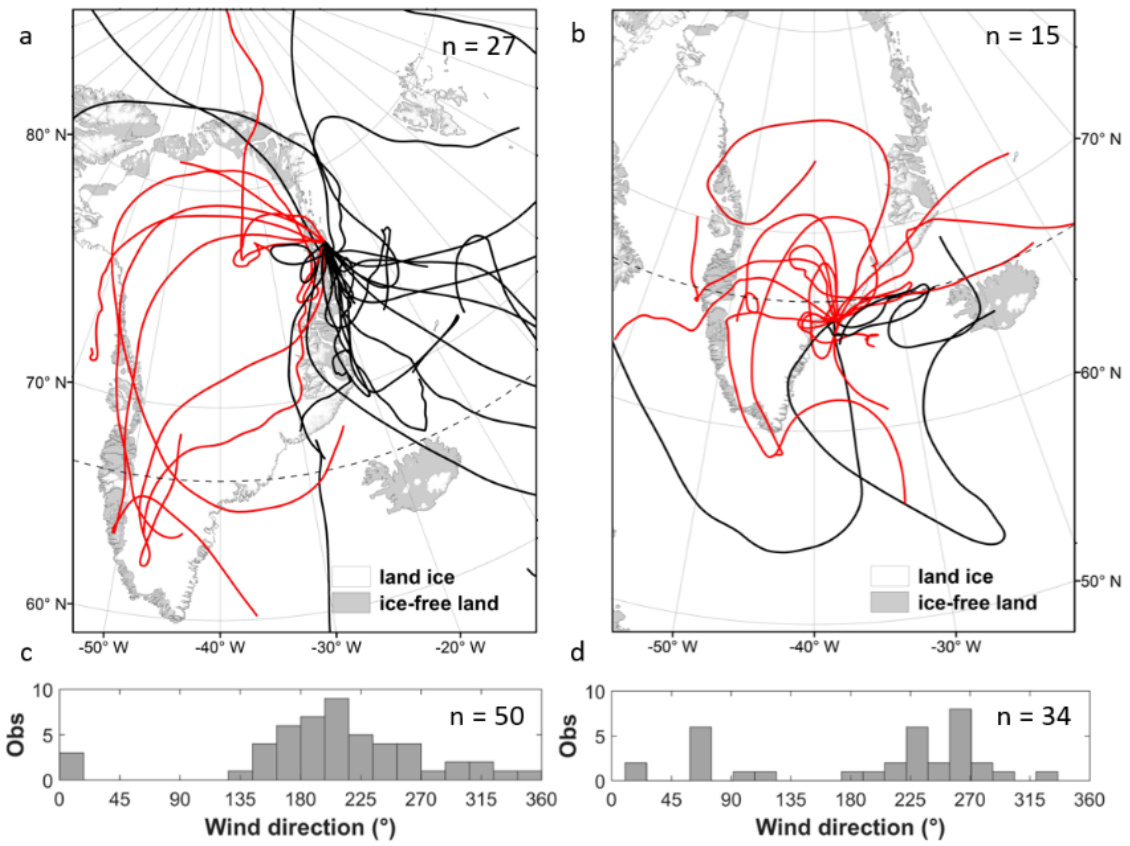

Figure 3-7. All 600 m a.g.l. 120-h back trajectories of air masses in 2000-2012 associated with (a) Class 5 over Danmarkshavn, and (b) Class 3 over Tasiilaq. Black lines are predominantly oceanic air masses and red lines have travelled over the Greenland Ice Sheet. Lower panels are the frequency distributions of wind directions at the 850 hPa level for the entire period 1980-2012 for (c) Class 5 over Danmarkshavn, and (d) Class 3 over Tasiilaq. Numbers of observations (n) are displayed in the upper right corner of each panel. Back trajectories are from NOAA's HYSPLIT model (http://www.ready.noaa.gov, accessed on 28 May 2017).

3.4.4 Support for IGRA fog process interpretation from time-lapse images

Of 1452 time-lapse images, fog was identified on 151 images. Of these, 16 were classified as being of the advective type and 9 occurred through stratus-base lowering (Figs. 3-8 a-b). Fog often displayed a sharp top, which is typical of thermally and dynamically stable atmospheric conditions (e.g. Koračin, 2017). Dissipation processes included fog retreat towards the ocean (12 images), fog lifting to a stratus (8 images, Fig. 3-8d), or dissipation from top by radiative heating or mixing processes (5 images) (c.f.

Gultepe et al., 2016). Multiple low-level clouds layers were observed during both formation (5 images) and dissipation stages (6 images, Figs. 3-8 c-d). Stratus-base lowering and fog lifting processes were found to occur within a period of 1.5-3 hours. Images from the mouth of the fjord were compared with surface and radiosonde observations obtained at Tasiilaq. Fog occurrence was ten times higher in the fjord than at Tasiilaq (151 vs. 15 observations), particularly in the western part, where sea ice and large icebergs were commonly found (e.g. Fig. 3-8c). Similarly, only 20 % of radiosondes (2 out of 10) at Tasiilaq captured fog events when fog was present in the fjord. These fog conditions displayed Class 3 thermodynamic profiles. Radiosondes that failed to capture fog layers all had Class 3 subsaturated profiles.

Figure 3-8. Examples of fog observations obtained from the time-lapse camera located at the mouth of Sermilik Fjord: (a) advection fog entering the fjord, (b) stratus base lowering into fog, (c) dissipating fog with several layers of low stratus, and (d) fog separating from stratus via subsaturation between the two layers (dissipation). The camera is approximately facing southwest, the open ocean is to the left and the inner fjord to the right.

3.5 Discussion

In Section 3.5.1, fog thermodynamic structure is compared to that of Arctic stratocumulus clouds from other studies. Section 3.5.2 infers fog formation and dissipation processes from fog thermodynamic classes, and Section 3.5.3 presents the methodological uncertainties and limitations of this research.

3.5.1 Comparison with Arctic stratocumulus clouds

Studies of sea fog thermodynamic structure have mostly been restricted to mid-latitudes (e.g. Pilié et al., 1979; Zhang et al., 2009; Huang et al., 2015). To our knowledge, a similar climatology of the thermodynamic structure of Arctic summer fog using in-situ observations has not been previously published. The available measurements of Arctic fog top with respect to the inversion base height consist of only a few field measurements (Sotiropoulou et al., 2016), and therefore results in this paper were also compared to studies on Arctic stratocumulus clouds. This is justified because: a) both are marine stratiform boundary-layer clouds usually capped by an inversion (Cotton and Anthes, 1989; Gultepe, 2007; Wood, 2012); b) both frequently originate from warm air advection (Nilsson and Bigg, 1996; Sedlar et al., 2012; Shupe et al., 2013; Sotiropoulou et al., 2014; Huang et al., 2015; Tjernström et al., 2015; Sotiropoulou et al., 2016); c) transitions can occur between fog and stratocumulus via the stratus stage (Koračin et al., 2001; Gao et al., 2007; Koračin et al., 2014; Huang et al., 2015); d) fog has geometrical characteristics similar to stratocumulus clouds (Welch and Wielicki, 1986); and e) stratocumulus clouds

are the most frequent cloud type in the Arctic melt season (Eastman and Warren, 2010) and studies over the Arctic Ocean have therefore mainly focused on the thermodynamic structure of these clouds (Sedlar and Tjernström, 2009; Sedlar et al., 2012; Sotiropoulou et al., 2014).

Similarities between our findings on Arctic fog and findings on Arctic fog or stratocumulus clouds from other studies over the Arctic pack ice during the melt season include four main observations: i) The majority of fog/stratocumulus events occurred with a LLI (c.f. Sedlar and Tjernström, 2009; Sedlar et al., 2012); ii) Fog/stratocumulus penetrating the inversion layer was the most common type at High-Arctic locations, and originated from the poleward advection of heat and moisture over cold surfaces (c.f. Sedlar and Tjernström, 2009; Sedlar et al., 2012; Shupe et al., 2013). This thermodynamic feature can also be related to a higher sea ice concentration at northern locations, as observed by Sotiropoulou et al. (2016) for fog over melting sea ice; iii) Fog/stratocumulus below or capped by the inversion layer was more frequent at locations closest to the coast and at lower latitudes, where sea ice concentration is lower (c.f. Sedlar et al., 2012; Sotiropoulou et al., 2016); iv) Surface layers were frequently statically unstable during fog/stratocumulus (c.f. Sedlar et al., 2012; Shupe et al., 2013; Sotiropoulou et al., 2014).

3.5.2 Arctic fog formation and dissipation process interpretation

The integrated analysis of observations or data from time-lapse images, air mass back trajectories, microwave radiometer temperature retrievals and fog-process literature (summarised in Sect. 3.1), suggests that fog thermodynamic classes in coastal East

Greenland represent stages of development of advection fog, stratus-base lowering, or fog lifting. Two main fog formation and three main fog dissipation mechanisms were inferred.

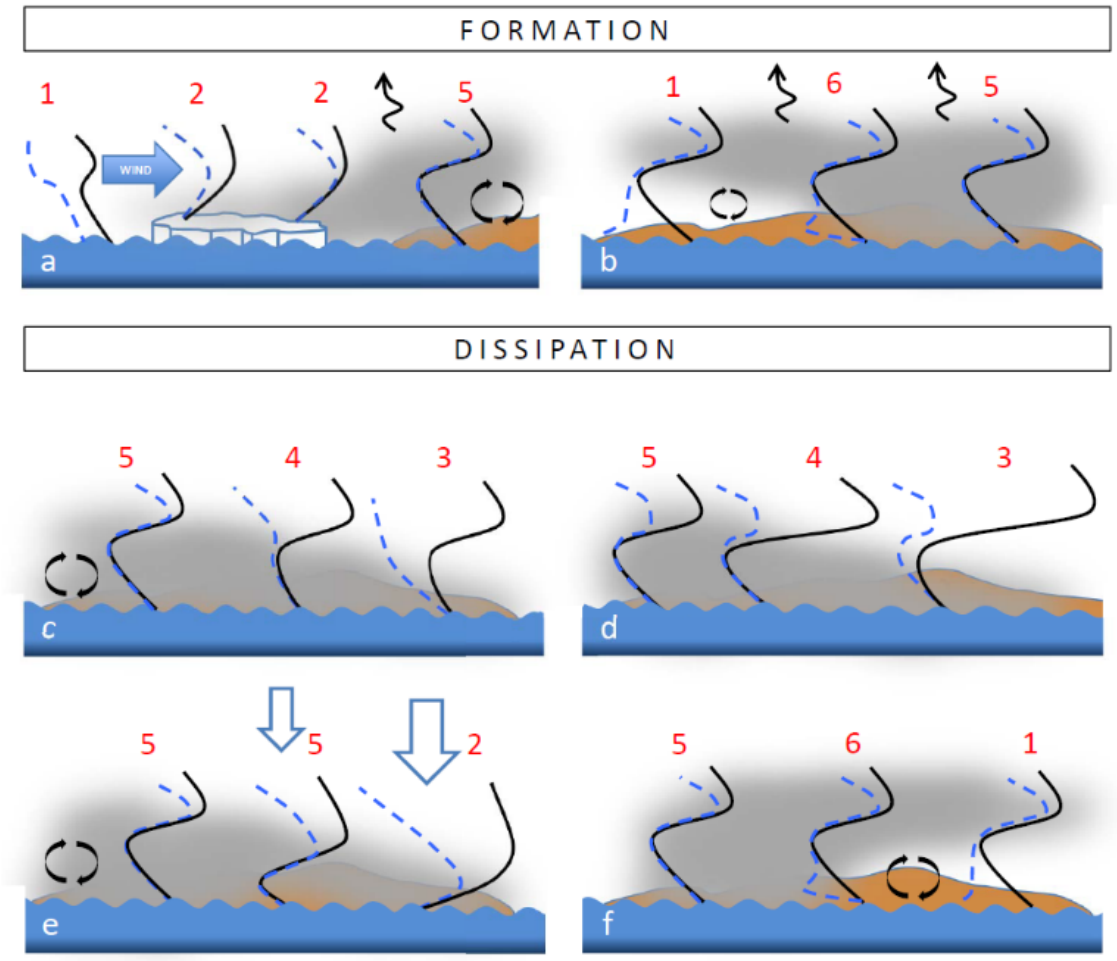

Figure 3-9. Fog formation (a-b) and dissipation (c-f) mechanims based on thermodynamic profiles: (a) advection fog development and growth; (b) stratus base lowering into fog; (c) fog thinning and dissipation through drying out due to entrainment of drier air from aloft; (d) fog thinning and dissipation due to warming aloft driven by entrainment of warm air and/or solar heating; (e) fog thinning and dissipation through large-scale subsidence (downward arrows); and (f) fog lifting to stratus. Fog classes are shown in red. Black curves are temperature profiles and dashed blue curves are dew point temperature profiles. Circular arrows represent turbulence in the mixed-layer and upward arrows (a-b) radiative cooling at the cloud top.

Figure 3-9a displays the thermodynamic profile development of the first formation mechanism, namely the typical development of advection fog from a warm and moist air

mass cooled down to its dew point temperature by contact with sea ice or cold water (e.g. Fig. 3-8a). Fog is then transported inland via sea breeze (Alt, 1979; Cappelen, 2015). As fog grows, radiative cooling at its top can result in a transition from a SBI to a LLI (Sotiropoulou et al., 2014; Kim and Yum, 2017), as observed in the ASCOS dataset. Fog was also observed to form by stratus-base lowering (Figs. 3-8b and 3-9b). The turbulence generated by cloud-top radiative cooling combined with the evaporation of cloud droplets below the cloud base results in an increase in humidity and the migration of the cloud base downward (e.g. Cotton and Anthes, 1989).

In the first fog dissipation mechanism, fog dissipates from the top due to entrainment of warm, dry air, subsidence, solar heating, or a combination of all three. Entrainment of warm, dry air from aloft into the fog layer (Fig. 3-9 c-d) leads to evaporation of the fog, through a reduction in the relative humidity due to the drying and/or warming, and thus a thinning of the fog layer (Gultepe et al., 2016). These processes result in a drier profile in the mixed layer (Classes 3 and 4). In Fig. 3-9e, large subsidence warming strengthens the inversion, lowers its base, and eventually switches the thermodynamic profile from a LLI to a SBI, resulting in either fog formation, if the initial stage was a stratus (Class 1 instead of Class 5 on Fig. 3-9e, not shown), or a thinning of the initial fog layer from Class 5 to Class 2 (Koračin et al., 2001; Lewis et al., 2003; Fig. 3-9e). The second dissipation mechanism is fog lifting to a stratus, which we infer to follow the thermodynamic evolution depicted in Fig. 3-9f. Here, Class 6 is hypothesised to be a transition profile between the mature fog (Class 5) and the stratus stages (Class 1). Class 6 almost exclusively occurred under statically unstable surface conditions over East Greenland, which is consistent with increased turbulence at the

surface that leads to the fog lifting mechanism (Cotton and Anthes, 1989; Koračin et al., 2001). The third dissipation mechanism is retreat of fog towards the ocean (Fig. 3-9c). Here, a retreat of the fog layer progressively results in a drier thermodynamic profile over time above the sounding site.

Class 3 was the dominant class over Tasiilaq, thus fog dissipation processes presented in Fig. 3-9 c-d frequently occurred in Southeast Greenland. This suggests that enhanced dissipation occurred in that region, which is consistent with the shorter fog duration in Tasiilaq compared to Danmarkshavn and Ittoqqortoormiit (Gueye, 2014). Classes 3 and 4 were also more frequent over East Greenland than over the Arctic Ocean (ASCOS). Sedlar et al. (2012) came to similar conclusions for stratocumulus clouds: the cloud regime capped by or occurring below the inversion base was more frequent over Barrow, northern coastal Alaska, compared to the Arctic Ocean (SHEBA – Surface Heat Budget of the Arctic Ocean - and ASCOS field campaigns). We therefore investigated factors that could favour a higher frequency of Classes 3-4 in these coastal lower latitude areas. The majority of back trajectories for Class 3 over Tasiilaq (Fig. 3-7b) were associated with drier and colder air masses originating from the ice sheet. This air mass origin and the fjord topography of Southeast Greenland likely promote fog dissipation through strong seaward katabatic wind (Klein and Heinemann, 2002; Cappelen, 2015). Another factor could be the latitudinal effect. Ittoqqortoormiit, Tasiilaq and Barrow have stronger diurnal variations of the solar elevation angle and lower sea ice concentrations in summer, leading to both fewer fog formation and more fog dissipation processes. This is corroborated by the fact that daily fog duration is shorter at Tasiilaq than at Danmarkshavn (Gueye, 2014). Further, land surface heating and turbulence can enhance

fog dissipation in coastal environments (Serreze and Barry, 2014; Cappelen, 2015). Higher land surface heating rates at lower latitudes can also generate stronger land and sea breeze cycles. The coastward advection and seaward retreat of fog are associated with these breezes (Cappelen et al., 2001), leading to fog having a stronger diurnal cycle in lower than at higher latitude coastal environments and compared to the open ocean (SHEBA/ASCOS). We postulate that the higher frequency of Classes 3-4 at Tasiilaq and Ittoqqortoormiit is due to a combination of all these environmental factors. These two classes could therefore represent dissipating stages of fog driven by a combination of the solar diurnal and land-sea breeze cycles, more frequent katabatic winds and enhanced turbulence. These concepts need to be further developed using numerical fog models (e.g. Gao et al., 2007; Bergot, 2016; Koračin, 2017).

3.5.3 Data uncertainties and dew point depression threshold sensitivity

Uncertainties linked to data collection, analyses and instrumental errors, could limit process observation and understanding. The major uncertainty in our method is assigning an optimal T_{dd} threshold, particularly because there is uncertainty of which surface observations are from radiosondes or from the nearby weather stations. To explore this, a sensitivity analysis was performed using thresholds ranging from 0 to 2°C, which correspond to a RH_w range of 85-100 %. The frequency distribution for each fog class under each threshold is reported in Fig. 3-10. Optimum T_{dd} thresholds were calculated based on the frequency distribution of Class 1, by maximising the distance between the Class 1 curve and the straight line connecting T_{dd} = 0°C and T_{dd} = 2°C. Optimum T_{dd} thresholds were 0.7°C for Danmarkshavn and Ittoqqortoormiit, and 0.4°C for Tasiilaq.

Fog classes affected by changes between the optimum and the 1°C threshold are Classes 3-6, which are different stages of development of the same fog process. Therefore, the choice of T_{dd} = 1°C threshold, instead of the optimum T_{dd} threshold, does not affect the overall observation of fog classes as related to particular fog processes.

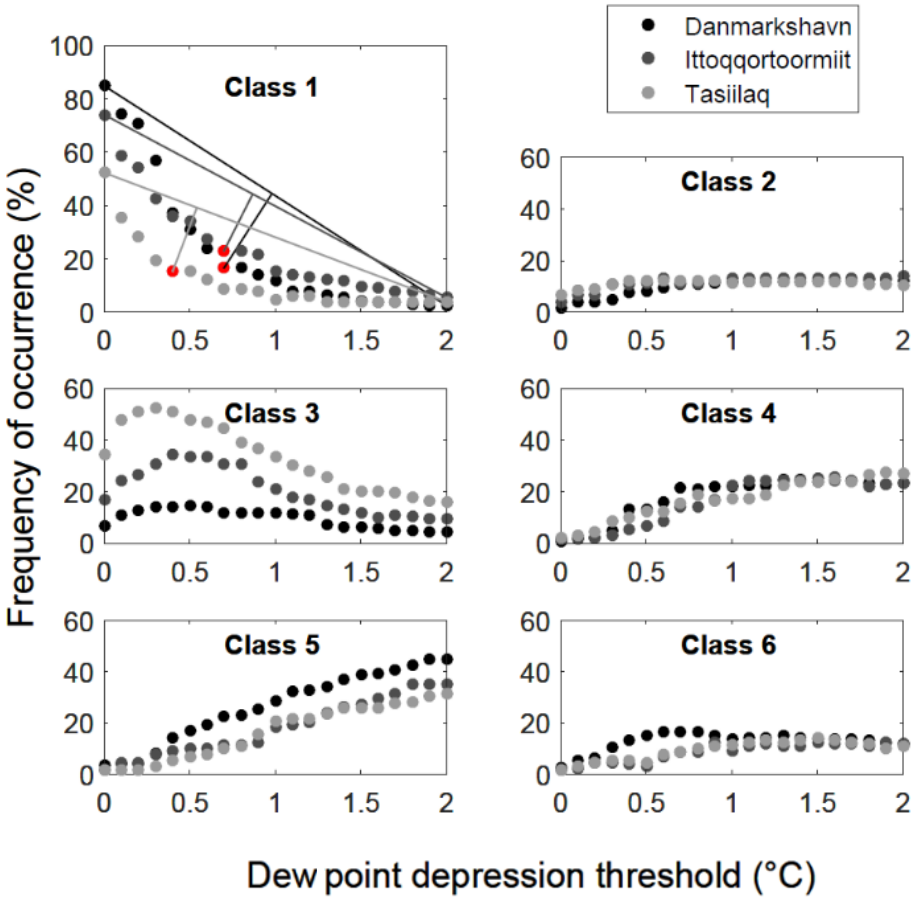

Figure 3-10. Frequency of fog classes as a function of dew point depression threshold. Red dots are optimum dew point depression thresholds determined from the maximum orthogonal distance (lines perpendicular to straight line joining first and last point) of Class 1 distribution. Note that the vertical scale for Class 1 is different.

The method presented here requires knowledge of surface-based weather conditions: when the 1°C T_{dds} threshold was applied to all soundings, irrespective of weather type, it indicated fog occurrence 25-36 % of the time. In this case, false positives included

precipitation (31-48 %), mist (14-20 %, which is easily explained by the arbitrary boundary between mist and fog) and no significant weather reported (7-13 %). The last category can be regarded as the only unexplainable false alarm, since the small T_{dds} in the precipitation and mist categories could be due to evaporation of the precipitation.

Comparing radiosonde profiles non-simultaneous with surface observations can result in more Class 1, particularly when fog dissipates rapidly. To investigate this, the frequency of fog thermodynamic Class 1 for soundings simultaneous with synoptic observations was calculated and compared to the frequency of all soundings. Although its proportion remained unchanged for Ittoqqortoormiit, soundings simultaneous with synoptic fog observations only had 2 % of excluded events in Danmarkshavn and no exclusion in Tasiilaq.

Due to an increased vertical resolution through time, instrument changes, or relocations, IGRA is not that well suited for longitudinal climatological analyses (Durre and Yin, 2008; Zhang and Seidel, 2011), except after 1992 over Greenland (Box and Cohen 2006). We therefore analysed the post-1992 period separately to investigate whether this could have affected the relative proportion of fog classes at each of the stations. These results (not shown) were the same as for the full period, except at Danmarkshavn where there were fewer excluded events (Class 1). Thus, our fog classification method is determined to be robust and its results appear to be valid for the entire period analysed.

Ingleby et al. (2014) determined that significant levels from IGRA accurately reproduced the initial high-resolution sounding. Although IGRA's dataset was assessed to be well

suited for studying the structure of the boundary layer (e.g. Zhang et al., 2011), the results from the present study question the ability of IGRA's significant levels to capture small-scale structures such as multi-layered low-level clouds. These features were frequently observed from the time-lapse camera while they were never detected from the nearby IGRA radiosonde station in Tasiilaq. Yet, multi-layer low-level clouds were frequently observed from the higher-resolution ASCOS radiosonde profiles.

3.6 Summary and conclusions

This study presented a novel automated method to retrieve Arctic fog conditions using thermodynamic profiles taken from the Integrated Global Radiosonde Archive (IGRA) database. Observations from the period 1980-2012 at three stations in coastal East Greenland were classified into six distinct fog classes using the following criteria to separate thermodynamic profiles: a 1°C surface dew point depression threshold, static stability of the surface layer, lower tropospheric inversion type, and fog top height with respect to inversion base height. Despite differences in vertical resolution and environmental conditions of ASCOS (Arctic Ocean) and IGRA (coastal East Greenland) radiosonde observations, the same fog classes were inferred. Using these six fog classes together with back trajectories, time-lapse images, and temperature profiles from the radiosonde and microwave radiometer from the ASCOS project, we hypothesise that these classes represent different stages of advection fog formation, development, and dissipation, which include processes of stratus-base lowering and fog lifting.

The thermodynamic structure of melt-season Arctic sea fog characterised in the present work was found to be consistent with results of past work on Arctic fog (Sotiropoulou et al., 2016) and Arctic stratocumulus clouds, a more common boundary-layer cloud with similar formation mechanisms (Sedlar and Tjernström, 2009; Sedlar et al., 2012; Shupe et al., 2013; Soritopoulou et al., 2014). Both boundary-layer cloud types usually occur under unstable surface layer conditions and with an elevated inversion base. At high latitudes, fog and stratocumulus clouds frequently penetrate the inversion base. Our analysis of back trajectories supports the poleward advection of heat and moisture hypothesised by Sedlar et al. (2012) to explain the persistence of such vertically extensive fog/clouds at high latitudes, while melting sea ice could be an additional factor promoting this thermodynamic characteristic (Sotiropoulou et al., 2016). At lower latitudes, fog and stratocumulus below or capped by the inversion layer were more frequent, which we hypothesise to be the result of enhanced dissipation processes from the combination of a higher solar elevation angle and an enhanced influence of topography and air masses originating from the ice sheet and adjacent land.

In addition, the following methodological conclusions can be drawn from the present work:

- Radiosonde profiles from IGRA were useful in detecting fog and characterising its diverse thermodynamic structure over Arctic locations.
- A 1°C dew point depression threshold is reasonable to capture occurrence of liquid and mixed-phase fog with $T > -10$°C.

- Uncertainty in the fog detection method developed here is about 5-15 %, but this can range between 4-9 % and 16-34 % when a 1.5°C or 0.5°C dew point depression threshold is used rather than the 1°C.
- Time-lapse images can be useful for the identification of fog type, formation and dissipation processes while back trajectory analysis can additionally be used to better understand fog formation and dissipation mechanisms related to aerosol sources and fog microphysics, which are crucial for numerical model development.

The thermodynamic classification presented in this chapter is meant to be applicable at any polar weather station, and allows investigation of predominantly liquid-phase fog processes and macrophysical properties at high latitudes. In future studies, results from this work supplemented by satellite observations, and additional data collected using research vessel-based platforms, and a ground-based project design for fog study as described in Gultepe et al. (2014), could be used for detailed fog research at high latitudes. This can lead to improved Arctic fog detection, monitoring and prediction, as well as a better understanding of fog and low cloud microphysics and dynamics, which play an important role in the Arctic surface energy budget.

CHAPTER 4. TEMPERATURE INVERSION CHARACTERISTICS OVER EAST GREENLAND IN RELATION TO FOG AND OTHER CLOUD COVER

4.1 Introduction

The Arctic has been receiving ample consideration due to its vulnerability to climate change and in turn its crucial importance for global climate (Serreze et al., 2007b; Ford and Furgal, 2009; IPCC, 2013; AMAP, 2017). High northern latitudes have been warming at more than twice the rate of the rest of the planet, which is an ongoing, perhaps even accelerating, phenomenon coined the Arctic Amplification (Serreze and Francis, 2006). Arctic Amplification is governed by feedback mechanisms such as albedo, lapse rate, water vapour, and cloud feedbacks which augment warming more than the effect of increase in greenhouse gases alone would do (Screen and Simmonds, 2010; Serreze and Barry, 2011; Taylor et al., 2013; Pithan and Mauritsen, 2014; AMAP, 2017). In part because of the complexity and large spatial variability of these feedback mechanisms, the Arctic climate system is not fully understood yet and its physical representation into global climate models requires improvements (Kattsov et al., 2005; Flato et al., 2013).

Knowledge of the near-surface lapse rate and low cloud thermodynamic structure is important for the calculation of surface energy balance (Braithwaite et al., 2006) and its accurate representation into regional and global climate models (Flato et al., 2013). The thermodynamic structure of Arctic low stratiform clouds has mostly been studied from ship campaign measurements (Sedlar and Tjernström, 2009, Sedlar et al., 2012, Shupe et al., 2013; Sotiropoulou et al., 2014; Sotiropoulou et al., 2016). Chapter 3 of this thesis

investigated fog thermodynamic profiles over East Greenland from the Integrated Global Radiosonde Archive (IGRA: Durre et al., 2006). Despite these studies, the relationship between low-level clouds and inversion characteristics during the Arctic melt season has not been fully investigated. In particular, a quantification of their interaction is lacking (Kahl et al., 1992; Sedlar and Tjernström, 2009; Devasthale et al., 2010; Hulth et al., 2010; Mernild and Liston, 2010) and this interaction will be the scope of this chapter. To investigate the relationship between low clouds and temperature inversions, our analysis will include general cloud cover fraction and fog observation. The majority of analysis will focus on fog observations, since these are the most reliable ground observations of clouds available for Arctic remote locations over long time scales, and because the occurrence of low stratus and fog have increased over the oceans (e.g. Schweiger, 2004; Eastman and Warren, 2010). This trend is in part because low cloud is generally initiated locally by enhanced evaporation due to sea ice decline, while middle and high cloud increases are mostly driven remotely by enhanced moisture transport from lower latitudes (Vavrus et al., 2011).

This study will be the first to compare and quantify lower tropospheric inversion characteristics during foggy and non-foggy weather conditions in the Arctic. To achieve this goal, temperature inversion retrievals from IGRA profiles (see also Chapter 3) will be based on the existing determination method presented by Kahl (1990). Additionally, a novel algorithm to retrieve fog top elevation from a combination of low-resolution radiosondes and ground-based synoptic observations will be introduced, and applied to IGRA over the period 1980-2016 at three East Greenland synoptic weather station locations with fog observations. The algorithm includes an improved interpolation

method for saturation between IGRA significant sounding levels. Even though the novel fog top elevation retrieval method is restricted to fog in this chapter, we argue that it can be extended to calculate cloud top elevation of other Arctic boundary-layer clouds, which represent the majority of cloud occurrence in the Arctic melt season. Ultimately, this study has the potential to advance the understanding of the interaction between low clouds and temperature inversions, and to improve cloud geometrical thickness retrievals from radiosondes, both of which have important implications for the Arctic surface energy budget.

This chapter is organised as follows. After this introduction, a brief background on temperature inversions, fog, and radiosonde data in the Arctic will be presented (Sect. 4.2). Then the study region will be introduced (Sect. 4.3) and data sources and methodology explained (Sect 4.4). The first set of results (Sect. 4.5.1) focuses on temperature inversion characteristics from IGRA during all weather, foggy and non-foggy conditions, and effects of wind speed and cloud cover fraction on these inversion characteristics. The second set of results concerns fog top elevation calculations and statistics (Sect. 4.5.2). The discussion includes a sensitivity analysis of the fog top elevation retrieval method (Sect. 4.6.1), a comparison of calculated fog top elevation with cloud top retrievals from an independent cloud altitude dataset from the Cloud-Aerosol Lidar and Infrared Pathfinder Satellite Observation (CALIPSO) (Sect. 4.6.2), and an investigation of the relationship between fog, low-clouds and inversion characteristics, and their implications for glacier surface energy balance (Sect. 4.6.3). The chapter is completed by the Summary and Conclusions (Sect. 4.7).

4.2 Background

4.2.1 Temperature inversions in the Arctic

Temperature inversions (i.e. increase of temperature with elevation; Oke, 1987) are common year-round in the Arctic, where their occurrence is related to synoptic patterns that are of a stable, mostly anticyclonic, configuration (Serreze et al., 1992; Marshall et al., 2007). Low-level tropospheric inversions display a pronounced seasonal pattern, with a maximum in the polar winter, when radiative input at the surface is zero or negligible. This mainly results in surface-based inversions (Marshall et al., 2006). In summer, low-level temperature inversions with an elevated base are a common feature of the low troposphere over the Arctic Ocean and coastal areas, where the proximity to open ocean influences local atmospheric humidity (Kahl, 1990; Kahl et al., 1992; Serreze et al., 1992; Kahl et al., 1996; Chutko and Lamoureux, 2009; Devasthale et al., 2010). Elevated inversions mainly originate from subsidence or advection (Busch et al., 1982). Surface-based inversions can also occur during the melt season as a result of ice and snow melt (Kahl et al., 1992; Miller et al., 2013), particularly over the Greenland Ice Sheet where the sinking cold air flows toward the ice sheet margins (Steffen and Box, 2001).

Temperature inversions can have complex effects on the Arctic surface energy budget, depending on their structure and potential coincidence with clouds. Mernild and Liston (2010) determined that the effect of temperature inversions alone reduced glacier-wide ablation by up to 21 % on Mittivakkat Glacier, East Greenland. Thus, a linear lapse rate is inappropriate to model glacier melt at higher elevations in the presence of temperature inversions. Over sea ice, in contrast, Chutko and Lamoureux (2009) found that temperature inversions were correlated with episodes of intense melt.

Several factors can influence temperature inversion properties. Surface turbulence from heat convergence (Oke, 1987) or high winds (Mernild and Liston, 2010) tend to weaken or destroy inversions (Bradley et al., 1992). Nonetheless, inversions in the Arctic and Antarctic were observed not to peak under calm conditions, but rather with winds between 3-10 $m\,s^{-1}$ (Hudson and Brandt, 2005; Miller et al., 2013). Even though precipitation can occur in the presence of inversions, high precipitation intensities lead to their destruction (Mernild and Liston, 2010). The influence of topography and warm air advection has also been identified as important factors in inversion break-up (Stone and Kahl, 1991). Low clouds weaken inversions because they increase the downward longwave radiation (Kahl, 1990; Stone and Kahl, 1991; Serreze et al., 1992; Hudson and Brandt, 2005; Bourne et al., 2010). From monthly statistics over Alert (Canadian Arctic) and coastal Alaska, inversion depth was suggested to be inversely correlated with cloud cover (Kahl, 1990; Kahl et al., 1992). Unlike other low clouds, however, fog on the Greenland Ice Sheet is associated with strong surface-based inversions because these are favourable conditions for fog formation (Miller et al., 2013).

4.2.2 Fog in the Arctic

Chapters 1, 2, and 3 of this thesis are focused on the definition, processes, climatology and character of Arctic fog in East Greenland. In this section, fog is only briefly described and the main focus is on its potential effect on the surface energy budget.

As with temperature inversions, low stratiform clouds, the most common cloud type during the Arctic melt season, strongly influence the surface energy budget (Klein and

Hartmann, 1993; Curry et al., 2000; Eastman and Warren, 2010). Among these, Arctic sea fog (visibility lower than 1 km: NOAA, 1995) frequently occurs as a result of warm air advection over sea ice and cold waters (Rae, 1951; Alt, 1979; Nilsson and Bigg, 1996; Svendsen et al., 2002, Hanesiak and Wang, 2005, Sotiropoulou et al., 2016). Sea breezes bring fog to coastal areas and up to a few tens of kilometres inland, where it is capped by warm continental air, which creates strong stability conditions (Alt, 1979; Lewis et al., 2003; Mernild et al., 2008; Cappelen, 2015). The high reflectivity of low clouds and fog cools the surface (shortwave cloud forcing) while their emissivity warms the surface (longwave cloud forcing). The net effect is usually warming of the surface, although this depends on the droplet size, liquid water path, surface albedo and the solar zenith angle (Nardino and Georgiadis, 2003; Shupe and Intrieri, 2004; Mauritsen et al., 2011). Indeed, liquid-bearing low clouds were attributed to enhance mass loss over the Greenland Ice Sheet (Bennartz et al., 2013; Miller et al., 2015; Van Tricht et al., 2016), except over low albedo zones of the ablation area (Wang et al., 2016; Hofer et al., 2017).

4.2.3 Radiosonde profiling of temperature inversions and fog

Radiosondes provide valuable information on temperature, humidity and wind profiles in the troposphere. They are used for operational weather forecasting and climate research. The Integrated Global Radiosonde Archive (IGRA: Durre et al., 2006) contains twice daily soundings available at stations worldwide since the 1940s (see Chapter 1, Fig. 1-2). The IGRA global network of radiosondes and rawinsondes has formerly been used to study the climatology of temperature inversions in the Arctic (Kahl, 1990; Bradley et al., 1992, Kahl et al., 1992; Serreze et al., 1992, Kahl et al., 1996; Chutko and Lamoureux,

2009; Zhang et al., 2011). Zhang et al. (2011) established a climatology of surface-based inversions from IGRA, which revealed that Danmarkshavn, the northernmost station in Greenland had the most frequent, deepest and strongest inversions over Greenland. The frequency of surface-based inversions increased over Greenland between 2000 and 2009; however, radiosonde data are affected by inhomogeneities in inversion depth and intensity so that trends cannot be calculated for those variables (Zhang and Seidel, 2011). General climatological trends in upper-air temperature have also been studied from IGRA data for all Greenland stations (Box and Cohen, 2006). Absolute humidity profiles from radiosondes, including humidity inversions (e.g. Nygård et al., 2014), are useful to study cloud formation and structure, and for nowcasting and forecasting of fog (Dorman et al., 2017). As for the IGRA temperature records, the IGRA humidity records are plagued by data inhomogeneities (Dai et al., 2011).

To our knowledge, only one fog top retrieval technique from soundings has been documented to date (US Bureau of Naval Personnel, 1965). It uses the intersection of the average mixing ratio between the bottom and top of the inversion with the dry-bulb temperature curve to calculate fog top elevation. It is presented for application to radiation fog with a surface-based inversion. However, this technique has not been applied to sea fog or fog with an elevated inversion, both of which frequently occur in the Arctic during the melt season (Kahl, 1990; Kahl et al., 1992; Serreze et al., 1992; see Chapter 3). Additionally, several attempts have been made to retrieve cloud base, top and thickness from low-resolution (Poore et al., 1995; Wang and Rossow, 1995; Chernykh and Eskridge, 1996) and high-resolution radiosonde profiles (Minnis et al., 2005; Zhang et al., 2010; Zhang et al., 2013), but these all disregard fog. Poore et al. (1995) used dew

point depression thresholds determined from aircraft measurements (AWS, 1979) for several temperature ranges: 2°C for temperatures above 0°C and 4°C for freezing temperatures above -20°C. Another technique, based on variations of relative humidity (*RH*) at cloud boundaries and within a cloud layer, was introduced by Wang and Rossow (1995) and later improved by Zhang et al. (2010). *RH* was converted with respect to ice at freezing temperatures and the minimum threshold for cloud boundary detection was 84 % (Wang and Rossow, 1995) or 90 % *RH* (Wang et al., 1999). A simple interpolation method for saturation between mandatory sounding levels of low-resolution soundings was applied to half the thickness of a layer bounded by a saturated and a subsaturated sounding level (Wang and Rossow, 1995). In addition to this interpolation algorithm being imprecise, these cloud thickness retrieval techniques do not perform well over Arctic locations (Jin et al., 2007; Zhang et al., 2013). Furthermore, no methods have been developed for, or applied to, Arctic fog or low stratiform clouds specifically, which are the most frequent cloud types during the Arctic melt season. Development of a specific fog and low-cloud detection method from radiosondes over high-latitude sites would therefore fill an important scientific gap.

4.3 Study site

Three radiosonde stations associated with World Meteorological Organization (WMO) synoptic weather stations were selected along the coast of East Greenland (Figure 4-1, Table 4-1), where fog is prevalent in summer (Cappelen, 2015; Chapter 2). These stations are part of the Integrated Global Radiosonde Archive (IGRA) network and operated by the Danish Meteorological Institute (DMI). The climate zonation ranges from Low Arctic (Tasiilaq), with seasonal sea ice and a strong diurnal solar cycle, to High Arctic (Ittoqqortoormiit and Danmarkshavn), with sea ice concentrations above 80 %, 24-hour daylight, and a dominance of low clouds and fog (Cappelen et al., 2001; Vinje, 2001; CAVM, 2003). The climate in Tasiilaq is strongly influenced by the presence of the Icelandic Low and the warm Irminger Current (Hanna and Cappelen, 2003; Cappelen, 2015). Tasiilaq experiences the strongest katabatic winds as well as the passage of cyclones, resulting in optically thicker clouds compared to more northern locations (Van Tricht et al., 2016).

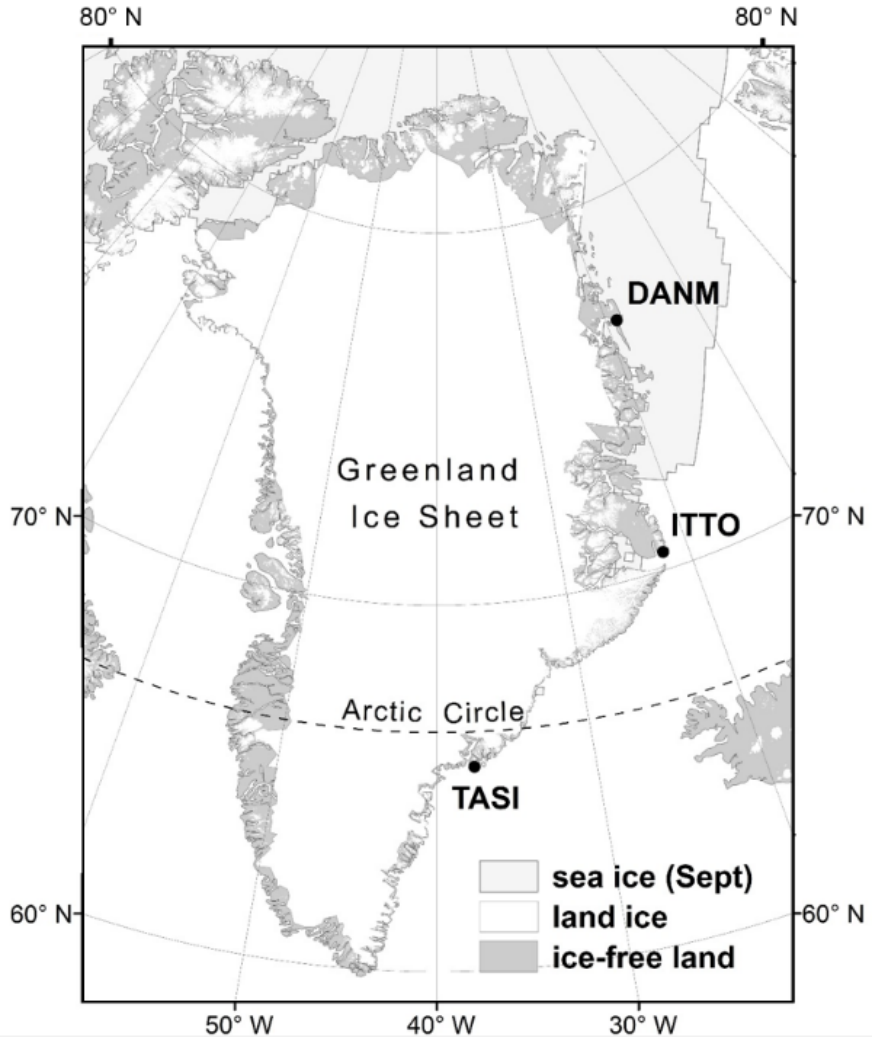

Figure 4-1. Location of radiosonde stations along the coast of East Greenland: Danmarkshavn (DANM), Ittoqqortoormiit (ITTO) and Tasiilaq (TASI). The September sea ice extent represents the median minimum seasonal extent (http://nsidc.org/data/nsidc-0051). Land ice is a combination of the Randolph Glacier Inventory (Pfeffer et al., 2014) and the Hydrologic Outlets of the Greenland Ice Sheet (Lewis and Smith, 2009).

Table 4-1. Geographic coordinates and distance to open water of IGRA radiosonde stations in East Greenland.

	WMO ID	Latitude[a] (°N)	Longitude[a] (°W)	Elevation[a] (m a.s.l.)	Distance from shore (km)	Distance to ocean (km)
Danmarkshavn	4320	76.7694	18.6681	11	0.12	6.47
Ittoqqortoormiit	4339	70.4844	21.9511	70	0.17	12.60
Tasiilaq	4360	65.6111	37.6367	54	0.25	2.24

[a] From https://www1.ncdc.noaa.gov/pub/data/igra/igra2-station-list.txt.

4.4 Data and methodology

4.4.1 Temperature inversions

4.4.1.1 Upper-air observations from IGRA radiosonde data

The radiosonde data analysis is presented for the period 1980-2016 in order to exclude station relocations, major changes in sonde type and radiation correction from inducing inhomogeneities in the datasets. For details on these inhomogeneities, refer to Chapter 3 of this thesis. Additionally, the analysis is restricted to the Arctic melt season months of May to August (hereafter referred to as "summer"), when two thirds to three quarters of fog occur in East Greenland (Gueye, 2014; and Chapter 2, Table 2-3). Within this time frame, twice daily radiosonde data were acquired through the quality-controlled Integrated Global Radiosonde Archive (IGRA, https://www.ncdc.noaa.gov/data-access/weather-balloon/integrated-global-radiosonde-archive: Durre et al., 2006). Launch times were either at 1100 and 2300 UTC, or at 1200 and 0000 UTC coincident with synoptic ground observations. The former are the majority of soundings before automation (see below), while the latter are all soundings after automation and some select soundings before automation.

Each radiosonde records temperature, humidity, atmospheric pressure, wind speed and direction. Soundings contain data at mandatory pressure levels (1000, 925, 850, 700, 500 hPa, etc.) and at additional significant thermodynamic levels to capture all slope breaks in temperature and humidity profiles between mandatory levels (Durre et al., 2006). In this work, only data below the 700 hPa (approximately 3000 m a.s.l.) pressure level are used.

Between 1980 and 2016 there has been an alternate use of Vaisala sonde types RS18/21 (until early 1980s), RS80, RS90 and RS92 (Table 4-2). After summer 2012, radiosonde launches at Tasiilaq became automated. Quality tests were performed on six months of soundings in 2014 and revealed that the availability and quality of soundings over that period did not reach WMO standards (Laursen, 2015). While this affects the frequency of radiosonde coverage at Tasiilaq from 2013 onwards, it did not affect the extracted fog profiles used in this chapter.

Table 4-2. Sonde types and uncertainty specifications for Vaisala sonde models in the troposphere (1080-100 hPa).

Model	Atmospheric pressure (hPa)	Dry-bulb temperature (K)	Relative humidity (%)	Calculated geopotential height (m)	Reference
VRS18/21	2	0.3	4	-	Richner and Phillips, 1982; Luers and Eskridge, 1998
VRS80	1	0.4	4	-	Richner and Phillips, 1982; Steinbrecht et al., 2008
VRS90	0.7-1.5	0.5	5	25	Luers, 1997; Antikainen et al., 2002
VRS92	1	0.5	5	20	Steinbrecht et al., 2008; Vaisala, 2017

4.4.1.2 Radiosonde analysis methodology

IGRA variables that were used for the analysis of temperature inversions include dry-bulb temperature (T in K, converted to °C), atmospheric pressure (P in hPa), and calculated geopotential height (Z in m). Although P is reported at every sounding level, Z is measured at just a few levels. IGRA calculation of the thickness of the layer dZ between

level i of known Z and level i+1 of unknown Z is made via the hydrostatic balance formula, which requires knowledge of T and P at i and i+1 levels:

$$dZ = \frac{R}{g}\left(\frac{T_i+T_{i+1}}{2}\right) ln\frac{P_i}{P_{i+1}}, \qquad \text{(Equation 4-1)}$$

where R is the ideal gas constant (287 J K^{-1} kg^{-1}) and g the gravitational acceleration (9.81 m s^{-2}) (from Durre and Yin, 2008, Eq. A1). Throughout this analysis calculated Z will be used only, and soundings with fewer than five levels below the 700 hPa level in T profiles are discarded as they are considered unreliable for the analysis of low tropospheric inversions (Kahl et al., 1992). In select case studies (Sect. 4.6.2) the reliability of calculated Z will be verified using measured Z. Finally, surface wind speed (w_s in m s^{-1}) at the first sounding level was used to analyse its effect on inversion characteristics.

Low tropospheric temperature inversions were characterised in terms of their base height (Z_{base}), top height (Z_{top}), depth (ΔZ) and intensity (ΔT) using the method from Kahl (1990). Figure 4-2 schematically illustrates this method in a Skew-T Log-P diagram. Here, Z_{base} is determined as the first level where T starts to increase with height. The inversion is classified as a surface-based inversion (SBI) when Z_{base} is at ground level and as a low-level inversion (LLI) when Z_{base} is elevated but below the 700 hPa pressure level (Kahl et al., 1992). Z_{top} is the altitude above the ground level at which T starts to decrease with height above Z_{base}. Thin layers (< 100 m) of positive temperature lapse rates between two inversion layers are considered to be part of the same inversion layer, as recommended by Kahl (1990) and Zhang and Seidel (2011). Z_{base} and Z_{top} are given

relative to ground level to allow for a comparison among stations. ΔZ is obtained by subtracting Z_{base} from Z_{top}, and ΔT calculated as the difference in T between Z_{top} and Z_{base}.

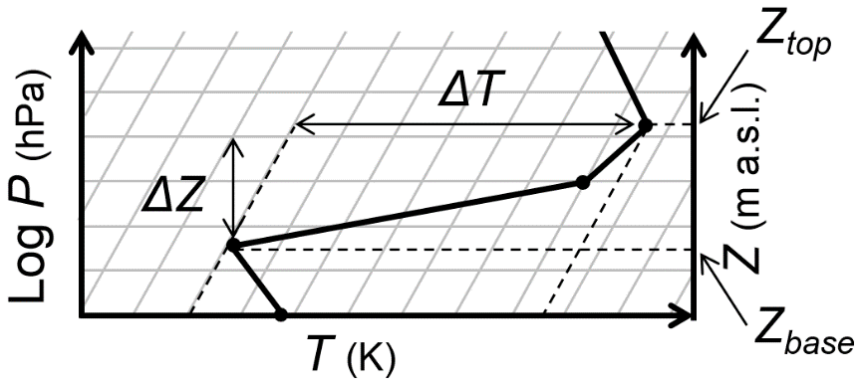

Figure 4-2. Inversion characteristics determined from a schematic Skew-*T* Log-*P* diagram: inversion base (Z_{base}), inversion top (Z_{top}), inversion depth (ΔZ) and inversion intensity (ΔT in K) (after Kahl, 1990). The pressure altitude *P* of significant levels, including at Z_{base} and Z_{top}, is given in hPa and their metric altitude, *Z*, in m a.s.l. Conversion from pressure to metric altitude is done via Equation 4-1.

4.4.2 Fog, cloud cover and wind

4.4.2.1 Surface observations of fog and cloud cover from synoptic weather stations

Fog conditions were extracted from a combination of archived present weather (*ww*) and visibility (*vv*) data provided by DMI for the three WMO synoptic weather stations. Observations were made at synoptic and intermediate hours (i.e. every 3 hours starting from 0000 UTC) until the early 2000s, when observations became automated and reported hourly (Bødtker, 2003). The manual and automated *ww* and *vv* fog and visibility codes used are explained in Chapter 2 Table 2-2 (WMO, 1995: tables 4677, 4680, 0 20 003 and 4377). Forward-scatter FD12P Vaisala Present Weather Sensor, with a Meteorological Optical Range accuracy of ± 10 %, is currently used to report automated *ww* and *vv* observations (Claus Nehring, pers. comm, May 2016). The analysis in this chapter was restricted to summer liquid or supercooled fog (surface *T* from radiosondes >

-10°C: Petterssen, 1956), which represents the vast majority of summer fog observations (see Chapter 2).

In order to analyse the general effect of clouds other than fog on temperature inversion characteristics, cloud cover fraction was extracted from weather data files that accompany DMI reports (Cappelen, 2017: http://www.dmi.dk/laer-om/generelt/dmi-publikationer/2013/). Our analysis distinguishes three cloud cover categories: i) clear-sky conditions (0 okta), ii) few and scattered clouds (1-4 oktas), and iii) broken and overcast conditions (5-8 oktas). Neither cloud type nor cloud elevation are available from DMI files, but it is well known that low clouds are dominant in Arctic coastal regions in summer (e.g. Klein and Hartmann, 1993; Key et al., 2004; Eastman and Warren, 2010). It is therefore assumed that cloud cover fraction, especially when broken to overcast, is representative of low-level cloud conditions.

4.4.2.2 Fog and fog top elevation calculation from IGRA soundings

From all summer IGRA soundings over the period 1980-2016, profiles coincident with fog were retrieved based on the combined analysis of synoptic fog observations (*ww* and *vv*) from DMI archived data and the dew point depression (T_{dd}) data available in IGRA files. As for *T* profiles, soundings with fewer than five levels in T_{dd} profiles below the 700 hPa level were excluded. Dew point temperature T_d (T-T_{dd}) was used for graphical analysis only (e.g.

Figure **4-3**). Because of the combined use of manned and automated synoptic *ww* and *vv* observations in this analysis, some soundings corresponded to ground observations (0000

UTC and 1200 UTC: soundings before automation, and all soundings after automation) while others did not (1100 UTC and 2300 UTC: soundings before automation).

Based on T_{dd}, *ww*, *vv*, and the time lag between ground and upper-air observations, three sounding categories, including two categories of fog, were defined for this analysis:

1) "Real Fog" cases: soundings corresponding to synoptic fog observations (*ww*, and *vv* < 1 km) or occurring at sounding times between two consecutive synoptic fog observations. Real fog soundings were additionally restricted to a surface dew point depression of $T_{dds} \leq 1$°C, a common value for saturation of advection fog (e.g. Koračin et al., 2014). This restriction captures almost all real fog observations at Tasiilaq and Danmarkshavn, and about 75 % of fog observations at Ittoqqortoormiit (see Chapter 3 Fig. 3-2). By extension, "saturation" will be defined in this paper as $T_{dd} \leq 1$°C. It corresponds to a relative humidity with respect to water > 93 % (Hardy, 1998);
2) "Marginal Fog" cases: soundings corresponding to *ww* codes of fog in patches, fog from a distance, shallow fog < 2 m a.g.l. (c.f. Croft et al., 1997), or, in the case of soundings not coincident with synoptic observations, real fog either immediately before or after the balloon launch, but not both. For marginal fog no threshold was set for T_{dds} or *vv*;
3) "Non-Fog" cases: soundings during all other weather conditions during summer.

For both real and marginal fog cases, soundings that were not coincident in time with synoptic fog observations represented 50-70 % of analysed upper-air observations over the study period (1980-2016).

Fog top pressure (*FTP*) and fog top elevation (*FTE*) for all real fog cases were computed from IGRA soundings using a novel method developed specifically for this purpose. This method is based on IGRA's T_{dd} profiles and will hereafter be referred to as the Dew point Depression Method (DDM). The DDM is illustrated in

Figure **4-3**. First, the pressure of the uppermost saturated level (P_{sat}) corresponding to the geopotential height Z_{sat} is determined as the uppermost level above a continuous saturated layer (Figure 4-3: grey shading). Here, $T_{dd} \leq 1$°C. *FTP* is the level where $T_{dd} = 1$°C. T_{dd} at P_{sat} is either 1°C (cases 1a and 1b) or < 1°C (Case 2). In Case 1a, P_{sat} is at ground level and $T_{dd} = 1$°C. Here, *FTP* is at the ground level and *FTE* is the geopotential height at the ground level (Z_0). In Case 1b, P_{sat} is above the surface and $T_{dd} = 1$°C. Here, fog is delimited by at least two saturated sounding levels and *FTE* corresponds to Z_{sat}. In Case 2, P_{sat} is elevated and $T_{dd} < 1$°C. The pressure difference (ΔP) between P_{sat} and *FTP* is determined geometrically on the Skew-*T* Log-*P* diagram by linear interpolation at 0.1 hPa intervals between P_{sat} and the next subsaturated level aloft (P_{sat+1}), until $T_{dd} = 1$°C. In this case, *FTE* is the sum of Z_{sat} (from IGRA datafiles) and the calculated saturated thickness above that level, which is obtained from a modification of Equation 4-1 under the assumption of hydrostatic balance and linear variation of T and T_d between two consecutive sounding levels. Thus, *FTE* for Case 2 is calculated as follows:

$$FTE = Z_{sat} + \frac{R}{g}\left(\frac{T_{sat}+FTT}{2}\right) ln\frac{P_{sat}}{FTP} \quad , \qquad \text{(Equation 4-2)}$$

where *FTE* and Z_{sat} are in m a.s.l.; R is 287 J K^{-1} kg^{-1}; g is 9.81 m s^{-2}; temperatures at P_{sat} (T_{sat}) and at the fog top (*FTT*) are in K, and P_{sat} and *FTP* are in hPa.

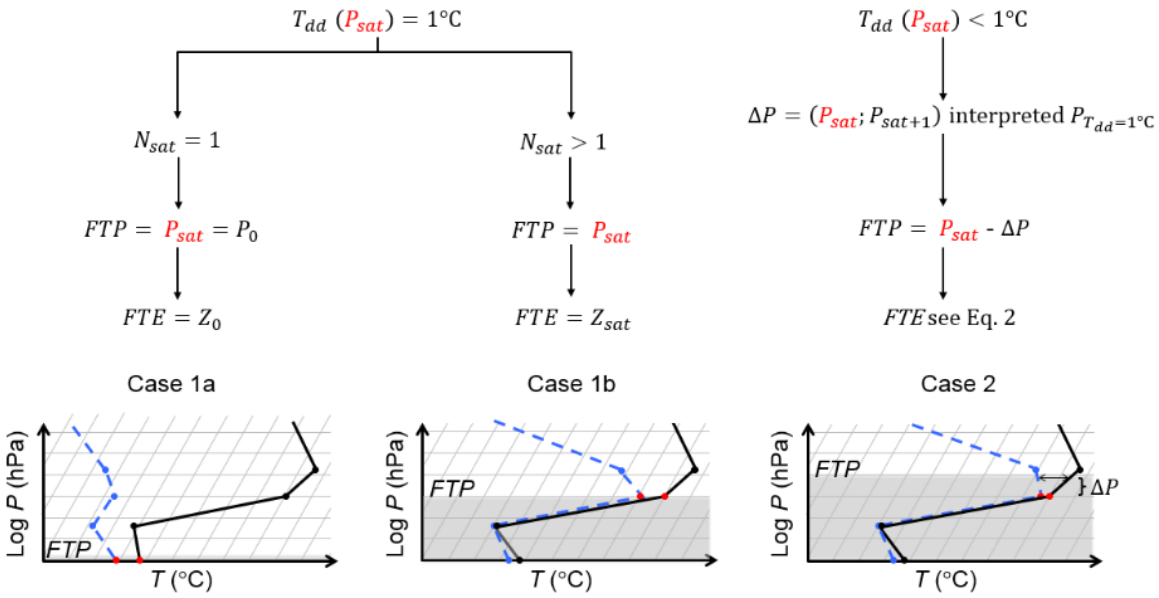

Figure 4-3. Dew point Depression Method (DDM) of determining fog top pressure (*FTP*) and fog top elevation (*FTE*) from dew point depression T_{dd} on a schematic Skew-*T* Log-*P* diagram, where the solid black curve is the dry-bulb temperature *T*, and the dashed blue curve the dew point temperature ($T_d = T - T_{dd}$). The uppermost saturated pressure level P_{sat} (red dots) corresponds to a geopotential height Z_{sat}, and is determined as the uppermost level above a continuous saturated layer (grey shading) where $T_{dd} \leq 1$°C. *FTP* is the level where $T_{dd} = 1$°C. N_{sat} is the number of saturated levels between the surface pressure P_0 and P_{sat}.

The newly developed DDM was used instead of the established "Mixing Ratio Method" (MRM) (US Bureau of Naval Personnel, 1965). The main reason for this choice was the inability of the MRM to calculate *FTE* in cases of negative T_d gradients above one single saturated sounding level (e.g. *FTE* below Z_{base}), which occur in up to 57 % of radiosonde profiles with fog over East Greenland (see Chapter 3). In Section 4.6.1 a comparative analysis of the DMM and MRM is performed on soundings with positive T_d gradients above the uppermost saturated sounding level and on all soundings with at least two saturated sounding levels. For this comparative analysis, the mixing ratio (g kg^{-1}) was extracted from IGRA datafiles.

Inversion characteristics during fog conditions were calculated using the method explained in Sect. 4.4.1.2 for all weather cases, with one exception: when a secondary weak inversion was present inside a fog layer below the main capping inversion, the inversion characteristics of that capping inversion were retained. These secondary inversions occurred in < 3 % of soundings. Z_{base}, ΔZ and ΔT were analysed for all real, marginal and non-fog soundings. In addition, for a better understanding of regional differences of inversion characteristics during fog conditions, statistics for Z_{base}, ΔZ and ΔT were computed for two categories of wind speed (< 5 m s^{-1} and ≥ 5 m s^{-1}) for all-weather, real fog, and non-fog conditions (see Sect. 4.4.2).

We statistically analysed the significance of differences in inversion base (Z_{base}), inversion top (Z_{top}), inversion depth (ΔZ), and inversion intensity (ΔT) among all-weather, non-foggy and foggy conditions, as well as the *FTE* among the three stations. The null hypothesis is that no significant difference occurs. Since none of the datasets were normally or lognormally distributed, statistical significance was assessed through the nonparametric Wilcoxon Rank Sum and the combined Kruskal-Wallis and Tukey's Honest Significant Difference tests at the 99 % confidence level.

4.4.2.3 Fog and low clouds from CALIPSO

In order to verify the fog top elevation results using the novel DDM method introduced in Sect. 4.4.2.2, IGRA-derived *FTE* were compared to an independent cloud altitude dataset from the Cloud-Aerosol Lidar and Infrared Pathfinder Satellite Observation (CALIPSO) Level 2 Cloud Layer product at 1 km along-track resolution (CAL_LID_L2_01kmCLay-Standard_V4-10 from https://www-calipso.larc.nasa.gov/). CALIPSO is a NASA satellite designed to profile global cloud layers along a sun-synchronous orbit with a 99-minute orbital period and 16-day repeat cycle. Among other instruments, CALIPSO carries CALIOP (Cloud-Aerosol Lidar with Orthogonal Polarization), an advanced imaging and lidar system that provides high-resolution vertical profiles of aerosols and clouds. CALIOP's vertical resolution is 30 m and its horizontal resolution is 335 m (Winker et al., 2009). CALIPSO has been used to accurately capture fog frequency and spatial distribution when no upper clouds are present (Kawai et al., 2015; Cermak, 2016).

From CALIPSO's temporal coverage from June 2006 onwards, and of the 16 parallel tracks nearest to each of the three East Greenland stations, undergraduate student Tyrell Nielsen selected those tracks and times that coincided closest to the three radiosonde locations and launch times. For Tasiilaq the closest CALIPSO track timing was in all cases > 3 hours earlier or later than its balloon launches and we therefore excluded this station from our comparison. Danmarkshavn and Ittoqqortoormiit have the nearest CALIPSO track lines at 1230 UTC and 1330 UTC, respectively, which are approximately coincident with their 1200 UTC radiosonde balloon launches. For these two stations, three or four grid points on the nearest CALIPSO tracks (Figure 4-4) were selected to

account for spatial variability in fog thickness. Danmarkshavn's nearest track line has the closest point only 2 km north of the station (Figure 4-4a: point 4), but as coastal mountainous topography can affect *FTE*, the nearest three coastal grid points, approximately 8 km east of the station, were also extracted from the same track line (Figure 4-4a: points 1-3). For Ittoqqortoormiit, the nearest optimal track line passes 28 km to the southwest over Scoresby Sund, from which three coastal grid points were selected (Figure 4-4b: points 1-3). For each of these 16-day repeat tracks between 2006 and 2016, the IGRA radiosonde profile and DMI *ww* data were checked for fog occurrence. Thin fog cases (*FTE* < 100 m a.s.l.) were excluded due to their large spatial and temporal variability. Since only four fog cases from the IGRA 2006-2016 datasets corresponded to the CALIPSO timing, we expanded our comparison analysis to include six additional cloud top elevations from low stratiform clouds without precipitation. Ten days with fog or low stratiform clouds could be compared to the CALIPSO lidar cloud altitude dataset, from which fog/cloud top heights were extracted using the maximum elevations of the lowermost cloud level in the Level 2 Cloud Layer product. The selected dates range from late April to early October to cover liquid fog and stratiform clouds in the early to late melt season.

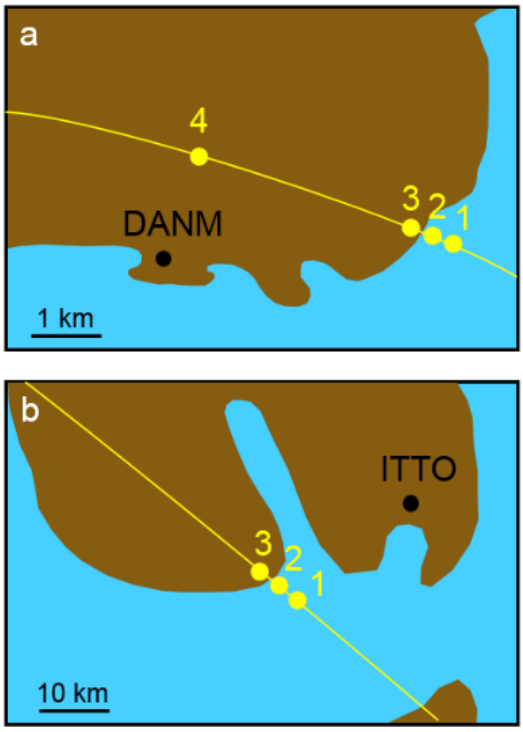

Figure 4-4. Schematic representation of selected grid points (yellow dots) from the optimal CALIPSO track line (yellow line) in the vicinity of (a) Danmarkshavn (DANM) and (b) Ittoqqortoormiit (ITTO). Grid points 1, 2 and 3 are the nearest coastal locations on a CALIPSO track to each IGRA station (8 km and 28 km, respectively). Grid point 4 (a) is the nearest CALIPSO point on land, 2 km north of Danmarkshavn.

4.4.3 Extent of the glacier ablation zone covered by fog and temperature inversions

The common occurrence and significant vertical extent of fog and temperature inversions could impact the ablation of Greenland coastal glaciers, which represent 38.9 mm of sea-level equivalent (Vaughan et al., 2013). The majority of Greenland glaciers are marine-terminating, and thus most of their ablation is from iceberg calving and basal melting. About half of glaciers peripheral to the Greenland Ice Sheet is located in the Geikie Plateau and Blosseville Kysten region, directly south of Scoresby Sund (Rastner et al., 2012). Of the 332 glaciers in this region, 180 are land-terminating and drain about 10 % of the glacierized area (~ 4000 km^2) (Jiskoot et al., 2003). The average snowline for this

region was 1050 m a.s.l. in late summer 2003-2005, resulting in a total ablation area of ~ 1800 km^2 (Stearns and Jiskoot, 2014).

To investigate what proportion of land-terminating glacier ablation area may be affected by the occurrence of fog and temperature inversions, we used the glacier hypsometric distribution of the 180 land-terminating glaciers in central East Greenland (Stearns and Jiskoot, 2014: Figure 8.6; See also Appendix 7) in combination with the *FTE* and Z_{top} distributions measured over the nearest station (Ittoqqortoormiit) during the late melt season (July-August). The calculated elevation ranges for *FTE* and Z_{top} were used to estimate the percentage of glacier ablation area under medium and maximum fog thickness, and medium and maximum inversion layer thickness.

4.5 Results and interpretation

4.5.1 Temperature inversion characteristics

4.5.1.1 All weather conditions

In total, 7786 summer soundings with ≥ 5 sounding levels below the 700 hPa pressure level were retrieved and analysed for Tasiilaq, 7271 for Danmarkshavn, and 7453 for Ittoqqortoormiit. Lower tropospheric inversions occur in 84 % of soundings at Tasiilaq, in 91 % of soundings at Danmarkshavn, and in 95 % of soundings at Ittoqqortoormiit. Most inversions are elevated, with frequencies ranging from 69 % at Tasiilaq to 79 % at Ittoqqortoormiit. Statistics of inversion characteristics for all summer soundings are presented in Figure 4-5. Median inversion base elevations (Z_{base}) are highest at Tasiilaq

(164 m a.s.l.) and lowest at Ittoqqortoormiit (129 m a.s.l.) compared to Danmarkshavn (149 m a.s.l.; $p < 10^{-3}$). Median inversion depths (ΔZ) range from 225-249 m (Figure 4-5b) and are significantly lower over Tasiilaq compared to the other two stations ($p < 10^{-8}$). Inversion intensities (ΔT) are significantly different among all stations, with Ittoqqortoormiit and Tasiilaq exhibiting the highest (ΔT = 2.6°C) and lowest (ΔT = 1.6°C) median values, respectively (Figure 4-5c, $p < 10^{-9}$).

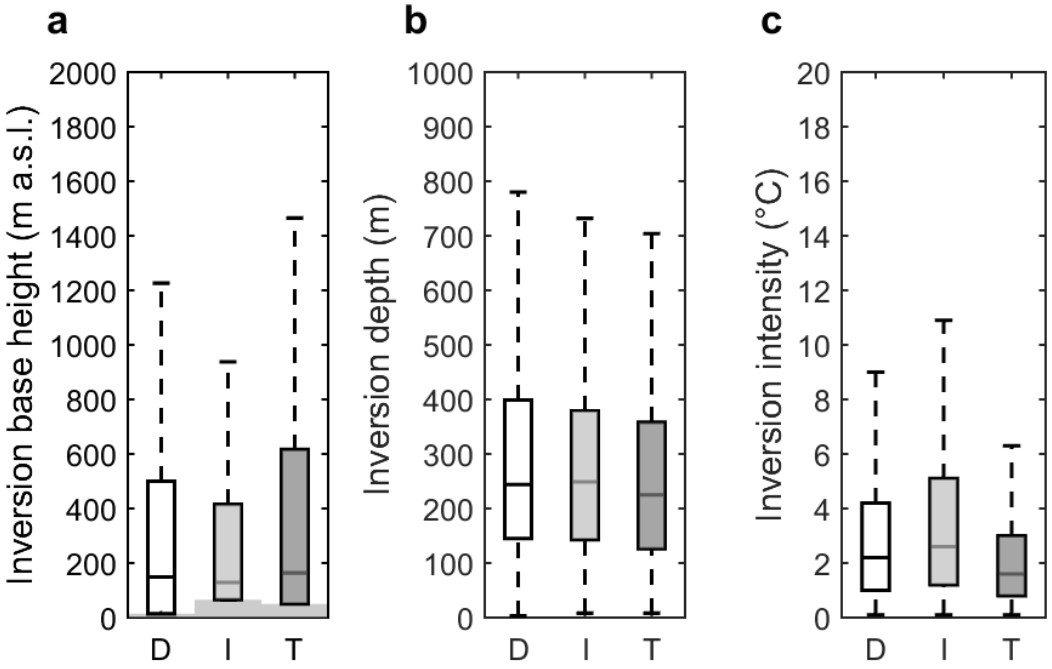

Figure 4-5. Inversion characteristics for summers of 1980-2016 during all weather conditions for Danmarkshavn (D), Ittoqqortoormiit (I) and Tasiilaq (T). Box and whisker plots show the median (horizontal line), lower and upper quartiles (bottom and top of box), and 5th and 95th percentiles (range) for (a) inversion base (Z_{base}), with ground elevation (horizontal light grey shading), (b) inversion depth (ΔZ), and (c) inversion intensity (ΔT).

4.5.1.2 Fog conditions

Real fog cases occur with a lower tropospheric inversion over 99 % of the time, of which 84-86 % exhibit a LLI. Inversion characteristics during real fog, marginal fog, and non-fog conditions are shown in Figure 4-6. These include about 150, 800, and 5000 observations, for each fog condition respectively, at each station. Median Z_{base} elevations during real fog are at 176-200 m a.s.l. (Figure 4-6a). Even though they appear marginally higher under foggy conditions, no significant difference transpires among foggy, non-foggy or marginal fog conditions ($p = 0.05$-0.19), nor among stations. Median ΔZ during marginal and real fog are 335-357 m and similar at all stations, but inversions are significantly deeper during fog conditions than during non-fog conditions (by 111-126 m on average, $p < 10^{-10}$, Figure 4-6b). Median ΔT during real fog conditions is significantly lower at Tasiilaq (3.8°C) than at Danmarkshavn (5.5°C: Figure 4-6c, $p < 10^{-5}$). The median ΔT during real fog is about twice as strong as for marginal fog for Danmarkshavn ($p < 10^{-5}$) and Tasiilaq ($p < 10^{-2}$) and 2-3 times stronger than for non-fog conditions at all stations ($p < 10^{-9}$). The largest differences in ΔT and ΔZ between foggy and non-fog conditions occur at Danmarkshavn.

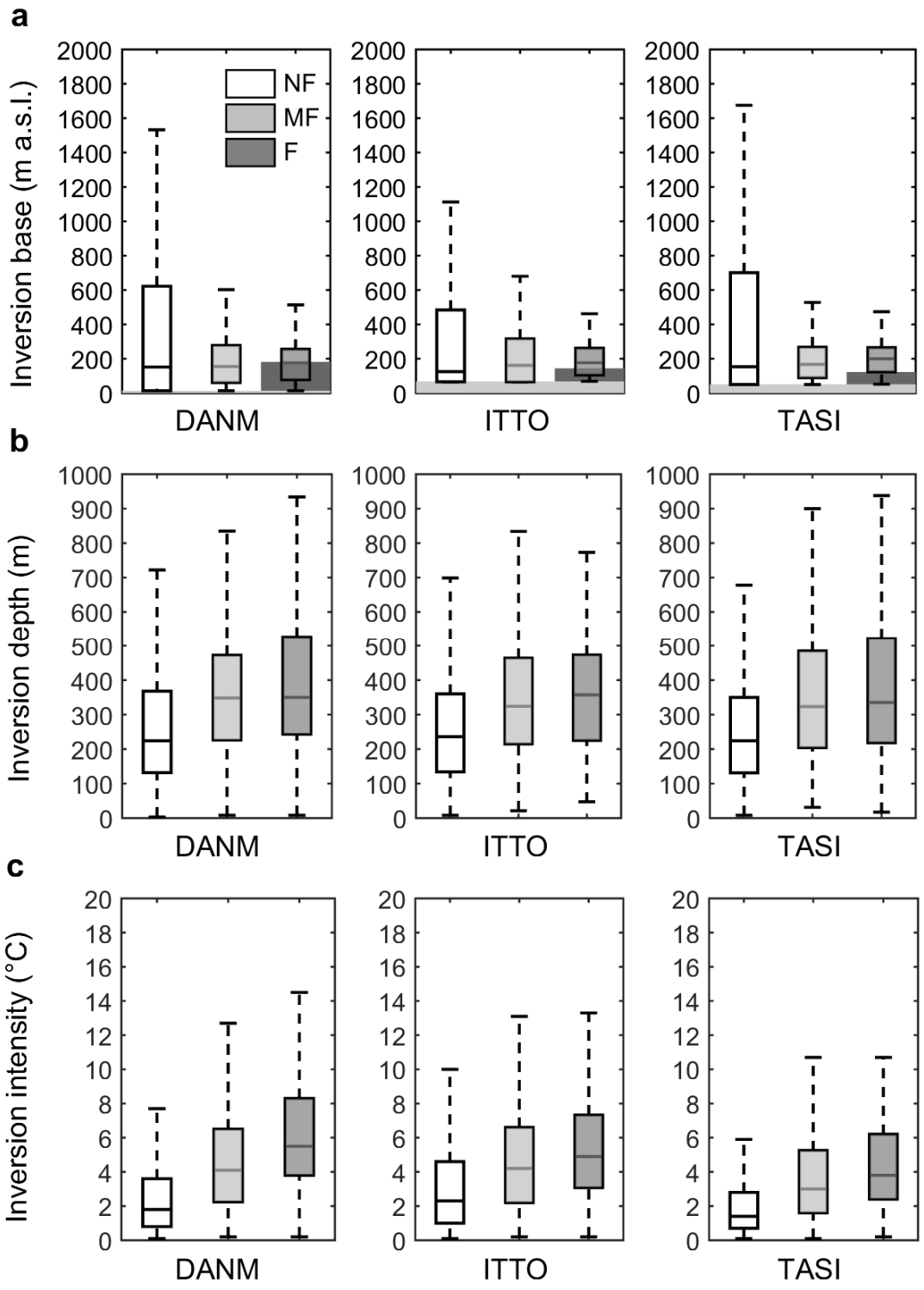

Figure 4-6. Inversion characteristics for summers of 1980-2016 during non-fog (NF), marginal fog (MF), and real fog (F) conditions over Danmarkshavn (DANM), Ittoqqortoormiit (ITTO) and Tasiilaq (TASI). Box and whisker plots for (a) inversion base (Z_{base}), with ground elevation (horizontal light grey shading) and median fog thickness above ground (dark grey shading, see Sect. 4.5.2), (b) inversion depth (ΔZ), and (c) inversion intensity (ΔT).

Inversion characteristics during non-fog conditions under different categories of winds speed (w_s) and cloud cover fraction are presented in Figure 4-7. These statistics include over 1000 observations for all cloud and wind speed categories, except for $w_s > 5$ m s^{-1} at Tasiilaq where n = 279. Only results for non-fog conditions are shown because these results are nearly identical to those for all-weather conditions, and because fog in East Greenland typically occurs at $w_s < 5$ m s^{-1} (see Chapter 2) and fog prevents human observers from making cloud observations. At all stations, Z_{base} is highest under broken-overcast conditions (Figure 4-7a, $p < 10^{-9}$). The median difference ranges from 100-306 m, with the highest inversion base at highest latitudes. At Ittoqqortoormiit and Tasiilaq inversions are weaker during dense cloud cover (median ΔT =0.6°C) than during clear-sky conditions (median ΔT = 1.6°C) ($p < 10^{-9}$), but this difference was not observed at Danmarkshavn (Figure 4-7c). Low w_s were associated with stronger (up to 1.2°C on average, $p < 0.01$, Figure 4-7f) and deeper (30-61 m, $p < 10^{-5}$, Figure 4-7e) inversions over all stations. Increased w_s significantly elevated Z_{base} over both Ittoqqortoormiit and Tasiilaq ($p < 10^{-6}$), but not over Danmarkshavn (Figure 4-7d). These conclusions remain unchanged when grouping w_s into three classes (< 5 m s^{-1}, 5-10 m s^{-1}, ≥ 10 m s^{-1}, not shown) instead of the two shown in Figure 4-7 d-f. During fog, however, inversion characteristics do not differ between low or high w_s conditions (not shown). Biases in this statistical analysis may exist due to the unequal sample sizes between the two distributions because w_s above 5 m s^{-1} are not common during fog (see Chapter 2).

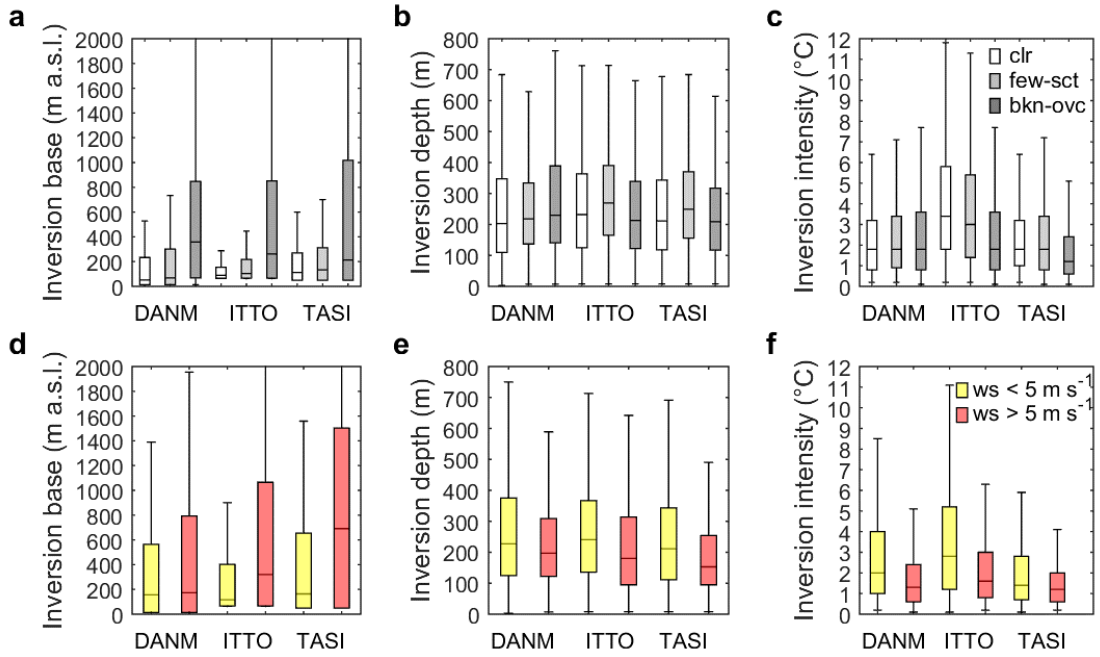

Figure 4-7. Box and whisker plots for Z_{base}, ΔZ and ΔT during non-fog weather conditions for (a-c) cloud cover classes ("clr": clear sky, "few-sct": few and scattered clouds, "bkn-ovc": broken and overcast), and (d-f) wind speed categories (ws).

In order to investigate the stability across the inversion layer as well as the interactions between fog and the inversion, temperature inversion slopes were normalised for all non-fog and real fog cases (Figure 4-8). Theoretically, two endmembers of normalised inversion slopes are concave-up and concave-down shapes. For the case of a concave-down shape, the largest increase of temperature is near the inversion top, whereas for a concave-up shape, it is near the inversion bottom. For the latter, the bottom of the inversion has stronger reverse lapse rates. Even though there is variability in the shape of the inversion structure, inversions have significantly ($p < 0.01$) more often concave-up profiles under fog conditions (61-65 %) compared to non-fog conditions (31-40 %), during which linear and concave-up profiles evenly dominate. This analysis was also performed on clear-sky conditions (not shown), of which the results are similar to non-fog conditions. The general shape of these normalised inversion profiles during fog are

consistent with results obtained by Sedlar et al. (2012) for summer Arctic stratocumulus clouds over the Arctic Ocean. The highest temperature increase occurs below a normalised height of 0.3 for both fog (this study) and stratocumulus clouds (Sedlar et al., 2012).

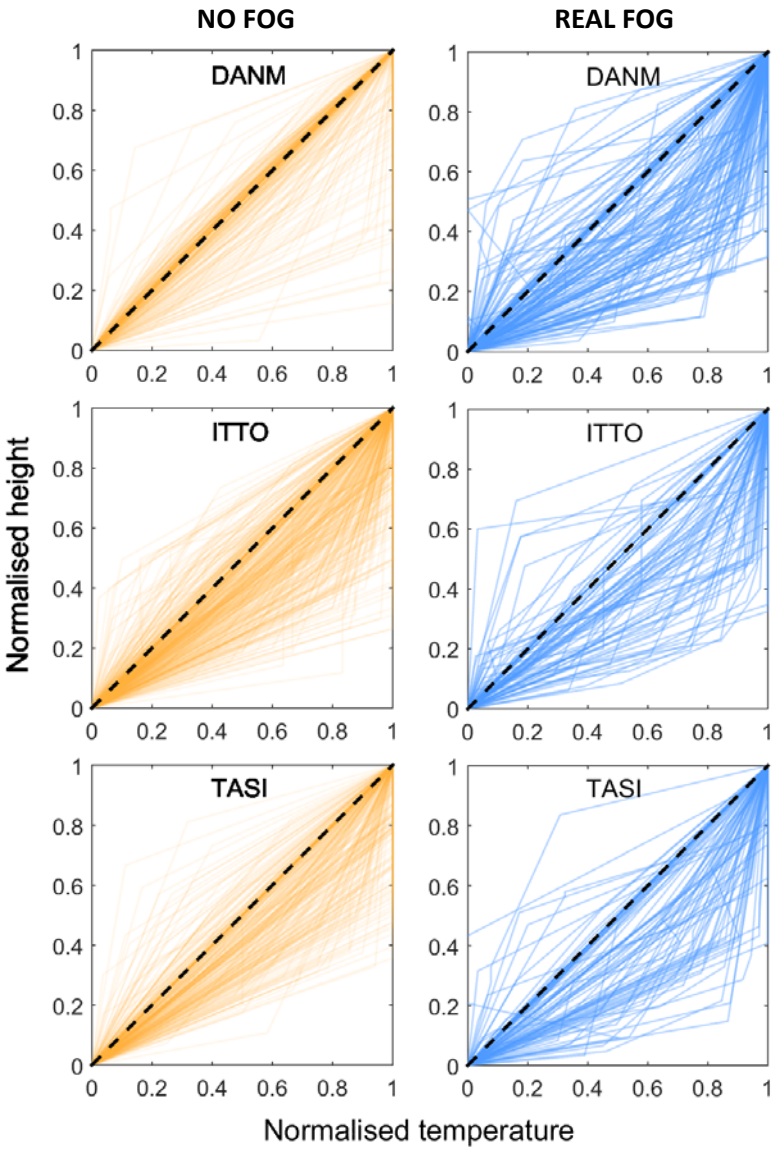

Figure 4-8. Normalised height as a function of normalised temperature across the temperature inversion for no fog events (left) and real fog events (right), over Danmarkshavn (DANM), Ittoqqortoormiit (ITTO) and Tasiilaq (TASI).

4.5.2 Fog top elevation and the inversion layer

Figure 4-9 displays fog top elevation (*FTE*) and median Z_{base} and Z_{top} distributions during fog. Median summer-averaged *FTE* are at 123, 145 and 182 m a.s.l. over Tasiilaq, Ittoqqortoormiit and Danmarkshavn, respectively. Fog thickness (*FTE* minus station elevation) over Danmarkshavn significantly differs from the other two sites ($p < 0.01$). However, *FTE* does not differ among stations. Danmarkshavn is also characterised by significant differences between early (May-June) and late (July-August) melt season ($p = 0.0031$), with a median late melt season *FTE* at 220 m a.s.l. (not shown). At Danmarkshavn, median summer-averaged *FTE* extends slightly above the median Z_{base}; in the late melt season, fog penetrates the inversion layer by on average 47 meters. In contrast, the median *FTE* is below the median Z_{base} at Ittoqqortoormiit and Tasiilaq. This coincides with classification results and inferred processes presented in Chapter 3, in which fog in Southeast Greenland was mostly located below the inversion layer and fog in Northeast Greenland frequently penetrated the inversion layer.

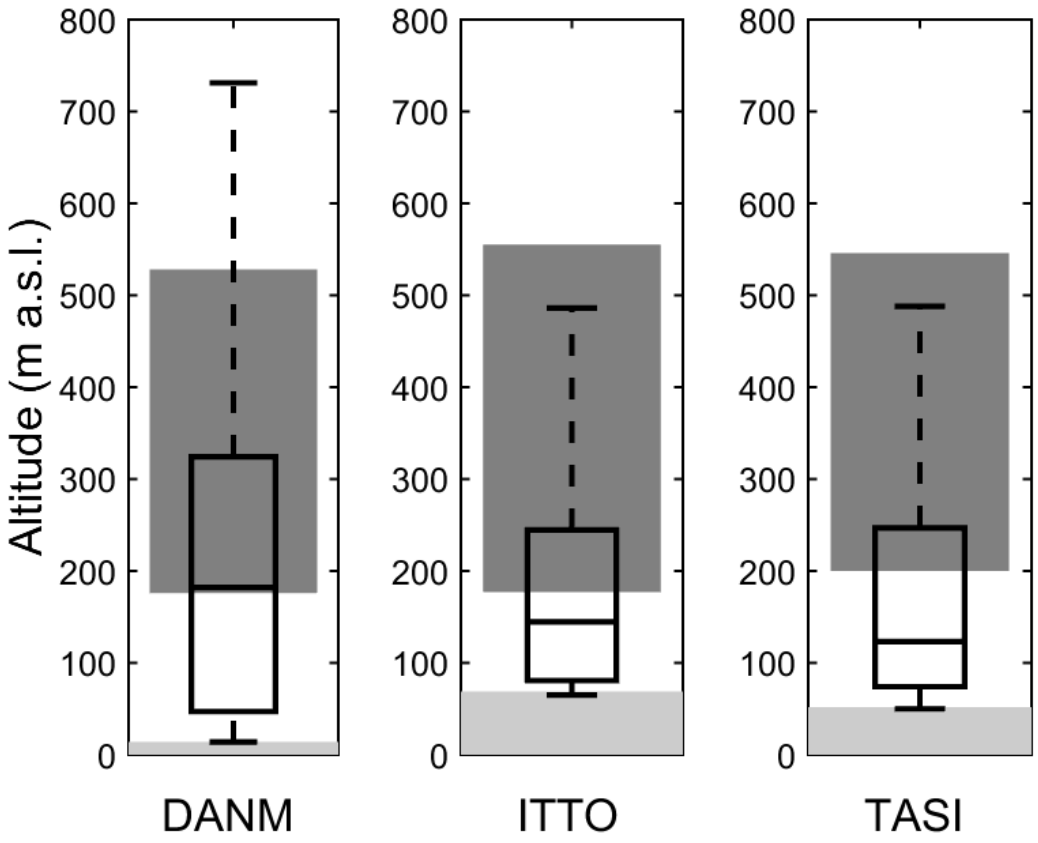

Figure 4-9. Fog top elevation (box and whisker plots) and median inversion layer (dark grey shading) over Danmarkshavn (DANM, n = 175), Ittoqqortoormiit (ITTO, n = 105) and Tasiilaq (TASI, n = 111) for summers of 1980-2016. The light grey shading is the ground elevation.

4.6 Discussion

4.6.1 Sensitivity analysis of fog top elevation calculation

The Dew point Depression Method (DDM) presented in this paper uses a dew point depression (T_{dd}) threshold of 1°C to determine air parcel saturation and the presence of fog. This T_{dd} threshold value was selected because it is most commonly used in literature (e.g. Meyer and Rao, 1999; Kim and Yum, 2010; Koračin et al., 2014) and because it captured the vast majority of real fog observations from radiosondes over East Greenland (see Sect. 4.4.2.2 and Chapter 3 Fig. 3-2). It is smaller than T_{dd} values traditionally used

for cloud detection at subzero temperatures (Poore et al., 1995). This section presents comparative analyses for *FTE* calculations made with: i) the Mixing Ratio Method (MRM: US Bureau of Naval Personnel, 1965) to test the validity of the DDM, and ii) a range of T_{dd} threshold values to test the sensitivity and robustness of the DDM.

The MRM does not explicitly require knowledge of T_{dd} because it is meant to be applicable to radiation fog with a SBI. However, knowledge of the saturation at Z_{base} is necessary to apply this method to fog with a LLI. The comparison between the DDM and the MRM was therefore performed using three T_{dd} thresholds (0.5°C; 1°C; 1.5°C), and on soundings with at least two saturated sounding levels ($T_{dd} \leq T_{dd}$ threshold) or with one saturated level and a positive dew point temperature gradient immediately above that level. Results for Danmarkshavn are displayed in Figure 4-10a. There is a systematic tendency of the DDM to lead to higher *FTE* values compared to the MRM (13-20 m higher on average). This difference appears more pronounced at higher T_{dd} thresholds. However, differences were not statistically significant at the 95 % confidence level and, moreover, are lower than the vertical precision of the calculated geopotential height (25 m). DDM and MRM therefore give consistent results for most fog cases. However, it is unsure how accurate either method is for *FTE* calculation of thin fog (< 100 m a.g.l.). High-resolution radiosondes can detect features that are at least 10 m thick, such as shallow fog, but lower-resolution radiosondes have limited capability to detect fog or clouds thinner than a few tens of meters (Zhang et al., 2010; Dorman et al., 2017). Some observations of thin fog in this analysis over East Greenland were assigned a fog thickness < 5 m, which is lower than the derived accuracy for geopotential height.

Moreover, DMI reported invisible sky at the time of these observations, suggesting an underestimation of the calculated *FTE* for fog thinner than 100 m.

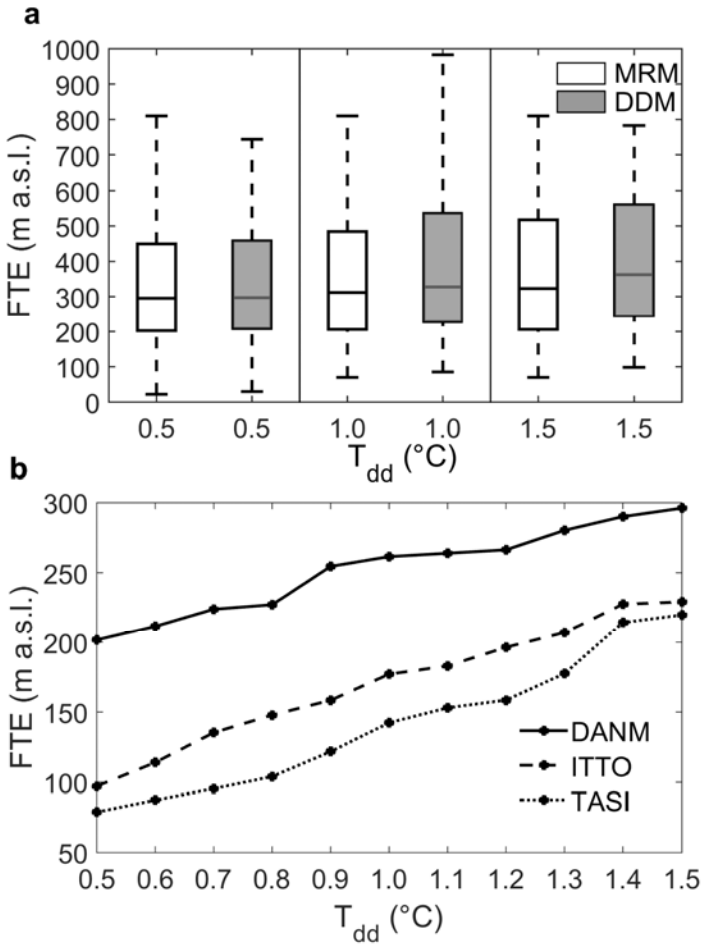

Figure 4-10. (a) Statistics of fog top elevation (*FTE*) retrieved from IGRA files over Danmarkshavn with the Mixing Ratio Method (MRM: US Bureau of Naval Personnel, 1965) and the Dew point Depression Method (DMD: this study) for three dew point depression (T_{dd}) thresholds (n = 72); (b) Median *FTE* over Danmarkshavn (DANM), Ittoqqortoormiit (ITTO) and Tasiilaq (TASI) as a function of T_{dd} threshold (DDM; n = 115, 74, 94). Standard deviations in (b) are 165-734 m, which is on the lower range of standard deviations in (a).

The sensitivity of the DDM to varying dew point depression (T_{dd}) thresholds was analysed for T_{dd} ranging from 0.5°C to 1.5°C, and for soundings with a surface $T_{dds} \leq$ 0.5°C (Figure 4-10b). Results show that *FTE* increases with a larger T_{dd} threshold, where differences between medians are 30-80 m when the T_{dd} threshold is changed by only 0.5°C (which is also the uncertainty in *T* measurements: Table 4-2). The average error

induced by the choice of T_{dd} threshold is therefore approximately 50 m. Together with the uncertainty in the calculated geopotential height (25 m), this represents an estimated cumulative error in calculated *FTE* of $\sqrt{50^2 + 25^2}$ = 56 m.

Under any T_{dd} threshold, Danmarkshavn always has the highest *FTE* values, followed by Ittoqqortoormiit and Tasiilaq (Figure 4-10b). The choice of the T_{dd} threshold therefore does not change the conclusions of this study, but the uncertainties due to the choice of the T_{dd} threshold are larger where median *FTE* is lower. This can be explained by the fact that shallow fog is usually determined by only one saturated sounding level. *FTE* may also be underestimated when hydrostatic balance terms (convection) are neglected at the local scale, particularly for cases of fog below the inversion layer. However, the large differences in *FTE* indicate that the choice of an accurate T_{dd} threshold is crucial for precise *FTE* calculation.

4.6.2 Comparison of fog top elevation with CALIPSO-derived cloud top elevation

Out of 149 CALIPSO tracks over Ittoqqortoormiit and 146 tracks over Danmarkshavn between May and October 2006-2016, a total of four fog and six low stratus cases were identified for comparison between IGRA and CALIPSO datasets (Table 4-3). For three of these cases, both measured and calculated *Z* from IGRA were available and are within a 3-m range of each other. This suggests that calculated *Z* can reliably be used for *FTE* calculations. The cumulative error in vertical accuracy of CALIPSO and IGRA is $\sqrt{30^2 + 25^2}$ = 39 m. Despite the various time lags and geographical distances between IGRA and CALIPSO, four cases (# 1, 4, 5, 8) have cloud top elevation values within the

cumulative error range, or for very thick fog within 10 % (# 4), and in addition have the same number of cloud layers (good agreement). For cases # 2, 3, 6, 7 and 9, both methods identify the low cloud layer, although CALIPSO reports significantly lower cloud top elevations (by 60-589 m), which in some cases may be due to spatial variability in the fog or cloud layers (reasonable agreement). In only one case (# 10), CALIPSO does not report the lower cloud layer detected by IGRA, which could be attributed to the attenuation of the signal by optically thick clouds aloft (Mace and Zhang, 2014).

Overall, in spite of the spatial and temporal differences between CALIPSO and IGRA, *FTE* from IGRA via the DDM is in reasonable to good agreement with CALIPSO retrievals for vertically extensive fog and low stratus, under T_{dd} threshold = 1°C. However, CALIPSO's vertical resolution of 30 m and the considerable distance between the IGRA station and nearest CALIPSO track line points prevent us from reliably verifying the DDM method results for shallow fog thickness (< 100 m a.g.l.), or to determine which method (DDM vs. MRM) is the most accurate to calculate *FTE* from radiosondes. The good agreement between cloud top elevation from CALIPSO and IGRA, via both the MRM and the DDM under the 1°C T_{dd} threshold, is encouraging. Both the DDM and the MRM are therefore more suitable over Arctic locations compared to methods using higher T_{dd} thresholds (Poore et al., 1995) or relative humidity thresholds (Wang and Rossow, 1995; Wang et al., 1999; Zhang et al., 2010). Also, interpolation methods used in MRM or DDM are more accurate than using the half the distance between saturated and subsaturated sounding levels as the cloud boundary (Wang and Rossow, 1995). Still, we suggest to use the DDM instead of the MRM because the DDM can be applied to any fog thermodynamic profile.

Table 4-3. Comparison of CALIPSO and IGRA low stratiform cloud top heights derived using the DDM.

Date[a]	CALIPSO[b] cloud top height (m a.s.l.)	IGRA cloud top range from calculated *Z*[c] (m a.s.l.)	IGRA cloud top range from measured *Z*[c] (m a.s.l.)	IGRA Inversion base height (m a.s.l.)	DMI ww 11UTC	DMI ww 12UTC	DMI/IGRA Cloud type[d]
			Danmarkshavn				
20/05/2016 (1)	NA 411* 352* 382*	411-426*	NA	411	110	100	Stratus with mist
05/08/2009 (2)	- 113* - -	173-180*	170-177	38	34	30	Fog
			Ittoqqortoormiit				
03/07/2007 (3)	178* 148* -	737*	739	737	NA	NA	Stratus
05/07/2008 (4)	1190** 1190** 2747**	1044-1095*	NA	618	NA	NA	Stratus
07/09/2008 (5)	1100* 1071* 1131*	964-1013*	NA	640	NA	NA	Fog
12/10/2009 (6)	1160** 1101** 1131*	1351-1355**	NA	1351	NA	NA	Stratus
27/07/2010 (7)	232** 262* -	409-412*	NA	351	NA	0	Stratus
27/05/2011 (8)	352* 382* 412*	449-471*	NA	449	80	0	Stratus
31/08/2011 (9)	1160** 1190** 1190**	1363**	1364	990	34	33	Fog
20/04/2015 (10)	4663* 4693* 4693*	454-457**	NA	395	110	131	Stratus and fog

[a]Observation time IGRA 1200 UTC; CALIPSO 1230 UTC (Danmarkshavn) or 1330 UTC (Ittoqqortoormiit); [b]CALIPSO data retrieved from three or four grid points (Figure 4-4). NA is no data; - is no cloud top height detected. [*]one cloud layer, [**]two cloud layers. [c]*Z* is the geopotential height. [d]Cloud type from DMI (surface) and IGRA profiles (aloft).

4.6.3 Temperature inversion characteristics comparison and interpretation

4.6.3.1 All-weather conditions

Results from this study show that temperature inversions were frequent (> 85 %) and mostly elevated over East Greenland during the melt season. Overall, the frequency of temperature inversions over East Greenland compares well with the inversion frequency measured with similar melt-season low-resolution radiosonde data over the Arctic Ocean and the Russian Arctic (> 85 %: Serreze et al., 1992; Kahl et al., 1996), but is generally higher than over Arctic coastal sites in Canada, Eurasia and Alaska, where inversions occur in > 60 % of soundings (Kahl, 1990; Kahl et al., 1992; Serreze et al., 1992). The inversion frequency reported over Tasiilaq is the same as obtained by Mernild and Liston (2010) from field measurements over summers 2005-2006 on a valley glacier within 25 km of that station. These comparisons suggest that post-1980 IGRA sounding significant levels are able to accurately capture the frequency of low-tropospheric temperature inversions at Tasiilaq.

IGRA data experienced an increase in vertical resolution through time because of major instrument changes and relocations (Antikainen et al., 2002; Durre and Yin, 2008). While only the post-1992 period is considered to be sufficiently accurate for longitudinal analysis of inversions depth over Greenland (Box and Cohen, 2006), Zhang et al. (2011) found that inversion depth and intensity records are also inhomogenous within that period. Since our study is not focused on trend analysis, we do not perform a full homogeneity test, but instead investigate whether the post-1992 change in vertical accuracy impacts statistics of inversion characteristics, and whether there are step-wise

changes in number of IGRA significant levels over time. For this purpose, we first extracted inversion characteristics for the post-1992 period separately and tested for considerable differences with the results from the 1980-2016 time period (Table 4-4). Inversion intensities (ΔT) were exactly the same over the two periods, while differences in inversion base elevations (Z_{base}) and inversion depths (ΔZ) were minimal (1-19 m and 14-19 m, respectively), with a slight tendency towards higher values in the 1980-2016 dataset. We therefore conclude that including the 1980-1992 time period does not affect the overall results of this study. In addition, we checked for step-wise changes in the number of IGRA significant levels for all stations for the entire IGRA record by plotting a time series of the average monthly number of levels below the 500 hPa pressure level between 1950-2016 (Appendix 6). This approach is consistent with the pan-Arctic analysis of IGRA data inhomogeneities by Zhang and Seidel (2011). Only two sudden increases in the IGRA data over Danmarkshavn are apparent (around 1984 and 2012), so that the majority of the period of record 1980-2016 is homogeneous in terms of number of levels. Despite these inhomogeneities, neither the statistics of inversion frequency were affected (cf. Zhang et al., 2011) nor should they have significantly impacted our median values of inversion characteristics. We therefore proceed with a comparison with other Arctic regions.

Table 4-4. Median inversion base elevation (Z_{base}), inversion depth (ΔZ) and inversion intensity (ΔT) over the period 1980-2016 and 1992-2016 for Danmarkshavn (DANM), Ittoqqortoormiit (ITTO) and Tasiilaq (TASI).

	1980-2016	1992-2016
DANM		
Z_{base} (m a.s.l.)	149	130
ΔZ (m)	244	225
ΔT (°C)	2.2	2.2
ITTO		
Z_{base} (m a.s.l.)	129	123
ΔZ (m)	249	235
ΔT (°C)	2.6	2.6
TASI		
Z_{base} (m a.s.l.)	164	163
ΔZ (m)	225	211
ΔT (°C)	1.6	1.6

Z_{base} over East Greenland are within the lower range of values reported over Alaskan sites (50-300 m a.g.l.: Kahl, 1990), but are much lower than those reported for the Canadian Arctic where the range is 100-400 m a.g.l. (Kahl et al., 1992). Inversion top elevations (Z_{top}) are higher than values measured by Mernild and Liston (2010) near Tasiilaq (500 vs. 300 m a.s.l.). Similar to what Zhang et al. (2011) found for annual SBIs, ΔZ for all summer low-level inversions (SBIs and LLIs) are lower over Southeast Greenland compared to Northeast Greenland. Contrary to the hypothesis of Kahl et al. (1992), cloud cover fraction does not impact ΔZ in coastal East Greenland. ΔZ values are similar to those measured over the Arctic Ocean (150-350 m: Sotiropoulou et al., 2016), but are shallower than over Eurasian/Russian (250-350 m: Serreze et al., 1992), Alaskan (300-500 m: Kahl, 1990) and most of the Canadian Arctic sites (200-500 m: Kahl et al., 1992).

Results for ΔT are consistent with results obtained by Zhang et al. (2011) over East Greenland for SBIs, with Danmarkshavn having stronger inversions than Tasiilaq. In

addition, we highlight that Ittoqqortoormiit is characterised by even stronger inversions, which may be due to the proximity of the cold waters of the Scoresby Sund (Sandel and Sandel, 1991). ΔT over East Greenland is similar to inversion strength in Arctic Canada (1-3°C: Kahl et al., 1992) and the Eurasian-Russian coastal Arctic regions (2-3°C: Serreze et al., 1992), and in the lower range of values measured over the Arctic Ocean (2-4°C: Sotiropoulou et al., 2016). However, ΔT is 2-3 times weaker than for Alaskan Arctic sites (4-7°C: Kahl, 1990). The lack of influence of cloud cover on ΔT over Danmarkshavn compared to the more southern stations could be due to regional differences in cloud properties. The weather in northern Greenland is dominated by local environmental conditions, such as sea ice and sea breeze, resulting in the dominance of fog and low-level clouds, whereas in southern Greenland optically thicker higher-level clouds dominate (Van Tricht et al., 2016). Further studies would be needed to assess the impact of low-level clouds on inversion characteristics over that region.

4.6.3.2 Fog conditions

The frequency of soundings analysed corresponding to marginal and real fog conditions is comparable to the overall reported frequency of fog occurrence over East Greenland, reaching 20 % in July (Cappelen, 2015; Chapter 2). This suggests that the presented analysis captures a representative proportion of fog conditions.

Fog over East Greenland is commonly 200 m thick, which is comparable to geometrical thicknesses reported for Arctic advection fog over the pack ice (Sotiropoulou et al., 2014; Tjernström et al., 2015; Sotiropoulou et al., 2016) and Antarctic coastal advection fog

(Gajananda et al., 2007). Extreme fog events can reach an elevation of up to 700 m a.s.l., which is comparable to cases of mid-latitude marine fog (Gao et al., 2007; Huang et al., 2015; Liu et al., 2016). At higher latitudes and during the late melt season, fog over East Greenland frequently resides inside the inversion layer (see also Chapter 3). This corroborates observations from Sotiropoulou et al. (2016) of fog often extending above Z_{base} over melting ice surfaces, related to warm and moist advection (Sedlar et al., 2012).

The presence of both fog and higher clouds tends to be associated with an elevated Z_{base}. However, fog and clouds have a contrasting effect on ΔT: while clouds generally weaken the inversion due to increased downward longwave radiation (e.g. Kahl, 1990), fog is associated with stronger inversions compared to fog-free conditions. Median ΔT were similar whether fog was below, capped or inside the inversion layer. This suggests that there is an environmental control on lower-tropospheric stability conditions, which in turn favours fog formation. Fog tends to be associated with more stable conditions because inversions efficiently trap moisture (e.g. Miller et al., 2013). High ΔT during fog can also be due to very low w_s, which is in itself associated with stronger inversions (Figure 4-7f). Similarly, the deeper inversions encountered during fog could be the result of calm conditions that allow the inversion to develop and settle.

The apparent latitudinal gradient in ΔT during fog conditions can be due to regional or local differences in atmospheric conditions. Danmarkshavn is characterised by the presence of sea ice throughout most of the summer and therefore under the influence of distinct local boundary-layer processes compared to the other two stations (see also Figure 4-1). The strong thermal gradient between the cold ocean and a warmer land

surface creates stronger and more frequent sea breezes associated with fog at Danmarkshavn (c.f. Chapter 2 Fig. 2-19). This could promote the occurrence of fog under very strong capping inversions (Miller et al., 2013, Koshiro and Shiotani, 2014). In addition, enhanced stability conditions are prevalent over the ice sheet because of radiative losses from the surface in all seasons (Steffen and Box, 2001). The presence of a high pressure ridge over Northeast and central Greenland could also contribute to establishing a strong capping inversion by subsidence processes (Ohmura and Reeh, 1991). The higher ΔT over Danmarkshavn during fog may therefore be related to a combination of local and regional-scale environmental factors that could promote fog formation.

Under clear-sky conditions both concave-up and linear normalised inversion slopes were observed, while when fog was present profiles showed a more pronounced and more frequent concavity (Figure 4-8). Concave-up inversion slopes often occur because the lower part of the inversion is where heat losses are highest (e.g. Oke 1987). Differential warm air advection, where the advection rate increases with height, can also result in concave-up inversion profiles. Processes, such as subsidence, can create a more linear profile (Triplet and Roche, 1986). Sedlar et al. (2012) theorised that vertical motion of air parcels with differential temperatures could straighten an initially concave-up profile when there is strong cloud top cooling near the inversion base. However, linear inversion slopes might also be due to the lack of significant sounding levels to capture the inversion concavity. Fog profiles might more often have sounding levels inside the inversion, especially for fog cases penetrating the inversion since a significant level is required to indicate the discontinuity in humidity profile (or fog top). This could contribute to the

highest proportion of concave-up profiles under fog compared to non-fog conditions. Aside from this potential bias in measurements, more frequent and enhanced concave-up profiles can reasonably be expected under most fog conditions because of the intense cooling rate of the fog layer and the warm air advection associated with fog (Sedlar et al., 2012). We could not investigate whether humidity inversions were coincident with concave-up profiles during fog, as observed by Sedlar et al. (2102) for cloud cases penetrating the inversion layer and associated with warm and moist advection, because of the coarse vertical resolution of the IGRA data. The level of highest cooling rate depends on the distribution of liquid water content (*LWC*) inside the cloud layer. In the case of a mature fog, the highest *LWC* values, hence the highest cooling rates, are expected to occur at or near the fog top (Roach et al., 1976; Kim and Yum, 2017), which also generally corresponds to Z_{base}. This leads to an enhanced concavity of the inversion profile. Other factors such as a more intense sea breeze and/or warm air advection aloft during fog could also promote a more concave-up inversion profile. However, a detailed analysis of process interpretation related to the inversion shape requires knowledge of emissivity profiles, related to the amount of condensated water, and the optical thickness of the fog layer. With the available data, we cannot conclude whether the enhanced concavity during fog is due to environmental conditions, denotes an effect of fog on the inversion or is simply due to an instrumental bias. This could be explored in future studies through the combined analysis of high-resolution radiosonde data and *LWC* profiles.

4.6.3.3 Potential impacts of inversions and fog on glacier melt

The comparison between glacier hypsometry and fog macrophysical characteristics reveals that fog of the most common thickness (median *FTE* ~150 m a.s.l.) covers only 2 % of the total glacier ablation area. However, vertically extensive fog (*FTE* ~ 600 m a.s.l.) can cover up to 30 % of it (~ 540 km^2). Inversions, which are both more frequent and more vertically extensive than fog, can affect ~15-100 % of the ablation area in this region (median Z_{top} ~ 500 m a.s.l.; maximum Z_{top} ~ 1000 m a.s.l. See Appendix 7).

The conventional use of a constant negative temperature lapse rate in temperature index melt models (e.g. Braithwaite, 1995; Hock, 2003; Braithwaite and Raper, 2007), even if smaller than the moist adiabatic lapse rate (6.58°C km^{-1}, Gardner et al., 2009), can introduce large errors in temperature and precipitation calculations (Braun and Hock, 2004; Braithwaite et al., 2006). Small lapse rates are a known feature over Arctic glaciers and impact calculated melt rates at higher elevations (Marshall et al., 2007; Hulth et al., 2010). Even though different values of constant negative lapse rates have been tested and implemented in both temperature index models (e.g. Huss et al., 2008; Gardner et al., 2009) and glacier surface energy balance models (e.g. Braun and Hock, 2004; Hock and Holmgren, 2005), these models rarely incorporate a variable or positive lapse rate to account for the effect of temperature inversions and low-level clouds. Gardner and Sharp (2009) showed that the use of a daily variable lapse rate strongly improved melt calculations. Accounting for this effect is not only important for glaciers (Mernild and Liston, 2010), but also for ice sheet modeling where inversions are frequently observed during the melt season (Hudson and Brandt, 2005; Miller et al., 2013). Results from the

work presented here provide a first approximation of regional inverse lapse rate strengths, elevations and depths, as well as fog top elevation, based on long-term observations in East Greenland. With the automated methods developed here this could be expanded to calculate these properties from pan-Arctic IGRA data, and thus provide more realistic input for regional glacier mass balance models (e.g. Giesen et al., 2016).

4.7 Summary and conclusions

In this chapter statistics for melt season inversion characteristics under foggy, non-foggy and all weather conditions in the period 1980-2016 over three East Greenland coastal sites were presented, based on the combined analysis of surface synoptic weather data and twice-daily upper-air observations from the Integrated Global Radiosonde Archive (IGRA). Moreover, a novel and robust method to retrieve predominantly liquid or supercooled fog geometrical thickness from low-resolution IGRA radiosondes over Arctic locations was introduced and tested.

Over East Greenland, inversions occur in > 85 % of summer soundings and are generally elevated (150 m a.s.l.) with a median inversion depth of 240 m and an inversion strength of 2°C. These characteristics are similar to those measured over the Arctic Ocean (Serreze et al., 1992; Sotiropoulou et al., 2016), but inversions in East Greenland are generally more frequent, lower and shallower compared to other coastal Arctic locations (Kahl, 1990; Kahl et al., 1992; Serreze et al., 1992). Inversion intensities over East Greenland are similar to values reported over other Arctic sites, except over coastal Alaska (Kahl, 1990). The similarity in inversion characteristics between East Greenland and the Arctic

Ocean suggests that, during the melt season, similar local environmental conditions, such as open water, sea ice or warm air advection, influence the structure of the boundary layer over these regions.

Retrieved fog top elevation is commonly 150-200 m a.s.l. but can reach an altitude of 700 m a.s.l., and frequently penetrates the elevated inversion layer over coastal regions during the late melt season. Compared to non-fog conditions, fog occurs under stronger, deeper and more concave-up inversions. Low wind speed could in part explain these differences. During fog, inversions are stronger at higher latitudes and we hypothesise that these regional differences are due to a combination of distinct boundary-layer and large-scale processes favouring fog formation. Fog top elevation calculated with the Dew point Depression Method (DDM) and retrieved from CALIPSO cloud top product were in reasonable agreement, despite the minor retrieval time lags and geographical distances between the measurement locations of these datasets. These results are encouraging, and suggest that fog top elevation for vertically extensive fog (> 100 m) can be estimated reliably by IGRA's low resolution soundings with a dew point depression threshold of 1°C. However, changing this threshold by only ± 0.5°C changes the median fog top elevation by 30 to 80 m, leading to a cumulative error of 56 m due to the choice of dew point depression threshold. Despite these uncertainties, the DDM is more suitable to retrieve fog top elevation over Arctic locations compared to other cloud detection methods using higher dew point depression or relative humidity thresholds from low-resolution radiosondes (Poore et al., 1995; Wang and Rossow, 1995; Wang et al., 1999). The DDM is also preferable compared to the Mixing Ratio Method (MRM: US Bureau of

Naval Personnel, 1965) since it allows calculation of fog top elevation on any fog thermodynamic profile.

The sensitivity of the radiosonde sensors used, measurement practices and environmental conditions at the stations (e.g. season and air temperature) could all impact dew point depression during fog. Over Arctic locations, we therefore recommend to calibrate the dew point depression threshold relative to surface observations (see Chapter 3 Fig. 3-2) to avoid underestimation (dew point depression threshold too low) or overestimation of fog top elevation (dew point depression threshold too high). The required calibration of dew point depression threshold on surface observations is the strength of this method since it has the potential to be applicable to any remote coastal Arctic (or Antarctic) WMO location where present weather, visibility and upper-air measurements exist together. However, it may have limited capability in calculating fog top elevation of thin fog (< 100 m). In future studies, a comparison between fog top elevations calculated from both low- and high-resolution radiosondes, with the ability to detect fog thicker than 10 m (Dorman et al., 2017), could be applied to firmly validate the presented DDM methodology. This includes determining which dew point depression threshold is the most appropriate, what minimum thickness of fog/cloud can be captured, evaluate whether inversion concavity is systematically detected, and assess whether IGRA low-resolution radiosonde data can be used for fog nowcasting and forecasting. Once established, the DDM could additionally be used to detect cloud base and top elevation from other Arctic boundary-layer clouds. The retrieved geometrical thickness, in conjunction with the analysis of temperature inversion characteristics, would allow a full investigation and quantification of the relationship between Arctic low clouds and

inversions. These results would contribute to a deeper understanding of low-level liquid-bearing Arctic stratiform clouds macrophysics, which will eventually serve in Arctic surface energy balance and numerical climate models.

Fog and temperature inversions can potentially cover a significant portion of glacier ablation area in central East Greenland. These results point towards the importance of incorporating the effect of both fog and variable lapse rates in glacier and ice sheet melt models and in the downscaling of temperature data for input in such models (e.g. Marshall et al., 2007). Hulth et al. (2010) previously suggested that radiosondes could be useful tools for determining melt at higher elevations. We recommend the use of radiosonde data for both the quantification of temperature and humidity lapse rates, and for the detection of fog and low-level cloud over glaciers. If a similar baseline climatology of temperature inversions during fog and non-fog conditions is obtained over any other Arctic location through the method presented in this chapter, an independent fog detection method (e.g. time-lapse camera, visibility sensor or present weather sensor) could be used as a proxy for the inversion structure and characteristics over glacierized areas. This information should refine glacier-wide calculation of radiation and turbulent heat fluxes. We suggest that accounting for differences in inversion characteristics during fog conditions will improve glacier melt estimates in coastal Arctic regions where fog and temperature inversions are frequent. Further research, including extensive field measurements of fog microphysics over glaciers, is needed to accurately quantify and model the radiative effect of fog and low clouds on glacier and ice sheet surface energy balance.

CHAPTER 5. SUMMARY AND CONCLUSIONS

5.1 Summary

In this thesis, a climatology of Arctic coastal fog, its macrophysical properties, and its interaction with tropospheric temperature inversions were presented. Fog and inversions were analysed using a combination of long-term records from present weather observations (1958-2016) and low-resolution radiosonde profiles (1980-2016) at four standard World Meteorological Organization synoptic weather stations operated by the Danish Meteorological Institute in coastal East Greenland. These stations are, from north to south, Danmarkshavn, Ittoqqortoormiit, Tasiilaq, and Prins Christian Sund.

In Chapter 2 it was demonstrated that fog in East Greenland mainly takes place during the Arctic melt season, when it can occur up to 20 % of the time. Fog onset usually coincides with the timing of sea ice break-up at the start of the melt season. Overall, summer (May-Aug) fog in East Greenland is associated with the advection of marine warm air masses over melting sea ice. This summer fog is predominantly in the liquid or supercooled phase, with temperatures around 0°C, relative humidity > 93 % and visibility < 500 m. At northernmost latitudes, fog is characterised by lower temperatures and relative humidity, higher visibility ranges, and lower sensitivity to the solar diurnal cycle, which is hypothesised to result from a combination of latitudinal effects and sustained sea breeze between the ice-covered northern ocean and the snow-free land.

In Chapter 3, thermodynamic profiles corresponding to fog conditions were retrieved and classified from the Integrated Global Radiosonde Archive (IGRA) into six distinct thermodynamic classes using a novel automated method developed for this purpose. This method is based on conditions including surface saturation, stability, inversion type and fog top height relative to inversion base height. Aided with the analysis of time-lapse imagery, air mass back-trajectories and high-resolution radiosonde profiles from the Arctic field campaign ASCOS (Tjernström et al., 2014), the six distinct thermodynamic characteristics are hypothesised to correspond to predominantly advection fog in a variety of formation, dissipation and mature stages. Consequently, radiosondes captured a majority of fog in the mature stage at High-Arctic locations, whereas fog was more often dissipating in the South. From this analysis it was also observed that summer fog at coastal East Greenland locations mainly occurs in the presence of low tropospheric inversions with an elevated base overlying an unstable surface layer. Regional differences were highlighted, with fog restricted to the mixed-layer at low latitudes and residing inside the inversion layer at northernmost locations.

In Chapter 4, Arctic summer thermal inversions and fog macrophysical properties were further investigated. The research presented in this chapter is the first to compare and quantify lower tropospheric inversion characteristics during full-fog, marginal-fog and non-fog weather conditions in the Arctic. The fog retrieval method developed in Chapter 3 was applied, and from all extracted radiosonde profiles fog top pressure and fog top elevation were retrieved using a novel method based on dew point depression. An existing method (Kahl, 1990) was applied to all summer soundings to extract tropospheric inversion characteristics. Lower tropospheric inversions occur in 85-95 % of soundings.

Most inversions are elevated, with the inversion base at ~150 m a.s.l., and a median inversion depth range of ~225-250 m. Neither differ significantly among stations. Inversion intensities are in the range 1-3°C and tend to be lower in the south. Median fog top elevation is 150-200 m a.s.l. Inversions are twice as strong, ~ 150 m deeper, and more concave-up under foggy than under non-foggy conditions. Fog can cover up to 30% of the ablation area of land-terminating glaciers in central East Greenland while the deeper inversions can cover the entire ablation area: both have the potential to reduce glacier melt. Most regional differences observed in fog characteristics and macrophysical properties are hypothesised to be associated with distinct environmental conditions, such as the presence of sea ice, the solar diurnal cycle, and the strength of sea breezes and katabatic winds. The comparison of the fog properties (Chapter 2) and the inversion characteristics (Chapters 3 and 4) between coastal East Greenland and Arctic Ocean regions suggests that similar environmental processes take place in both regions. Lastly, the multiple sensitivity analyses and comparisons with independent fog macrophysical property retrieval methods presented in this thesis suggest that both the novel fog classification and fog top elevation retrieval methods are robust, and the latter may be superior to pre-existing methods.

5.2 Overall conclusions

In this thesis the following research questions were addressed:

1. What is the annual and seasonal frequency of occurrence of fog in East Greenland?

Over the period 1958-2016, the average monthly number of fog days at the station is fewer than one fog day (3 %) during the cold season (October-March) and up to seven fog days (22 %) during the melt season (May-August). When all fog situations (real and marginal) are considered, the average monthly number of fog days is 1-7 fog days (3-25 %) during the cold season and up to 15 fog days (50 %) during the warm season. Over the period 1981-2003, synoptic real fog observations (at the station) occur 1-2 % of the time annually, and 2-6 % of the time in summer in coastal East Greenland. In contrast, fog observations including fog at the station and marginal fog occur 5-15 % of the time annually and 11-29 % of the time in summer.

2. What are the annual and daily timing patterns of fog, and how do these relate to wind and sea ice conditions?

Between two thirds and three quarters of fog occurs between May and August, and the timing of fog onset and sea ice break-up coincides, but may both be a function of the general onset of the melt season. Fog has a pronounced diurnal pattern, with a maximum frequency in the late morning and a minimum occurring in the late afternoon. This appears to be mainly driven by the solar diurnal cycle but possibly exacerbated by katabatic winds and a lower sea ice concentration at southern locations. Coastal fog is often associated with sea breeze occurrence, especially in the afternoon.

3. Which types of fog occur in East Greenland and what are their temperature, humidity and visibility characteristics?

The main fog types occurring in coastal East Greenland include advection fog and stratus-base lowering fog. Radiation fog is rare. Fog in East Greenland occurs with air temperatures around 0°C, relative humidity > 93 % and most fog is dense with visibility < 500 m. Horizontal visibility and sky visibility conditions are reasonably correlated.

4. Can we classify fog according to their thermodynamic profiles from radiosondes and can we infer fog processes from specific profiles?

The analysis of radiosonde data allowed us to classify fog thermodynamic profiles into six classes: i) fog observed at the synoptic station but missed by sounding: this may represent stratus-base lowering or fog lifting processes, ii) fog with a surface-based inversion (early development stage of advection fog), iii) fog below a low-level inversion (dissipating stage), iv) fog capped by a low-level inversion (dissipating stage), v) fog penetrating a low-level inversion (mature stage), and vi) fog below a saturated low-level inversion (transition to fog by stratus-base lowering or dissipation of fog by lifting to a stratus).

5. Can we optimise fog top elevation retrievals from IGRA radiosonde profiles so that they can be applied to all thermodynamic profiles?

The novel Dew point Depression Method (DDM) presented in this thesis allows for interpolation of saturation conditions between IGRA's significant levels, hence derivation of fog top pressure and consequently fog top elevation. The DDM can be applied to any

fog thermodynamic profile, including profiles with negative dew point temperature gradients. The DDM method is therefore a superior method to retrieve fog top elevation from low-resolution radiosondes.

6. How thick is fog in East Greenland and how does this compare to fog in other Polar regions?

Fog in East Greenland is often 150-200 m thick, which is similar to values measured for advection fog over the Arctic Ocean (Sotiropoulou et al., 2014; Tjernström et al., 2015; Sotiropoulou et al., 2016) and along Antarctic coasts (Gajananda et al., 2007). Extreme fog cases can be up to 700 m thick, similar in thickness to that measured in mid-latitude advection fog (Gao et al., 2007; Huang et al., 2015; Liu et al., 2016), yet only rarely reported in the Arctic regions (Sotiropoulou et al., 2016).

7. How often do temperature inversions occur in East Greenland, what are their characteristics and how do these compare with temperature inversions in other Polar regions?

During all-weather conditions, low-level tropospheric temperature inversions occur in > 85 % of summer soundings, > 70 % of temperature inversions are elevated, with a base around 150 m a.s.l., a depth of ~ 240 m and a median strength of 2°C. Temperature inversions in East Greenland are more frequent, lower and shallower compared to other coastal Arctic locations (Kahl, 1990; Kahl et al., 1992; Serreze et al., 1992), but are similar to those over the Arctic Ocean (Serreze et al., 1992; Sotiropoulou et al., 2016). Inversion intensities over East Greenland are similar to values reported elsewhere in the Arctic, but are lower than in coastal Alaska (Kahl, 1990).

8. How do fog and temperature inversion properties relate to each other?

In coastal East Greenland summer soundings, temperature inversions occur much more frequently than fog (> 85 % vs. 20 %), while advection fog usually occurs simultaneously with temperature inversions. This is likely because mechanisms such as warm air advection and sea breeze both establish low-level inversions and promote fog formation. Fog is associated with more frequent (> 99 % vs. > 85 %) deeper (~350 m vs. ~240 m) and stronger (~4-5°C vs. ~2°C) inversions compared to non-foggy situations. Local environmental conditions, such as low wind speed, allow strong and deep inversions to develop. In addition, strong stability conditions favour fog formation and lifetime. It is hypothesised that the stronger and deeper inversions occurring during fog are a result of local and synoptic-scale processes rather than triggered by fog itself, although no firm conclusions can be drawn from the analysis presented in this thesis, due to limitations in the datasets used.

9. What are the regional differences in all the above characteristics of fog and temperature inversions along the East Greenland latitudinal transect?

Fog characteristics vary between Low-Arctic and High-Arctic locations along the coast of East Greenland. At Low-Arctic locations, fog is dense (visibility ~ 300 m), mainly restricted to morning hours, and associated with temperatures around the freezing point and relative humidity close to 100 %. Here, summer fog is exclusively in the liquid phase. At High-Arctic sites, temperatures (< 0°C) and relative humidity during fog are lower (> 93 %), and visibility during fog is higher (~ 500 m). At these higher latitudes sea breeze is stronger and more sustained throughout the day, due to the thermal gradient between the frequently ice-covered ocean and snow-free land, bringing fog to coastal areas at any

time of the day. Fog geometrical thickness and thermodynamic profiles also show latitudinal variations. Fog is often shallow and confined below or capped by an elevated inversion base at Low-Arctic sites, whereas it is vertically extensive and often penetrates the inversion layer at High-Arctic locations. It is hypothesised that fog is more often or for longer periods in the mature stage at northern locations. Under all weather conditions, inversions are strongest in central East Greenland and weakest in the southeast. When fog is present, however, inversion intensity becomes higher with increasing latitude. It is hypothesised that these regional differences reflect different environmental conditions, such as sea ice concentration, across-shore thermal gradients, sea breeze occurrence, katabatic winds and solar diurnal variations.

10. How much glacier surface area in East Greenland can potentially be affected by overlying fog and temperature inversions?

Fog can potentially cover up to 30 % of the ablation area of land-terminating glaciers in the central East Greenland region, and temperature inversions up to 100 % of the ablation area. This represents 540 to 1800 km^2 of glacierized terrain, respectively, and further research is needed to investigate the effects on the surface energy budget of these glacier regions.

5.3 Suggestions for further research

This thesis research did not include an analysis of sea surface temperature (*SST*) related to the occurrence of sea breeze and fog. In future studies, the gradient between air temperature from WMO synoptic weather stations operated by DMI in coastal East Greenland and daily *SST* (Reynolds et al., 2007) needs to be analysed as a proxy for sea breeze strength in these coastal regions (cf. Piskozub et al., 2017). Simultaneously, differences between dew point air temperature (T_d) and *SST* could be analysed in conjunction with fog occurrence. This would address the question of whether the condition $T_d - SST \geq 0$°C has potential to be used as an indicator or predictor for summer fog occurrence in Arctic coastal regions.

Further analysis should also include ceilometer measurements of vertical visibility (e.g. Nowak et al., 2008; Haeffelin et al., 2010), and horizontal visibility and radiative fluxes measured at full surface energy balance stations over ice and ice-free surfaces. This could address the question whether horizontal visibility can be used as a proxy for fog top elevation or for the net radiative effect of fog on glaciers. Additionally, ceilometers can be used to monitor transitions between fog and stratus (Dorman, 2017), which were frequently observed in East Greenland from the analysis of time-lapse imagery at Sermilik Fjord presented in Chapter 3 of this thesis.

There are numerous real-time video cameras and private time-lapse cameras deployed for non-meteorological purposes. In the Arctic region, these often contain fog images, which are usually discarded from analyses because they are undesirable. However, time-lapse

images can provide a valuable way to analyse fog frequency, duration, timing and often vertical extent (Dorman, 2017). Such studies are currently being conducted in the Glaciology and Geoscience Laboratory at the University of Lethbridge (e.g. Jiskoot et al., 2016). Since the analysis of such datasets is time-consuming, a semi-automated fog identification algorithm based on pixel colour, or contrast between two adjacent regions in a single scene, needs to be developed. Additionally, combining time-lapse images with radiosonde data and airborne platforms such as Unmanned Aerial Vehicles (e.g. Gultepe et al., 2017) could provide a valuable option to investigate the relationship between fog visibility, microphysical properties and macrophysical properties.

Further climatological studies of fog should include the homogenisation of fog and visibility data from DMI in order to study trends in fog occurrence, and whether changes in fog conditions can be related to long-term changes in sea ice conditions, ocean temperature and climate indices, such as the Arctic Oscillation, North Atlantic Oscillation and Greenland Blocking indices.

The thermodynamic classification and fog top elevation calculation (Dew point Depression Method) presented in Chapters 3 and 4 of this thesis could be further explored for differences in fog macrophysical properties and thermal inversion properties. Chapter 3 also suggested that temperature retrievals from *microwave radiometers* (MWRs) could be useful for the study of the evolution of temperature inversions during fog over the Arctic Ocean. However, moisture profiles were not available from the MWR used during the ASCOS campaign in summer 2008, so that the validation of fog thermodynamic profiles from IGRA radiosondes was not possible from this ASCOS MWR. Analysis of

high temporal resolution humidity and temperature profiles of the boundary layer will help to test the hypothesis in Chapter 3 that thermodynamic profiles represent fog development stages. The RPG-HATPRO provides vertical profiles of both temperature and humidity in the boundary layer (Rose and Czekala, 2005). Such MWRs have previously been used to study the dynamics of radiation fog and stratus-base lowering into fog over land (Degefie et al., 2015; Wærsted et al., 2017), but, to our knowledge, a similar study has not been conducted in the Arctic. Since September 2016, a RPG-HATPRO MWR is deployed on Disko Island, West Greenland, operated by Asiaq, Greenland Survey (Dr. Jakob Abermann, pers. comm., Dec 2016). It is planned that data from summer 2017 and beyond will be analysed in future collaborative studies, using some of the methods developed in this thesis. This type of analysis will test the hypothesis made in Chapter 3 of this thesis, as well as to improve our understanding of fog formation and dissipation mechanisms in Greenland coastal regions. This work should also allow answering the questions about whether MWR can be used to nowcast Arctic fog, and to better understand the processes related to the development of fog.

Further analysis of wind profiles within Arctic fog would provide valuable information in terms of fog dynamics. IGRA has limited vertical resolution to study wind profiles in the boundary layer. Although the use of high-resolution radiosondes would offer a finer vertical resolution of wind, radiosondes do not provide information on vertical motion, which is important for transfers of momentum, heat and moisture in the boundary-layer (Stull, 1988) and turbulence fluxes within a fog layer (Kim and Yum, 2017). To study these processes, systems such as low power *Sonic Detection and Ranging* (SODAR) wind profilers have been suggested by, e.g., Dabas et al. (2012), as these provide 3-D wind

profiles with 10 m vertical resolution in the boundary layer every minute (Bradley, 2007). SODAR and *Light Detection and Ranging* (Lidar) systems can further provide accurate fog top detection (Zhang et al., 2010; Dabas et al., 2012; Haeffelin, 2016; Zhu et al., 2017). These could therefore be used to validate the fog top elevation method presented in this thesis (DDM: Chapter 4). High-resolution radiosondes could further be used to validate the interpolation algorithm of DDM.

In summary, the following steps should be taken to validate the DDM presented in this thesis:

1. Use of high-resolution radiosondes in conjunction with IGRA low-resolution radiosondes to validate the interpolation algorithm;
2. Use of MWR data to validate the thermodynamic classification of fog profiles and associated processes;
3. Use of Lidar/SODAR in conjunction with radiosonde measurements to validate fog top elevation retrievals from radiosondes.

Once the DDM is firmly established, this method could be applied to other Arctic coastal sites where both IGRA profiles and present weather observations exist. The automated classification schemes presented in Chapters 3 and 4 of this thesis could then be used to derive pan-Arctic fog thermodynamic structure, fog top elevation as well as inversion characteristics statistics from IGRA to better understand the regional variations in fog and inversion occurrences and link these to local environmental and mesoscale conditions. A study of fog around the North Atlantic Arctic of this kind has been initiated during this

PhD work between Dr. Hester Jiskoot (PhD supervisor), Gaëlle Gilson (author of this thesis), and a team led by Dr. Ewa Łupikasza (University of Silesia, Poland), and will be continued beyond this PhD. Ultimately, a pan-Arctic analysis of fog types, temperature inversions, and fog top elevation could be done using the techniques presented in this thesis.

If homogenisation techniques are applied to the IGRA dataset, temporal trends in fog thickness in relation to inversion characteristics could be investigated over coastal East Greenland but also across the North Atlantic Arctic. Such a study could help answering several research questions. These may include: Have fog top elevation and inversion characteristics changed over the past decades, and what is the spatial distribution of possible changes? How can such changes be related to changes in the Arctic environment, such as sea ice conditions, ocean and air temperatures, or in local and large-scale circulation? How are fog and temperature inversions expected to change under a warming Arctic?

It was suggested in Chapter 4 that fog occurrence be used to derive an approximation of inversion characteristics over coastal glaciers in other Arctic regions. In regions where statistics of fog top elevation and inversion characteristics can be calculated, e.g. by using the methods presented in Chapter 4 of this thesis, median fog top elevation and inversion characteristics could be incorporated into distributed glacier surface energy balance models (e.g. Hock and Holmgren, 2005; Huss et al., 2008), in order to quantify the effect of these low-level conditions on Arctic coastal glacier melt and mass balance. Then it can be systematically analysed and quantified whether fog in Arctic regions is associated with

a reduction in melt energy at glacier surfaces. This knowledge can then be used to asses how future changes in fog will impact the surface energy balance of Arctic glaciers.

Ultimately, more detailed field measurements are needed to fully understand fog microphysical properties, in relation to fog development stages, particularly over melting ice surfaces. Among others, a method to calculate fog top elevation from surface turbulence measurements such as the one developed by Román-Cascón et al. (2015) for radiation fog could be developed for advection fog, including in the Arctic. Extensive field instrumentation has already been deployed to study Arctic ice fog (Gultepe et al., 2014), but an intensive field campaign dedicated to Arctic summer, predominantly-liquid fog, is still missing. Such a study would greatly improve the understanding of fog microphysical and macrophysical properties and processes, which will lead to better nowcasting and forecasting of fog in high-latitude regions. It would additionally increase knowledge of the radiative effect of fog and low-level clouds on the Arctic surface energy budget, and how changes in fog occurrence will impact the surface energy budget of the Greenland Ice Sheet and Arctic glaciers, which have important contributions to current and future sea-level rise (Meier et al., 2007; Vaughan et al., 2013).

REFERENCES

Abermann J, Hansen B, Lund M, Wacker S, Karami M, Cappelen J (2017) Hotspots and key periods of Greenland climate change during the past six decades. Ambio, 46(1), 3-11

Alt BT (1979) Investigation of summer synoptic climate controls on the mass balance of Meighen Ice Cap. Atmos-Ocean 17(3):181-199

Arctic Monitoring and Assessment Programme (AMAP) (2017) Snow, Water, Ice and Permafrost in the Arctic (SWIPA) 2017. Arctic Monitoring and Assessment Programme (AMAP), Oslo, Norway. xiv + 269 pp

Ambaum MH, Hoskins BJ, Stephenson DB (2001) Arctic oscillation or North Atlantic oscillation? J Clim 14(16):3495-3507

Antikainen V, Paukkunen A, Jauhiainen H (2002) Measurement accuracy and repeatability of Vaisala RS90 Radiosonde. Vaisala news 159:11-13

Air Weather Service (AWS) (1979) the use of the skew-T, log P diagram in analysis and forecasting. AWS/TR-79/006, Air Weather Service, Scott AFB, IL, 150 pp

Baguskas SA, Loik ME (2015) Using Coastal Fog to Support Sustainable Water Use in a California Agricultural System. AGU Fall Meeting Abstract # A33H-0279

Baliles MD (1959) History of Observational Instructions on Fog. Key to Meteorol Records Documentation 3.031, U. S. Weather Bureau

Bendix J (1995) A case study on the determination of fog optical depth and liquid water path using AVHRR data and relations to fog liquid water content and horizontal visibility. Remote Sens 16(3):515-530

Bendix J, Thies B, Cermak J, Nauß T (2005) Ground fog detection from space based on MODIS daytime data - A feasibility study. Weather Forecast 20(6):989-1005

Bennartz R, Shupe MD, Turner DD, Walden VP, Steffen K, Cox CJ, Hulie MS, Miller NB, Pettersen C (2013) July 2012 Greenland melt extent enhanced by low-level liquid clouds. Nature 496(7443):83-86

Bergot T (2016) Large-eddy simulation study of the dissipation of radiation fog. Q J R Meteorol Soc 142:1029-1040

Billings WD, Peterson KM (1992) Some possible effects of climatic warming on Artic tundra ecosystems of the Alaskan North Slope. In: Robert PL, Thomas LE (eds.) Global Warming and Biological Diversity, Yale University Press, New Haven, pp. 233–243

Bødtker E (2003) Observation Systems 2003, Technical Report 03-16, Ministry of Transport, Danish Meteorological Institute, Copenhagen, 10 pp

Bourne SM, Bhatt US, Zhang J, Thoman R (2010) Surface-based temperature inversions in Alaska from a climate perspective. Atmos Res 95(2):353-366

Bowling SA, T Ohtake CS Benson (1968) Winter pressure systems and ice fog in Fairbanks, Alaska. J Appl Meteor 7:961–968

Box JE (2006) Greenland ice sheet surface mass-balance variability: 1991–2003. Ann Glaciol 42(1):90-94

Box JE, Cohen AE (2006) Upper-air temperatures around Greenland: 1964-2005. Geophys Res Lett 33(12):10.1029/2006GL025723

Bradley S (2007) Atmospheric acoustic remote sensing: principles and applications. Boca Raton: CRC Press. 296p. ISBN 978-0-8493-3588-4

Bradley RS, Keimig FT, Diaz HF (1992) Climatology of surface-based inversions in the North American Arctic. J Geophys Res Atmos 97(D14):15699-15712

Braithwaite RJ (1995) Positive degree-day factors for ablation on the Greenland ice sheet studied by energy-balance modelling. J Glaciol 41(137):153-160

Braithwaite RJ, Raper SC (2007) Glaciological conditions in seven contrasting regions estimated with the degree-day model. Ann Glaciol 46(1):297-302

Braithwaite RJ, Raper SC, Chutko K (2006) Accumulation at the equilibrium-line altitude of glaciers inferred from a degree-day model and tested against field observations. Ann Glaciol 43(1):329-334

Braun M, Hock R (2004) Spatially distributed surface energy balance and ablation modelling on the ice cap of King George Island (Antarctica). Global Planet Change 42(1):45-58

Braun C, Hardy DR, Bradley RS, Sahanatien V (2004) Surface mass balance of the Ward Hunt Ice Rise and Ward Hunt Ice Shelf, Ellesmere Island, Nunavut, Canada. J Geophys Res Atmos 109(D22):1-9

Brooks CK (1979) Geomorphological observations at Kangerdlugssuaq, East Greenland. Medd Grønl Geosci 1, 24 pp.

Busch N, Ebel U, Kraus H, Schaller E (1982) The structure of the subpolar inversion-capped ABL. Meteorol Atmos Phys 31(1):1-18

Cappelen J, Jørgensen BV, Laursen EV (2001) The Observed Climate of Greenland, 1958-99-with Climatological Standard Normals, 1961-90. Technical report 00-18, Danish Meteorological Institute, Copenhagen, 149 pp

Cappelen J, Laursen EV, Jørgensen PV, Kern-Hansen C (2011) DMI monthly climate data collection 1768-2010, Denmark, the Faroe Islands and Greenland. Technical Report 05-05, Danish Meteorological Institute, Copenhagen, 53 pp

Cappelen J (2015) Greenland - DMI Historical Climate Data Collection 1784-2014. Technical report 15-04, Danish Meteorological Institute, Copenhagen, 97 pp

Cavalieri DJ, Crawford J, Drinkwater M, Emery WJ, Eppler DT, Farmer LD, Goodberlet M, Jentz R, Milman A, Morris C, Onstott R, Schweiger A, Shuchman R, Steffen K, Swift CT, Wackerman C, Weaver RL (1992) NASA Sea Ice Validation Program for the DMSP SSM/I: Final Report. NASA Technical Memorandum 104559. National Aeronautics and Space Administration, Washington, D. C. 126 pp

Cavalieri DJ, Parkinson CL, Gloersen P, Zwally HJ (1996) updated yearly. Sea Ice Concentrations from Nimbus-7 SMMR and DMSP SSM/I-SSMIS Passive Microwave Data, Version 1. (NSIDC-0051). Boulder, Colorado USA. NASA National Snow and Ice Data Center Distributed Active Archive Center

Cermak J (2016) Fog frequency and properties from active-sensor satellite data. AGU Fall Meeting Abstract # A21L-07

Cesana G, Kay JE, Chepfer H, English JM, Boer G (2012) Ubiquitous low-level liquid-containing Arctic clouds: New observations and climate model constraints from CALIPSO-GOCCP. Geophys Res Lett 39(20):10.1029/2012GL053385

Chernykh IV, Eskridge RE (1996) Determination of cloud amount and level from radiosonde soundings. J Appl Meteorol 35:1362–1369

Chutko KJ, Lamoureux SF (2009) The influence of low-level thermal inversions on estimated melt-season characteristics in the central Canadian Arctic. Int J Climatol 29(2):259-268

Circumpolar Arctic Vegetation Map (CAVM) (2003) Scale: 1:7,500,000. Conservation of Arctic Flora and Fauna (CAFF) Map No. 1. U.S. Fish and Wildlife Service, Anchorage, Alaska

Conway JP, Cullen NJ (2016) Cloud effects on surface energy and mass balance in the ablation area of Brewster Glacier, New Zealand. Cryosphere 10(1):313-328

Cotton WR, Anthes RA (1989) Fogs and Stratocumulus Clouds. In: Cotton WR, Anthes RA (eds.) Storm and Cloud Dynamics (International Geophysics Series 44). Academic Press, San Diego, California, pp 303-367

Croft PJ, Pfost RL, Medlin JM, Johnson GA (1997) Fog forecasting for the southern region: A conceptual model approach. Weather Forecast 12(3):545-556

Curry JA, Ebert EE, Herman GF (1988) Mean and turbulence structure of the

summertime Arctic cloudy boundary layer. Q J R Meteorol Soc 114(481):715-746

Curry JA, Schramm JL, Rossow WB, Randall D (1996) Overview of Arctic cloud and radiation characteristics. J Clim 9(8):1731-1764

Curry JA, Hobbs PV, King MD, Randall DA, Minnis P, Isaac GA, Pinto JO, Uttal T, Bucholtz A, Cripe DG, Gerber H, Fairall CW, Garrett TJ, Hudson J, Intrieri JM, Jakob C, Jensen T, Lawson P, Marcotte D, Nguyen L, Pilewskie P, Rangno A, Rogers DC, Strawbridge KB, Valero FPJ, Williams AG, Wylie D (2000) FIRE Arctic clouds experiment. Bull Am Meteorol Soc 81(1):5-29

Dabas A, Remy S, Bergot T (2012) Use of a sodar to improve the forecast of fogs and low clouds on airports. Pure Appl Geophys 169(5-6):769-781

Dai A, Wang J, Thorne PW, Parker DE, Haimberger L, Wang XL (2011) A new approach to homogenize daily radiosonde humidity data. J Clim 24(4):965-991

Degefie DT, El-Madany TS, Hejkal J, Held M, Dupont JC, Haeffelin M, Klemm O (2015) Microphysics and energy and water fluxes of various fog types at SIRTA, France. Atmos Res 151:162-175

Deser C, Tomas R, Alexander M, Lawrence D (2010) The seasonal atmospheric response to projected Arctic sea ice loss in the late 21st century, J Clim 23(2):333–351

Desmet PG, Cowling RM (1999) Biodiversity, habitat and range-size aspects of a flora from a winter-rainfall desert in north–western Namaqualand, South Africa. Plant Ecol 142:23–33

Devasthale A, Willén U, Karlsson K-G, Jones CG (2010) Quantifying the clear-sky temperature inversion frequency and strength over the Arctic Ocean during summer and winter seasons from AIRS profiles. Atmos Chem Phys 10(12):5565-5572

Dorman CE (2017) Early and Recent Observational Techniques for Fog. In Marine Fog: Challenges and Advancements in Observations, Modeling, and Forecasting (pp. 153-244). Springer International Publishing

Dorman CE, Mejia J, Koračin D, McEvoy D (2017) Worldwide Marine Fog Occurrence and Climatology. In Marine Fog: Challenges and Advancements in Observations, Modeling, and Forecasting (pp. 7-152). Springer International Publishing

Dorninger M, Whiteman CD, Bica B, Eisenbach S, Pospichal B, Steinacker R (2011) Meteorological events affecting cold-air pools in a small basin. J Appl Meteorol Climatol 50(11):2223-2234

Dowdeswell JA, Whittington RJ, Hodgkins R (1992) The sizes, frequencies, and freeboards of East Greenland icebergs observed using ship radar and sextant. J Geophys Res Oceans 97(C3):3515-3528

Durre I, Yin X (2008) Enhanced radiosonde data for studies of vertical structure. Bull Am Meteorol Soc 89(9):1257-1262

Durre I, Vose RS, Wuertz DB (2006) Overview of the Integrated Global Radiosonde Archive. J Clim 19(1):53-68

Eastman R, Warren SG (2010) Arctic Cloud Changes from Surface and Satellite Observations. J Clim 23(15):4233-4242

Eastman R, Warren SG (2014). Diurnal cycles of cumulus, cumulonimbus, stratus, stratocumulus, and fog from surface observations over land and ocean. J Clim 27(6):2386-2404

Fessehaye M, Abdul-Wahab SA, Savage MJ, Kohler T, Gherezghiher T, Hurni H (2017) Assessment of fog-water collection on the eastern escarpment of Eritrea. Water Int 42(8):1022-1036

Flato G, Marotzke J, Abiodun B, Braconnot P, Chou SC, Collins W, Cox P, Driouech F, Emori S, Eyring V, Forest C, Gleckler P, Guilyardi E, Jakob C, Kattsov V, Reason C, Rummukainen M (2013) Evaluation of Climate Models. In: Climate Change 2013: The Physical Science Basis. Contribution of Working Group I to the Fifth Assessment Report of the Intergovernmental Panel on Climate Change [Stocker, T.F., D. Qin, G.-K. Plattner, M. Tignor, S.K. Allen, J. Boschung, A. Nauels, Y. Xia, V. Bex and P.M. Midgley (eds.)]. Cambridge University Press, Cambridge, United Kingdom and New York, NY, USA

Ford JD, Furgal C (2009) Foreword to the special issue: climate change impacts, adaptation and vulnerability in the Arctic. Polar Res 28(1):1-9

Friedlein MT (2004) Dense Fog Climatology: Chicago O'hare International Airport July 1996–April 2002. Bull Am Meteorol Soc 85(4):515-517

Gaffen DJ (1993) Historical changes in radiosonde instruments and practices. WMO/TD-No. 541. Instruments and Observing Methods Report No. 50. World Meteorological Organization, Geneva, Switzerland, 123 pp

Gajananda K, Dutta HN, Lagun VE (2007) An episode of coastal advection fog over East Antarctica. Curr Sci 93(5):654-659

Gao S, Lin H, Shen B, Fu G (2007) A heavy sea fog event over the Yellow Sea in March 2005: Analysis and numerical modeling. Adv Atmos Sci 24(1):65-81

Gardner AS, Sharp M (2007) Influence of the arctic circumpolar vortex on the mass balance of Canadian High Arctic glaciers. J Clim 20(18):4586-4598

Gardner AS, Sharp M (2009) Sensitivity of net mass-balance estimates to near-surface temperature lapse rates when employing the degree-day method to estimate glacier melt. Ann Glaciol 50 (50):80–86

Gardner AS, Sharp MJ, Koerner RM, Labine C, Boon S, Marshall SJ, Burgess DO, Lewis D (2009) Near-surface temperature lapse rates over Arctic glaciers and their implications for temperature downscaling. J Clim 22(16):4281-4298

Garreaud R, Barichivich J, Christie DA, Maldonado A (2008) Interannual variability of the coastal fog at Fray Jorge relict forests in semiarid Chile. J Geophys Res Biogeosciences 113(G4):10.1029/2008JG000709

Gathman SG, Larson RE (1974) Marine Fog Observations in the Arctic (No. NRL-7693). Naval Research Lab Washington DC, 28 pp

Giesen R, Hock R, Marzeion B, Bliss A, Hirabayashi Y, Huss M, Radic V, Slangen A (2016) GlacierMIP-A model intercomparison of global-scale glacier mass-balance models and projections. EGU Abstract # EPSC2016-9938.

Glickman T (2000) Glossary of Meteorology, Second Edition. Am Meteorol Soc 855, Boston, MA, 565 pp

Gotaas Y, Benson CS (1965) The effect of suspended ice crystals on radiative cooling. J Appl Meteorol 4:446-453

Groves DG, Francis JA (2002) Variability of the Arctic atmospheric moisture budget from TOVS satellite data. J Geophys Res Atmos 107(D24):10.1029/2002JD002285

Guadarrama-Cetina J, Mongruel A, Medici M-G, Baquero E, Parker AR, Milimouk-Melnytchuk I, Gonzáles-Viñas W, Beysens D (2014) Dew condensation on desert beetle skin. Eur Phys J 37(109)

Gueye S (2014) Frequency, timing and temporal patterns of regional coastal Arctic fog in East Greenland. MSc Thesis, University of Amsterdam, Netherlands

Gultepe I (2007) Fog and boundary layer clouds: fog visibility and forecasting. Springer Science and Business Media / Birkhäuser Science, Basel, 308 pp

Gultepe I (2015) Mountain Weather: Observation and Modeling. In R. Dmowska (Ed.) Advances in Geophysics, Elsevier, 56:229-312

Gultepe I, Isaac GA, Key J, Intrieri J, Starr DC, Strawbridge KB (2004) Dynamical and microphysical characteristics of Arctic clouds using integrated observations collected over SHEBA during the April 1998 FIRE. ACE flights of the Canadian Convair. Meteorol Atmos Phys 85(4):235-263

Gultepe I, Müller MD, Boybeyi Z (2006) A new visibility parameterization for warm-fog applications in numerical weather prediction models. J Appl Meteorol Climatol 45(11):1469-1480

Gultepe I, Tardif R, Michaelides SC, Cermak J, Bott A, Bendix J, Müller MD, Pagowski M, Hansen B, Ellrod E, Jacobs W, Toth G, Cober SG (2007) Fog research: A review of past achievements and future perspectives. Pure Appl Geophys 164(6-7):1121-1159

Gultepe I, Hansen B, Cober SG, Pearson G, Milbrandt JA, Platnick S, Taylor P, Gordon M, Oakley JP (2009) The fog remote sensing and modeling field project. Bull Am Meteorol Soc 90(3):341-359

Gultepe I, Kuhn T, Pavolonis M, Calvert C, Gurka J, Heymsfield AJ, Liu PSK, Zhou B, Ware R, Ferrier B, Milbrandt J, Bernstein B (2014) Ice fog in arctic during FRAM–Ice Fog project: aviation and nowcasting applications. Bull Am Meteorol Soc 95(2):211-226

Gultepe I, Zhou B, Milbrandt J, Bott A, Li Y, Heymsfield AJ, Ferrier B, Ware R, Pavolonis M, Kuhn T, Gurka J, Liu P, Cermak J (2015). A review on ice fog measurements and modeling. Atmos Res 151:2-19

Gultepe I, Fernando HJS, Pardyjak ER, Hoch SW, Silver Z, Creegan E, Leo LS, Pu Z, De Wekker FJ, Hang C (2016) An overview of the MATERHORN fog project: Observations and predictability. Pure Appl Geophys 173(9):2983-3010

Gultepe I, Heymsfield A, Fernando J, Ware R (2017) UAV Applications for Thermodynamic Profiling: Emphasis on Ice Fog Visibility. EGU Abstracts # EGU2017-10439-1

Haeffelin M (2016) Exploring microphysical, radiative, dynamic and thermodynamic processes driving fog and low stratus clouds using ground-based Lidar and Radar measurements. EGU Abstracts # EPSC2016-6263

Haeffelin M, Bergot T, Elias T, Tardif R, Carrer D, Chazette P, Colomb M, Drobinski P, Dupont E, Dupont J-C, Gomes L, Musson-Genon L, Pietras C, Plana-Fattori A, Protat A, Rangognio J, Raut J-C, Rémy S, Richard D, Sciare J, Zhang X (2010) PARISFOG: shedding new light on fog physical processes. Bull Am Meteorol Soc 91(6):767-783

Hanesiak JM, Wang XL (2005) Adverse-weather trends in the Canadian Arctic. J Clim 18(16):3140-3156

Hanessian J (1960) The Antarctic Treaty 1959. Int'l & Comp L Q 9(3):436-480

Hanna E, Cappelen J (2003) Recent cooling in coastal southern Greenland and relation with the North Atlantic Oscillation. Geophys Res Lett 30(3):10.1029/2002GL015797

Hanna E, Jones JM, Cappelen J, Mernild SH, Wood L, Steffen K, Huybrechts P (2013) The influence of North Atlantic atmospheric and oceanic forcing effects on 1900–2010 Greenland summer climate and ice melt/runoff. Int J Climatol 33(4):862-880

Hansen B, Gultepe I, King P, Toth G, Mooney C (2007) Visualization of seasonal-diurnal climatology of visibility in fog and precipitation at Canadian airports, AMS Annual Meeting, 16th Conf. Appl. Climatology, San Antonio, Texas, 14–18 January, 2007, CD

Hansen BU, Sigsgaard C, Rasmussen L, Cappelen J, Hinkler J, Mernild SH, Petersen D, Tamstorf MP, Rasch M, Hasholt B (2008) Present-day climate at Zackenberg. Adv Ecol Res 40:111-149

Hardy B (1998) Determination of relative humidity in subzero temperatures. RH System, Albuquerque, New Mexico, USA Copyright, 5 pp

Hautiére N, Tarel JP, Lavenant J, Aubert D (2006) Automatic fog detection and estimation of visibility distance through use of an onboard camera. Mach Vis Appl 17(1):8-20

Heintzenberg J, Leck C, Birmili W, Wehner B, Tjernström M, Wiedensohler A (2006) Aerosol number–size distributions during clear and fog periods in the summer high Arctic: 1991, 1996 and 2001. Tellus Ser B Chem Phys Meteorol 58(1):41-50

Hill AJ, Dawson TE, Shelef O, Rachmilevitch S (2015) The role of dew in Negev Desert plants. Oecol 178(2):317-327

Hock R (2003) Temperature index melt modelling in mountain areas. J Hydrol 282(1):104-115

Hock R (2005) Glacier melt: a review of processes and their modelling. Prog Phys Geogr 29(3):362-391

Hock R, Holmgren B (1996) Some aspects of energy balance and ablation of Storglaciären, northern Sweden. Geografiska Annaler. Series A. Phys Geogr 78:121-131

Hock R, Holmgren B (2005) A distributed surface energy-balance model for complex topography and its application to Storglaciären, Sweden. J Glaciol 51(172):25-36

Hofer S, Tedstone AJ, Fettweis X, Bamber JL (2017) Decreasing cloud cover drives the recent mass loss on the Greenland Ice Sheet. Sci Adv 3(6):e1700584

Huang H, Liu H, Huang J, Mao W, Bi X (2015) Atmospheric boundary layer structure and turbulence during sea fog on the southern China coast. Mon Weather Rev 143(5):1907-1923

Hudson SR, Brandt RE (2005) A look at the surface-based temperature inversion on the Antarctic Plateau. J Clim 18(11):1673-1696

Hudson JG, Noble S, Jha V (2011) On the relative role of sea salt cloud condensation nuclei (CCN). J Atmos Chem 68(1):71-88

Hulth J, Rolstad C, Trondsen K, Rodby RW (2010) Surface mass and energy balance of Sorbreen, Jan Mayen, 2008. Ann Glaciol 51(55):110-119

Huss M, Farinotti D, Bauder A, Funk M (2008) Modelling runoff from highly glacierized alpine drainage basins in a changing climate. Hydrol Proc 22(19):3888-3902

Ingleby B, Fucile E, Vasiljevic D, Kral T, Isaksen L (2014) Use of BUFR radiosonde and surface observations at ECMWF. Using ECMWF Forecast workshop, 4-6 June 2014, Reading, UK

Inoue K, Yoshimoto M, Abe H (1997) Cloud physical property of sea fog induced by Yamase in the Sanriku seashore. J Agric Meteorol 53:21–28

IPCC (2013) Summary for Policymakers. In: Stocker TF, Qin D, Plattner G-K, Tignor M, Allen SK, Boschung J, Nauels A, Xia Y, Bex V, Midgley PM (eds.) Climate Change 2013: The Physical Science Basis. Contribution of Working Group I to the Fifth Assessment Report of the Intergovernmental Panel on Climate Change. Cambridge University Press, Cambridge, United Kingdom and New York, NY, USA, pp 1–30

Jakobson E, Vihma T (2010) Atmospheric moisture budget in the Arctic based on the ERA-40 reanalysis. Int J Climatol 30(14):2175-2194

Jin X, Hanesiak J, Barber D (2007) Detecting cloud vertical structures from radiosondes and MODIS over Arctic first-year sea ice. Atmos Res 83(1):64-76.

Jiskoot H, Mueller MS (2012) Glacier fragmentation effects on surface energy balance and runoff: field measurements and distributed modelling. Hydrol Proc 26(12):1861-1875

Jiskoot H, Murray T, Luckman A (2003) Surge potential and drainage-basin characteristics in East Greenland. Ann Glaciol 36(1):142-148

Jiskoot H, Juhlin D, St Pierre H, Citterio M (2012) Tidewater glacier fluctuations in central East Greenland coastal and fjord regions (1980s–2005). Ann Glaciol 53(60):35-44

Jiskoot H, Harvey T, Gilson G (2015) Arctic Coastal Fog over Greenland Glaciers using an Improved MODIS Fog Detection Method and Ground Observations. AGU Fall Meeting Abstract # C53A-0762

Jiskoot H, Fox TA, Nolan M (2016) The Effects of Fog on the Surface Energy Balance of McCall Glacier, Alaska: Combining Time-Lapse Photography with Weather Station Data. AGU Fall Meeting Abstract # C41E-0716

Ju J, Xiao K, Yao X, Bai H, Jiang L (2013) Bioinspired conical copper wire with gradient wettability for continuous and efficient fog collection. Adv Mater 25(41):5937-5942

Kahl JD (1990) Characteristics of the low-level temperature inversion along the Alaskan Arctic coast. Int J Climatol 10(5):537-548

Kahl JD, Serreze MC, Schnell RC (1992) Tropospheric low-level temperature inversions in the Canadian Arctic. Atmos-Ocean 30(4):511-529

Kahl JD, Martinez DA, Zaitseva NA (1996) Long-term variability in the low-level inversion layer over the Arctic Ocean. Int J Climatol 16(11):1297-1313

Kattsov VM, Källén E and others (2005) Future climate change: modeling and scenarios for the Arctic. In: ACIA, 2005. Arctic Climate Impact Assessment. Cambridge University Press, pp 99-150

Kawai H, Yabu S, Hagihara Y, Koshiro T, Okamoto H (2015) Characteristics of the cloud top heights of marine boundary layer clouds and the frequency of marine fog over mid-latitudes. J Meteorol Soc Jap Ser II 93(6):613-628

Kawai H, Koshiro T, Endo H, Arakawa O, Hagihara Y (2016) Changes in marine fog in a warmer climate. Atmos Sci Lett 17(10):548-555

Kay JE, L'Ecuyer T, Chepfer H, Loeb N, Morrison A, Cesana G (2016) Recent advances in Arctic cloud and climate research. Current Clim Change Rep 2(4):159-169

Key EL, Minnett PJ, Jones RA (2004) Cloud distributions over the coastal Arctic Ocean: surface-based and satellite observations. Atmos Res 72(1):57-88

Khalilian V (2016) A fog and low visibility climatology for selected stations in the Western Canadian Arctic, MSc Thesis, University of Victoria, Canada.

Kim CK, Yum SS (2010) Local meteorological and synoptic characteristics of fogs formed over Incheon international airport in the west coast of Korea. Adv Atmos Sci 27(4):761-776

Kim CK, Yum SS (2017) Turbulence in Marine Fog. In: Koračin D, Dorman CE (eds.) Marine Fog: Challenges and Advancements in Observations, Modeling, and Forecasting. Springer International Publishing, pp 245-271

Klein, SA, Hartmann DL (1993) The seasonal cycle of low stratiform clouds. J Clim 6(8):1587-1606

Klein T, Heinemann G (2002) Interaction of katabatic winds and mesocyclones near the eastern coast of Greenland. Meteorol Appl 9(4):407-422

Klemm O, Lin N (2016) What causes observed fog trends: air quality or climate change. Aerosol Air Qual Res 16(5):1131-1142

Koenig SJ, DeConto RM, Pollard D (2014) Impact of reduced Arctic sea ice on Greenland ice sheet variability in a warmer than present climate. Geophys Res Lett 41(11):10.1002/2014GL059770

Koerner RM (2005) Mass balance of glaciers in the Queen Elizabeth Islands, Nunavut, Canada. Ann Glaciol 42(1):417-423

Koračin D (2017) Modeling and Forecasting Marine Fog. In: Koračin D, Dorman C (eds) Marine Fog: Challenges and Advancements in Observations, Modeling, and Forecasting. Springer International Publishing, Cham, pp. 425-475

Koračin D, Lewis J, Thompson WT, Dorman CE, Businger JA (2001) Transition of stratus into fog along the California coast: Observations and modeling. J Atmos Sci 58(13):1714-1731

Koračin D, Dorman CE, Lewis JM, Hudson JG, Wilcox EM, Torregrosa A (2014) Marine fog: A review. Atmos Res 143:142-175

Koshiro, T., Shiotani, M. (2014). Relationship between low stratiform cloud amount and estimated inversion strength in the lower troposphere over the global ocean in terms of cloud types. Journal of the Meteorological Society of Japan Ser II 92(1):107-120

Kumai M (1973) Arctic fog droplet size distribution and its effect on light attenuation. J Atmos Sci 30(4):635-643

Kumai M, Francis KE (1962) Size distribution and liquid water content of fog, Northwestern Greenland. Res Rept 100, USACRREL, 13 pp

LaDochy S (2005) The disappearance of dense fog in Los Angeles: Another urban impact? Phys Geogr 26(3):177-191

Lange OL (2003) Photosynthetic productivity of the epilithic lichen Lecanora muralis: long-term field monitoring of CO2 exchange and its physiological interpretation: II. Diel and seasonal patterns of net photosynthesis and respiration. FLORA 198(1):55-70

Laursen EV (2015) Performance of the Automatic Balloon Launcher of Radiosonde Station 04360 Tasiilaq, November 2012 – June 2015. Tech. Rep. 15-12. Danish Meteorological Institute, Copenhagen, 26 pp

Lazzara MA (2008) A diagnostic study of Antarctic fog. PhD Thesis, University of Wisconsin-Madison

LeBoeuf R, de la Jara E (2014) Quantitative goals for large-scale fog collection projects as a sustainable freshwater resource in northern Chile. Water Int 39(4):431-450

Leck C, Bigg EK (1999) Aerosol production over remote marine areas-A new route. Geophys Res Lett 26(23):10.1029/1999GL010807

Leipper DF (1994) Fog on the US west coast: A review. Bull Am Meteorol Soc 75(2):229-240

Lewis P (2004) Forecasting advective sea fog with the use of classification and regression tree analysis for Kunsan air base. MSc Thesis, Air Force Institute of Technology, Ohio

Lewis SM, Smith LC (2009) Hydrologic drainage of the Greenland Ice Sheet. Hydrol Proc 23(14):2004-2011

Lewis JM, Koračin D, Rabin R, Businger J (2003) Sea fog off the California coast: Viewed in the context of transient weather systems. J Geophys Res Atmos 108(D15):10.1029/2002JD002833

Liu Y, Key JR, Liu Z, Wang X, Vavrus SJ (2012) A cloudier Arctic expected with diminishing sea ice. Geophys Res Lett 39(5):10.1029/2012GL051251

Liu DY, Yan WL, Yang J, Pu MJ, Niu SJ, Li ZH (2016) A study of the physical processes of an advection fog boundary layer. Boundary-Layer Meteorol 158(1):125-138

Luers JK (1997) Temperature error of the Vaisala RS90 radiosonde. J Atmos Ocean Technol 14(6):1520-1532

Luers JK, Eskridge RE (1998) Use of radiosonde temperature data in climate studies. J Clim 11(5):1002-1019

Mace GG, Zhang Q (2014) The CloudSat radar-lidar geometrical profile product (RL-GeoProf): Updates, improvements, and selected results. J Geophys Res Atmos 119(15):9441-9462

Marshall S (2012) The cryosphere. Princeton University Press. ix+288 pp

Marshall SJ, Sharp MJ, Burgess DO, Anslow FS (2007) Near-surface-temperature lapse rates on the Prince of Wales Icefield, Ellesmere Island, Canada: Implications for regional downscaling of temperature. Int J Climatol 27:385–398

Mauritsen T, Sedlar J, Tjernström M, Leck C, Martin M, Shupe M, Sjogren S, Sierau B, Persson POG, Brooks IM, Swietlicki E (2011) An Arctic CCN-limited cloud-aerosol regime. Atmos Chem Phys 11(1):65-173

Meier MF, Dyurgerov MB, Rick UK, O'Neel S, Pfeffer WT, Anderson RS, Anderson SP, Glazovsky AF (2007) Glaciers dominate eustatic sea-level rise in the 21st century. Science 317(5841):1064-1067

Meng ZY, Xu XB, Wang T, Zhang XY, Yu XL, Wang SF, Lin WL, Chen YZ, Jiang YA, An XQ (2010) Ambient sulfur dioxide, nitrogen dioxide, and ammonia at ten background and rural sites in China during 2007–2008. Atmos Environ 44(21):2625-2631

Mernild SH, Liston GE (2010) The Influence of Air Temperature Inversions on Snowmelt and Glacier Mass Balance Simulations, Ammassalik Island, Southeast Greenland. J Appl Meteorol Climatol 49(1):47-67

Mernild SH, Hansen BU, Jakobsen BH, Hasholt B (2008) Climatic conditions at the Mittivakkat Glacier catchment (1994-2006), Ammassalik Island, SE Greenland, and in a 109-year perspective (1898-2006). Geogr Tidssk-Den 108(1):51-72

Meyer WD, Rao GV (1999) Radiation fog prediction using a simple numerical model. Pure Appl Geophys 155(1):57-80

Miller NB, Turner DD, Bennartz R, Shupe MD, Kulie MS, Cadeddu MP, Walden VP (2013) Surface-based inversions above central Greenland. J Geophys Res Atmos 118(2):495-506

Miller NB, Shupe MD, Cox CJ, Walden VP, Turner DD, Steffen K (2015) Cloud radiative forcing at Summit, Greenland. J Clim 28(15):6267-6280

Minnis P, Yi Y, Huang J, Ayers K (2005) Relationships between radiosonde and RUC-2 meteorological conditions and cloud occurrence determined from ARM data. J Geophys Res 110 (D23):10.1029/2005JD006005

Murray T, Scharrer K, James TD, Dye SR, Hanna E, Booth AD, Selmes N, Luckman A, Hughes ALC, Cook S, Huybrechts P (2010) Ocean regulation hypothesis for glacier dynamics in southeast Greenland and implications for ice sheet mass changes. J Geophys Res Earth Surf 115(F3):10.1029/2009JF001522

Nakanishi M, Niino H (2006) An improved Mellor–Yamada level-3 model: Its numerical stability and application to a regional prediction of advection fog. Boundary-Layer Meteorol 119(2):397-407

Nardino M, Georgiadis T (2003) Cloud type and cloud cover effects on the surface radiative balance at several Polar sites. Theor Appl Climatol 74(3-4):203-215

National Oceanic and Atmospheric Administration (NOAA) (1995) Surface weather observations and reports, Federal Meteorological Handbook No. 1, Department of Commerce, NOAA, 94 pp

Nilsson ED (1996) Planetary boundary layer structure and air mass transport during the International Arctic Ocean Expedition 1991. Tellus Ser B Chem Phys Meteorol 48(2):178-196

Nilsson ED, Bigg EK (1996) Influences on formation and dissipation of high arctic fogs during summer and autumn and their interaction with aerosol. Tellus Ser B Chem Phys Meteorol 48(2):234-253

Norris JR (1998) Low cloud type over the ocean from surface observations. Part I: Relationship to surface meteorology and the vertical distribution of temperature and moisture. J Clim 11(3):369-382

Nowak D, Ruffieux D, Agnew JL, Vuilleumier L (2008) Detection of fog and low cloud boundaries with ground-based remote sensing systems. J Atmos Ocean Technol 25(8):1357-1368

Nygård T, Valkonen T, Vihma T (2014) Characteristics of Arctic low-tropospheric humidity inversions based on radio soundings. Atmos Chem Phys 14:1959-1971

Oke TR (1987) Boundary layer climates – 2nd ed, Methuen & Co. Ltd, 289 pp

Ohmura A, Reeh N (1991) New precipitation and accumulation maps for Greenland. J Glaciol 37(125):140-148

O'Neill HB, Burn CR, Kokelj SV, Lantz TC (2015) 'Warm'Tundra: Atmospheric and Near-Surface Ground Temperature Inversions Across an Alpine Treeline in Continuous Permafrost, Western Arctic, Canada. Permafr Periglac Proc 26(2):103-118

Orellana MV, Matrai PA, Leck C, Rauschenberg CD, Lee AM, Coz E (2011) Marine microgels as a source of cloud condensation nuclei in the high Arctic. Proc Natl Acad Sci USA 108(33):13612-13617

Overland JE (1985) Atmospheric boundary layer structure and drag coefficients over sea ice. J Geophys Res Oceans 90(C5):9029-9049

Pagowski M, Gultepe I, King P (2004) Analysis and modeling of an extremely dense fog event in southern Ontario. J Appl Meteorol 43(1):3-16

Palm SP, Strey ST, Spinhirne J, Markus T (2010) Influence of Arctic sea ice extent on polar cloud fraction and vertical structure and implications for regional climate. J Geophys Res Atmos 115(D21):10.1029/2010JD013900

Parker AR, Lawrence CR (2001) Water capture by a desert beetle. Nature 414:33-34

Pedersen SH, Tamstorf M P, Abermann J, Westergaard-Nielsen A, Lund M, Skov K, Sigsgaard C, Mylius MR, Hansen BU, Liston GE, Schmidt NM (2016) Spatiotemporal characteristics of seasonal snow cover in Northeast Greenland from in situ observations. Arct Antarct Alp Res 48(4):653-671

Petrich C, Eicken H (2010) Growth, structure and Properties of Sea Ice. In: Thomas DN, Dieckmann GS (eds.) Sea Ice, Second Edition. Blackwell Publishing Ltd. pp 23-77

Petterssen S (1956) Weather Analysis and Forecasting, Second Edition, Vol. 2, McGraw-Hill Publ. Inc., New York, 266 pp

Pfeffer WT, Arendt AA, Bliss A, Bolch T, Cogley JG, Gardner AS, Hagen JO, Hock R, Kaser G, Kienholz C, Miles ES, Moholdt G, Mölg N, Paul F, Radić V, Rastner P, Raup BH, Rich J, Sharp MJ, the Randolph Consortium (2014) The Randolph Glacier Inventory: a globally complete inventory of glaciers. J Glaciol 60(221):537-552

Pilié RJ, Mack EJ, Rogers CW, Katz U, Kocmond WC (1979) The formation of marine fog and the development of fog-stratus systems along the California coast. J Appl Meteorol 18(10):1275-1286

Piskozub J, Cisek M, Gutowska D, Makuch P, Petelski T (2017) Mesoscale breeze circulation over Spitsbergen (Svalbard Archipelago). EGU Abstract # EGU2017-5665

Pithan F, Mauritsen T (2014) Arctic amplification dominated by temperature feedbacks in contemporary climate models. Nat Geosci 7(3):181-184

Pithan F, Medeiros B, Mauritsen T (2014) Mixed-phase clouds cause climate model biases in Arctic wintertime temperature inversions. Clim Dyn 43(1-2):289-303

Poore KD, Wang J, Rossow WB (1995) Cloud layer thicknesses from a combination of surface and upper-air observations. J Clim 8(3):550-568

Prik ZM (1960) Osnovnye rezul'taty meteorologicheskogo izucheniia Arktiki. (Main results of Arctic meteorological research.) Problemy Arktiki i Antarktiki, [Leningrad], 4:76-90

Przybylak R (2016) Cloudiness. In: Przybylak (ed) The Climate of the Arctic (pp. 111-126). Springer International Publishing

Rae RW (1951) Climate of the Canadian Arctic Archipelago. Meteorological Service of Canada, 90 pp

Rastner P, Bolch T, Mölg N, Machguth H, Paul F (2012) The first complete glacier inventory for the whole of Greenland. Cryosphere 6:1483-1495

Reiquam H, Diamond M (1959) Investigation of fog whiteout. Res Rept 52, USACRREL (SIPRE), 18 pp

Reynolds RW, Smith TM, Liu C, Chelton DB, Casey KS, Schlax MG (2007) Daily high-resolution-blended analyses for sea surface temperature. J Clim 20(22):5473-5496

Richner H, Phillips PD (1982. The radiosonde intercomparison SONDEX spring 1981, Payerne. Pure Appl Geophys 120(5-6):852-1198

Roach WT, Brown R, Caughey SJ, Garland JA, Readings CJ (1976) The physics of radiation fog: I–a field study. Q J R Meteorol Soc 102(432):313-333

Roach WT, Brown R, Caughey SJ, Crease BA, Slingo A (1982) A field study of nocturnal stratocumulus: I. Mean structure and budgets. Q J R Meteorol Soc 108(455):103-123

Rogers AN, Bromwich DH, Sinclair EN, Cullather RI (2001) The atmospheric hydrologic cycle over the Arctic basin from reanalyses. Part II: Interannual variability. J Clim 14(11):2414-2429

Román-Cascón C, Yagüe C, Steeneveld G-Y, Sastre M, Arrillaga JA, Maqueda G (2015) Estimating fog-top height through near-surface micrometeorological measurements. Atmos Res 170:76-86

Rose T, Czekala H (2005) Accurate Atmospheric Profiling with the RPG-HATPRO Humidity and Temperature Profiler. Operating manual. Radiometer Physic, GmbH, Meckenheim, Germany

Sandell HT, Sandell B (1991) Archaeology and environment in the Scoresby Sund fjord. Museum Tusculanum Press

Sandell H, Sandell B (1996) Polar bear hunting and hunters in Ittoqqortoormiit/Scoresbysund, NE Greenland. Arctic Anthropol 33(2):77-93

Saunders PM (1964) Sea smoke and steam fog. Q J R Meteorol Soc 90(384):156-165

Schneider W, Budéus G (1994) The north east water polynya (Greenland Sea). Polar Biol 14(1):1-9

Schweiger AJ (2004) Changes in seasonal cloud cover over the Arctic seas from satellite and surface observations. Geophys Res Lett 31(12):10.1029/2004GL020067

Screen JA, Simmonds I (2010) The central role of diminishing sea ice in recent Arctic temperature amplification. Nature 464(7293):1334-1337

Sedlar J, Tjernström M (2009) Stratiform cloud—inversion characterization during the Arctic melt season. Boundary-Layer Meteorol 132(3):455-474

Sedlar J, Shupe MD, Tjernström M (2012) On the relationship between thermodynamic structure and cloud top, and its climate significance in the Arctic. J Clim 25(7):2374-2393

Serreze MC, Barry RG (2005) The Arctic Climate System. Dessler AJ, Houghton JT, Rycroft MJ (eds), Cambridge University Press, 385 pp

Serreze MC, Barry RG (2011) Processes and impacts of Arctic amplification: A research synthesis. Global Planet Change 77(1-2):85-96

Serreze MC, Barry RG (2014) The Arctic climate system. Cambridge University Press, 2nd edition, 415 pp

Serreze MC, Francis JA (2006) The Arctic amplification debate. Clim Change 76(3-4):241-264

Serreze MC, Schnell RC, Kahl JD (1992) Low-level temperature inversions of the Eurasian Arctic and comparisons with Soviet drifting station data. J Clim 5(6):615-629

Serreze MC, Barrett AP, Slater AG, Steele M, Zhang J, Trenberth KE (2007a) The large-scale energy budget of the Arctic. J Geophys Res Atmos 112(D11):10.1029/2006JD008230

Serreze MC, Holland MM, Stroeve J (2007b) Perspectives on the Arctic's shrinking sea-ice cover. Science 315(5818):1533-1536

Shaw GE (1995) The Arctic haze phenomenon. Bull Am Meteorol Soc 76(12);2403-2413

Shupe MD, Intrieri JM (2004) Cloud radiative forcing of the Arctic surface: The influence of cloud properties, surface albedo, and solar zenith angle. J Clim 17(3):616-628

Shupe MD, Persson POG, Brooks IM, Tjernström M, Sedlar J, Mauritsen T, Sjogren S, Leck C (2013) Cloud and boundary layer interactions over the Arctic sea ice in late summer. Atmos Chem Phys 13:9379-9400

Smith SL, Bonnaventure PP (2017) Quantifying surface temperature inversions and their impact on the ground thermal regime at a High Arctic site. Arct Antarct Alp Res 49(1):173-185

Smith LC, Stephenson SR (2013) New Trans-Arctic shipping routes navigable by midcentury. Proc Natl Acad Sci USA 110(13):E1191-E1195.

Sobik M, Błaś M (2016) http://fog-conf.meteo.uni.wroc.pl/index.php/frequency-of-fog-a-global-outlook

Sotiropoulou G, Sedlar J, Tjernström M, Shupe MD, Brooks IM, Persson POG (2014) The thermodynamic structure of summer Arctic stratocumulus and the dynamic coupling to the surface. Atmos Chem Phys 14(22):12573-12592

Sotiropoulou G, Tjernström M, Sedlar J, Achtert P, Brooks BJ, Brooks IM, Persson POG, Prytherch J, Salisbury DJ, Shupe MD, Johnston PE, Wolfe D (2016) Atmospheric Conditions during the Arctic Clouds in Summer Experiment (ACSE): Contrasting Open Water and Sea Ice Surfaces during Melt and Freeze-Up Seasons. J Clim 29(24):8721-8744

Stearns LA, Jiskoot H (2014) Glacier fluctuations and dynamics around the margin of the Greenland Ice Sheet. In Global Land Ice Measurements from Space (pp. 183-204). Springer Berlin Heidelberg

Steffen K, Box J (2001) Surface climatology of the Greenland ice sheet: Greenland Climate Network 1995–1999. J Geophys Res Atmos 106(D24):33951-33964

Stein AF, Draxler RR, Rolph GD, Stunder BJB, Cohen MD, Ngan F (2015) NOAA's HYSPLIT atmospheric transport and dispersion modeling system. Bull Am Meteorol Soc 96(12):2059-2077

Steinbrecht W, Claude H, Schönenborn F, Leiterer U, Dier H, Lanzinger E (2008) Pressure and temperature differences between Vaisala RS80 and RS92 radiosonde systems. J Atmos Ocean Technol 25(6):909-927

Stone RS, Kahl JD (1991) Variations in boundary layer properties associated with clouds and transient weather disturbances at the South Pole during winter. J Geophys Res Atmos 96(D3):5137-5144

Sträter E, Westbeld A, Klemm O (2010) Pollution in coastal fog at Alto Patache, Northern Chile. Environ Sci Pollut Res 17(9):1563-1573

Struthers H, Ekman AML, Glantz P, Iversen T, Kirkevåg A, Mårtensson EM, Seland Ø, Nilsson ED (2011) The effect of sea ice loss on sea salt aerosol concentrations and the radiative balance in the Arctic. Atmos Chem Phys 11(7):3459-3477

Stull RB (1988) An Introduction to Boundary Layer Meteorology. Kluwer Academic Publishers, Dordrecht, 670 pp

Svendsen H, Beszczynska-Møller A, Hagen JO, Lefauconnier B, Tverberg V, Gerland S, Ørbæk JB, Bischof K, Papucci C, Zajaczkowski M, Azzolini R, Bruland O, Wiencke C, Winther J-G, Dallman W (2002) The physical environment of Kongsfjorden–Krossfjorden, an Arctic fjord system in Svalbard. Polar Res 21(1):133-166

Tarasick DW, Bottenheim JW (2002) Surface ozone depletion episodes in the Arctic and Antarctic from historical ozonesonde records. Atmos Chem Phys 2(3):197-205

Taylor PC, Cai M, Hu AX, Meehl J, Washington W, Zhang GJ (2013) A decomposition of feedback contributions to polar warming amplification. J Clim 26(18):7023-7043

Telford JW, Chai SK (1984) Inversions, and fog, stratus and cumulus formation in warm air over cooler water. Boundary-Layer Meteorol 29(2):109-137

Thompson DW, Wallace JM (1998) The Arctic Oscillation signature in the wintertime geopotential height and temperature fields. Geophys Res Lett 25(9):10.1029/98GL00950

Tjernström M, Birch CE, Brooks IM, Shupe MD, Persson POG, Sedlar J, Mauritsen T, Leck C, Paatero J, Szczodrak M, Wheeler CR (2012) Meteorological conditions in the central Arctic summer during the Arctic Summer Cloud Ocean Study (ASCOS). Atmos Chem Phys 12(15):6863-6889

Tjernström M, Leck C, Birch CE, Bottenheim JW, Brooks BJ, Brooks IM, Bäcklin L, Chang RY-W, de Leeuw G, Di Liberto L, de la Rosa S, Granath E, Graus M, Hansel A, Heintzenberg J, Held A, Hind A, Johnston P, Knulst J, Martin M, Matrai PA, Mauritsen

T, Müller M, Norris SJ, Orellana M.V, Orsini DA, Paatero J, Persson POG, Gao Q, Rauschenberg C, Ristovski Z, Sedlar J, Shupe MD, Sierau B, Sirevaag A, Sjogren S, Stetzer O, Swietlicki E, Szczodrak M, Vaattovaara P, Wahlberg N, Westberg M, Wheeler CR (2014) The Arctic Summer Cloud Ocean Study (ASCOS): overview and experimental design. Atmos Chem Phys 14(6):2823-2869

Tjernström M, Shupe MD, Brooks IM, Persson POG, Prytherch J, Salisbury DJ, Sedlar J, Achtert P, Brooks BJ, Johnston PE, Sotiropoulou G, Wolfe D (2015) Warm-air advection, air mass transformation and fog causes rapid ice melt. Geophys Res Lett, 42(13): 10.1002/2015GL064373

Toth G, Gultepe I, Milbrandt J, Hansen B, Pearson G, Fogarty C, Burrows W (2010). The environment Canada handbook on fog and fog forecasting. Environment Canada, 1-117

Triplet JP, Roche G (1986) Météorologie générale, troisième édition. Paris: Ecole Nationale de la Meteorologie. 317 pp

Ukhanova EV (1971) Fogs and visibility. In: Dolgin IM (Ed) Meteorological Conditions of the non-Soviet Arctic, Gidrometeoizdat, Leningrad, pp 142-151 (in Russian)

US Bureau of Naval Personnel (1965) Chapter 5: Forecasting Severe Weather Features. In: Aerographer's mate 1 & C. Washington, US. Govt. Print. Off., 1960-61

Uttal T, Curry JA, Mcphee MG, Perovich DK, Moritz RE, Maslanik JA, Guest PS, Stern HL, Moore JA, Turenne R, Heiberg A, Serreze MC, Wylie DP, Persson OG, Paulson CA, Halle C, Morison JH, Wheeler PA, Makshtas A, Welch H, Shupe MD, Intrieri JM, Stamnes K, Lindsey RW, Pinkel R, Pegau WS, Stanton TP, Grenfeld TC (2002) Surface heat budget of the Arctic Ocean. Bull Am Meteorol Soc 83(2):255-275

Vaisala (2002) Weather Sensor FD12P User's Guide. M210296en-A, Helsinki, 154 pp

Vaisala (2006) Vaisala HUMICAP® Humidity and Temperature Probes HMP45A/D https://www.vaisala.com/sites/default/files/documents/HMP45AD-User-Guide-U274EN.pdf

Vaisala (2017) Radiosonde RS92 : http://www.vaisala.com/en/products-/soundingsystemsandradiosondes/radiosondes/Pages/RS92.aspx (accessed on May 28, 2017)

van Angelen JH, Van den Broeke MR, Kwok R (2011) The Greenland Sea Jet: A mechanism for wind-driven sea ice export through Fram Strait. Geophys Res Lett 38(12):10.1029/2011GL047837

van den Broeke MR, Enderlin EM, Howat IM, Noël BP (2016) On the recent contribution of the Greenland ice sheet to sea level change. Cryosphere 10(5):1933

Van Tricht K, Lhermitte S, Lenaerts JT, Gorodetskaya IV, L'Ecuyer TS, Noël B, van den Broeke MR, Turner DD, Van Lipzig NP (2016) Clouds enhance Greenland ice sheet meltwater runoff. Nat Commun 7(10266)

Vaughan DG, Comiso JC, Allison I, Carrasco J, Kaser G, Kwok R, Mote P, Murray T, Paul F, Ren J, Rignot E, Solomina O, Steffen K, Zhang T (2013) Observations: Cryosphere Supplementary Material. In: Stocker TF, Qin D, Plattner G-K, Tignor M, Allen SK, Boschung J, Nauels A, Xia Y, Bex V, Midgley PM (eds.) Climate Change 2013: The Physical Science Basis. Contribution of Working Group I to the Fifth Assessment Report of the Intergovernmental Panel on Climate Change. Available from www.climatechange2013.org and www.ipcc.ch

Vavrus S, Holland MM, Bailey DA (2011) Changes in Arctic clouds during intervals of rapid sea ice loss. Clim Dyn 36(7-8):1475-1489

Vihma T, Screen J, Tjernström M, Newton B, Zhang X, Popova V, Deser C, Holland M, Prowse T (2016) The atmospheric role in the Arctic water cycle: A review on processes, past and future changes, and their impacts. J Geophys Res Biogeosci 121(3):586-620

Vinje T (2001) Fram Strait ice fluxes and atmospheric circulation: 1950-2000. J Clim 14(16):3508-3517

Wærsted EG, Haeffelin M, Dupont JC, Delanoë J, Dubuisson P (2017) Radiation in fog: Quantification of the impact on fog liquid water based on ground-based remote sensing. Atmos Chem Phys 17:10811:10835

Wang J, Rossow WB (1995) Determination of cloud vertical structure from upper-air observations. J Appl Meteorol 34(10):2243-2258

Wang J, Rossow WB, Uttal T, Rozendaal M (1999) Variability of cloud vertical structure during ASTEX observed from a combination of rawinsonde, radar, ceilometer and satellite. Mon Weather Rev 127:2484–2502

Wang W, Zender CS, van As D, Smeets P, van den Broeke MR (2016) Cloud-Induced Stabilization of Greenland Surface Melt. AGU Fall Meeting Abstract # A23M-08

Welch RM, Wielicki BA (1986) The stratocumulus nature of fog. J Appl Meteorol Clim 25(2):101-111

Winker DM, Vaughan MA, Omar A, Hu Y, Powell KA, Liu Z, Hunt WH, Young SA (2009) Overview of the CALIPSO mission and CALIOP data processing algorithms. J Atmos Ocean Technol 26(11):2310-2323

Wood R (2012) Stratocumulus clouds. Mon Weather Rev 140(8):2373-2423

World Meteorological Organization (WMO) (1995) Manual on Codes, Volume I.1: part A – Alphanumeric Codes. WMO-No. 306, Geneva, 503 pp

World Meteorological Organization (WMO) (2017) International Cloud Atlas (2017 edition). https://cloudatlas.wmo.int/

Zhang YH, Seidel DJ (2011) Challenges in estimating trends in Arctic surface-based inversions from radiosonde data. Geophys Res Lett 38(17):10.1029/2011GL048728

Zhang T, Stamnes K, Bowling SA (1996) Impact of clouds on surface radiative fluxes and snowmelt in the Arctic and Subarctic. J Clim 9(9):2110-2123

Zhang SP, Xie SP, Liu QY, Yang YQ, Wang XG, Ren ZP (2009) Seasonal variations of Yellow Sea fog: Observations and mechanisms. J Clim 22(24):6758-6772

Zhang J, Chen H, Li Z, Fan X, Peng L, Yu Y, Cribb M (2010) Analysis of cloud layer structure in Shouxian, China using RS92 radiosonde aided by 95 GHz cloud radar. J Geophys Res Atmos 115(D7):10.1029/2010JD014030

Zhang Y, Seidel DJ, Golaz JC, Deser C, Tomas RA (2011) Climatological characteristics of Arctic and Antarctic surface-based inversions. J Clim 24(19):5167-5186

Zhang J, Li Z, Chen H, Cribb M (2013) Validation of a radiosonde-based cloud layer detection method against a ground-based remote sensing method at multiple ARM sites. J Geophys Res Atmos 118(2):846-858

Zhong L, Hua L, Luo D (2018) Local and external moisture sources for the Arctic warming over the Barents-Kara Seas. J Clim (early online release):10.1175/JCLI-D-17-0203.1

Zhu J, Chen Y, Zhang L, Jia X, Feng Z, Wu G, Yan X, Zhai J, Wu Y, Chen Q, Zhou X, Wang Z, Zhang C, Kang L, Chen J, Wu P (2017) Demonstration of measuring sea fog with an SNSPD-based Lidar system. Sci Rep 7(1):15113

APPENDICES

APPENDIX 1: Wind roses with 16 cardinal directions of surface wind speed and direction for all summer weather and summer fog observations in the morning (AM) and in the afternoon (PM), corresponding to Fig. 2-19.

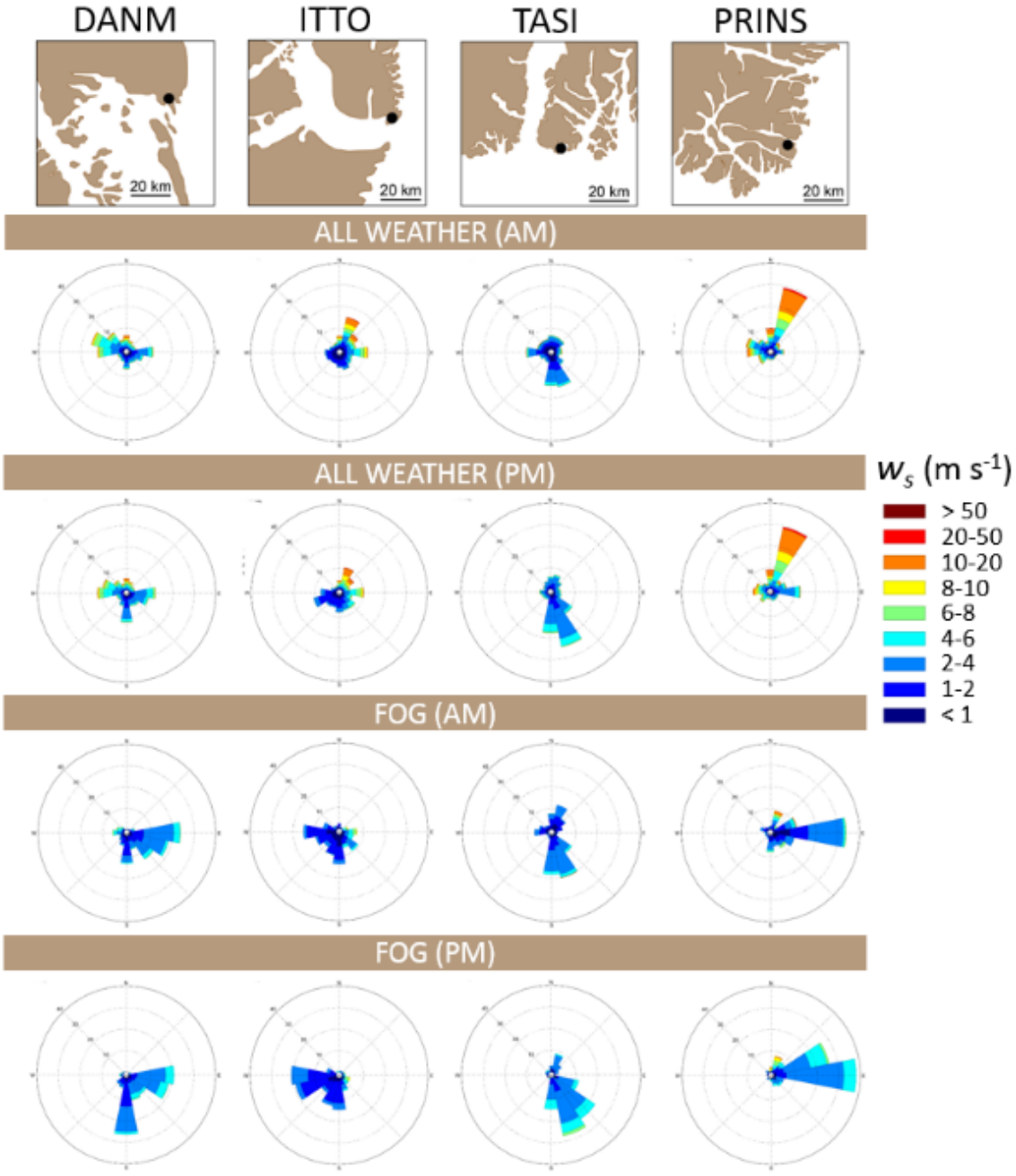

APPENDIX 2: Wind roses with surface wind speed and direction occurring immediately after the end of summer fog.

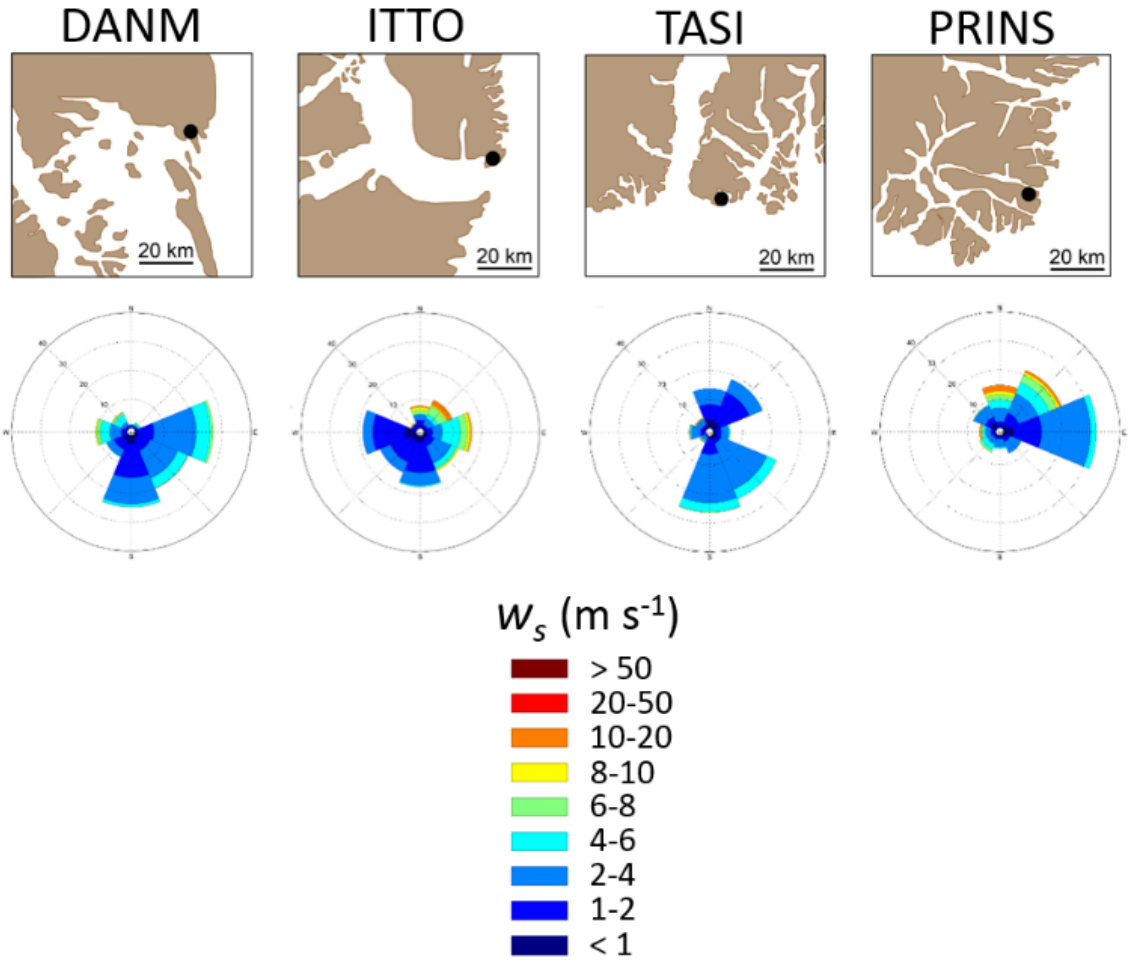

APPENDIX 3: Examples of standardised combined graph of surface and upper-air observations (Skew-*T* Log-*P* diagrams: main plot). Subplots include wind direction (solid red line, right plot) and specific humidity (solid black line, right plot), surface temperature and dew point temperature time series with fog events (vertical grey bars, upper left plot).

Class 1:

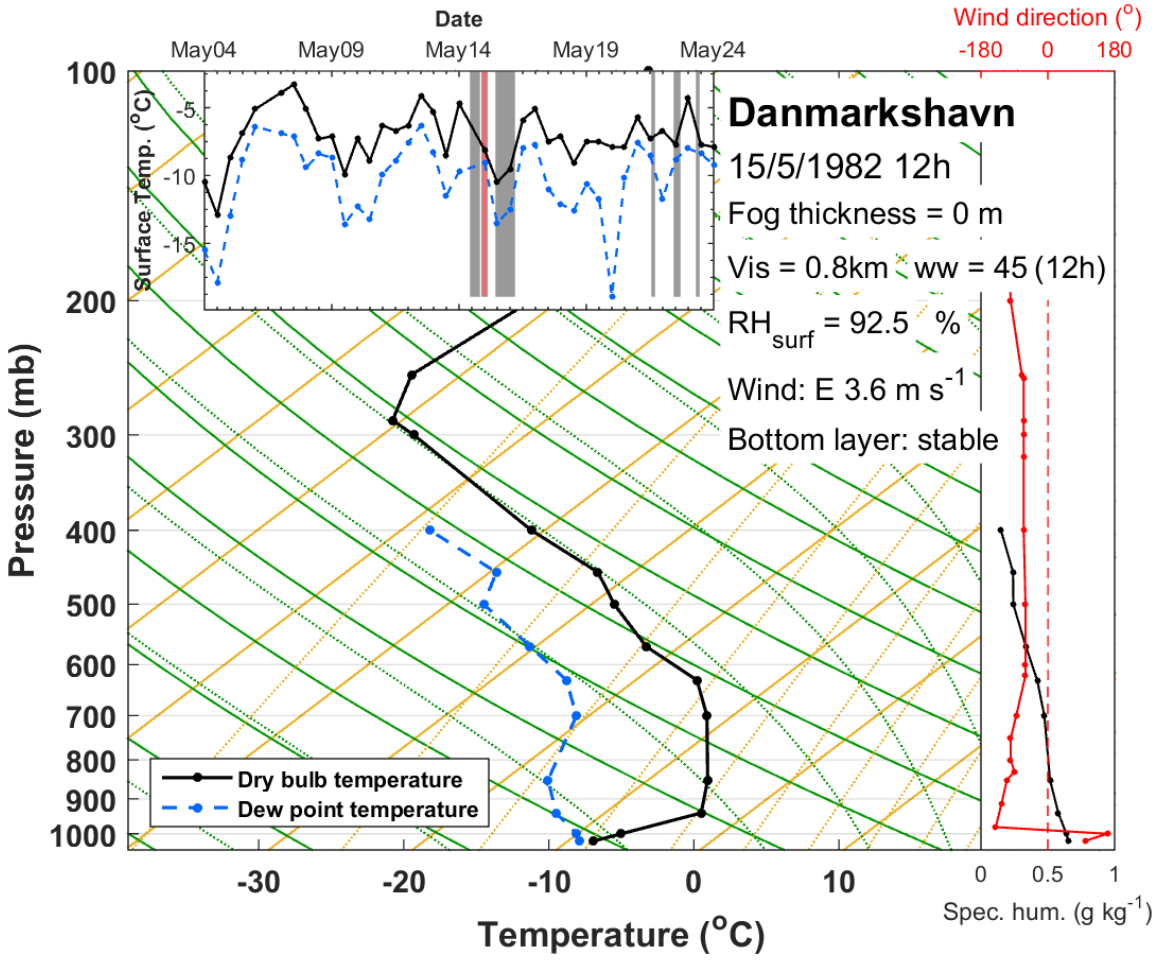

Class 2 (alternative 1):

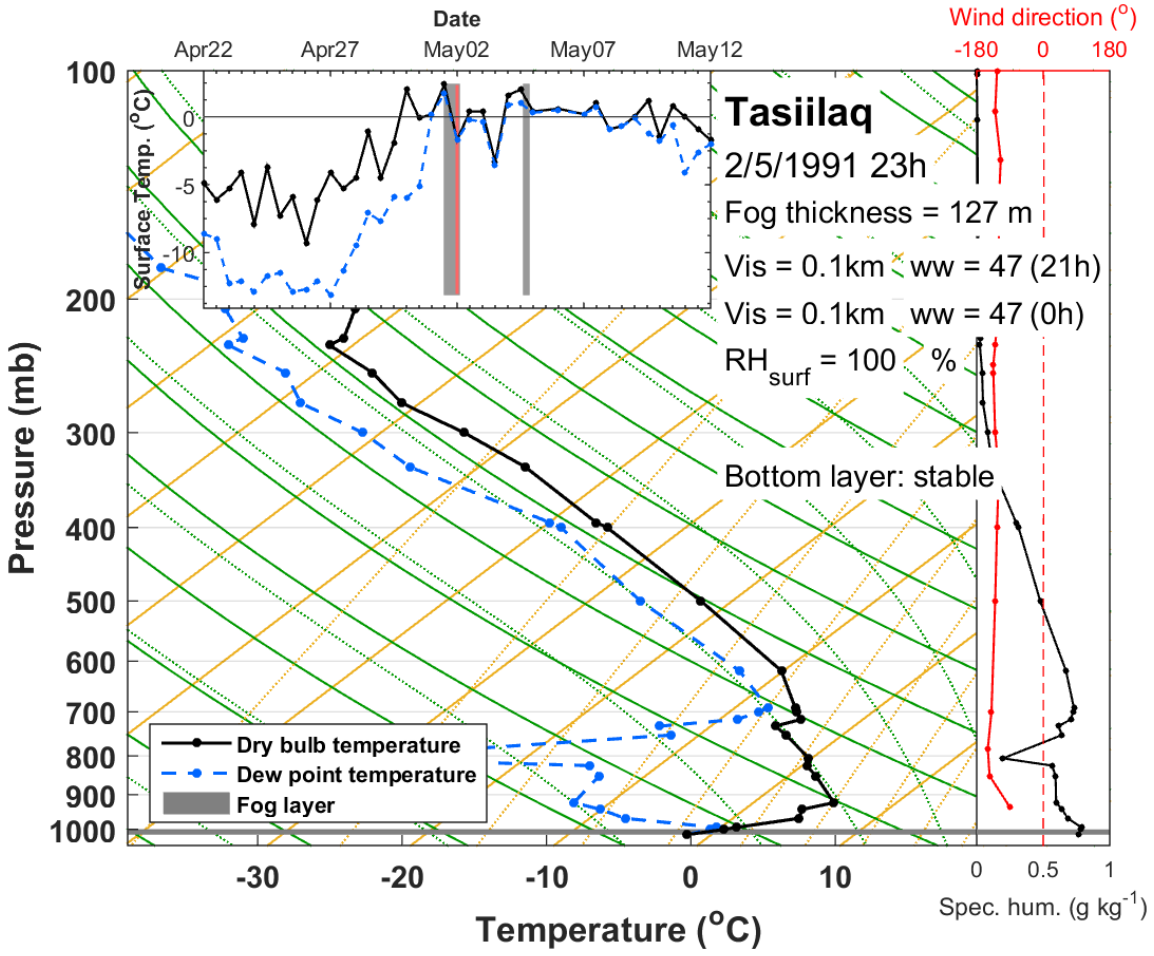

Class 2 (alternative 2):

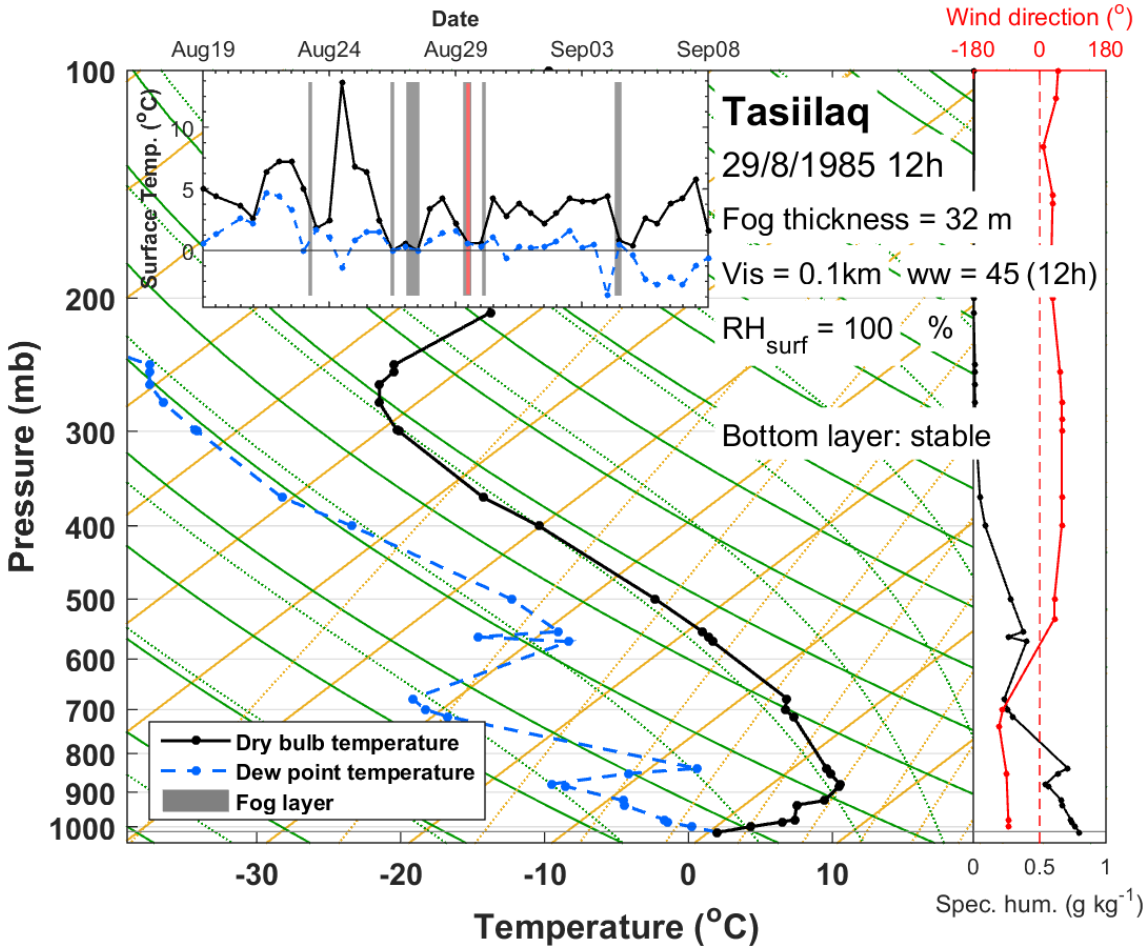

Class 3:

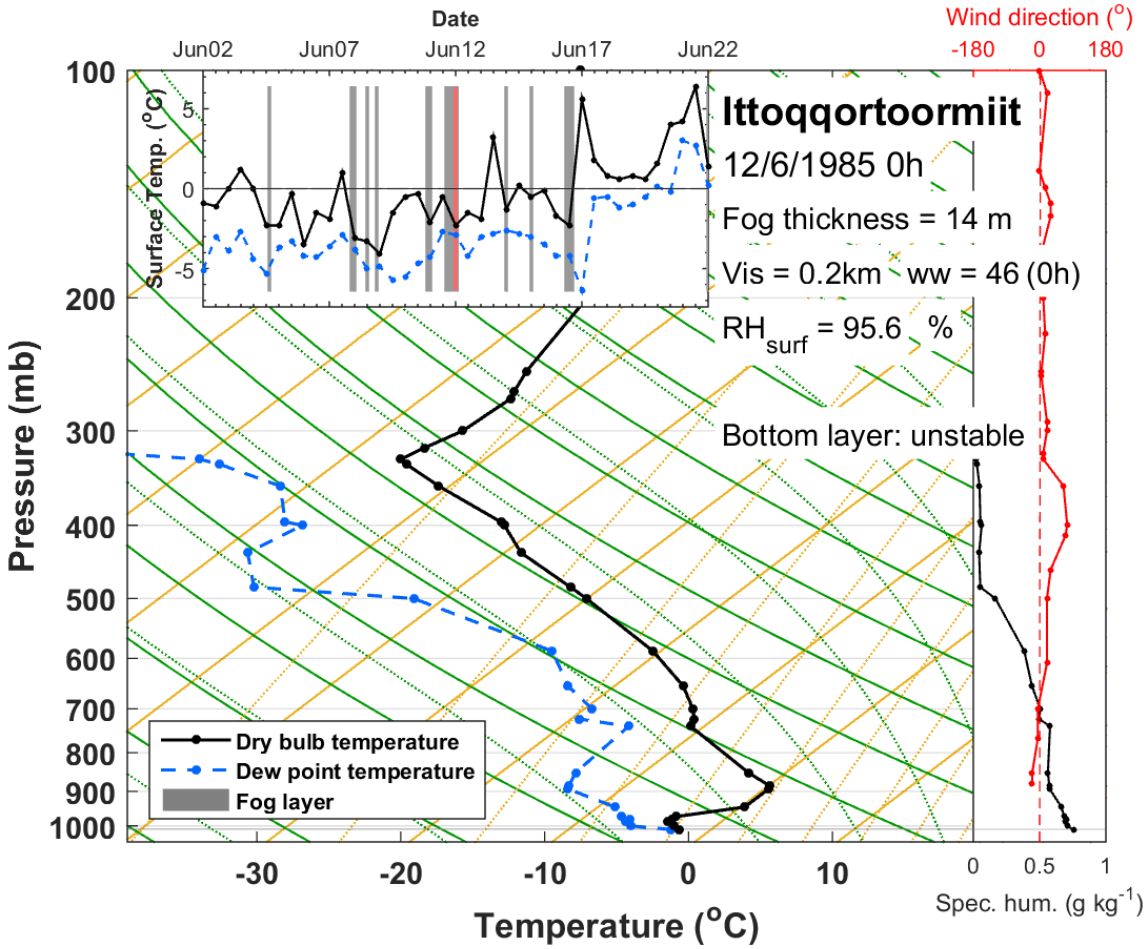
Date
Jun02
Jun07
Jun12
Jun17
Jun22
Wind direction (°)
-180
0
180
Surface Temp. (°C)
5
0
-5
Ittoqqortoormiit
12/6/1985 0h
Fog thickness = 14 m
Vis = 0.2km ww = 46 (0h)
RH surf = 95.6 %
Bottom layer: unstable
Pressure (mb)
100
200
300
400
500
600
700
800
900
1000
Dry bulb temperature
Dew point temperature
Fog layer
-30
-20
-10
0
10
Temperature (°C)
0
0.5
1
Spec. hum. (g kg-1)

Class 4:

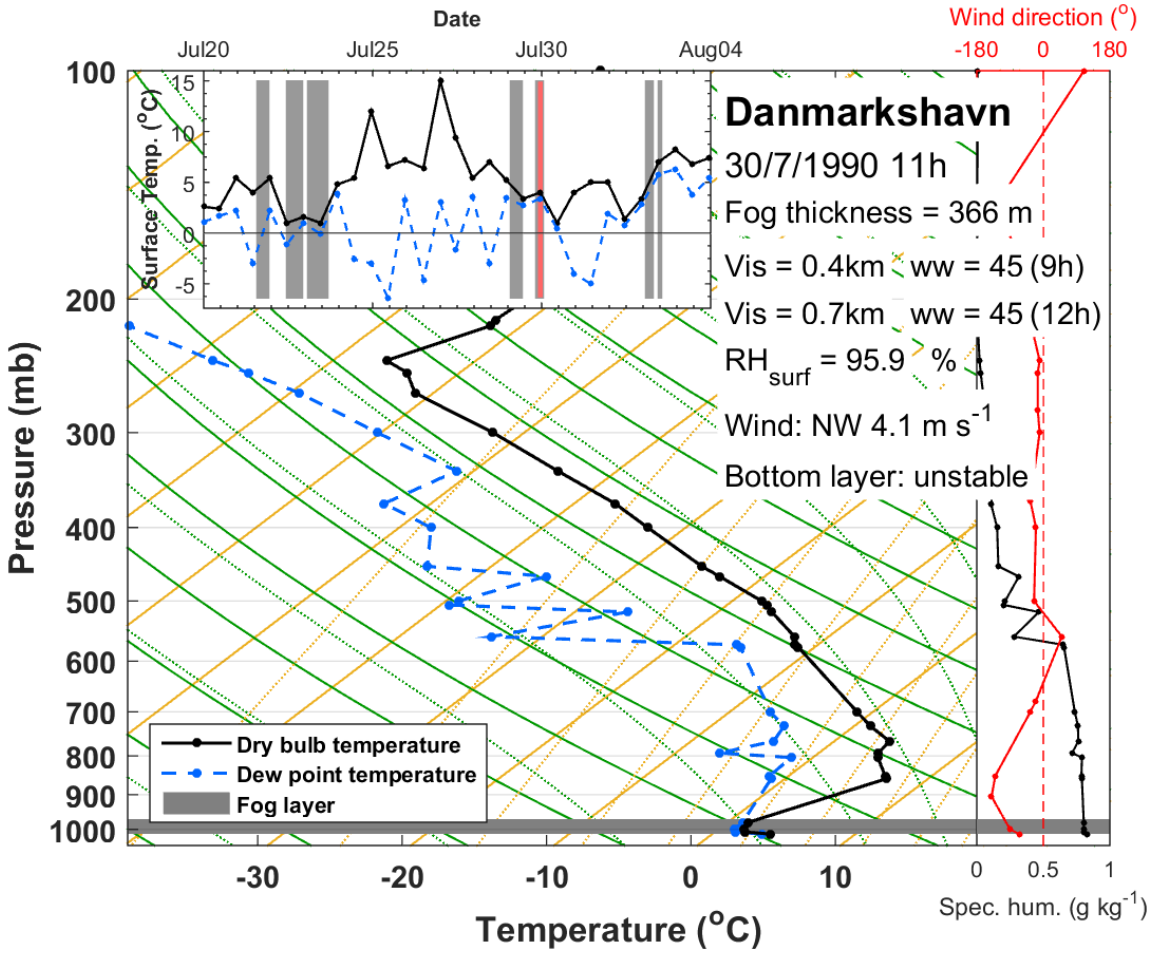
Date
Jul20
Jul25
Jul30
Aug04
Wind direction (°)
-180
0
180
Surface Temp. (°C)
15
10
5
0
-5
Danmarkshavn
30/7/1990 11h
Fog thickness = 366 m
Vis = 0.4km ww = 45 (9h)
Vis = 0.7km ww = 45 (12h)
RH surf = 95.9 %
Wind: NW 4.1 m s-1
Bottom layer: unstable
Pressure (mb)
100
200
300
400
500
600
700
800
900
1000
Dry bulb temperature
Dew point temperature
Fog layer
-30
-20
-10
0
10
Temperature (°C)
0
0.5
1
Spec. hum. (g kg-1)

Class 5:

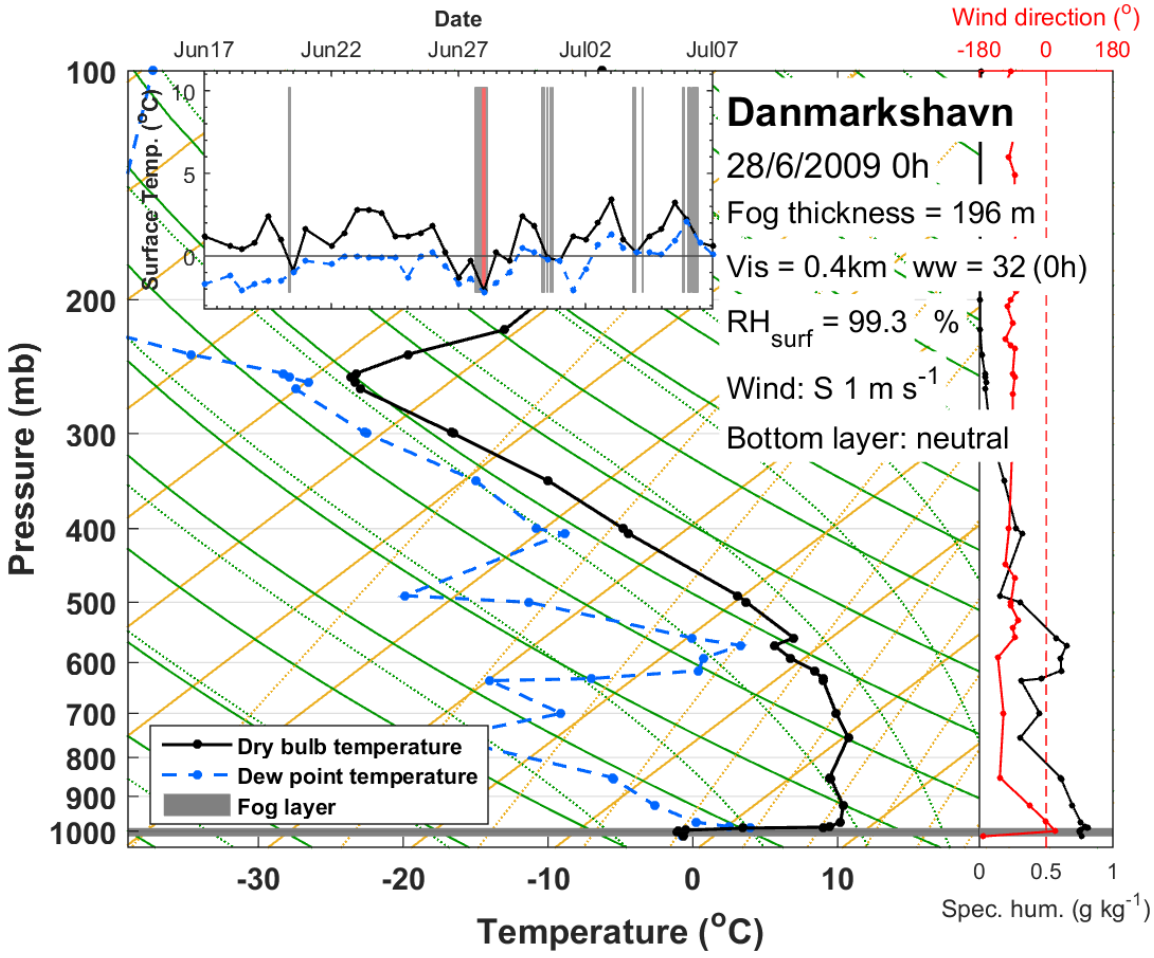
Date
Jun17
Jun22
Jun27
Jul02
Jul07
Wind direction (°)
-180
0
180
Surface Temp. (°C)
10
5
0
Danmarkshavn
28/6/2009 0h
Fog thickness = 196 m
Vis = 0.4km ww = 32 (0h)
RH surf = 99.3 %
Wind: S 1 m s-1
Bottom layer: neutral
Pressure (mb)
100
200
300
400
500
600
700
800
900
1000
Dry bulb temperature
Dew point temperature
Fog layer
-30
-20
-10
0
10
Temperature (°C)
0
0.5
1
Spec. hum. (g kg-1)

Class 6:

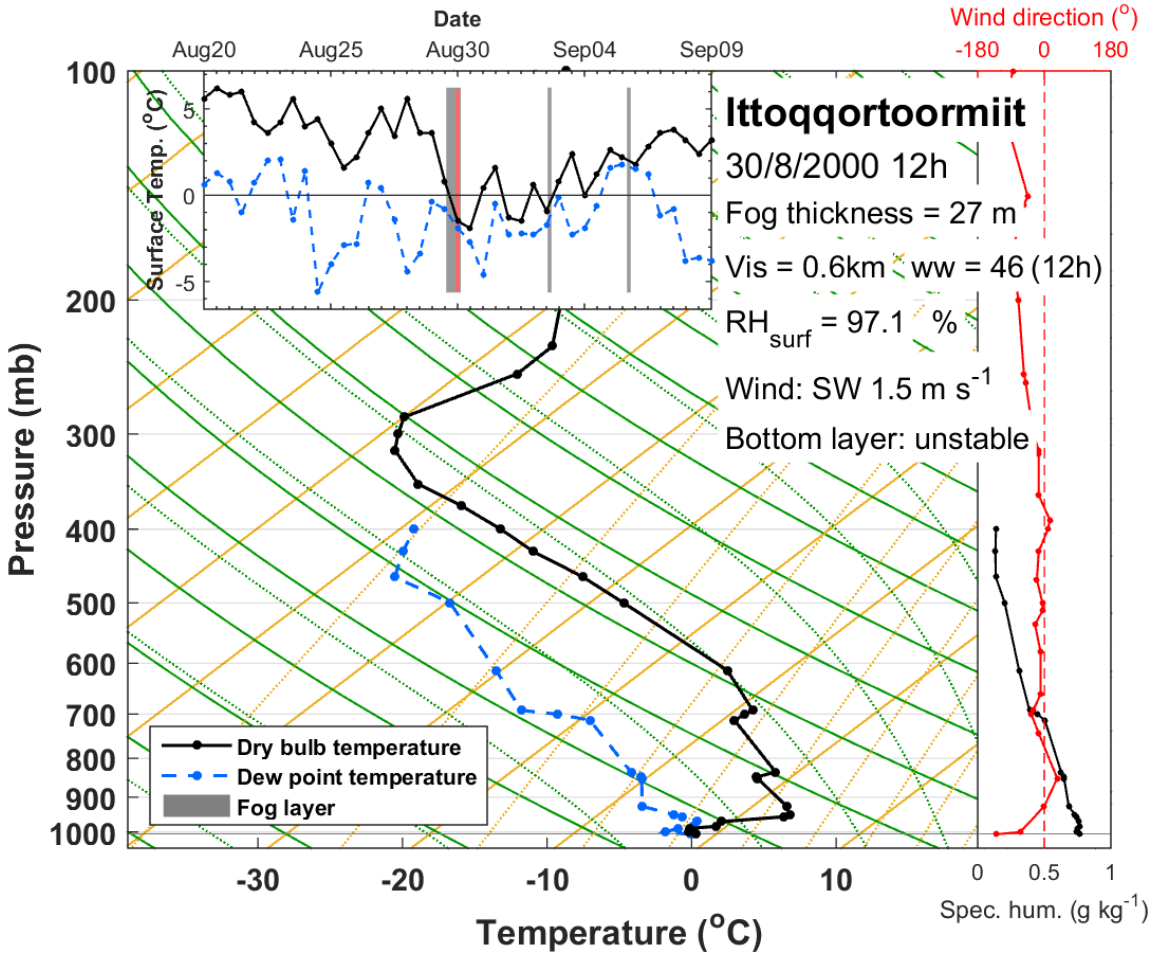
Date
Aug20
Aug25
Aug30
Sep04
Sep09
Wind direction (°)
-180
0
180
Surface Temp. (°C)
5
0
-5
Ittoqqortoormiit
30/8/2000 12h
Fog thickness = 27 m
Vis = 0.6km ww = 46 (12h)
RH surf = 97.1 %
Wind: SW 1.5 m s-1
Bottom layer: unstable
Pressure (mb)
100
200
300
400
500
600
700
800
900
1000
Dry bulb temperature
Dew point temperature
Fog layer
-30
-20
-10
0
10
Temperature (°C)
0
0.5
1
Spec. hum. (g kg-1)

Fog without inversion:

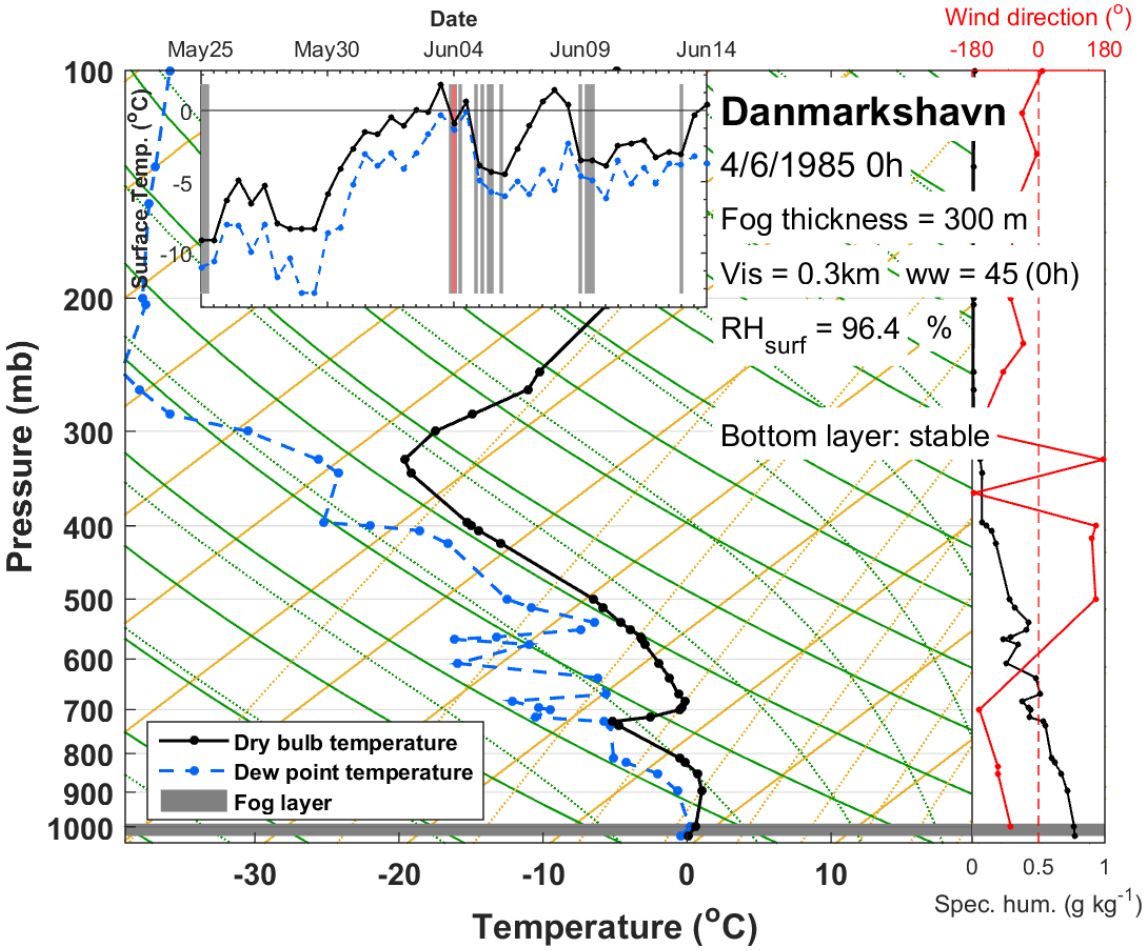

APPENDIX 4: Matlab script to generate standardised combined graph of surface observations and upper-air profiles.

```
% ------------------------------------------------------------------- %
% Script generating standardised combined graph of surface observations
% and upper-air profiles, including a Skew-T Log-P diagram with the fog
% layer, vertical profiles of wind direction and specific humidity, and
% time series of surface temperature, dew point temperature and fog
events.
% Surface observations are from the Danish Meteorological Institute.
% Upper-air observations are from the Integrated Global Radiosonde
Archive (IGRA).
% Author: Gaelle F. Gilson (Feb 2018)
% Contact: gaellegilson86@gmail.com
% ------------------------------------------------------------------- %

clear all
close all

% Insert year, month, day and time of sounding
yyyy = 2000;
mm = 8;
dd = 30;
time = 12; % UTC

% Select station
for stat=2:2
    switch stat
        case 1, station_nb = 4320; station = 'Danmarkshavn';
        case 2, station_nb = 4339; station = 'Ittoqqortoormiit';
        case 3, station_nb = 4360; station = 'Tasiilaq';
    end
end

dwpt_threshold = 1; % dew point depression threshold obtained from
boxplots of surface dew point depression
(radiosonde_dewpoint_boxplot.m). Can be modified
T_threshold = -10; % Temperature threshold for warm fog


%-------------------------------------%
% open IGRA file (derived variables) %
%-------------------------------------%

radiosonde = load(sprintf('C:/Gaelle/Matlab/IGRA/%s/derived-
por/%s_derived_v2.mat',num2str(station_nb),num2str(station_nb)));

year_hdr = radiosonde.ans.headers(:,2);
month_hdr = radiosonde.ans.headers(:,3);
day_hdr = radiosonde.ans.headers(:,4);
time_hdr = radiosonde.ans.headers(:,5);
```

```
% check whether sounding exists
ind = find(year_hdr == yyyy & month_hdr == mm & day_hdr == dd & time_hdr
== time);
if isempty(ind)
    continue
end

% select sounding
sounding = radiosonde.ans.soundings{1,ind};

% Basic variables
pr=sounding(:,1); % pressure used for most calculations (in Pa)
pz=pr/100; % pressure that will be used for plotting (in mb)
tz=(sounding(:,4)-2731.5)/10;
rhz=sounding(:,13)/10;

% virtual potential temperature (for stability calculations)
VPTEMP = (sounding(:,9)-2731.5)/10;

% Characterization of bottom layer
if VPTEMP(2)-VPTEMP(1)<0 % unstable
    stability = -1;
elseif VPTEMP(2)-VPTEMP(1)>0 % stable
    stability = 1;
elseif VPTEMP(2)==VPTEMP(1) % neutral
    stability = -1;
end

%-------------------------------------%
% open IGRA file (measured variables) %
%-------------------------------------%

radiosonde_datapor = load(sprintf('C:/Gaelle/Matlab/IGRA/IGRA-data-
por/data_2017/%s_datapor.mat',num2str(station_nb)));
ind_datapor = find(radiosonde_datapor.s.headers(:,2)==yyyy &
radiosonde_datapor.s.headers(:,3)==mm &
radiosonde_datapor.s.headers(:,4)==dd &
radiosonde_datapor.s.headers(:,5)==time);

% check whether sounding exists
if isempty(ind_datapor) % if datapor doesn't exist, Td doesn't exist and
no plot or calculations can be made
    continue
end

% select sounding
sounding_datapor = radiosonde_datapor.s.soundings{1,ind_datapor};

% Wind parameters
wd_datapor_pre = sounding_datapor(:,9); % wind direction in degrees
ws_datapor = sounding_datapor(:,10)/10; % wind speed in m/s

% Dew point depression Tdd
Tdd_datapor = sounding_datapor(:,8);
Tdd_datapor(Tdd_datapor == -9999) = NaN;
```

```
Tdd = Tdd_datapor/10;

k=0;
for ind_pr = 1:length(Tdd)
    if sounding_datapor(ind_pr,6) == -9999 % if temperature doesnt
exist, than missing Td is because of missing observation
        continue
    else
        k=k+1;
        Tdd_adj_level(k,1) = Tdd(ind_pr,1);
    end
end

% Calculate dew point temperature: tdz = tz - Tdd
if length(tz) < length(Tdd_adj_level)
    for i = 1:length(tz)
        if Tdd_adj_level(i,1) == -888.8
            Tdd_adj_level(i,1) = NaN;
            tdz_datapor(i,1) = NaN;
        else
            tdz_datapor(i,1) = tz(i,1) - Tdd_adj_level(i,1);
        end
    end
elseif length(tz) >= length(Tdd_adj_level)
    for i = 1:length(Tdd_adj_level)
        if Tdd_adj_level(i,1) == -888.8
            Tdd_adj_level(i,1) = NaN;
            tdz_datapor(i,1) = NaN;
        else
            tdz_datapor(i,1) = tz(i,1) - Tdd_adj_level(i,1);
        end
    end
end

e = sounding(:,10); % vapour pressure in Pa*10 (must divide by 1000 to
get mb or hPa)
ew_sound = sounding(:,11); % Saturation vapour pressure from sounding in
Pa*10 (must divide by 1000 to get mb or hPa)
r = 622*((e/1000)./(pz-(e/1000))); % mixing ratio in g/kg
rw_calc = 622*((ew_sound/1000)./(pz-(ew_sound/1000)));% Calculated
saturation mixing ratio in g/kg
spec_humid = r./(1+r); % specific humidity

% Nb of levels below 700 mb in tz and tdz profiles
Nb_levels_700mb_T = find(pz==700);
if isempty(Nb_levels_700mb_T) % in case 700mb level missing
    Nb_levels_700mb_T = length(find(pz>=750));
end
Nb_levels_700mb_Td = find(sounding_datapor(:,4)==70000);
if isempty(Nb_levels_700mb_Td) % in case 700mb level missing
    Nb_levels_700mb_Td = length(find(sounding_datapor(:,3)>=75000));
end

if tz(1,1) <= T_threshold || Nb_levels_700mb_T < 5 || Nb_levels_700mb_Td
< 5 % remove observation of mixed-phase or ice fog and soundings with
```

```
less than 5 levels between the surface and 700mb pressure level in
either T or Td profile (after Kahl et al., 1992)
    continue
end

%-------------------------------------%
%      Inversion characteristics      %
%-------------------------------------%

% Inversion base
clear i
for i=1:length(tz)
    if tz(i+1)-tz(i)>0
        level_inv_base = i;
        inv_base = sounding(i,3);
        break
    end
end

% Inversion top
clear i
for i=level_inv_base:length(pz)-1
    if tz(i+1)-tz(i)<=0
        level_inv_top = i;
        inv_top = sounding(i,3);
        break
    end
end

% Inversion depth
inv_depth = inv_top - inv_base;

%-------------------------------------%
%    Surface T & Td from SOUNDINGS    % % for upper-left plot
%-------------------------------------%

radiosonde_temp_before_pre=zeros(20,8); % select 10 preceding soundings
for i=1:20
    radiosonde_t = radiosonde_datapor.s.soundings{1,ind_datapor-i}(1,:);
    radiosonde_temp_before_pre(i,1:length(radiosonde_t))=radiosonde_t;
    radiosonde_temp_before_pre_hdr(i,:) =
radiosonde_datapor.s.headers(ind_datapor-i,1:5); % header gives the date
and time
    clear radiosonde_t
end

radiosonde_temp_before = flipud(radiosonde_temp_before_pre);
radiosonde_temp_before_hdr = flipud(radiosonde_temp_before_pre_hdr);

radiosonde_temp_after=zeros(21,8); % select the sounding and 10 after
for i=1:21
    radiosonde_t = radiosonde_datapor.s.soundings{1,ind_datapor+i-
1}(1,:);
    radiosonde_temp_after(i,1:length(radiosonde_t))=radiosonde_t;
```

```
    radiosonde_temp_after_hdr(i,:) =
radiosonde_datapor.s.headers(ind_datapor+i-1,1:5); % header gives the
date and time
    clear radiosonde_t
end

radiosonde_temp = [radiosonde_temp_before_hdr radiosonde_temp_before
    radiosonde_temp_after_hdr radiosonde_temp_after];

T_sounding = (radiosonde_temp(:,11))/10;
T_sounding(T_sounding == -999.9)= NaN;
Td_sounding = (radiosonde_temp(:,11)/10) - (radiosonde_temp(:,13)/10); %
T-Tdd = Td

for i=1:length(radiosonde_temp)
    dates_graph(i) =
datenum(radiosonde_temp(i,2),radiosonde_temp(i,3),radiosonde_temp(i,4),r
adiosonde_temp(i,5),0,0);
end

Binary_obs_pos = zeros(length(radiosonde_temp),1);
for i=1:length(Binary_obs_pos)
    if i==21
        Binary_obs_pos(i,1) = max(T_sounding);
    else
        Binary_obs_pos(i,1) = 0;
    end
end

Binary_obs_neg = zeros(length(radiosonde_temp),1);
for i=1:length(Binary_obs_neg)
    if i==21
        Binary_obs_neg(i,1) = min(Td_sounding);
    else
        Binary_obs_neg(i,1) = 0;
    end
end

% Calculate variables for SKEW-T LOG-P DIAGRAM (main plot)

p=[1050:-25:100];
lnP=transpose(p);
skewT=[-48:2:50];
[ps1,ps2]=size(p);
ps=max(ps1,ps2);
[ts1,ts2]=size(skewT);
ts=max(ts1,ts2);

for i=1:ts,
    for j=1:ps,
        tem(i,j)=skewT(i)+30.*log(0.001.*p(j));
        thet(i,j)=(273.15+tem(i,j)).*(1000./p(j)).^.286; % Ra/Cpa =
287/1005 = 0.286
        ew=6.11.*10^(7.5.*tem(i,j)./(237.3+tem(i,j))); % Formula from
NOAA, checked against empirical table from Triplet et Roche
```

```
        rw(i,j)=622.*ew./(p(j)-ew); % Values for iso-rw lines
        thetaea(i,j)=thet(i,j).*exp(2.5.*rw(i,j)./(tem(i,j)+273.15));
    end
end

p=transpose(p);
skewT=transpose(skewT);
temp=transpose(tem);
O=transpose(thet);
Ow=transpose(thetaea);
rw=transpose(sqrt(rw));

% Calculate wind speed and direction from radiosonde

Wind_surf_raw = ((sounding(1,15)/10)^2+(sounding(1,17)/10)^2)^0.5;
Wind_surf = round(Wind_surf_raw,1);

for w = 1:length(sounding(:,15))
    tan_alpha(w,1) = sounding(w,17)/sounding(w,15);
    alpha_rad(w,1) = atan(tan_alpha(w,1));
    alpha_degrees(w,1) = (alpha_rad(w,1) * 180) / pi; % in degrees on
the trigonometric circle
    if alpha_degrees(w,1)<0
        alpha_degrees(w,1)=alpha_degrees(w,1)+360;
    else
        alpha_degrees(w,1)=alpha_degrees(w,1);
    end
    if alpha_degrees(w,1)>=0 & alpha_degrees(w,1)<90 % 1st quadrant
        wd_compass(w,1) = 90 - alpha_degrees(w,1) + 180;
    elseif alpha_degrees(w,1)>=90 & alpha_degrees(w,1)<180 % 2nd
quadrant
        wd_compass(w,1) = 270 - (alpha_degrees(w,1) - 180);
    elseif alpha_degrees(w,1)>=180 & alpha_degrees(w,1)<270 % 3rd
quadrant
        wd_compass(w,1) = alpha_degrees(w,1) - 90;
    else % 4th quadrant
        wd_compass(w,1) = 360 - (alpha_degrees(w,1) - 270);
    end
    if wd_compass(w,1)>180 & wd_compass(w,1)<=360
        wd_compass(w,1) = wd_compass(w,1) - 360; % to get negative
angles for plotting
    end
    ws_compass(w,1) = ((sounding(w,15)/10)^2+(sounding(w,17)/10)^2)^0.5;
end

Wd_whole_profile = wd_compass; % Wind direction profile

% Set negative values for winds between 180 and 360 degrees (for right
plot)
clear i
wd_datapor = zeros(length(wd_datapor_pre),1);
for i = 1:length(wd_datapor_pre)
    if wd_datapor_pre(i,1) > 180 && wd_datapor_pre(i,1) <= 360
        wd_datapor(i,1) = wd_datapor_pre(i,1) - 360;
    else
        wd_datapor(i,1) = wd_datapor_pre(i,1);
```

```
    end
end

% Convert wind direction from degrees to cardinal directions
if wd_datapor(1,1) >= -22.49 && wd_datapor(1,1) <= 22.49 &&
ws_compass(1,1) > 0
    Wd_cardinal_IGRA = 'N';
elseif wd_datapor(1,1) >= 22.5 &&  wd_datapor(1,1) <=67.49
    Wd_cardinal_IGRA = 'NE';
elseif wd_datapor(1,1) >= 67.5 &&  wd_datapor(1,1) <=112.49
    Wd_cardinal_IGRA = 'E';
elseif wd_datapor(1,1) >= 112.5 &&  wd_datapor(1,1) <=157.49
    Wd_cardinal_IGRA = 'SE';
elseif wd_datapor(1,1) >= 157.5 &&  wd_datapor(1,1) <=180 ||
wd_datapor(1,1) >= -180 && wd_datapor(1,1) <=-157.49
    Wd_cardinal_IGRA = 'S';
elseif wd_datapor(1,1) >= -157.5 &&  wd_datapor(1,1) <=-112.49
    Wd_cardinal_IGRA = 'SW';
elseif wd_datapor(1,1) >= -112.5 && wd_datapor(1,1) <=-67.49
    Wd_cardinal_IGRA = 'W';
elseif wd_datapor(1,1) >= -67.5 &&  wd_datapor(1,1) <=-22.5
    Wd_cardinal_IGRA = 'NW';
else
    Wd_cardinal_IGRA = ' '; % if Wd_whole_profile(1,1) = 0 means there
is no wind OR if there is no wind direction reported
end

T_apparent = tz + ((1050-pz)/24.392);
Td_apparent = tdz_datapor + ((1050-pz)/24.392);

ind_pz_max = find(pz==100 | (pz <= 110 & pz >= 90));

%-------------------------------------%
%     F O G    T H I C K N E S S     %
%-------------------------------------%

ind_sat = find(Tdd_adj_level<= dwpt_threshold);

if length(ind_sat) == max(ind_sat) % continuous fog (no subsaturated
layer between fog and stratus)
    N_fog_levels = max(ind_sat); % Nb of levels capturing fog
elseif length(ind_sat) < max(ind_sat) % subsaturated layer between fog
and stratus or only higher clouds above the fog
    clear k
    for k=1:max(ind_sat) % k+1 will give the level that is subsaturated
        if Tdd_adj_level(k+1,1)>= dwpt_threshold
            break
        end
    end
    if k<length(ind_sat)
        N_fog_levels = k; % Nb of levels in the fog is determined to be
below that subsaturation
    end
end
```

```
di=0.1; % 0.1 hPa increments: vertical resolution wanted

if Tdd_adj_level(N_fog_levels,1) == 1 % in case highest saturated level
is Tdd, no interpolation: fog top == geopotential height of that
sounding level
    Thick_layer = sounding(N_fog_levels,3)-sounding(1,3); % fog
thickness = fog top elevation minus ground elevation
    fog_top_P = pz(N_fog_levels);
    fog_top_T = tz(N_fog_levels);
else
    if isnan(tdz_datapor(N_fog_levels+1)) % take second level if NaN
        % line segment for T
        x1  = [tz(N_fog_levels) tz(N_fog_levels+2)];
        if x1(1,1) == x1(1,2) % isotherm = script problem
            x1  = [tz(N_fog_levels) tz(N_fog_levels+2)];
            if x1(1,1) == x1(1,2)
                x1  = [tz(N_fog_levels) tz(N_fog_levels+3)];
            end
        end
        y1  = [-pz(N_fog_levels) -pz(N_fog_levels+2)];
        % line segment for Td
        x2  = [tdz_datapor(N_fog_levels) tdz_datapor(N_fog_levels+2)];
        if x2(1,1) == x2(1,2) % isotherm = script problem
            x2  = [tdz_datapor(N_fog_levels)
tdz_datapor(N_fog_levels+2)];
        end
        y2  = [-pz(N_fog_levels) -pz(N_fog_levels+2)];
    else
        % line segment for T
        x1  = [tz(N_fog_levels) tz(N_fog_levels+1)];
        if x1(1,1) == x1(1,2) % isotherm = script problem
            x1  = [tz(N_fog_levels) tz(N_fog_levels+2)];
            if x1(1,1) == x1(1,2)
                x1  = [tz(N_fog_levels) tz(N_fog_levels+3)];
            end
        end
        y1  = [-pz(N_fog_levels) -pz(N_fog_levels+1)];
        % line segment for Td
        x2  = [tdz_datapor(N_fog_levels) tdz_datapor(N_fog_levels+1)];
        if x2(1,1) == x2(1,2) % isotherm = script problem
            x2  = [tdz_datapor(N_fog_levels)
tdz_datapor(N_fog_levels+2)];
        end
        y2  = [-pz(N_fog_levels) -pz(N_fog_levels+1)];
    end

    for i = 1:100 % length of iteration: 0.1 hPa*100 = 10hPa = maximum
depth of interpolation (can be modified HERE)
        % line that intersects both
        x3 = [-20 20];
        y3 = [-pz(N_fog_levels)+(i*di) -pz(N_fog_levels)+(i*di)];

        % fit linear polynomial
        p1 = polyfit(x1,y1,1);
        p2 = polyfit(x2,y2,1);
        p3 = polyfit(x3,y3,1);
```

```
        % calculate intersection
        x_intersect13 = fzero(@(x) polyval(p1-p3,x),3);
        y_intersect13 = polyval(p1,x_intersect13);
        x_intersect23 = fzero(@(x) polyval(p2-p3,x),3);
        y_intersect23 = polyval(p2,x_intersect23);

        dewpoint_level(i) = abs(x_intersect13-x_intersect23);
    end

    if dewpoint_level(1,1) > dwpt_threshold % in case fog ONLY at
surface
        fog_top_P = pz(1,1);
        Thick_layer = 0; % Fog thickness
        fog_top_T = tz(1,1);
    else
        fog_top_P =  pz(N_fog_levels) - max(find(dewpoint_level <=
dwpt_threshold))*di;
        y3 = [-pz(N_fog_levels)+(max(find(dewpoint_level <=
dwpt_threshold))*di) -pz(N_fog_levels)+(max(find(dewpoint_level <=
dwpt_threshold))*di)];
        x3 = [-20 20];
        p3 = polyfit(x3,y3,1);
        x_intersect13 = fzero(@(x) polyval(p1-p3,x),3);
        y_intersect13 = polyval(p1,x_intersect13);
        x_intersect23 = fzero(@(x) polyval(p2-p3,x),3);
        y_intersect23 = polyval(p2,x_intersect23);
        fog_top_T = fzero(@(x) polyval(p1-p3,x),3);
        dz = 287 * 9.81^-1 *
((tz(N_fog_levels)+273.15+fog_top_T+273.15)/2) *
log(pz(N_fog_levels)/fog_top_P);
        Thick_layer = sounding(N_fog_levels,3)-sounding(1,3)+ dz; % Fog
thickness
    end
end

pen_depth = Thick_layer - (inv_base - sounding(1,3)); % thickness of fog
penetrating the inversion layer
FTE = Thick_layer + sounding(1,3); % Fog top elevation

%---------------------------------%
% Open met data to get vv and ww  %
%---------------------------------%

% Horizontal visibility (vv) and weather code (ww) are not always
observed as the same time as radiosonde

if yyyy >= 2013 % same time observations after 2013

    DMI = load('C:\Gaelle\DMI fog
data\DMI_fog_data\vv_ww_2013_2016.dat');
    ind_DMI = find(DMI(:,1) == station_nb & DMI(:,2) == yyyy & DMI(:,3)
== mm & DMI(:,4) == dd & DMI(:,5) == time);
    ww = DMI(ind_DMI,10)-100;
    vv = DMI(ind_DMI,9);
```

```
    horiz_vis = vv/1000;

    % Extract fog days in the time series "radiosonde_temp"
    index_time_series = find((DMI(:,1) == station_nb & DMI(:,2)== yyyy &
(DMI(:,3)==radiosonde_temp(1,3) & DMI(:,4)>=radiosonde_temp(1,4))) |
((DMI(:,1) == station_nb & DMI(:,2)== yyyy &
(DMI(:,3)==radiosonde_temp(end,3) &
DMI(:,4)<=radiosonde_temp(end,4)))));
    for i=1:length(index_time_series)
        timestamp(i,1) =
datenum(DMI(index_time_series(i),2),DMI(index_time_series(i),3),DMI(inde
x_time_series(i),4),DMI(index_time_series(i),5),0,0);
    end


    Binary_fog_pos = zeros(length(timestamp),1);
    for i=1:length(Binary_fog_pos)
        if  DMI(index_time_series(i),10)-100 == 30 |
(DMI(index_time_series(i),10)-100 >= 32 & DMI(index_time_series(i),10)-
100 <= 35)
            Binary_fog_pos(i,1) = max(T_sounding);
        else
            Binary_fog_pos(i,1) = 0;
        end
    end

    Binary_fog_neg = zeros(length(timestamp),1);
    for i=1:length(Binary_fog_neg)
        if DMI(index_time_series(i),10)-100 == 30 |
(DMI(index_time_series(i),10)-100 >= 32 & DMI(index_time_series(i),10)-
100 <= 35)
            Binary_fog_neg(i,1) = min(Td_sounding);
        else
            Binary_fog_neg(i,1) = 0;
        end
    end

else

    % Open met data file prior to 2013

    load(sprintf('C:/Gaelle/DMI fog
data/DMI_fog_data/DMI_%s.dat',num2str(station_nb))) % data set with fog
observation
    DMI = eval(sprintf('DMI_%s',num2str(station_nb)));
    ind_DMI = find(DMI(:,4) == yyyy & DMI(:,3) == mm & DMI(:,2) == dd &
DMI(:,5) == (time));
    ww = DMI(ind_DMI,7); % present weather
    vv = DMI(ind_DMI,6); % visibility

    if ~isempty(vv) % for souding coindiding with surface observations,
convert vv codes to visibility (table 4377: WMO, 1995)

        if vv >= 0 && vv <= 50
            horiz_vis = (vv/10);
```

```
        elseif vv >= 56 && vv <= 80
            horiz_vis = (vv-50);
        elseif vv == 81
            horiz_vis = 35;
        elseif vv == 82
            horiz_vis = 40;
        elseif vv == 83
            horiz_vis = 45;
        elseif vv == 84
            horiz_vis = 50;
        elseif vv == 85
            horiz_vis = 55;
        elseif vv == 86
            horiz_vis = 60;
        elseif vv == 87
            horiz_vis = 65;
        elseif vv == 88
            horiz_vis = 70;
        elseif vv == 89
            horiz_vis = '>70';
        elseif vv == 90
            horiz_vis = '<0.05';
        elseif vv == 91
            horiz_vis = 0.05;
        elseif vv == 92
            horiz_vis = 0.2;
        elseif vv == 93
            horiz_vis = 0.5;
        elseif vv == 94
            horiz_vis = 1;
        elseif vv == 95
            horiz_vis = 2;
        elseif vv == 96
            horiz_vis = 4;
        elseif vv == 97
            horiz_vis = 10;
        elseif vv == 98
            horiz_vis = 20;
        else
            horiz_vis = '>35';
        end

    elseif isempty(ind_DMI) % if sounding not coincident with surface
observations

        clear ind_DMI
        if time == 11 % morning soundings
            ind_DMI_pre = find(DMI(:,4) == yyyy & DMI(:,3) == mm &
DMI(:,2) == dd & DMI(:,5) == 9);
            ind_DMI_after = find(DMI(:,4) == yyyy & DMI(:,3) == mm &
DMI(:,2) == dd & DMI(:,5) == 12);
        elseif time == 23 & dd == 30 & mm == 6 % night soundings, end of
June
            ind_DMI_pre = find(DMI(:,4) == yyyy & DMI(:,3) == mm &
DMI(:,2) == dd & DMI(:,5) == 21);
```

```
            ind_DMI_after = find(DMI(:,4) == yyyy & DMI(:,3) == mm+1 &
DMI(:,2) == dd-29 & DMI(:,5) == 0);
        elseif time == 23 & dd == 31 & (mm == 5 | mm == 7 | mm == 8) %
night soundings, end of May, July or August
            ind_DMI_pre = find(DMI(:,4) == yyyy & DMI(:,3) == mm &
DMI(:,2) == dd & DMI(:,5) == 21);
            ind_DMI_after = find(DMI(:,4) == yyyy & DMI(:,3) == mm+1 &
DMI(:,2) == dd-30 & DMI(:,5) == 0);
        else % night soundings, not end of month
            ind_DMI_pre = find(DMI(:,4) == yyyy & DMI(:,3) == mm &
DMI(:,2) == dd & DMI(:,5) == 21);
            ind_DMI_after = find(DMI(:,4) == yyyy & DMI(:,3) == mm &
DMI(:,2) == dd+1 & DMI(:,5) == 0);
        end

        ww_pre = DMI(ind_DMI_pre,7); % present weather before radiosonde
        vv_pre = DMI(ind_DMI_pre,6); % visibility before radiosonde
        ww_after = DMI(ind_DMI_after,7); % present weather after
radiosonde
        vv_after = DMI(ind_DMI_after,6); % visibility after radiosonde

        % Convert vv codes to visibility (table 4377: WMO, 1995)
        if ~isempty(vv_pre)
            if vv_pre >= 0 && vv_pre <= 50
                horiz_vis_9h = (vv_pre/10);
            elseif vv_pre >= 56 && vv_pre <= 80
                horiz_vis_9h = (vv_pre-50);
            elseif vv_pre == 81
                horiz_vis_9h = 35;
            elseif vv_pre == 82
                horiz_vis_9h = 40;
            elseif vv_pre == 83
                horiz_vis_9h = 45;
            elseif vv_pre == 84
                horiz_vis_9h = 50;
            elseif vv_pre == 85
                horiz_vis_9h = 55;
            elseif vv_pre == 86
                horiz_vis_9h = 60;
            elseif vv_pre == 87
                horiz_vis_9h = 65;
            elseif vv_pre == 88
                horiz_vis_9h = 70;
            elseif vv_pre == 89
                horiz_vis_9h = '>70';
            elseif vv_pre == 90
                horiz_vis_9h = '<0.05';
            elseif vv_pre == 91
                horiz_vis_9h = 0.05;
            elseif vv_pre == 92
                horiz_vis_9h = 0.2;
            elseif vv_pre == 93
                horiz_vis_9h = 0.5;
            elseif vv_pre == 94
                horiz_vis_9h = 1;
            elseif vv_pre == 95
```

```
            horiz_vis_9h = 2;
        elseif vv_pre == 96
            horiz_vis_9h = 4;
        elseif vv_pre == 97
            horiz_vis_9h = 10;
        elseif vv_pre == 98
            horiz_vis_9h = 20;
        else
            horiz_vis_9h = '>35';
        end
    end
    if ~isempty(vv_after)
        if vv_after >= 0 && vv_after <= 50
            horiz_vis_12h = (vv_after/10);
        elseif vv_after >= 56 && vv_after <= 80
            horiz_vis_12h = (vv_after-50);
        elseif vv_after == 81
            horiz_vis_12h = 35;
        elseif vv_after == 82
            horiz_vis_12h = 40;
        elseif vv_after == 83
            horiz_vis_12h = 45;
        elseif vv_after == 84
            horiz_vis_12h = 50;
        elseif vv_after == 85
            horiz_vis_12h = 55;
        elseif vv_after == 86
            horiz_vis_12h = 60;
        elseif vv_after == 87
            horiz_vis_12h = 65;
        elseif vv_after == 88
            horiz_vis_12h = 70;
        elseif vv_after == 89
            horiz_vis_12h = '>70';
        elseif vv_after == 90
            horiz_vis_12h = '<0.05';
        elseif vv_after == 91
            horiz_vis_12h = 0.05;
        elseif vv_after == 92
            horiz_vis_12h = 0.2;
        elseif vv_after == 93
            horiz_vis_12h = 0.5;
        elseif vv_after == 94
            horiz_vis_12h = 1;
        elseif vv_after == 95
            horiz_vis_12h = 2;
        elseif vv_after == 96
            horiz_vis_12h = 4;
        elseif vv_after == 97
            horiz_vis_12h = 10;
        elseif vv_after == 98
            horiz_vis_12h = 20;
        else
            horiz_vis_12h = '>35';
        end
    end
end
```

```
    % Extract fog days in the time series "radiosonde_temp"

    index_time_series = find((DMI(:,4)== yyyy &
(DMI(:,3)==radiosonde_temp(1,3) &
DMI(:,2)>=radiosonde_temp(1,4)))|(DMI(:,4)== yyyy
&(DMI(:,3)==radiosonde_temp(end,3) &
DMI(:,2)<=radiosonde_temp(end,4))));
    for i=1:length(index_time_series)
        timestamp(i,1) =
datenum(DMI(index_time_series(i),4),DMI(index_time_series(i),3),DMI(inde
x_time_series(i),2),DMI(index_time_series(i),5),0,0);
    end

    if station_nb == 4320
        ind_aws_met = find(DMI(:,3) == 12 & DMI(:,2) == 30 & DMI(:,4) ==
2008 & DMI(:,5) == 12); %select when weather codes switch from manned to
automated
    elseif station_nb == 4339
        ind_aws_met = find(DMI(:,3) == 8 & DMI(:,2) == 17 & DMI(:,4) ==
2005 & DMI(:,5) == 15);
    elseif station_nb == 4360
        ind_aws_met = find(DMI(:,3) == 8 & DMI(:,2) == 5 & DMI(:,4) ==
2005 & DMI(:,5) == 15);
    elseif station_nb == 4390
        ind_aws_met = find(DMI(:,3) == 9 & DMI(:,2) == 22 & DMI(:,4) ==
2003 & DMI(:,5) == 0);
    end

    Binary_fog_pos = zeros(length(timestamp),1);
    for i=1:length(Binary_fog_pos)
        if index_time_series(i,1)<ind_aws_met &
DMI(index_time_series(i),7)>=42 & DMI(index_time_series(i),7)<=49
            Binary_fog_pos(i,1) = max(T_sounding);
        elseif index_time_series(i,1) >= ind_aws_met &
(DMI(index_time_series(i),7)==30 | (DMI(index_time_series(i),7)>=32 &
DMI(index_time_series(i),7)<=35))
            Binary_fog_pos(i,1) = max(T_sounding);
        else
            Binary_fog_pos(i,1) = 0;
        end
    end

    Binary_fog_neg = zeros(length(timestamp),1);
    for i=1:length(Binary_fog_neg)
        if index_time_series(i,1) <ind_aws_met &
DMI(index_time_series(i),7)>=42 & DMI(index_time_series(i),7)<=49
            Binary_fog_neg(i,1) = min(Td_sounding);
        elseif index_time_series(i,1) >= ind_aws_met &
(DMI(index_time_series(i),7)==30 | (DMI(index_time_series(i),7)>=32 &
DMI(index_time_series(i),7)<=35))
            Binary_fog_neg(i,1) = min(Td_sounding);
        else
            Binary_fog_neg(i,1) = 0;
        end
    end
```

```
end


%-%-%-%-%-%-%-%-%-%-%
%      P L O T      %
%-%-%-%-%-%-%-%-%-%-%

% f = figure('visible','off'); % set figure invisible if figure drawing
%crashes the computer

f = figure;

% 1. Sounding on Skew-T log-P (main plot)
% ---------------------------------------

% Basic Skew-T Log P graph
h=contour(skewT,lnP,temp,16,'Color',[0.93 0.69 0.13],'LineStyle','-
','LineWidth',1);
hold on
set(gca,'ytick',[1000:100:100])
set(gca,'yscale','log','ydir','reverse')
set(gca,'fontweight','bold')
set(gca,'ytick',[100:100:1000])
set(gca,'ygrid','on')
hold on
h=contour(skewT,lnP,O,24,'Color',[0 0.6 0],'LineStyle','-
','LineWidth',1); %dry adiabate
hw=contour(skewT,lnP,rw,24,'Color',[0.93 0.69
0.13],'LineStyle',':','LineWidth',1); %constant mixing ratio
hh=contour(skewT,lnP,Ow,24,'Color',[0 0.6
0],'LineStyle',':','LineWidth',1); %moist adiabate
xlabel('Temperature (^oC)','fontweight','bold','fontsize',16)
xlim([-39 29]);
ylabel('Pressure (mb)','fontweight','bold','fontsize',16)
set(gca, 'xtick',[-30:10:10])
set(gca,'FontSize',14)

% Draw fog layer
if ~isempty(fog_top_P)
    v1 = [-40 pz(1,1); -40 fog_top_P; 20 fog_top_P; 20 pz(1,1)];
    f1 = [1 2 3 4];
    fog_polygon = patch('Faces',f1,'Vertices',v1,'FaceColor',[.5 .5
.5],'EdgeColor','none'); % fog thickness 'FaceAlpha',.6
end

% Plot T and Td
plot1 = plot(Td_apparent(1:ind_pz_max,1),pz(1:ind_pz_max,1),'Color',[0
0.4 1],'LineStyle','--','LineWidth',1.5,'Marker','.','MarkerSize',15);
plot2 =
plot(T_apparent(1:ind_pz_max,1),pz(1:ind_pz_max,1),'Color','k','LineStyl
e','-','LineWidth',1.5,'Marker','.','MarkerSize',15);
```

```
% 2. Vertical profile of wind direction and specific humidity (right)
% ------------------------------------------------------------------

find(pz == 100);
if isempty(ans)
    max_level = find(pz <= 110 & pz >= 90);
else
    max_level = find(pz == 100);
end
pz_datapor = sounding_datapor(:,4)/100;

find(pz_datapor == 100); % same for datapor sounding
if isempty(ans)
    max_level_datapor = find(pz_datapor <= 110 & pz_datapor >= 90);
else
    max_level_datapor = find(pz_datapor == 100);
end

% convert pressure so that it graphically corresponds to main Skew-T
plot
pression_apparente = -8.79*log(pz)+61.171; % obtained with fitting curve
in excel
pression_apparente_crop = pression_apparente(1:max_level,1); % crop at
100 mb
pression_apparente_datapor =  -8.79*log(pz_datapor)+61.171; % do the
same with data_por in order to use the wind direction graph
pression_apparente_datapor_crop =
pression_apparente_datapor(1:max_level_datapor,1);
axes('Position',[0.8 0.11 0.105 0.815],'Color','none')

% Report fog layer on wind and humidity graph
if ~isempty(fog_top_P)
    fog_top_P_apparent = -8.79*log(fog_top_P)+61.171;
    v2 = [0 pression_apparente_crop(1,1); 0 fog_top_P_apparent; 1
fog_top_P_apparent; 1 pression_apparente_crop(1,1)];
    f2 = [1 2 3 4];
    fog_polygon2 = patch('Faces',f2,'Vertices',v2,'FaceColor',[.5 .5
.5],'EdgeColor','none'); % fog thickness
end

hold on

% Plot specific humidity
line(spec_humid(1:max_level,1),pression_apparente_crop,'Color','k','Line
Style','-','LineWidth',1,'Marker','.','MarkerSize',10);
ax1 = gca; % current axes
set(gca, 'Color',[1 1 1]) % set background plot to white
ylim([0.0230 pression_apparente(max_level,1)]) % 0.0230 cm = pression
apparente for 1050mb
xlim([0 1]);
set(gca,'ytick',[])
set(gca,'yticklabel',[])
xlabel('Spec. hum. (g kg^-^1)');
ax1_pos = ax1.Position; % position of first axes
ax2 = axes('Position',ax1_pos,...
    'XAxisLocation','top',...
```

```
    'YAxisLocation','right',...
    'Color','none');
set(ax2, 'XColor', [1 0 0])

% Plot wind direction
wd_datapor(wd_datapor == -9999) = NaN;
ind_wd_datapor_nonNAN = find(~isnan(wd_datapor(1:max_level_datapor,1)));
% find levels with real values
clear i
for i=1:length(ind_wd_datapor_nonNAN)
%(wd_datapor(1:max_level_datapor,1))
    pression_apparente_datapor_crop_wd(i,1) =
pression_apparente_datapor(ind_wd_datapor_nonNAN(i,1),1);
end
line(wd_datapor(~isnan(wd_datapor(1:max_level_datapor,1))),pression_appa
rente_datapor_crop_wd,'Color','r','LineStyle','-
','LineWidth',1,'Marker','.','MarkerSize',10);
ind_wd = find(~isnan(Wd_whole_profile));
ind_wd_crop = ind_wd(find(ind_wd(ind_wd <= max_level)),1);
for wdcrop = 1:length(ind_wd_crop)
    pression_apparente_crop_wd(wdcrop,1) =
pression_apparente_crop(ind_wd(wdcrop),1);
end
line([0 pression_apparente_crop_wd(1,1)],[0
pression_apparente_crop_wd(end,1)],'Color','r','LineStyle','--
','LineWidth',0.5);
ylim([0.0230 pression_apparente(max_level,1)]) % 0.0230 cm = pression
apparente for 1050mb
xlim([-180 180]);
set(gca,'xtick',[-180,0,180])
set(gca,'ytick',[])
set(gca,'yticklabel',[])
xlabel('Wind direction (^o)','Color','r');


% 3. Summary of surface and upper-air observations (upper right corner)
% ------------------------------------------------------------------------

% Text: Station, observation date and time
text(-
1.9,0.95,sprintf('%s',num2str(station)),'fontweight','bold','FontSize',1
8,'Color','k','Background','w','Units','normalized')
text(-1.9,0.88,sprintf('%s/%s/%s
%sh',num2str(dd),num2str(mm),num2str(yyyy),num2str(time)),'FontSize',16,
'Background','w','Units','normalized');

% Fog thickness
if ~isempty(FTE)
    text(-1.9,0.82,sprintf('Fog thickness = %s
m',num2str(round(Thick_layer))),'FontSize',14,'Color','k','Background','
w','Units','normalized') % set%s
end
```

```
% 3.1 same time events

if exist('horiz_vis','var')

    % vv and ww
    text(-0.5,0.75,sprintf('ww = %s',
num2str(ww)),'FontSize',14,'Color','k','Background','w','Units','normali
zed')
    if horiz_vis == '>70'
        text(-1.9,0.75,sprintf('Vis %skm',
num2str(horiz_vis)),'FontSize',14,'Color','k','Background','w','Units','
normalized')
    else
        text(-1.9,0.75,sprintf('Vis = %skm',
num2str(horiz_vis)),'FontSize',14,'Color','k','Background','w','Units','
normalized')
    end
    text(0.4,0.75,sprintf('(%sh)',
num2str(time)),'FontSize',14,'Color','k','Background','w','Units','norma
lized')

    % surface RH value
    text(-1.9,0.67,sprintf('RH_s_u_r_f =
%s',num2str(rhz(1,1))),'FontSize',14,'Color','k','Background','w','Units
','normalized')
    text(-
0.35,0.68,'%','FontSize',14,'Color','k','Background','w','Units','normal
ized')

    % Surface wind
    if ~isnan(Wind_surf)
        text(-1.9,0.60,sprintf('Wind: %s %s m s^-^1',
num2str(Wd_cardinal_IGRA),num2str(Wind_surf)),'FontSize',14,'Color','k',
'Background','w','Units','normalized')
    elseif isnan(Wind_surf) && ~isnan(ws_compass(1,1))
        text(-1.9,0.60,sprintf('Wind: %s %s m s^-^1',
num2str(Wd_cardinal_IGRA),num2str(ws_compass(1,1))),'FontSize',14,'Color
','k','Background','w','Units','normalized')
    end

    % Characterization of bottom layer
    if VPTEMP(2)-VPTEMP(1)<0
        text(-1.9,0.53,sprintf('Bottom layer:
unstable'),'FontSize',14,'Color','k','Background','w','Units','normalize
d')
    elseif VPTEMP(2)-VPTEMP(1)>0
        text(-1.9,0.53,sprintf('Bottom layer:
stable'),'FontSize',14,'Color','k','Background','w','Units','normalized'
)
    elseif VPTEMP(2)==VPTEMP(1)
        text(-1.9,0.53,sprintf('Bottom layer:
neutral'),'FontSize',14,'Color','k','Background','w','Units','normalized
')
    end

end
```

```
% 3.2 extensive events

% (a) Preceding radiosonde
% vv and ww
if exist('vv_pre','var')
    if  horiz_vis_9h == '>70'
        text(-1.9,0.75,sprintf('Vis %skm',
num2str(horiz_vis_9h)),'FontSize',14,'Color','k','Background','w','Units
','normalized')
    else
        text(-1.9,0.75,sprintf('Vis = %skm',
num2str(horiz_vis_9h)),'FontSize',14,'Color','k','Background','w','Units
','normalized')
    end
    text(-0.5,0.75,sprintf('ww = %s',
num2str(ww_pre)),'FontSize',14,'Color','k','Background','w','Units','nor
malized')
    text(0.4,0.75,sprintf('(%sh)', num2str(time-
2)),'FontSize',14,'Color','k','Background','w','Units','normalized')
    text(-0.5,0.75,sprintf('ww = %s',
num2str(ww_pre)),'FontSize',14,'Color','k','Background','w','Units','nor
malized')
    text(0.4,0.75,sprintf('(%sh)', num2str(time-
2)),'FontSize',14,'Color','k','Background','w','Units','normalized')
end

% (b) Following radiosonde
% vv and ww
if exist('vv_after','var')
    if horiz_vis_12h == '>70'
        text(-1.9,0.69,sprintf('Vis %skm',
num2str(horiz_vis_12h)),'FontSize',14,'Color','k','Background','w','Unit
s','normalized')
    else
        text(-1.9,0.69,sprintf('Vis = %skm',
num2str(horiz_vis_12h)),'FontSize',14,'Color','k','Background','w','Unit
s','normalized')
    end
    text(-0.5,0.69,sprintf('ww = %s',
num2str(ww_after)),'FontSize',14,'Color','k','Background','w','Units','n
ormalized')
    if time == 11
        text(0.4,0.69,sprintf('(%sh)',
num2str(time+1)),'FontSize',14,'Color','k','Background','w','Units','nor
malized')
    elseif time == 23
        text(0.4,0.69,sprintf('(%sh)', num2str(time-
23)),'FontSize',14,'Color','k','Background','w','Units','normalized')
    end

    % surface RH
    text(-1.9,0.62,sprintf('RH_s_u_r_f = %s',num2str(rhz(1,1))),
'FontSize',14,'Color','k','Background','w','Units','normalized')
    text(-0.35,0.63,'%','FontSize',14,'Color','k','Background','w',
'Units','normalized')
```

```
    % Surface wind
    if ~isnan(Wind_surf)
        text(-1.9,0.55,sprintf('Wind: %s %s m s^-^1',
num2str(Wd_cardinal_IGRA),num2str(Wind_surf)),'FontSize',14,'Color','k',
'Background','w','Units','normalized')
    elseif isnan(Wind_surf) && ~isnan(ws_compass(1,1))
        text(-1.9,0.55,sprintf('Wind: %s %s m s^-^1',
num2str(Wd_cardinal_IGRA),num2str(ws_compass(1,1))),'FontSize',14,'Color
','k','Background','w','Units','normalized')
    end

    % Characterization of bottom layer
    if VPTEMP(2)-VPTEMP(1)<0
        text(-1.9,0.48,sprintf('Bottom layer:
unstable'),'FontSize',14,'Color','k','Background','w','Units','normalize
d')
    elseif VPTEMP(2)-VPTEMP(1)>0
        text(-1.9,0.48,sprintf('Bottom layer:
stable'),'FontSize',14,'Color','k','Background','w','Units','normalized'
)
    elseif VPTEMP(2)==VPTEMP(1)
        text(-1.9,0.48,sprintf('Bottom layer:
neutral'),'FontSize',14,'Color','k','Background','w','Units','normalized
')
    end
end

% Legend
legend
if exist('fog_polygon','var') && Thick_layer>0
    L=legend([plot2 plot1 fog_polygon],{'Dry bulb temperature','Dew
point temperature','Fog layer'});
else
    L=legend([plot2 plot1],{'Dry bulb temperature','Dew point
temperature'});
end
set(L,'Location','SouthWest','fontsize',10);
axes('Position',[0.8 -0.1 0.15 0.05],'Color','none')
set(gca, 'Color',[1 1 1])


% 4. Time series of surface T, Td and fog events (upper left corner)
% ------------------------------------------------------------------

% Set location and size of the graph
axes('Position',[0.19 0.675 0.4 0.25],'Color','none')
set(gca, 'Color',[1 1 1])

% Plot all individual fog events
hbar3 = bar(timestamp(1:end,1),Binary_fog_pos);
set(hbar3,'FaceColor',[.6 .6 .6],'EdgeColor',[.6 .6 .6])
hold on
hbar4 = bar(timestamp(1:end,1),Binary_fog_neg);
set(hbar4,'FaceColor',[.6 .6 .6],'EdgeColor',[.6 .6 .6])
```

```
% Plot one sounding analyzed on time series
hbar1 = bar(dates_graph(1,1:end),Binary_obs_pos,0.4);
set(hbar1,'FaceColor',[1 .4 .4],'EdgeColor',[.6 .6 .6])
hbar2 = bar(dates_graph(1,1:end),Binary_obs_neg,0.4);
set(hbar2,'FaceColor',[1 .4 .4],'EdgeColor',[.6 .6 .6])

% Plot surface T and Td
plot5 = plot(dates_graph(1,1:end),T_sounding,'Color',[0 0 0],
'LineWidth',.9,'Marker','.','MarkerSize',10); % air temperature from
soundings
plot6 = plot(dates_graph(1,1:end),Td_sounding,'Color',[0 0.4 1],
'LineStyle','--','LineWidth',.9,'Marker','.','MarkerSize',10);

% Display options
set(gca,'XTick',[dates_graph(1,1):5:dates_graph(1,end)])
ylim([min(Td_sounding)-1 max(T_sounding)+1])
ylabel('Surface Temp. (^oC)','fontweight','bold','fontsize',10)
xlabel('Date','fontweight','bold','fontsize',10)
set(gca,'XAxisLocation','top')
set(gca,'XMinorTick','on','YMinorTick','on')
datetick('x','mmmdd','keepticks') % date format

% --------------------------------%
% 5. Save figure to output folder %
% --------------------------------%

savdir = sprintf('C:/Gaelle/Matlab/IGRA/Emagram/output/%s/
Sounding_%s_%s_%s_%s_%s.png',num2str(station_nb),num2str(station_nb),num
2str(yyyy),num2str(mm),num2str(dd),num2str(time));
saveas(f, savdir, 'png')
```

APPENDIX 5: Automated Matlab script to extract fog thermodynamic profiles.

```
% ------------------------------------------------------------------------------- %
% Script part 1 of 2: extraction of soundings during which is it very likely to have
% fog. Creates a table input for script part 2 of 2.
% Author: Gaelle F. Gilson (Feb 2018)
% Contact: gaellegilson86@gmail.com
% ------------------------------------------------------------------------------- %

clear all
close all

for stat=1:1 % select station(s)
    switch stat
        case 1, station_nb = 4320; station = 'Danmarkshavn';
        case 2, station_nb = 4339; station = 'Ittoqqortoormiit';
        case 3, station_nb = 4360; station = 'Tasiilaq';
    end
end

%%%%%%%%%%%%%%%%%%%%%%%%%%%%%%%%%%
% Open met data to get ww events  %
%%%%%%%%%%%%%%%%%%%%%%%%%%%%%%%%%%

load(sprintf('C:/Gaelle/DMI fog data/DMI_fog_data/DMI_%s.dat',num2str(station_nb))) %↙
data set with fog observation
DMI = eval(sprintf('DMI_%s',num2str(station_nb)));

year = DMI(:,4);
month = DMI(:,3);
day = DMI(:,2);
time = DMI(:,5);

% Dates when weather codes switch from manned to automated (obtained from
% DMI files --> this needs to be set manually if using other weather
% stations!!) If overlap period between manned and automated observations,
% follow steps on lines 38-40, 57-65 and 75-80.

if station_nb == 4320
    ind_aws_start = find(month == 4 & day == 22 & year == 1993 & time == 0);
    ind_aws_end = find(month == 12 & day == 30 & year == 2008 & time == 12);
elseif station_nb == 4339
    ind_aws = find(month == 8 & day == 17 & year == 2005 & time == 15);
elseif station_nb == 4360
    ind_aws = find(month == 8 & day == 5 & year == 2005 & time == 15);
elseif station_nb == 4390
    ind_aws = find(month == 9 & day == 22 & year == 2003 & time == 0);
end

clear i
for i = 1:length(DMI)
    if stat == 2 | stat == 3
        if i<ind_aws && DMI(i,7)>=42 && DMI(i,7)<=49 % manned observations
            DMI(i,8) = 1; % means there is fog
        elseif i>=ind_aws && (DMI(i,7)==30 | DMI(i,7)==32 | DMI(i,7)==33 | DMI(i,7)==↙
34 | DMI(i,7)== 35) % automated observations
            DMI(i,8) = 1; % means there is fog
        else
```

```
 55             DMI(i,8) = 0; % means there is no fog
 56         end
 57     elseif stat == 1 % for Danmarkshavn there is an overlap period for manned and↙
automated observations
 58         if i<ind_aws_end && DMI(i,7)>=42 && DMI(i,7)<=49
 59             DMI(i,8) = 1; % means there is fog
 60         elseif i>=ind_aws_start && (DMI(i,7)==30 | DMI(i,7)==32 | DMI(i,7)==33 | DMI↙
(i,7)== 34 |(DMI(i,7)>=42 && DMI(i,7)<=49))
 61             DMI(i,8) = 1; % means there is fog
 62         else
 63             DMI(i,8) = 0; % means there is no fog
 64         end
 65     end
 66 end
 67
 68
 69 %%%%%%%%%%%%%%%%%%%%%%%%%
 70 % Extensive fog events %   % --> Radiosonde between two consecutive synoptic fog↙
observations at the weather station
 71 %%%%%%%%%%%%%%%%%%%%%%%%%
 72
 73 clear i
 74
 75 if stat == 1
 76     ind_change_start = find(DMI(:,4)==1997 & DMI(:,3)==5 & DMI(:,2)==1);
 77     ind_change_start_4320 = ind_change_start(1,1);
 78     ind_change_end = find(DMI(:,4)==2001 & DMI(:,3)==7 & DMI(:,2)==31);
 79     ind_change_end_4320 = ind_change_end(end,1);
 80 end
 81
 82 for i = 1:length(DMI)-1
 83     if stat == 1 & i >= ind_change_start_4320 & i < ind_change_end_4320 % change of↙
format from 1997 to 31/7/2001 where 3hr observations reported as 1h-rows
 84         if (DMI(i,5)==9 | DMI(i,5)==10) & DMI(i+3,5)==12 & DMI(i,2)==DMI(i+3,2) & DMI↙
(i,8)==1 & DMI(i+3,8)==1 % if fog before and after radiosonde launch time
 85             Fog_11h(i,:) = DMI(i,:);
 86             Fog_11h(i,8) = 1; % means fog is very likely at 11h
 87             Fog_11h(i,5) = 11; % replace time by 11h
 88         elseif (DMI(i,5)==21 | DMI(i,5)==22) & DMI(i+3,5)==0 & DMI(i+3,2)==DMI(i,2)+1↙
& DMI(i,8)==1 & DMI(i+3,8)==1 % if fog before and after radiosonde launch time
 89             Fog_11h(i,:) = DMI(i,:);
 90             Fog_11h(i,8) = 1; % means fog is very likely at 23h
 91             Fog_11h(i,5) = 23; % replace time by 23h
 92         elseif (DMI(i,5)==21 | DMI(i,5)==22) & DMI(i+3,5)==0 & DMI(i+3,3)==DMI(i,3)+1↙
& DMI(i+3,2)==1 & DMI(i,8)==1 & DMI(i+3,8)==1 % end of month
 93             Fog_11h(i,:) = DMI(i,:);
 94             Fog_11h(i,8) = 1; % means fog is very likely at 23h
 95             Fog_11h(i,5) = 23; % replace time by 23h
 96         end
 97     elseif stat == 1 & (i < ind_change_start_4320 | i >=  ind_change_end_4320) %↙
Danmarkshavn regular format
 98         if (DMI(i,5)==9 | DMI(i,5)==10) & DMI(i+1,5)==12 & DMI(i,2)==DMI(i+1,2) & DMI↙
(i,8)==1 & DMI(i+1,8)==1 % if fog before and after radiosonde launch time
 99             Fog_11h(i,:) = DMI(i,:);
100             Fog_11h(i,8) = 1; % means fog is very likely at 11h
101             Fog_11h(i,5) = 11; % replace time by 11h
```

```
102         elseif (DMI(i,5)==21 | DMI(i,5)==22) & DMI(i+1,5)==0 & DMI(i+1,2)==DMI(i,2)+1↙
& DMI(i,8)==1 & DMI(i+1,8)==1 % if fog before and after radiosonde launch time
103             Fog_11h(i,:) = DMI(i,:);
104             Fog_11h(i,8) = 1; % means fog is very likely at 23h
105             Fog_11h(i,5) = 23; % replace time by 23h
106         elseif (DMI(i,5)==21 | DMI(i,5)==22) & DMI(i+1,5)==0 & DMI(i+1,3)==DMI(i,3)+1↙
& DMI(i+1,2)==1 & DMI(i,8)==1 & DMI(i+1,8)==1 % end of month
107             Fog_11h(i,:) = DMI(i,:);
108             Fog_11h(i,8) = 1; % means fog is very likely at 23h
109             Fog_11h(i,5) = 23; % replace time by 23h
110         end
111     else % other stations
112         if (DMI(i,5)==9 | DMI(i,5)==10) & DMI(i+1,5)==12 & DMI(i,2)==DMI(i+1,2) & DMI↙
(i,8)==1 & DMI(i+1,8)==1 % if fog before and after radiosonde launch time
113             Fog_11h(i,:) = DMI(i,:);
114             Fog_11h(i,8) = 1; % means fog is very likely at 11h
115             Fog_11h(i,5) = 11; % replace time by 11h
116         elseif (DMI(i,5)==21 | DMI(i,5)==22) & DMI(i+1,5)==0 & DMI(i+1,2)==DMI(i,2)+1↙
& DMI(i,8)==1 & DMI(i+1,8)==1 % if fog before and after radiosonde launch time
117             Fog_11h(i,:) = DMI(i,:);
118             Fog_11h(i,8) = 1; % means fog is very likely at 23h
119             Fog_11h(i,5) = 23; % replace time by 23h
120         elseif (DMI(i,5)==21 | DMI(i,5)==22) & DMI(i+1,5)==0 & DMI(i+1,3)==DMI(i,3)+1↙
& DMI(i+1,2)==1 & DMI(i,8)==1 & DMI(i+1,8)==1 % end of month
121             Fog_11h(i,:) = DMI(i,:);
122             Fog_11h(i,8) = 1; % means fog is very likely at 23h
123             Fog_11h(i,5) = 23; % replace time by 23h
124         end
125     end
126
127
128 end
129 Fog_11h(any(Fog_11h(:,8)==0,2),:) = []; % remove rows with no data
130
131 % select summer only & after 1980
132
133 ind_summer = find(Fog_11h(:,3)>=5 & Fog_11h(:,3)<=8 & Fog_11h(:,4)>=1980);
134
135 Fog_11h_summer_extensive = Fog_11h(ind_summer,:);
136
137 clear Fog_11h
138
139 %%%%%%%%%%%%%%%%%%%%%%%%
140 % Same time fog events %  % --> Radiosonde coinciding with fog observation at the↙
weather station
141 %%%%%%%%%%%%%%%%%%%%%%%%
142
143 radiosonde = load(sprintf('C:/Gaelle/Matlab/IGRA/%s/%s_derived_v2.mat',num2str↙
(station_nb),num2str(station_nb))); % extract radiosondes
144
145 clear i
146 for i=1:length(DMI)
147     match = find(radiosonde.ans.headers(:,2)==DMI(i,4) & radiosonde.ans.headers(:,3)↙
== DMI(i,3) & radiosonde.ans.headers(:,4)==DMI(i,2) & radiosonde.ans.headers(:,5)==DMI(i,↙
5));
148     if isempty(match)
```

```
149         continue
150     else
151         match1(i,1) = 1;
152         clear match
153     end
154 end
155
156 ind_fog_radiosonde = find(match1(:,1)==1);
157
158 ind_after_1980 = find(DMI(:,4)>= 1980);
159
160 clear i
161 for i=1:length(ind_fog_radiosonde)
162     if ind_fog_radiosonde(i,1)>=ind_after_1980(1,1)
163         table_results_pre(i,:) = DMI(ind_fog_radiosonde(i,1),:);
164     end
165 end
166
167 table_results_pre(any(table_results_pre==0,2),:) = [];
168 ind_summer_same_time = find(table_results_pre(:,3)>=5 & table_results_pre(:,3)<=8);
169 Fog_11h_summer_same_time = table_results_pre(ind_summer_same_time,:);
170
171 % merge same time and extensive events into one table
172 Fog_11h_pre = [Fog_11h_summer_extensive(:,1:7)
173     Fog_11h_summer_same_time(:,1:7)];
174 Fog_11h = [Fog_11h_pre zeros(length(Fog_11h_pre),20)]; % save separately as a .dat↙
file and use in script part 2 of 2
175
```

```
% ------------------------------------------------------------------------------ %
% Script part 2 of 2: automated extraction of fog thermodynamic profiles
% from the Integrated Global Radiosonde Archive (IGRA) 1980-2012.
% Author: Gaelle F. Gilson (Feb 2018)
% Contact: gaellegilson86@gmail.com
% ------------------------------------------------------------------------------ %

clear all
close all

for stat=1:1 % select station(s)
    switch stat
        case 1, station_nb = 4320; station = 'Danmarkshavn';
        case 2, station_nb = 4339; station = 'Ittoqqortoormiit';
        case 3, station_nb = 4360; station = 'Tasiilaq';
    end
end

% extract file with sounding dates and times corresponding to fog (obtained
% from Script part 1 of 2). this file includes riming fog

Fog_11h = load(sprintf('C:/Gaelle/Matlab/IGRA/Emagram/output/Fog_11h_%s_rime.dat',↙
num2str(station_nb)));

dd = Fog_11h(:,2);
mm = Fog_11h(:,3);
yyyy = Fog_11h(:,4);
time = Fog_11h(:,5);

% open IGRA files
radiosonde = load(sprintf('C:/Gaelle/Matlab/IGRA/%s/derived-por/%s_derived_v2.mat',↙
num2str(station_nb),num2str(station_nb)));
radiosonde_datapor = load(sprintf('C:/Gaelle/Matlab/IGRA/IGRA-data-por/data_2017/%↙
s_datapor.mat',num2str(station_nb)));

year_hdr = radiosonde.ans.headers(:,2);
month_hdr = radiosonde.ans.headers(:,3);
day_hdr = radiosonde.ans.headers(:,4);
time_hdr = radiosonde.ans.headers(:,5);

dwpt_threshold = 1; % dew point depression threshold obtained from boxplots of↙
surface dew point depression (radiosonde_dewpoint_boxplot.m). Can be modified
T_threshold = -10; % Temperature threshold for warm fog


for j=1:length(Fog_11h)
    ind_sounding = find(year_hdr == Fog_11h(j,4) & month_hdr == Fog_11h(j,3) &↙
day_hdr == Fog_11h(j,2) & time_hdr == Fog_11h(j,5));
    if isempty(ind_sounding) & Fog_11h(j,5) == 11
        clear ind_sounding
        ind_sounding = find(year_hdr == Fog_11h(j,4) & month_hdr == Fog_11h(j,3) &↙
day_hdr == Fog_11h(j,2) & time_hdr == 12);
    elseif isempty(ind_sounding) & Fog_11h(j,5) == 23 & ((Fog_11h(j,2)<30 & Fog_11h↙
(j,3)==6)|(Fog_11h(j,2)<31 & (Fog_11h(j,3)==5 | Fog_11h(j,3)==7 | Fog_11h(j,3)==8))) %↙
23h observation, not end of month
        clear ind_sounding
```

```
 49          ind_sounding = find(year_hdr == Fog_11h(j,4) & month_hdr == Fog_11h(j,3) &↙
day_hdr == Fog_11h(j,2)+1 & time_hdr == 0);
 50      elseif isempty(ind_sounding) & Fog_11h(j,5) == 23 & ((Fog_11h(j,2)==30 & Fog_11h↙
(j,3)==6)|(Fog_11h(j,2)==31 & (Fog_11h(j,3)==5 | Fog_11h(j,3)==7 | Fog_11h(j,3)==8))) %↙
23h observation, end of month
 51          clear ind_sounding
 52          ind_sounding = find(year_hdr == Fog_11h(j,4) & month_hdr == Fog_11h(j,3)+1 &↙
day_hdr == 1 & time_hdr == 0);
 53      end
 54      if isempty(ind_sounding)
 55          Fog_11h(j,8:14)=NaN;
 56      else
 57          % radiosonde data with derived variables (used also for T and P)
 58          sounding = radiosonde.ans.soundings{1,ind_sounding};
 59          pr=sounding(:,1); % pressure used for most calculations (in Pa)
 60          pz=pr/100; % pressure that will be used for plotting on skew-T diagram (in↙
mb)
 61          tz=(sounding(:,4)-2731.5)/10;
 62          % optional: report surface temp in final file if mixed-phase or ice
 63          % fog (for other analyses)
 64          if tz(1,1) <= T_threshold
 65              Fog_11h(j,8) = tz(1,1);
 66          else
 67              Fog_11h(j,8) = 0;
 68          end
 69          % radiosonde data with measured variables (used to obtain Td)
 70          radiosonde_datapor = load(sprintf('C:/Gaelle/Matlab/IGRA/%s/%s_datapor.mat',↙
num2str(station_nb),num2str(station_nb)));
 71          time_datapor = radiosonde_datapor.s.headers(:,5); % time
 72          ind_datapor = find(radiosonde_datapor.s.headers(:,2)==Fog_11h(j,4) &↙
radiosonde_datapor.s.headers(:,3)==Fog_11h(j,3) & radiosonde_datapor.s.headers(:,4)↙
==Fog_11h(j,2) & radiosonde_datapor.s.headers(:,5)==Fog_11h(j,5));
 73          if isempty(ind_datapor) % if datapor doesn't exist, Td doesn't exist and no↙
plot or calculations can be made
 74              continue
 75          end
 76          sounding_datapor = radiosonde_datapor.s.soundings{1,ind_datapor};
 77
 78          % dew point depression (Tdd)
 79          Tdd_datapor = sounding_datapor(:,6);
 80          Tdd_datapor(Tdd_datapor == -9999) = NaN;
 81          Tdd = Tdd_datapor/10;
 82
 83          % virtual potential temperature (for stability calculations)
 84          VPTEMP = (sounding(:,9)-2731.5)/10;
 85
 86          % Characterization of bottom layer
 87          if VPTEMP(2)-VPTEMP(1)<0 % unstable
 88              stability = -1;
 89          elseif VPTEMP(2)-VPTEMP(1)>0 % stable
 90              stability = 1;
 91          elseif VPTEMP(2)==VPTEMP(1) % neutral
 92              stability = -1;
 93          end
 94          Fog_11h(j,9) = stability; % reports stability of surface layer in final file
 95
```

```
        k=0;
        for ind_pr = 1:length(Tdd)
            if sounding_datapor(ind_pr,5) == -9999 % if temperature doesnt exist, then missing Td is because of missing observation
                continue
            else
                k=k+1;
                Tdd_adj_level(k,1) = Tdd(ind_pr,1);
            end
        end

        % Calculate dew point temperature: tdz = tz - Tdd
        if length(tz) < length(Tdd_adj_level)
            for i = 1:length(tz)
                if Tdd_adj_level(i,1) == -888.8
                    Tdd_adj_level(i,1) = NaN;
                    tdz_datapor(i,1) = NaN;
                else
                    tdz_datapor(i,1) = tz(i,1) - Tdd_adj_level(i,1);
                end
            end
        elseif length(tz) >= length(Tdd_adj_level)
            for i = 1:length(Tdd_adj_level)
                if Tdd_adj_level(i,1) == -888.8
                    Tdd_adj_level(i,1) = NaN;
                    tdz_datapor(i,1) = NaN;
                else
                    tdz_datapor(i,1) = tz(i,1) - Tdd_adj_level(i,1);
                end
            end
        end

        % Nb of levels below 700 mb in tz and tdz profiles
        Nb_levels_700mb_T = find(pz==700);
        if isempty(Nb_levels_700mb_T) % in case 700mb level missing
            Nb_levels_700mb_T = length(find(pz>=750));
        end
        Nb_levels_700mb_Td = find(sounding_datapor(:,3)==70000);
        if isempty(Nb_levels_700mb_Td) % in case 700mb level missing
            Nb_levels_700mb_Td = length(find(sounding_datapor(:,3)>=75000));
        end

        Fog_11h(j,10)= Nb_levels_700mb_T; % report in existing table the number of levels (optional)
        Fog_11h(j,11)= Nb_levels_700mb_Td;

        if tz(1,1) <= T_threshold || Nb_levels_700mb_T < 5 || Nb_levels_700mb_Td < 5 % remove observation of mixed-phase or ice fog and soundings with less than 5 levels between the surface and 700mb pressure level in either T or Td profile (after Kahl et al., 1992)
            continue
        end

        % Variables used for calculation of stability
        e = sounding(:,10); % vapour pressure in Pa*10 (must divide by 1000 to get mb or hPa)
```

```
146         ew_sound = sounding(:,11); % Saturation vapour pressure from sounding in
Pa*10 (must divide by 1000 to get mb or hPa)
147         r = 622*((e/1000)./(pz-(e/1000))); % mixing ratio in g/kg
148         rw_calc = 622*((ew_sound/1000)./(pz-(ew_sound/1000)));% Calculated saturation
mixing ratio in g/kg
149
150         % Determine saturated sounding levels
151         ind_sat = find(Tdd_adj_level(1:Nb_levels_700mb_T,1)<= dwpt_threshold);
152         if length(ind_sat)>1
153             if ind_sat(2,1)-ind_sat(1,1)>4 % two separate cloud layers (not only
stratus above fog)
154                 clear ind_sat
155                 ind_sat=1;
156             end
157         end
158         if length(ind_sat)>20 % do not consider unlikely soundings (too saturated)
159             Fog_11h(j,8:14)=NaN;
160             continue
161         end
162
163         % Inversion base
164         clear i
165         for i=1:length(tz)
166             if tz(i+1)-tz(i)>0
167                 level_inv_base = i;
168                 inv_base = sounding(i,3);
169                 break
170             end
171         end
172
173         Fog_11h(j,12)= inv_base;
174
175         clear i
176         for i=level_inv_base:length(pz)-1
177             if tz(i+1)-tz(i)<=0
178                 level_inv_top = i;
179                 inv_top = sounding(i,3);
180                 break
181             end
182         end
183
184         inv_depth = inv_top - inv_base;
185
186         % Find saturated stable layer
187
188         for i=1:length(pz)
189             Adia_s(i,1) = (273.15+tz(i,1)).*(1000./pz(i,1)).^.286; % Dry adiabats
(Potential Temperature)
190             Adia_h(i,1) = Adia_s(i,1).*exp(2.5.*rw_calc(i,1)./(tz(i,1)+273.15)); %
Moist Adiabats
191         end
192
193         for i=1:length(pz)-1
194             Grad_Adia_s(i,1) = Adia_s(i+1,1)- Adia_s(i,1);
195             Grad_Adia_h(i,1) = Adia_h(i+1,1)- Adia_h(i,1);
196         end
```

```
197
198         Binary_stable = zeros(length(pz)-1,1);
199         for i = 1:length(pz)-2
200             if Grad_Adia_s(i,1) >= 0 && Grad_Adia_h(i,1) >= 0
201                 Binary_stable(i+1,1) = 1; % layer is absolutely stable
202             else
203                 Binary_stable(i+1,1) = 0; % layer is unstable (absolute instability,↙
conditional instability, etc)
204             end
205         end
206
207         if Grad_Adia_s(1,1) >= 0
208             Binary_stable(1,1) = 1;
209         end
210
211         Binary_saturated = zeros(length(pz),1);
212         for i=1:length(Tdd_adj_level)
213             if Tdd_adj_level(i,1) <= dwpt_threshold
214                 Binary_saturated(i,1) = 1; % layer is considered saturated
215             else
216                 Binary_saturated(i,1) = 0; % layer is considered subsaturated
217             end
218         end
219
220         Binary_saturated_stable = zeros(length(Binary_stable),1);
221         for i=1:length(Binary_stable)
222             if Binary_saturated(i,1) == 1 && Binary_stable(i,1) == 1
223                 Binary_saturated_stable(i,1) = 1;
224             else
225                 Binary_saturated_stable(i,1) = 0;
226             end
227         end
228
229         % Calculate the thickness of the stable AND saturated layer (below
230         % 850 hPa)
231
232         if max(find(Binary_saturated == 1)) < find(pz==850) % resonably high to be↙
above the boundary layer (and above fog)
233             ind_geop = find(Binary_saturated == 1); % find indices of ssturated layer↙
to get geopotential height
234             if isempty(ind_geop)
235             elseif ind_geop == 1
236                 ind_geop = find(Binary_saturated == 1);
237             end
238         elseif max(find(Binary_saturated == 1)) >= find(pz==850)
239             ind_geop = find(Binary_saturated(find(pz>850),1)); % if saturated stable↙
layers 'too high', do not consider them
240             if isempty(ind_geop)
241                 ind_geop = find(Binary_saturated(find(pz>850),1));
242             end
243         elseif isempty(find(pz==850))
244             ind_pr = find(pz>850);
245             ind_geop = find(Binary_saturated == 1);
246             if length(ind_pr)<max(ind_geop)
247                 ind_geop = ind_geop(end-1,1); % does not consider higher value↙
because too high
```

```
248             end
249         else
250             ind_geop = find(Binary_saturated == 1);
251         end
252
253         if isempty(ind_geop) | ind_geop(1,1) > dwpt_threshold % if surface Tdd too↙
high to have fog OR if only stratus
254             fog_type = 1; % fog thermodynaic class type
255             Thick_layer = NaN; % fog thickness
256             pen_depth = NaN; % penetration of fog inside inversion
257             fog_top_P = NaN; % fog top pressure
258             fog_top_T = NaN; % fog top temperature
259             stability = NaN; % stability of bottom layer
260         else
261
262
263             % CALCULATE FOG TOP ELEVATION AND THICKNESS
264
265             if length(ind_sat) == max(ind_sat) % continuous fog (no subsaturated↙
layer between fog and stratus)
266                 N_fog_levels = max(ind_sat); % Nb of levels capturing fog
267             elseif length(ind_sat) < max(ind_sat) % subsaturated layer between fog↙
and stratus or only higher clouds above the fog
268                 clear k
269                 for k=1:max(ind_sat) % k+1 will give the level that is subsaturated
270                     if Tdd_adj_level(k+1,1)>= dwpt_threshold
271                         break
272                     end
273                 end
274                 if k<length(ind_sat)
275                     N_fog_levels = k; % Nb of levels in the fog is determined to be↙
below that subsaturation
276                 end
277             end
278
279             di=0.1; % 0.1 hPa increments: vertical resolution wanted
280
281             if Tdd_adj_level(N_fog_levels,1) == 1 % in case highest saturated level↙
is Tdd, no interpolation: fog top == geopotential height of that sounding level
282                 Thick_layer = sounding(N_fog_levels,3)-sounding(1,3); % fog thickness↙
= fog top elevation minus ground elevation
283                 fog_top_P = pz(N_fog_levels);
284                 fog_top_T = tz(N_fog_levels);
285             else
286                 if isnan(tdz_datapor(N_fog_levels+1)) % take second level if NaN
287                     % line segment for T
288                     x1  = [tz(N_fog_levels) tz(N_fog_levels+2)];
289                     if x1(1,1) == x1(1,2) % isotherm = script problem
290                         x1  = [tz(N_fog_levels) tz(N_fog_levels+2)];
291                         if x1(1,1) == x1(1,2)
292                             x1  = [tz(N_fog_levels) tz(N_fog_levels+3)];
293                         end
294                     end
295                     y1  = [-pz(N_fog_levels) -pz(N_fog_levels+2)];
296                     % line segment for Td
297                     x2  = [tdz_datapor(N_fog_levels) tdz_datapor(N_fog_levels+2)];
```

```
298                     if x2(1,1) == x2(1,2) % isotherm = script problem
299                         x2  = [tdz_datapor(N_fog_levels) tdz_datapor↙
(N_fog_levels+2)];
300                     end
301                     y2  = [-pz(N_fog_levels) -pz(N_fog_levels+2)];
302                 else
303                     % line segment for T
304                     x1  = [tz(N_fog_levels) tz(N_fog_levels+1)];
305                     if x1(1,1) == x1(1,2) % isotherm = script problem
306                         x1  = [tz(N_fog_levels) tz(N_fog_levels+2)];
307                         if x1(1,1) == x1(1,2)
308                             x1  = [tz(N_fog_levels) tz(N_fog_levels+3)];
309                         end
310                     end
311                     y1  = [-pz(N_fog_levels) -pz(N_fog_levels+1)];
312                     % line segment for Td
313                     x2  = [tdz_datapor(N_fog_levels) tdz_datapor(N_fog_levels+1)];
314                     if x2(1,1) == x2(1,2) % isotherm = script problem
315                         x2  = [tdz_datapor(N_fog_levels) tdz_datapor↙
(N_fog_levels+2)];
316                     end
317                     y2  = [-pz(N_fog_levels) -pz(N_fog_levels+1)];
318                 end
319
320                 for i = 1:100 % length of iteration: 0.1 hPa*100 = 10hPa = maximum↙
depth of interpolation (can be modified HERE)
321                     % line that intersects both
322                     x3 = [-20 20];
323                     y3 = [-pz(N_fog_levels)+(i*di) -pz(N_fog_levels)+(i*di)];
324
325                     % fit linear polynomial
326                     p1 = polyfit(x1,y1,1);
327                     p2 = polyfit(x2,y2,1);
328                     p3 = polyfit(x3,y3,1);
329
330                     % calculate intersection
331                     x_intersect13 = fzero(@(x) polyval(p1-p3,x),3);
332                     y_intersect13 = polyval(p1,x_intersect13);
333                     x_intersect23 = fzero(@(x) polyval(p2-p3,x),3);
334                     y_intersect23 = polyval(p2,x_intersect23);
335
336                     dewpoint_level(i) = abs(x_intersect13-x_intersect23);
337                 end
338
339                 if dewpoint_level(1,1) > dwpt_threshold % in case fog ONLY at surface
340                     fog_top_P = pz(1,1);
341                     Thick_layer = 0; % Fog thickness
342                     fog_top_T = tz(1,1);
343                 else
344                     fog_top_P =  pz(N_fog_levels) - max(find(dewpoint_level <=↙
dwpt_threshold))*di;
345                     y3 = [-pz(N_fog_levels)+(max(find(dewpoint_level <=↙
dwpt_threshold))*di) -pz(N_fog_levels)+(max(find(dewpoint_level <= dwpt_threshold))*di)];
346                     x3 = [-20 20];
347                     p3 = polyfit(x3,y3,1);
348                     x_intersect13 = fzero(@(x) polyval(p1-p3,x),3);
```

```
349                     y_intersect13 = polyval(p1,x_intersect13);
350                     x_intersect23 = fzero(@(x) polyval(p2-p3,x),3);
351                     y_intersect23 = polyval(p2,x_intersect23);
352                     fog_top_T = fzero(@(x) polyval(p1-p3,x),3);
353                     dz = 287 * 9.81^-1 * ((tz(N_fog_levels)+273.15+fog_top_T+273.15)↙
/2) * log(pz(N_fog_levels)/fog_top_P);
354                     Thick_layer = sounding(N_fog_levels,3)-sounding(1,3)+ dz; % Fog↙
thickness
355                 end
356             end
357
358             pen_depth = Thick_layer - (inv_base - sounding(1,3)); % thickness of fog↙
penetrating the inversion layer
359             FTE = Thick_layer + sounding(1,3); % Fog top elevation
360
361             % FIND FOG TYPE
362
363             if isnan(tdz_datapor(2)) % if second level of tdz is missing
364                 if tz(3)<tz(1) & tdz_datapor(3)<tdz_datapor(1)
365                     if Binary_saturated(1) == 1 & Binary_saturated(2) == 0 &↙
(Binary_saturated(3) == 1 | Binary_saturated(4) == 1)
366                         fog_type = 6; % fog below saturated inversion (stratus)
367                     elseif level_inv_base == max(ind_geop) & Tdd_adj_level(1,1) <=↙
dwpt_threshold & (level_inv_top-level_inv_base == 1 |level_inv_top-level_inv_base == 2) &↙
pen_depth<(inv_depth/2) % if inversion delimited by only two levels and fog doesn't↙
extend up to 50% inversion depth
368                         fog_type = 4; % fog capped by LLI
369                     elseif level_inv_base == max(ind_geop) & Tdd_adj_level(1,1) <=↙
dwpt_threshold & (level_inv_top-level_inv_base == 1 |level_inv_top-level_inv_base == 2) &↙
pen_depth>(inv_depth/2) % if inversion delimited by only two levels but fog extends above↙
50% of inv. depth
370                         fog_type = 5; % fog inside LLI
371                     elseif level_inv_base < max(ind_geop) & Tdd_adj_level(1,1) <=↙
dwpt_threshold
372                         fog_type = 5; % fog inside LLI
373                     elseif level_inv_base > max(ind_geop) & Tdd_adj_level(1,1) <=↙
dwpt_threshold
374                         fog_type = 3; % fog below LLI
375                     elseif Tdd_adj_level(1,1) > dwpt_threshold
376                         fog_type = 1; % missed
377                     end
378                 elseif tz(3) > tz(1) & Tdd_adj_level(1,1) <= dwpt_threshold
379                     fog_type = 2; % fog with SBI
380                 end
381
382             elseif tz(1,1) < T_threshold; % if ice or mixed-phase fog
383                 fog_type = NaN;
384             elseif Tdd_adj_level(1,1) > dwpt_threshold % if surface is subsaturated
385                 fog_type = 1; % missed
386             elseif (isempty(level_inv_base) | inv_base > sounding(find(pz==700),3)) &↙
Tdd_adj_level(1,1) <= dwpt_threshold % if no inversion
387                 fog_type = 0; % other
388
389             elseif tz(2) <= tz(1) % if no level is missing and low-level inversion↙
(LLI)
390                 if Binary_saturated(1) == 1 & Binary_saturated(2) == 0 &↙
```

```
(Binary_saturated(3) == 1 | Binary_saturated(4) == 1 | Binary_saturated(5) == 1)
                    fog_type = 6; % fog below saturated inversion (stratus)
                elseif level_inv_base == max(ind_geop) & Tdd_adj_level(1,1) <=
dwpt_threshold & (level_inv_top-level_inv_base == 1 |level_inv_top-level_inv_base == 2) &
pen_depth<(inv_depth/2)
                    fog_type = 4; % fog capped by LLI
                elseif level_inv_base == max(ind_geop) & Tdd_adj_level(1,1) <=
dwpt_threshold & level_inv_top-level_inv_base >2  & pen_depth<(inv_depth/2)
                    fog_type = 4; % fog capped by LLI
                elseif level_inv_base == max(ind_geop) & Tdd_adj_level(length
(ind_geop),1) == dwpt_threshold
                    fog_type = 4; % fog capped by LLI
                elseif level_inv_base == max(ind_geop) & Tdd_adj_level(1,1) <=
dwpt_threshold & (level_inv_top-level_inv_base == 1 |level_inv_top-level_inv_base == 2) &
pen_depth>(inv_depth/2)
                    fog_type = 5; % fog inside LLI
                elseif level_inv_base < max(ind_geop) & Tdd_adj_level(1,1) <=
dwpt_threshold & Binary_saturated(2) == 1
                    fog_type = 5; % fog inside LLI
                elseif level_inv_base > max(ind_geop) & Tdd_adj_level(1,1) <=
dwpt_threshold
                    fog_type = 3; % fog below LLI
                end

            elseif tz(2) > tz(1) & Tdd_adj_level(1,1) <= dwpt_threshold % if no level
is missing and surface-based inversion (SBI)
                fog_type = 2; % fog with SBI
            else
                fog_type = 0; % other
             end
        end

        Fog_11h(j,13)= fog_type;

    end
    clear sounding ind_sounding pz pr Nb_levels_700mb_T Nb_levels_700mb_Td fog_type
ind_geop Binary_saturated_stable Binary_saturated Binary_stable ind_pr level_inv_base
inv_base tdz_datapor tz Adia_s Adia_h radiosonde_datapor ind_datapor sounding_datapor
Tdd_datapor Tdd Tdd_adj_level k
    clear pen_depth Thick_layer N_fog_levels dewpoint_level fog_top_P fog_top_T dz
ind_sat p1 p2 p3 x1 x2 x3 y1 y2 y3 x_intersect13 y_intersect13 x_intersect23
y_intersect23 pen_depth
end

% figure

for n=1:6
    N_fog_type(n,1) = length(find(Fog_11h(:,13)==n));
end

f = figure;
labels = {'','','','','',''};
p = pie(N_fog_type,labels);
set(gca,'Fontsize',16);
hp = findobj(p, 'Type', 'patch');

```

```
% setting different colours for each fog class
classes = {'class 1','class 2','class 3','class 4','class 5','class 6'};
set(hp(1), 'FaceColor', [1 1 1]);
set(hp(2), 'FaceColor', [1 0.8 0.1]);
set(hp(3), 'FaceColor',[0.45 0.75 1]);
set(hp(4), 'FaceColor',[0.3 0.6 1]);
set(hp(5), 'FaceColor',[0.15 0.45 1]);
set(hp(6), 'FaceColor',[0 0.3 1]);

legend(hp,classes,'Position',[-0.01 0.25 0.2
0.5],'Orientation','vertical','Fontsize',18);
set(p(2:2:12),'FontSize',12);
title(sprintf('Fog Classes (%s)',num2str(station)),'Position',[0.07 1.26],'Fontsize',
24);

savdir = sprintf('C:/Gaelle/Matlab/IGRA/Emagram/output/Fog_classes_%s.png',num2str
(station));
saveas(f, savdir, 'png')

```

APPENDIX 6: Time series of monthly average number of significant IGRA levels below or including the 500 hPa pressure level over Danmarkshavn (DANM), Ittoqqortoormiit (ITTO) and Tasiilaq (TASI).

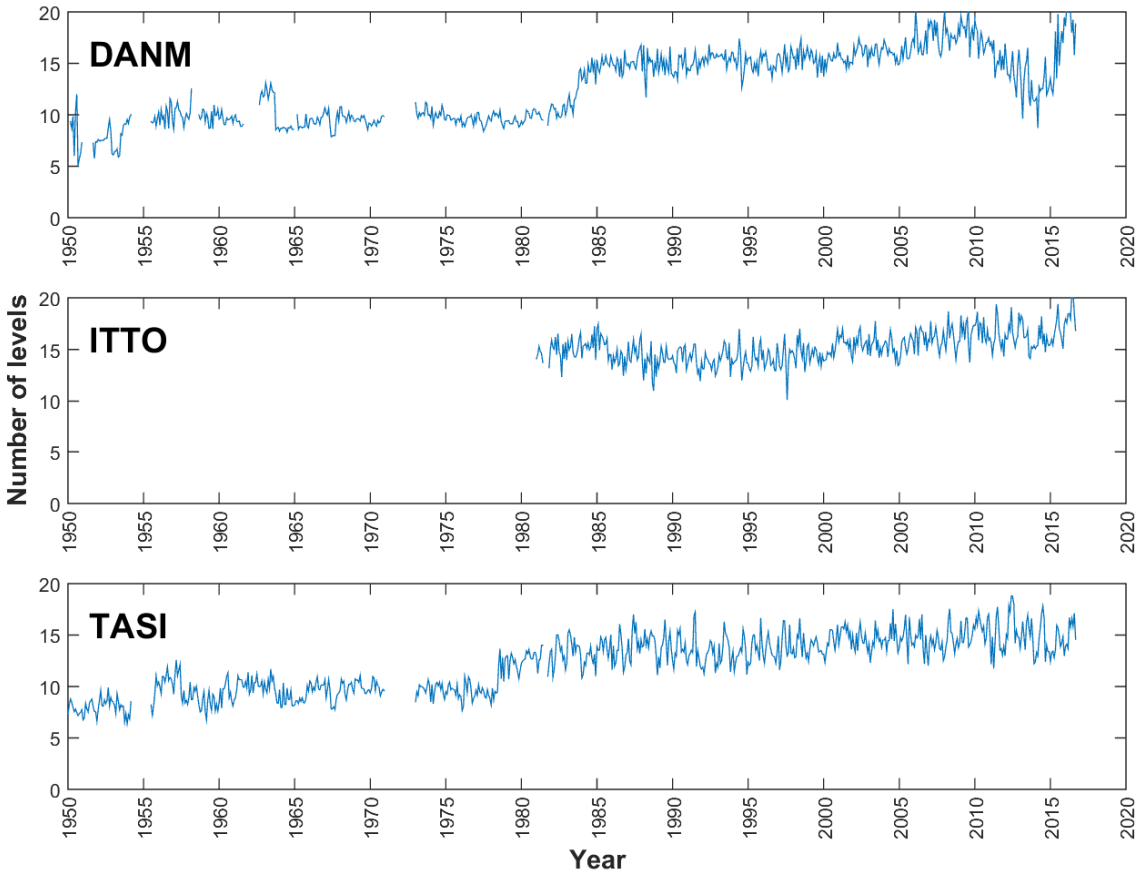

APPENDIX 7: Normalised hypsometry of 180 land-terminating glaciers of the Geike Plateau (centraleast Greenland) and proportion of ablation area potentially covered by median and maximum fog (dark blue dashed lines) and temperature inversions (light blue dashed lines). After Stearns and Jiskoot (2014) Fig. 8.6.